

IMPACTS OF KINEMATIC LINKS WITH A GRANULAR MATERIAL

Except where reference is made to the work of others, the work described in this dissertation is my own or was done in collaboration with my advisory committee. This dissertation does not include proprietary or classified information.

Seunghun Lee

Certificate of Approval:

George Flowers
Professor
Mechanical Engineering

Dan B. Marghitu, Chair
Professor
Mechanical Engineering

Nels Madsen
Professor
Mechanical Engineering

John Y. Hung
Professor
Electrical and Computer Engineering

George Flowers
Dean
Graduate School

IMPACTS OF KINEMATIC LINKS WITH A GRANULAR MATERIAL

Seunghun Lee

A Dissertation

Submitted to

the Graduate Faculty of

Auburn University

in Partial Fulfillment of the

Requirements for the

Degree of

Doctor of Philosophy

Auburn, Alabama
August 10, 2009

IMPACTS OF KINEMATIC LINKS WITH A GRANULAR MATERIAL

Seunghun Lee

Permission is granted to Auburn University to make copies of this dissertation at its discretion, upon the request of individuals or institutions and at their expense. The author reserves all publication rights.

Signature of Author

Date of Graduation

VITA

Seunghun Lee, son of Kyuwan Lee and Junghye Ahn was born on March 25, 1971, in Seoul, South Korea. He had completed the degree of B.S. in 1994 from Korea Military Academy and the degree of M.S. in 2000 from University of Tsukuba, Japan. He joined the Mechanical Engineering Department at Auburn University in September 2005.

DISSERTATION ABSTRACT

IMPACTS OF KINEMATIC LINKS WITH A GRANULAR MATERIAL

Seunghun Lee

Doctor of Philosophy, August 10, 2009
(M.S., University of Tsukuba, 2000)

186 Typed Pages

Directed by Dan B. Marghitu

The impact of kinematic links into a granular material is studied. In the impact process through the granular material defined as a conglomeration of discrete solids, the most important force governing the motion of a body is the resistance force of the granular matter. The resistance force acting on the body is studied as a linear superposition of a static (depth-dependent) resistance force and a dynamic (velocity-dependent) frictional force by considering the characteristics of the granular material acting like solid and liquid. The impact models considered are spheres, mathematical pendulum, compound pendulum, open kinematic chains, and elastic links. The impact is observed from the contact moment until the rest using various initial conditions. In this study, the impact angle and the initial velocity are the dominant conditions deciding the whole impact process. The results of the simulations and the experiments are analyzed based on the initial impact conditions. For most of the analyzed impact systems including elastic objects, the system under high force impact (higher initial velocity) comes to rest faster in the granular matter than the same system under low-force impacts (lower initial velocity).

ACKNOWLEDGMENTS

I would like to thank Professor Marghitu for providing me the opportunity to conduct research in this exciting field and guidance during the course of this work. I would also like to thank the government of South Korea for offering me the chance to study abroad at government expense. I would also like to thank all my advisory committee members, Professors George Flowers, Nels Madsen, and John Y. Hung for their suggestions. Finally, I wish thank all the professors, staff, and students I have interacted with throughout this study and Auburn University for a peaceful study environment.

I wish to dedicate this work to my wife, Hye Yon Cho, whose endless love and support in my life has enabled what I have accomplished including this work and has always been the origin of my desire to move forward.

Style manual or journal used Journal of Approximation Theory (together with the style known as “auphd”). Bibliography follows van Leunen’s *A Handbook for Scholars*.

Computer software used The document preparation package T_EX (specifically L^AT_EX) together with the departmental style-file `auphd.sty`, Adobe Illustrator CS, and Mathematica 6.0.

TABLE OF CONTENTS

LIST OF FIGURES		x
1	INTRODUCTION	1
2	DESCRIPTION OF THE PROBLEM	5
2.1	Coordinate system	7
2.2	Description of the models	9
2.2.1	Impact of a rigid sphere	9
2.2.2	Single impact of a planar kinematic chain	9
2.2.3	Multiple impacts of a planar kinematic chain with n links	12
2.3	Generalized coordinates	13
3	FORCE ANALYSIS	16
3.1	Dynamic frictional force F_d	17
3.2	Static resistance force F_s	19
3.2.1	Horizontal static resistance force F_{sh}	20
3.2.2	Vertical static resistance force F_{sv}	22
3.3	Air drag force	23
3.4	Application to the impact models	24
4	IMPACT OF RIGID OBJECTS	28
4.1	Impact of a rigid sphere	29
4.1.1	Impact of a mathematical pendulum	29
4.1.2	Oblique impact of a rigid sphere	36
4.2	Single impact with a granular medium	42
4.2.1	Impact of a free rigid link	42
4.2.2	Impact of a planar kinematic chain	52
4.3	Multiple impacts of a planar kinematic chain	70
5	IMPACT OF FLEXIBLE LINKS	83
5.1	Free elastic link	85
5.1.1	Transverse vibration of a free link	85
5.1.2	Modeling	87
5.1.3	Equations of motion	89
5.1.4	Simulation results	93
5.2	Elastic compound pendulum	99
5.2.1	Transverse vibration of an elastic compound pendulum	99
5.2.2	Modeling of an articulated elastic compound pendulum	102

5.2.3	Simulation results of the articulated elastic compound pendulum . . .	106
5.2.4	Modeling of a cantilevered elastic compound pendulum	114
5.2.5	Simulation results of the cantilevered elastic compound pendulum .	118
6	EXPERIMENTS	129
6.1	Experimental system	129
6.2	Experimental results	132
6.2.1	Impact of a free link	132
6.2.2	Impact of a rigid compound pendulum	137
7	CONCLUSION	144
	BIBLIOGRAPHY	147
	APPENDICES: MATHEMATICA PROGRAMS	152
A	MATHEMATICAL PENDULUM	153
B	OBLIQUE IMPACT OF A SPHERE	155
C	RIGID FREE LINK	157
D	RIGID COMPOUND PENDULUM	159
E	RIGID DOUBLE PENDULUM	162
F	TWO LINK KINEMATIC CHAIN WITH TWO IMPACT POINTS	165
G	ELASTIC FREE LINK	168
H	ELASTIC COMPOUND PENDULUM	171

LIST OF FIGURES

2.1	Coordinate system for rigid impact bodies	8
2.2	Coordinate system for flexible impact bodies	8
2.3	Oblique impact of a sphere	10
2.4	Impact of a mathematical pendulum	10
2.5	Impact of a free link	11
2.6	Single impact of a kinematic chain	12
2.7	Multiple impacts of a kinematic chain	13
3.1	Air drag force impeding the motion of the compound pendulum	24
3.2	Moving angle, q_m , of a link in planar motion	26
4.1	Free body diagram of a mathematical pendulum in impact	29
4.2	Impact results of the mathematical pendulum into a granular medium for $q(0) = 15^\circ$	33
4.3	Impact results of the mathematical pendulum into a granular medium for $q(0) = 45^\circ$	34
4.4	Impact results of the mathematical pendulum into a granular medium for $q(0) = 75^\circ$	35
4.5	Free body diagram of a rigid sphere in oblique impact	36
4.6	Impact results of the rigid sphere into a granular medium for $q(0) = 15^\circ$	39
4.7	Impact results of the rigid sphere into a granular medium for $q(0) = 45^\circ$	40
4.8	Impact results of the rigid sphere into a granular medium for $q(0) = 75^\circ$	41
4.9	Free body diagram of a free rigid link in impact	43

4.10	Impact results of the rigid cylinder type link for $q(0) = 0^\circ$	47
4.11	Resistance force F_d and F_s for $q(0) = 0^\circ$	48
4.12	Total resistance force F_R for $q(0) = 0^\circ$	49
4.13	Impact results of the rigid cylinder type link for $q(0) = 32^\circ$	50
4.14	Impact results of the rigid cylinder type link for $q(0) = 55^\circ$	51
4.15	Free body diagram of a single impact of a planar kinematic chain	52
4.16	Compound pendulum	58
4.17	Impact results of the rigid compound pendulum for $q(0) = 22^\circ$	59
4.18	Impact results of the rigid compound pendulum for $q(0) = 31^\circ$	60
4.19	Impact results of the rigid compound pendulum for $q(0) = 45^\circ$	61
4.20	Impact results of the rigid compound pendulum for $q(0) = 61.5^\circ$	62
4.21	Double pendulum	63
4.22	Angular velocities \dot{q}_1 and \dot{q}_2 results of the double pendulum impact for $q_1(0) = 30^\circ$, $q_2(0) = 75^\circ$, and $\dot{q}_1(0) = \dot{q}_2(0) = -1, -3, -5$ rad/s	65
4.23	Velocities v_{T_x} and v_{T_z} results of the double pendulum impact for $q_1(0) = 30^\circ$, $q_2(0) = 75^\circ$, and $\dot{q}_1(0) = \dot{q}_2(0) = -1, -3, -5$ rad/s	66
4.24	Angular velocities \dot{q}_1 and \dot{q}_2 results of the double pendulum impact for $q_1(0) = 75^\circ$, $q_2(0) = 30^\circ$, $\dot{q}_1(0) = -5$ rad/s, and $\dot{q}_2(0) = -1, -3, -5$ rad/s	67
4.25	Velocities v_{T_x} and v_{T_z} results of the double pendulum impact for $q_1(0) = 75^\circ$, $q_2(0) = 30^\circ$, $\dot{q}_1(0) = -5$ rad/s, and $\dot{q}_2(0) = -1, -3, -5$ rad/s	68
4.26	Free body diagram of multiple impacts of a planar kinematic chain	71
4.27	Two link kinematic chain with two impact points model	71
4.28	Velocities $v_{T_{1z}}$ and $v_{T_{2z}}$ results of the two link kinematic chain for $q_1(0) = 330^\circ$, $q_2(0) = 45^\circ$, and $v_{A_z}(0) = 1, 3, 5$ m/s	77
4.29	Velocities $v_{T_{1z}}$ and $v_{T_{2z}}$ results of the two link kinematic chain for $q_1(0) = 330^\circ$, $q_2(0) = 45^\circ$, and $\dot{q}_1(0) = -\dot{q}_2(0) = 1, 3, 5$ rad/s	78
4.30	Velocities $v_{T_{1z}}$ and $v_{T_{2z}}$ results of the two link kinematic chain for $q_1(0) = 330^\circ$, $q_2(0) = 45^\circ$, and $\dot{q}_1(0) = 1, 3, 5$ rad/s	79

4.31	Velocities v_{T1z} and v_{T2z} results of the two link kinematic chain for $q_1(0) = 330^\circ$, $q_2(0) = 45^\circ$, and $\dot{q}_2(0) = -1, -3, -5$ rad/s	80
5.1	Transverse vibrations of a flexible link	83
5.2	Free elastic link	84
5.3	Displacement z_T and velocity v_{Tz} results of the flexible link for $q_1(0) = 32^\circ$ and $\dot{q}_z(0) = 1.26, 1.87, 2.33$ m/s	95
5.4	Displacement q_2 and velocity \dot{q}_2 results of the flexible link for $q_1(0) = 32^\circ$ and $\dot{q}_z(0) = 1.26, 1.87, 2.33$ m/s	96
5.5	Displacement z_T and velocity v_{Tz} results of the flexible link for $q_1(0) = 55^\circ$ and $\dot{q}_z(0) = 1.45, 1.98, 2.43$ m/s	97
5.6	Displacement q_2 and velocity \dot{q}_2 results of the flexible link for $q_1(0) = 55^\circ$ and $\dot{q}_z(0) = 1.45, 1.98, 2.43$ m/s	98
5.7	Articulated elastic compound pendulum	100
5.8	Cantilevered elastic compound pendulum	100
5.9	Angle q_1 and angular velocity \dot{q}_1 results of the articulated elastic compound pendulum for $q_1(0) = 30^\circ$ and $\dot{q}_1(0) = -1, -3, -5$ rad/s	107
5.10	Displacement q_2 and velocity \dot{q}_2 results of the articulated elastic compound pendulum for $q_1(0) = 30^\circ$ and $\dot{q}_1(0) = -1, -3, -5$ rad/s	108
5.11	Angle q_1 and angular velocity \dot{q}_1 results of the articulated elastic compound pendulum for $q_1(0) = 60^\circ$ and $\dot{q}_1(0) = -1, -3, -5$ rad/s	109
5.12	Displacement q_2 and velocity \dot{q}_2 results of the articulated elastic compound pendulum for $q_1(0) = 60^\circ$ and $\dot{q}_1(0) = -1, -3, -5$ rad/s	110
5.13	Angle q_1 and angular velocity \dot{q}_1 results of the articulated elastic compound pendulum for $q_1(0) = 75^\circ$ and $\dot{q}_1(0) = -1, -3, -5$ rad/s	111
5.14	Displacement q_2 and velocity \dot{q}_2 results of the articulated elastic compound pendulum for $q_1(0) = 75^\circ$ and $\dot{q}_1(0) = -1, -3, -5$ rad/s	112
5.15	Angle q_1 and angular velocity \dot{q}_1 results of the cantilevered elastic compound pendulum for $q_1(0) = 22^\circ$ and $\dot{q}_1(0) = -1.75, -3.38, -4.66$ rad/s	119
5.16	Displacement q_2 and velocity \dot{q}_2 results of the cantilevered elastic compound pendulum for $q_1(0) = 22^\circ$ and $\dot{q}_1(0) = -1.75, -3.38, -4.66$ rad/s	120

5.17	Angle q_1 and angular velocity \dot{q}_1 results of the cantilevered elastic compound pendulum for $q_1(0) = 31^\circ$ and $\dot{q}_1(0) = -3.31, -6.24, -8.41$ rad/s	121
5.18	Displacement q_2 and velocity \dot{q}_2 results of the cantilevered elastic compound pendulum for $q_1(0) = 31^\circ$ and $\dot{q}_1(0) = -3.31, -6.24, -8.41$ rad/s	122
5.19	Angle q_1 and angular velocity \dot{q}_1 results of the cantilevered elastic compound pendulum for $q_1(0) = 45^\circ$ and $\dot{q}_1(0) = -2.66, -6.47, -9.06$ rad/s	123
5.20	Displacement q_2 and velocity \dot{q}_2 results of the cantilevered elastic compound pendulum for $q_1(0) = 45^\circ$ and $\dot{q}_1(0) = -2.66, -6.47, -9.06$ rad/s	124
5.21	Angle q_1 and angular velocity \dot{q}_1 results of the cantilevered elastic compound pendulum for $q_1(0) = 61.5^\circ$ and $\dot{q}_1(0) = -2.70, -6.54, -9.17$ rad/s	125
5.22	Displacement q_2 and velocity \dot{q}_2 results of the cantilevered elastic compound pendulum for $q_1(0) = 61.5^\circ$ and $\dot{q}_1(0) = -2.70, -6.54, -9.17$ rad/s	126
6.1	Free link applied for experiments	130
6.2	Compound pendulum applied for experiments	130
6.3	Motion measurement system Optotrak 3020	131
6.4	Experimental and simulation results of the cylinder type rigid link for $q(0) = 0^\circ$	134
6.5	Experimental and simulation results of the cylinder type rigid link for $q(0) = 32^\circ$	135
6.6	Experimental and simulation results of the cylinder type rigid link for $q(0) = 55^\circ$	136
6.7	Experimental and simulation results of the compound pendulum for $q(0) = 22^\circ$	139
6.8	Experimental and simulation results of the compound pendulum for $q(0) = 31^\circ$	140
6.9	Experimental and simulation results of the compound pendulum for $q(0) \approx 45^\circ$	141
6.10	Experimental and simulation results of the compound pendulum for $q(0) = 61.5^\circ$	142
6.11	Stopping time results of the compound pendulum	143

CHAPTER 1

INTRODUCTION

A granular material is a simple mixture of solid particles. Grains such as rice, soils including sand, and artificial granules such as fertilizer, glass beads, ball bearings, and pills can be classified as granular materials. Even snow is considered as a granular medium in the study of avalanche phenomenon. Powder is a special class of granular material. It is composed of much fine particles compared with the usual granular material. Due to its characteristics, inhomogeneous, disordered, and anisotropic on a microscopic scale [1], the powder can flow much easily when agitated.

An individual granule is solid and shares the physical properties of solid matter. A granular in its conglomerated state acts like a solid in the case when the kinetic energy of individual grains is low and the grains keep a stationary state. However individual grains begin to loose the stationary state and the granular material begins to fluidize acting liquid-like in case when the external driving forces including tilting and shaking exceed the stationary conditions. Roughly speaking the granular medium may flow such as ordinary fluids. According to circumstances, the granular material may act even like a gas when the external driving forces act intensively and the contacts between the grains become highly sporadic.

The first approach of the granular medium was based on the contact and the collision of solid particles [2, 3, 4, 5, 6, 7, 8, 9, 10]. The other approach was based on fluid mechanics and hydrodynamics approach taking the fluid-like characteristics of the materials into account [11, 12, 13, 14, 15].

Even though granular materials show similarities, they exhibit unusual behaviors compared with solids, liquids, or gases. For example, when granular materials are oscillated by shaking or vibrating containers, they become inhomogeneous in space and time. They are

segregated and reorganized [16, 17, 18, 19, 20, 21, 22]. And the compaction happens also by the vibration of the package container [23, 24, 25, 26, 27, 28]. In some cases, the pressure of a granular material located in tall containers is non-linear with the depth of the material due to the contact force generated between granules or between granules and the container walls [29]. These contact forces constitute a network of forces at large scale [30, 31, 32, 33, 34, 35]. Granular materials show also complicated behaviors such as formation of arches, convection rolls, pattern formation, and dynamical instabilities [36].

In industry, the granular materials are the second-most manipulated material (the first one is water) [36]. Not only most raw materials exist as the form of granules but also many final products are manufactured as granular materials. Therefore the study of this material can be applied to industries such as food, pharmaceutical, mining, chemical, semiconductor, agriculture, and construction. Disasters in nature such as landslides and avalanches show the importance of the study of the granular medium.

The impact with a granular material is also an interesting subject in the field of engineering. The impact with a granular material is not a simple problem because the phenomena of contact, collision, and flow simultaneously happen when a body impacts the material. Of course, the major phase state of granular material is decided by the penetrating velocity of an impacting body in the granular material. In the case of high speed impact, the characteristic of the granular material in the vicinity of a rigid body is similar to a fluid. The granular material acts like a solid when the penetrating speed of the body is slow. However in usual impact cases the behaviors of the granular materials exhibit the combined form of these characteristics.

Most early studies of the impact penetrating problems started from high speed impact and were motivated by military applications. Benjamin Robins carried out experiments in gunnery and wrote “New Principles in Gunnery” (1742), which contains a description of his ballistic pendulum. His work was translated into German by Leonhard Euler (1745) [37] and Euler added annotations of his own. Jean-Victor Poncelet developed Poncelet’s model in his book “Cours de Mecanique Industrielle” (1829). This model is considered as

the most venerable and classical empirical formula to calculate the penetration resistance of a target stricken by a flat-nosed projectile [38].

The study having begun from high speed impact area attracts attention recently again at relatively low speed regime in granular physics. Penetrating granular medium with a rigid body at very low speed and the impact cratering including the impact penetration are the representative areas. In the area of penetrating granular medium at low speed, the horizontal resistance force by granular materials [39], jamming and fluctuations of the resistance force [40, 41], shape effects on the resistance force [42], and the vertical resistance force [43, 44] were studied. In the case of the impact cratering, the size, the depth, and the form of the crater with the initial impact conditions of a rigid body were studied [45, 46, 47, 48, 49, 50, 51, 52]. To develop a force law model for the granular impacts and to find a mathematical formula in order to measure the impact force of objects dropped represent a new interest in this field of the study [51].

The resistance force models, linear to the depth of a body [50, 53], linear to the velocity of a body [46], and linear to the square of velocity of a body [49] have been studied to explain the motion in the granular materials. Tsimring and Volfson studied the impact cratering by penetration of large projectiles into a dry granular medium [48]. In their study they proposed for the resistance force model the sum of a velocity dependent drag force and a depth dependent resistance force. A depth dependent resistance force (static resistance force) of a rigid body in a granular matter has been studied in granular physics prior to their study. The static resistance force model has been developed for the horizontal motion in [39, 40, 41, 42] and for the vertical motion in [43, 44].

The models of the resistance force impeding the motion of a rigid body in a granular materials and high speed motion capture cameras enabled to simulate and to confirm the velocity of the bodies. Ambroso, Kamien, and Durian [49] studied the time dependance of a rigid sphere impacting and concluded the stopping time taking for a rigid body to stop from the moment of impact is a function of the geometry and the initial impact velocities. Hou, Peng, Liu, Lu, and Chan [50] studied the deceleration of projectiles impacting with

the medium and they concluded the stopping time is not a linear function of initial impact velocity. The paper of Katsuragi and Durian has sparked new interest in the field of impact with a granular matter regarding the stopping time of a rigid body. They introduced the resistance force model proposed by [48] to study the impact of a rigid sphere and verified with a line-scan digital CCD camera [51]. They analyzed an interesting phenomenon, how rapidly a sphere impacting a granular medium slows upon collision and they clarified the relation between the stopping time of a rigid body and the initial impact velocity in a vertical impact situation. Analysis shows that as the speed at which the spheres impact the medium increases, the sooner it will come to rest for the vertical impact. Lee and Marghitu extended the study to the model of a rigid body obliquely impacting the medium and reported similar results even in the case of oblique impact [54].

As mentioned, granular materials are ubiquitous. Hence the impact with a granular can take place in various granular material environments. This means its study can be applied in numerous areas such as robotic locomotion, tracked vehicles, and heavy duty construction equipments. Especially military operation environments are closely related with this study because in general the military operations happens in outfields such as soil, sand, mud, or mixed environments. Therefore developing or planning to develop multi-legged military robots for surveillance or carrying cannot avoid the continuous impact with the granular materials. From this view point, the study of the impact with granular medium can be applied to development including the design, the manufacture, and the optimization of the operations of these multi-body systems.

In this study we focused on modeling and simulation of kinematic chains impacting a granular medium using the resistance force model verified by Katsuragi [51] as the sum of a velocity dependent drag force and a depth dependent resistance force. We also analyzed the relation among initial impact velocities, stopping time, and penetrating depth based on the experimental and the simulation results. To our best knowledge this is the first time when a mathematical model is proposed, analyzed, and experimentally verified for the impact of kinematic links impacting into a granular matter.

CHAPTER 2

DESCRIPTION OF THE PROBLEM

The purpose of this study is to analyze the impact and penetrating motion of a particle and kinematic chains into a granular material. As introduced, the impact of spheres and cylinders with a granular material have been studied by various researches from high to low speed impact taking into account the depth and the width of the crater. However, most studies were restricted in one vertical direction. There had not been studies regarding the general impact conditions such as oblique impact and penetration with low initial impact velocity although almost all real impact problems happen under this oblique condition.

In this study, the motions of impact bodies are restricted to planar motion. In order to analyze the collision effect, the models of a single impact point and multiple impact points are chosen as analytical models. The single impact point model includes the oblique impact of a sphere, a mathematical pendulum, and single impact of a planar kinematic chain. For multiple impact points model, a planar kinematic chain having multi contacts with a granular medium is studied. The impact of a planar kinematic chain is separately studied as a rigid and as a flexible model.

Basically the most important component in modeling the impact with a granular material is to understand the resistance forces originated from the granular material. There had been studies about granular physics in order to explain the unusual characteristics of granular materials at high and low speeds. However there are not enough researches studying the problems of resistance forces impeding the motion of a rigid body in a granular material. In this study, the resistance forces affecting the motion of a body are studied based on the characteristics of a granular material acting fluid-like and solid-like. Based on these

characteristics of a granular material, the resistance forces are studied as the dynamic frictional force (velocity-dependent force) which is modeled from fluid dynamics and the static resistance force (depth-dependent force) which is modeled from solid particle contacts.

There are various mathematical modeling methods such as the equations of Newton-Euler, Lagrange, and Kane. In this study, the descriptions of the dynamics of the system of particles and kinematic chains are formulated using the Newton-Euler equations. Lagrange's and Kane's equations can be also applied and were tested but there are no differences in the numerical results using different methods.

Initial impact conditions are decisive factors for the motion of the particle and the kinematic chain during penetration phase in the case that there are no drive force and no moment to move and to rotate the links. Of course, the initial states of a granular material including density and volume fraction are also a very important components because the resistance forces strongly depend on them. However the initial states of the granular material utilized in experiments and simulations are assumed not to change during the experiments in order to investigate the effects of the initial impact conditions. An actual granular material test bed was prepared as equally as possible at every impact experiment. Under this assumption, the most important initial conditions for impact problem are the angle and the velocity at the impact moment. The experiments and the simulations are performed under these conditions of various initial impact angles and velocities and the results are compared.

The simulations of the models are basically performed utilizing `NDSolve` function of Mathematica and this software is considered as sufficient to solve the O.D.E.s formulated by Newton-Euler equations. Due to the characteristics of the resistance forces acting always opposite to the direction of motion of an impact object, the simulation should solve repeatedly, should start and stop when the motion of the rigid body changes direction until the rest of the rigid body. The simulation are performed with variable and fixed step methods.

The experiments are performed several times for a certain initial impact angle and velocity. At every experiment, the granular material of test bed is plowed and flatted to provide almost the same state of the material and to avoid ageing effects arising in

repeated experiments. The data attained from the repeated experiments are averaged to minimize the effects of abnormalities such as fluctuation phenomenon which can occur during experiments. Experimental data are applied to find the resistance force coefficients and the experimental results will be compared with the simulation results to verify the impact models. As an experimental equipment, NDI (Northern Digital Inc.) optotrak system is utilized for the motion capturing of impact objects and the digitizing of the captured data. The system can capture the position of markers within the RMS accuracy of 0.1mm and can track up to 256 markers. The position of the impact body was captured with 3D data cartesian coordinate system with 500 frames/s.

The impact and penetrating motions of a particle and kinematic chains obtained from simulations and experiments will be analyzed and compared based on the initial impact conditions. We analyze how the initial impact conditions affect the penetration including the depth and transition of the velocity after impact. Especially, the effects of the initial impact conditions, deceleration and stopping time from the moment of impact until the rest of an impact body will be evaluated. Until now only the vertical impact of a sphere type was reported [51] and our study will evaluate the effects of initial impact angle including oblique impact for rigid and elastic links.

2.1 Coordinate system

The motion of the considered systems are in 2D (planar motion). For describing the motion of the impact object composed of rigid bodies, the system utilizes a fixed frame because it is sufficient to describe the planar motion of the models with a fixed cartesian coordinate system. The x -axis is horizontal, with the positive sense directed to the right, the z -axis is vertical, with the positive sense directed downward, and y -axis is perpendicular to the plane of motion as shown in Fig. 2.1. The planar motion of an impact rigid body will be in the xz plane. The origin of the coordinate system will be fixed. The unit vectors for the x -axis is \mathbf{i}_0 , the y -axis is \mathbf{j}_0 , and the z -axis is \mathbf{k}_0 . The angle between the z -axis and the link i of kinematic chain consisting of n interconnected rigid links is denoted by q_i

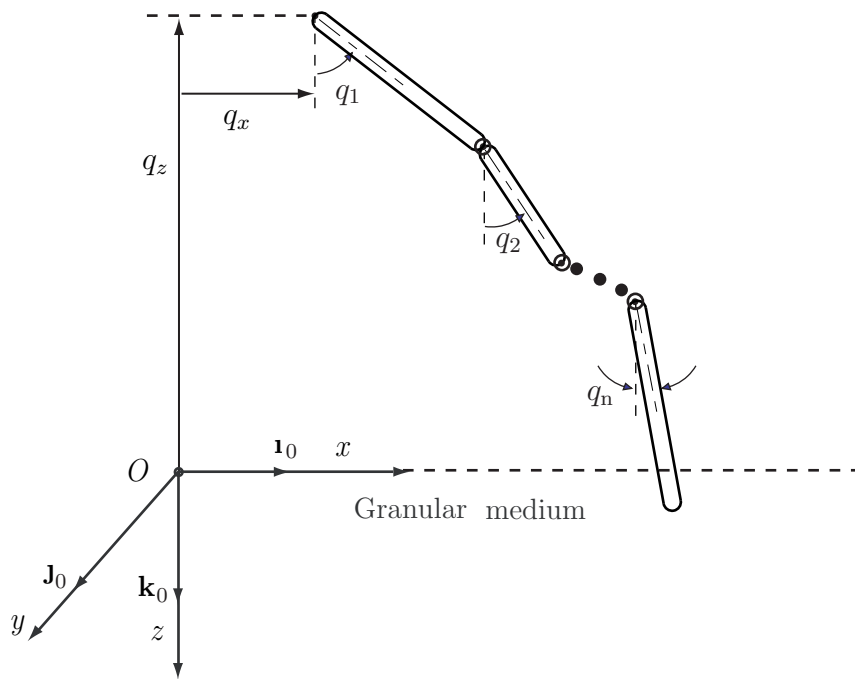


Figure 2.1: Coordinate system for rigid impact bodies

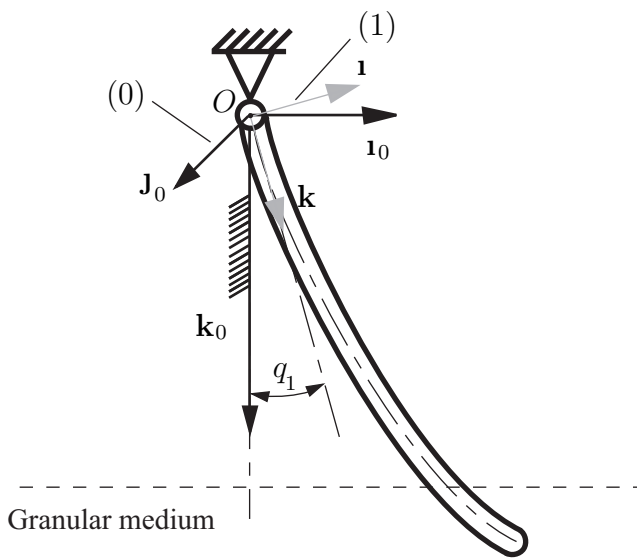


Figure 2.2: Coordinate system for flexible impact bodies

($i = 1, 2, 3, \dots, n$). The displacement from the origin to a certain point is denoted by q_x in x -axis and by q_z in z -axis. For describing the motion of kinematic chain composed of flexible bodies, the system utilizes a fixed frame and a rotating reference frame as shown in Fig. 2.1. The motion of the flexible bodies are described in a fixed reference frame (0) of unit vectors $[\mathbf{i}_0, \mathbf{j}_0, \mathbf{k}_0]$ and a mobile (rotating) reference frame (1) of unit vectors $[\mathbf{i}, \mathbf{j}, \mathbf{k}]$.

2.2 Description of the models

2.2.1 Impact of a rigid sphere

A general representations of a sphere and a mathematical pendulum impacting a granular material are shown in Figs. 2.3 and 2.4. The impact is initiated when the sphere (mass m_s and diameter d_s) strikes the surface of a granular material. In this study, its diameter d_s is considered relatively small and then its motion is assumed to be the motion of a particle. The initial impact conditions are represented as initial linear velocity and initial impact angle. The motion of the sphere will be observed based on the initial impact conditions. In particular, the impact by the sphere does not change the direction of the velocity after the impact moment but the mathematical pendulum can changes the direction of the velocity on z direction when the sphere passes through vertical axis. Therefore the impact by the mathematical pendulum may lead to several outcomes depending on initial impact the angles and the velocity.

2.2.2 Single impact of a planar kinematic chain

Impact of a free link

The link utilized for the impact model has the length L , the mass m_c , and the diameter d_c as shown in Fig. 2.5. The impact is initiated when the end T strikes the surface of a granular material. This problem is studied based on the continuum modeling and additionally a flexible model is simulated in order to compare the flexible elastic body and the rigid body. The initial conditions are given by the linear vertical impact velocity and angular position.

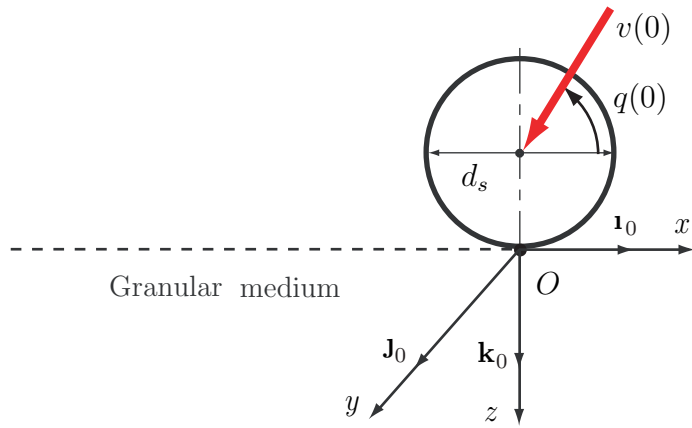


Figure 2.3: Oblique impact of a sphere

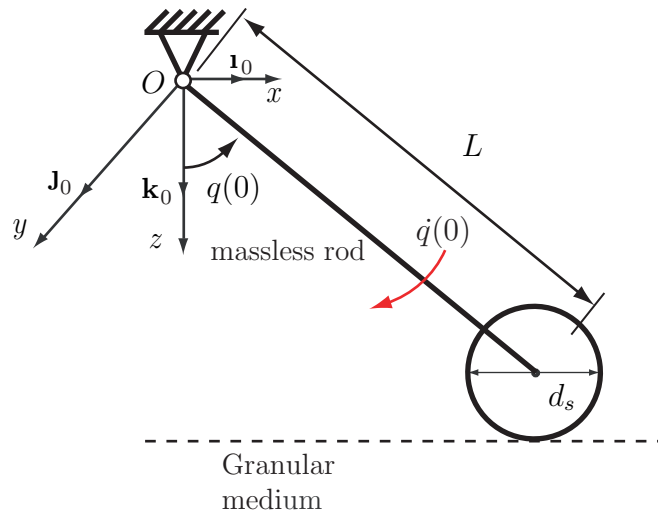


Figure 2.4: Impact of a mathematical pendulum

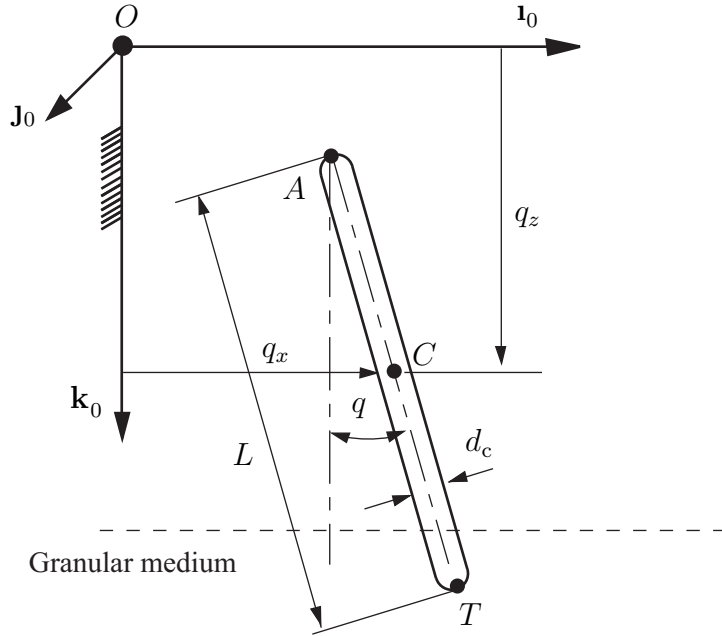


Figure 2.5: Impact of a free link

Even though there is no tangential force at the initial impact moment, after impact the horizontal resistance force is generated by the rotating link.

Single impact of a planar kinematic chain with n links

A schematic representation of a kinematic chain consisting of n interconnected rigid links $1, 2, 3, \dots, n$ is shown in Fig. 2.6. The kinematic chain has the rotational joints at A_i ($i = 0, 1, 2, \dots, n - 1$) and each link i has the length L_i , the mass m_i , and the same diameter as d_c . The impact is initiated when the end last T of the link n strikes the surface of a granular material. The initial combination of the linear and rotational impact motion are considered as initial impact conditions. The impact may lead to several consequences depending on initial conditions such as the initial impact angles of the links and the velocity of the tip at the impact moment as well as the characteristics of a granular medium such as resistance force coefficients. The case when only the last link n is penetrating the granular medium is considered and modeled in this study. This problem is also studied as an elastic model and a rigid model for the special case $n = 1$ (compound pendulum).

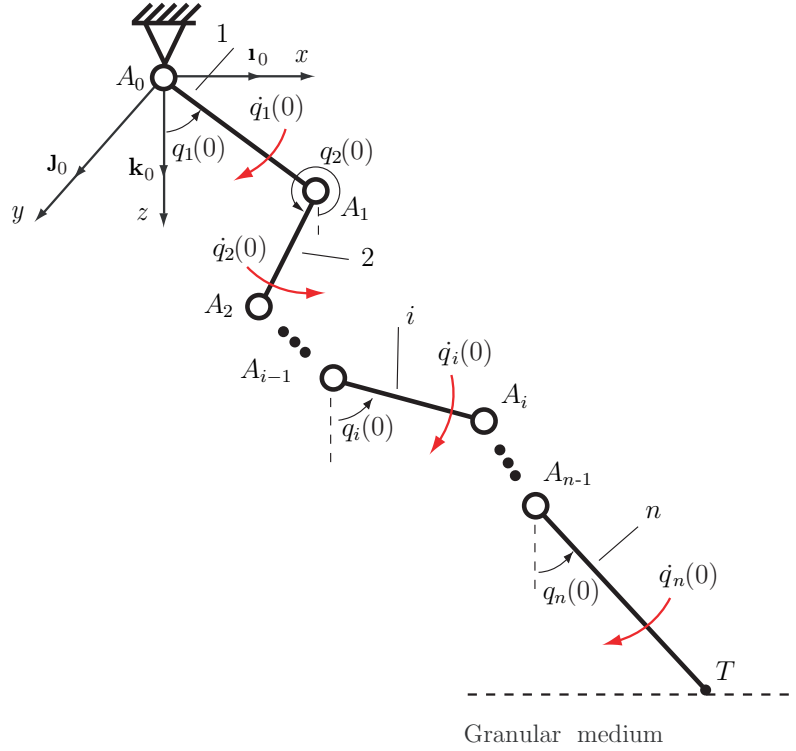


Figure 2.6: Single impact of a kinematic chain

2.2.3 Multiple impacts of a planar kinematic chain with n links

A schematic representation of a kinematic chain consisting of n interconnected rigid links $1, 2, 3, \dots, n$ and l joints A_i ($i = 1, 2, 3, \dots, l$) is shown in Fig. 2.7. Each link i has the length L_i , the mass m_i , and the same diameter, d_c . Immediately before impact the end links of the kinematic chain can be resting on the surface surfaces, impacting the surface, or not interacting with the surface. The impact is initiated when a specific end T_j ($j = 1, 2, 3, \dots, m$) or all ends of the chain strike the surface S_j . The angle of the surface with the horizontal is θ_j . The combination of the linear and the rotational impact displacements are considered as initial impact conditions. The impact initiated at T_j may also lead to several outcomes depending on the initial impact conditions as well as the characteristics of a granular medium.

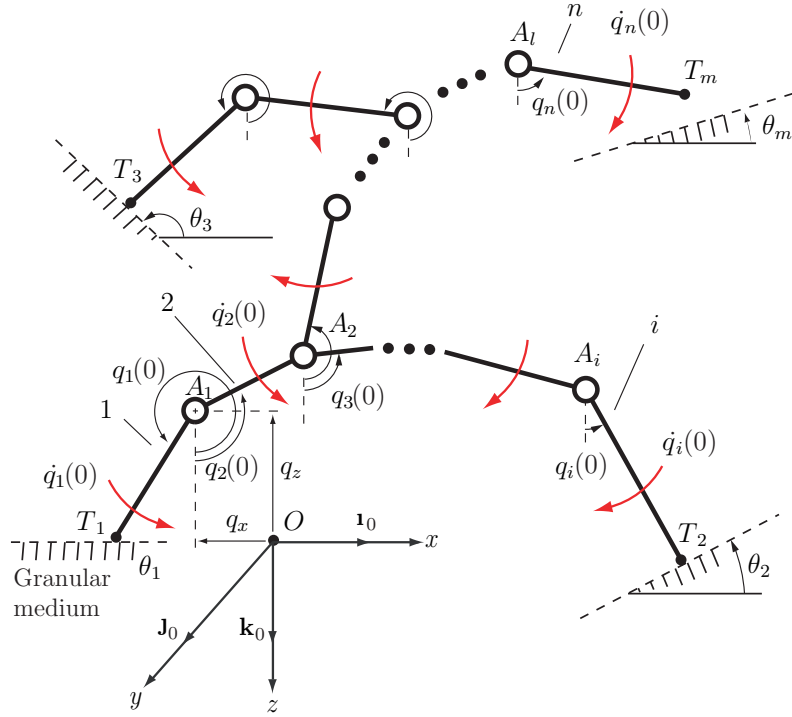


Figure 2.7: Multiple impacts of a kinematic chain

2.3 Generalized coordinates

In the case of the oblique impact of a sphere, the impact and the penetrating motion of the rigid body is restricted to xz plane. The numbers of degrees of freedom for the oblique impact of the sphere is 2. Hence the generalized coordinates of the model can be expressed by displacements in the xz plane as

$$\mathbf{q} = \{q_x, q_z\}^T, \quad (2.1)$$

where q_x and q_z represents the displacements from the origin to the mass center of the sphere in x -axis and in z -axis respectively.

In order to describe the motion of a rigid free link impacting and penetrating a granular medium, at least three position coordinates are required even though the motion is restricted to xz plane. Two displacement coordinates q_x and q_z and one angular position coordinates

q can be considered as generalized coordinates of the model as

$$\mathbf{q} = \{q_x, q_z, q\}^T. \quad (2.2)$$

For a flexible free link, the generalized coordinates include the coordinates of the rigid free link and additionally the elastic coordinates because the position of each point on the link depends on the deformation of the link which is represented by infinity superposition of deformation. The generalized coordinates can be given as

$$\mathbf{q} = \{q_x, q_z, q_1, q_2 \dots q_\infty\}^T. \quad (2.3)$$

In the model of a single impact of kinematic chains, the impact and the penetrating motion of each link is translational and rotational simultaneously (Fig. 2.6). Each link i has one relative degree of freedom with respect to the link $i - 1$, and therefore the number of D.O.F. is n . Angles, q_i s, are changing with time at the instant of interest and even translational motion of each link can be described by the angles. Therefore the angles q_i s are appropriate generalized coordinates describing the motion of the kinematic chain and the generalized coordinates can be expressed by $n \times 1$ -dimensional vector as

$$\mathbf{q} = \{q_1, q_2, q_3, \dots, q_n\}^T. \quad (2.4)$$

The mathematical and the compound pendulum are particular cases with $n = 1$. However, for the flexible compound pendulum, the generalized coordinates can be represented as the rigid and elastic coordinates as

$$\mathbf{q} = \{q_1, q_2, q_3, \dots q_\infty\}^T. \quad (2.5)$$

For multiple impacts of a planar kinematic chain, the number of D.O.F. is $n + 2$ (Fig. 2.7). The generalized coordinates, q_x and q_z , are the displacements from the origin to a

certain particular point. The angles, q_i , and the displacements, q_x and q_z , are changing with time at the instant of interest and can be considered as generalized coordinates describing the motion of the kinematic chain. The generalized coordinates can be expressed by $(n + 2) \times 1$ -dimensional vector as

$$\mathbf{q} = \{q_x, q_z, q_1, q_2, q_3, \dots, q_n\}^T. \quad (2.6)$$

CHAPTER 3

FORCE ANALYSIS

For the impact with penetration into a granular medium, the most important interaction forces between the body and the medium is the resistance force of the medium on the body from the moment of impact until the body stops. Even after the body stops, the reaction forces between the kinematic chain and the granular medium exist due to the gravity force and the static resistance force.

There are various models of resistance forces that act upon the body during penetration process. The Bingham's model is defined as $F_R = F_0 + bv$ and has been utilized in the case when the drag is viscous. The model is originated for a viscoplastic material that behaves as a solid at low stresses but flows as a viscous fluid at high stress. Bruyn and Walsh applied this model and calculated the penetration of spheres into loose granular material [46]. The Poncelet's model $F_R = F_0 + cv^2$ is originated from high speed impact and has been applied in the situation when the drag is inertia, where v is velocity of the body relative to a medium, b and c are drag coefficients. The Bingham's model has recently been advocated for granular impact, while the Poncelet's model has long been used for ballistics applications [49].

Allen, Mayfield, and Morrison [55, 56] suggested the resistance force model including the Bingham's and the Poncelet's model as $F_R = Av^2 + Bv + C$ in the study of projectile penetrating sand, where A is a classical fluid dynamic drag parameter, B is a deceleration parameter due to kinetic friction on the surface of the projectile, and C is the deceleration force due to the inherent structural characteristics of the target material.

However, some recent research results [39, 40, 41, 42, 43, 44] indicate that the static resistance force, defined as a constant for the Bingham's and the Poncelet's models, depends on the depth of penetration linearly or non-linearly. Lohse, Rauhe, Bergmann, and van der

Meer formulated the resistance force model made up of the only static resistance force [53]. They suggested the resistance force as $F_R = kz$, where k is a constant and z is the penetrated depth. Tsimring and Volfson [48] proposed a resistance force model based on the Poncelet’s model and the static resistance force model studied in [39] as a generalized Poncelet’s model. The total resistance forces acting on a moving body into a granular matter can be generalized as the sum of the static resistance force characterized by a depth-dependent friction force as well as the dynamic frictional force characterized by a velocity-dependent drag force as

$$F_R = F_s(z) + F_d(v), \quad (3.1)$$

where F_s is the static resistance force and F_d is the dynamic frictional force. With this approach the resistance force model can utilize the solid-like and fluid-like characteristics simultaneously.

Another possible force impeding the body penetrating a granular medium is generated by air resistance. In some case, air drag force plays an important role adding the disturbing force to an object moving such as the motion of a car. The air drag force depends on the density of the medium and on the velocity of the moving object. However the effect of this resistance force in the problem of the impacting with a granular is not important because the simulation results show ignorable differences.

3.1 Dynamic frictional force F_d

The dynamic frictional force F_d is conceptually the same force as “drag” widely used in the field of fluid dynamics. Even though the state of a granular matter is not a fluid but a solid, individual grains begin to lose stationary state in their contacts and a granular material begins to fluidize acting liquid-like when external driving forces including tilting and shaking exceed the condition of stationary. From this fluid-like behavior of a granular

matter, the resistance force is assumed to be as a drag force impeding the body motion [57, 58, 59, 60, 61].

In case of the impact with a granular material, once a body penetrates through the granular matter after impact, the matter contacting with the moving body partly acts like a fluid and this resistance force begins to be generated by the relative movement of the body with the granular material and acts in a direction opposite to the instantaneous relative velocity of the body. Hence, in the case of impact with the granular material, the force is generated from the moment of impact until the rest of the body. The dynamic frictional force acts no more as the resistance force impeding the motion of a body when the body and the granular material keep stationary state. The force is a velocity-dependent force unlike ordinary resistive friction force such as the static resistance force which depends on depth of body in a granular material.

Like the drag force model in fluid dynamics, the dynamic frictional force F_d also had been modeled as a linear drag force or a quadratic drag force. Therefore the Bingham's model utilizing a linear drag force model had been advocated for low speed granular impact, while the Poncelet's model utilizing a quadratic drag force had long been used for ballistics applications [49]. However the research results using a dilute granular flow condition which is not affected by the static resistance force [57, 59, 61] and the research results at low speed impact [48, 51] show that the quadratic drag force model is more suitable for the dynamic frictional force F_d than the linear drag force model even at relatively low speed regime. The dynamic frictional force can be modeled as

$$\mathbf{F}_d = -\frac{\mathbf{v}}{|\mathbf{v}|} \eta_d \rho_g A_r \mathbf{v} \cdot \mathbf{v}, \quad (3.2)$$

where $-\mathbf{v}/|\mathbf{v}|$ term is applied because the dynamic frictional force acting on the opposed direction of the velocity vector \mathbf{v} , η_d is a drag coefficient determined from experimental results, ρ_g is the density of the granular medium, and A_r is the reference area of the body.

3.2 Static resistance force F_s

The static resistance force is an internal resisting force and appears when an external force is applied to a body. This resistance force does not depend on the velocity or the acceleration of a body and acts as an internal stress. Therefore this force acts as a main resistance force when a body penetrates a granular medium at low speed.

The existence of this force not existing in a fluid can be observed easily. When a body is put on the granular material, the body starts to penetrate vertically through the granular material but does not sink beyond a certain depth. The body stops to penetrate in the material due to this resistance force unlike an usual fluid in which a body sinks unlimitedly without a lift force such as buoyancy.

Even though this resistance force play an important role in a body penetrating a granular material, the force had not been highlighted comparatively in the early studies. Most models including the Bingham's and the Poncelet's models have considered this force as a mere constant. Because the dynamic frictional force originated from a velocity-dependent drag force acts as a main resistance force in the study at relatively high speed impact, the static resistance force was modeled using a simple form.

However, the theoretical modeling of this force originated from the characteristics of a granular material even in stationary state is not that easy to be determined. Various research results explain the origin of this resistance force as the network of forces generated from contacts between granules within the material pile [30, 33, 31, 34, 32, 35].

In the case of impact with a granular material problem, the force acting on a body is not generated only by interacting between granules in contacts. Describing interacting forces of a certain moment during the continuous penetrating process, the force interacts between a penetrating body and granules located on the body circumference and the interacts of the contacting forces among the granules in the vicinity of the body are expanded to other granules of a granular container. As a consequence, the interacts of the contacts between granules become to form a force chain in a granular containing bed as bulk scale.

The reason this resistance force is not easily explained in the impact penetrating problem is that the force is transmitted following consecutive granular medium movement propagation such as chain reaction beginning with serial displacements of granules placed at the path of the moving body and ending with large scale reorganization of granules in the container. That means the forces and their spatial correlations, specifically in response to forces at the granular system boundaries do not represent fixed structure. Force chains are connected newly or disconnected continuously until the rest of penetration. This process is strongly influenced by properties of a granular matter, the external shape of a body, packaging state of medium, even the form of a vessel containing medium [41, 62]. Any insignificant changes during the continuous penetration can increase uncertainties of the propagation chain. These uncertainties in a real impact problem make the forces not to propagate uniformly through the granular matter but localized along directional force chains. The inhomogeneous force propagation and the irregular grain reorganization cause the fluctuation of the static resistance force in direction and magnitude [41, 42, 63, 64, 65]. Due to this complicated process of transmitting the force, there are few general continuum theories completely describing the static resistance force [44]. In this study, we considered horizontal and vertical static resistance forces developed by theoretical and empirical approaches.

3.2.1 Horizontal static resistance force F_{sh}

Horizontal static resistance force is defined as an internal impeding force acting on the horizontal direction. When a body penetrates a granular material, it is not easy to separate and to measure this force individually without the effect of dynamic frictional force F_d . The experiments related with the horizontal static resistance forces were performed at very slow speed such as 0.04 - 1.4 mm/s [39, 40, 41].

Albert, Pfeifer, Barabási, and Schiffer [39] applied a probability approach to model this resistance force. They used the force chain model developed by Coppersmith, Liu, Majumdar, Narayan, and Witten [30] in order to model the mean horizontal static resistance force. According to the chain model of Coppersmith *et al.*, the force chains transmitting the

propagation of contact forces are built up based on the force fractions that act on a given particle of the matter. The force fraction is unequally split and transmitted to the adjacent particles. The traces of these force fractions are built as the form of chain in the granular material pile. For a particle to move horizontally relative to a granular matter which is restricted by the force chain, the probability of the particle immersed at a certain depth position, exceeding a critical force necessary to make the granule slip relative to another, should be 1 when a certain external force is applied horizontally on this particle. Expanding this concept of small particle to a body, the probabilities of all granules contacting with a body, exceeding a critical force necessary to make the granules slip relative to others, should simultaneously be 1 at any depth position when a certain external force F is applied on a body horizontally for a body immersed in the granular matter to penetrate horizontally.

The calculated minimum force F satisfying this probability condition of a vertically immersed cylinder type body is $F = \eta_h g \rho_g H^2 d_c$, where g is the gravitational acceleration, H is the immersed length of the cylinder, d_c is the diameter of the cylinder, and η_h is a constant depending on the medium properties such as surface friction, morphology, packing of the grains, etc. [39]. Using the same process, the horizontal static resistance force of the cylinder including the state of immersion, at any slope, can be generalized as

$$\mathbf{F}_{sh} = -\frac{\mathbf{v}_h}{|\mathbf{v}_h|} \eta_h g \rho_g z_T^2 d_c, \quad (3.3)$$

where \mathbf{v}_h is the horizontal velocity vector of a body and z_T is the depth of the immersed cylinder tip. For a sphere, the horizontal static resistance force is

$$\mathbf{F}_{sh} = -\frac{\mathbf{v}_h}{|\mathbf{v}_h|} \eta_h g \rho_g d_s^2 z_T, \quad (3.4)$$

where d_s is the diameter of the sphere. Equations (3.3) and (3.4) show that the horizontal static resistance force is a function of the granular properties, the immersed surface area, and the depth.

Even though Eqs. (3.3) and (3.4) do not reflect the periodical force fluctuation such as stick and slip phenomena which were confirmed in some real cases, experimental data show that the equation can be applied for the static resistance force model not only in the case of little fluctuation phenomenon but also for large fluctuation because the calculated force represents the average static force of fluctuation [41, 42]. In addition, this modeling approach reveals that inertia of the body and the friction force between granules and the body surface in contact have negligible contribution to the horizontal static resistance force. In other words, any body only with the same shape can cause almost the same results regardless of the body's properties such as density and surface friction.

3.2.2 Vertical static resistance force F_{sv}

The vertical static resistance force is defined as an internal impeding resistance acting on the vertical axis. Although most researches regarding the impact with a granular material focus on the vertical direction, the studies about the static resistance force in this direction are not enough or are limited. Simple models of this force applied as a mere constant [46, 49] and linear function of the immersed depth of a body in a restricted range [51, 53]. However, basically this force is known as a nonlinear function of the immersion depth [43, 44].

The reason that there are very few continuum models for this force in a granular system is originated from complex force distribution. Even simple experimental result shows the contacts of granules increase exponentially by the force loaded externally [31, 34] and especially the effects by the container bottom boundary increase the non-linearity of this resistance force [43, 62]. In addition, the problem of the direction loaded by external force makes the modeling of this force even more difficult.

Hill, Yeung, and Koehler [44] suggested an empirical equation with coefficients calculated from the experimental data as

$$\mathbf{F}_{sv} = -\frac{\mathbf{v}_v}{|\mathbf{v}_v|} \eta_v (z_T/l)^\lambda g \rho_g V, \quad (3.5)$$

where \mathbf{v}_v is the vertical velocity vector of a body, V is the immersed volume of the body, and l is the lateral dimension. The coefficients η_v and λ are depending on the shape of the body, the properties of the granular matter, the shape of medium container, and the moving direction such as plunging and withdrawing.

When Eq. (3.5) is applied with the coefficients η_v and λ to a dynamic model, the noticeable conditions for modeling are the inclination and the moving direction of the body. The coefficients based on the empirical data [44] reveal that the inclination of a body has little effect on the vertical static resistance force however this force changes drastically by the moving directions. For the cylinder type body, whether the axis is vertical or horizontal, the coefficients η_v and λ are approximately 10 and 1.4 for plunging motion and 0.5 and 1.7 for withdrawing motion in their experiments.

3.3 Air drag force

Air can also act as the medium impeding the motion of an impacting body besides the granular medium. For some cases, the air drag force acts as a main resistance force disturbing the motion. However, the air drag force that can act as an additional resistance force acting on the impact object is not considered in this study because the force is too weak compared with the resistance force of the granular medium. The simulation of a moving compound pendulum shows the difference between the air drag force applied to the model and not applied to the model is as small as possibly to be ignored. The calculated time of the force applied to the compound pendulum model for the pendulum released at 45° to pass through vertical plane is 0.164954 s and that of the model not applying the force is 0.164932 s. The difference between these times is only 0.000022 s. The air drag force is calculated as $F = 1/2 C_d A_r \rho_{air} v_C^2$ where C_d is the drag coefficient, ρ_{air} is the density of air, and v_C is the velocity of the center of the mass [66]. As the condition of air for this simulation, the air density $\rho_{air} = 1.2045 \text{ kg/m}^3$ (20 °C and 1 ATM) and the drag coefficients $C_d = 0.93$ for cylinder [66] are utilized. The applied dimensions of the compound pendulum are the length 0.15 m, the diameter 0.00635 m, and the density of the steel $7.7 \times 10^3 \text{ kg/m}^3$.

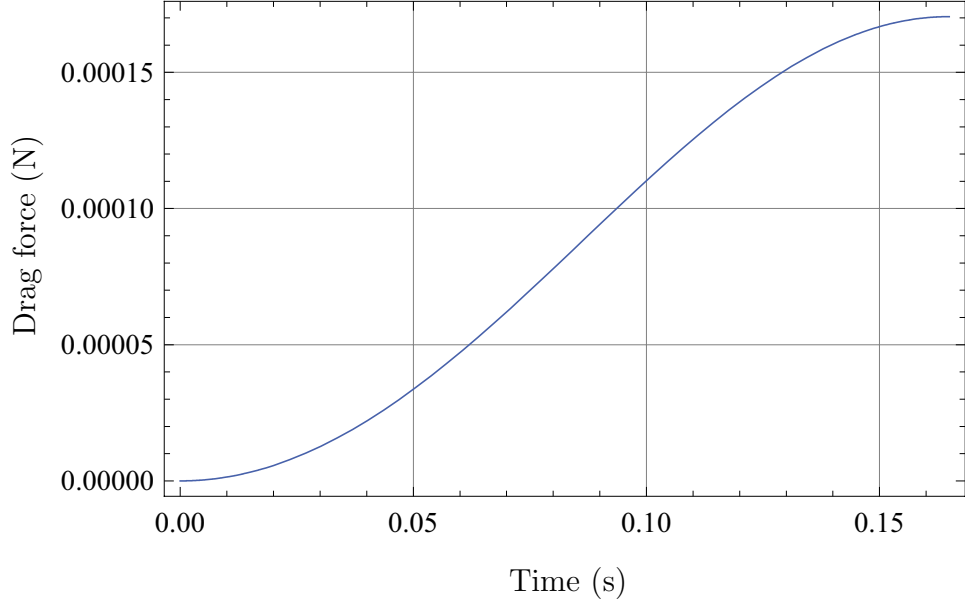


Figure 3.1: Air drag force impeding the motion of the compound pendulum

Figure 3.1 shows the air drag force acting at the compound pendulum. The reason that the air drag resistance is small even compared with the dynamic frictional force is the difference between the density of the air and the granular medium (sand). In this study, the density of the sand applied as a granular medium is 2500 kg/m^3 . Considering the weakness of the air drag resistance force, only resistance force by the granular medium is assumed to act against an impact in this study.

3.4 Application to the impact models

In the case when the impact object is considered as a particle, there is no restriction to apply Eqs. (3.2), (3.3), (3.4), and (3.5) because the acting points of the dynamic frictional force and the static resistance force are consistent with each other. In addition the magnitude and the direction of the dynamic frictional force depend only on that acting point. However, in the case when the impact object is regarded as a continuum, there can be differences between the application points of the resistance forces (between the dynamic frictional force and the static resistance force). It is also difficult to decide the magnitude

and the direction of the dynamic frictional force because the magnitude and the direction of the velocities of points on the impact object are not the same.

In this study, the centroid point of the immersed part of the body is assumed to be application point for the resistance force. Under these assumptions, Eqs. (3.2), (3.3), (3.4), and (3.5) are newly rewritten as

$$\mathbf{F}_d = -\frac{\mathbf{v}_E}{|\mathbf{v}_E|} \eta_d \rho_g A_r \mathbf{v}_E \cdot \mathbf{v}_E = -\mathbf{v}_E \eta_d \rho_g A_r |\mathbf{v}_E|, \quad (3.6)$$

$$\mathbf{F}_{sh} = -\frac{\mathbf{v}_{E_x}}{|\mathbf{v}_{E_x}|} \eta_h g \rho_g z_T^2 d_c = [-\text{sign}(v_{E_x}) \eta_h g \rho_g z_T^2 d_c] \mathbf{1}_0, \quad (3.7)$$

$$\mathbf{F}_{sh} = -\frac{\mathbf{v}_{E_x}}{|\mathbf{v}_{E_x}|} \eta_h g \rho_g d_s^2 z_T = [-\text{sign}(v_{E_x}) \eta_h g \rho_g d_s^2 z_T] \mathbf{1}_0, \quad (3.8)$$

$$\mathbf{F}_{sv} = -\frac{\mathbf{v}_{E_z}}{|\mathbf{v}_{E_z}|} \eta_v (z_T/l)^\lambda g \rho_g V = [-\text{sign}(v_{E_z}) \eta_v (z_T/l)^\lambda g \rho_g V] \mathbf{k}_0, \quad (3.9)$$

where \mathbf{v}_E is the velocity vector of the centroid point of the immersed part of a body, \mathbf{v}_{E_x} represents the velocity vector composed of the horizontal component of \mathbf{v}_E , and \mathbf{v}_{E_z} represents the velocity vector of the vertical component of \mathbf{v}_E . Equations (3.7) and (3.8) represent the horizontal static resistance force for a cylinder type body and for a sphere respectively. With this approach, the resistance force \mathbf{F}_R is applied as $\mathbf{F}_R(\mathbf{v}_E, z_T)$ in the equations of motion.

When the impact object is characterized as a particle, the terms of the resistance force are calculated easily. The velocity vector of the resistance force application point E , \mathbf{v}_E , is the same as the velocity vector of the mass center C , \mathbf{v}_C . The reference area A_r is calculated as $\pi d_s^2/4$ for sphere type objects. The immersed depth z_T is the same as the vertical coordinate of the mass center C and the immersed volume V is calculated as $\pi d_s^3/6$ for the sphere type objects and d_s^3 for rectangular typed objects. In this case, the term of lateral dimension l for calculating the vertical static resistance force is d_s . Therefore the

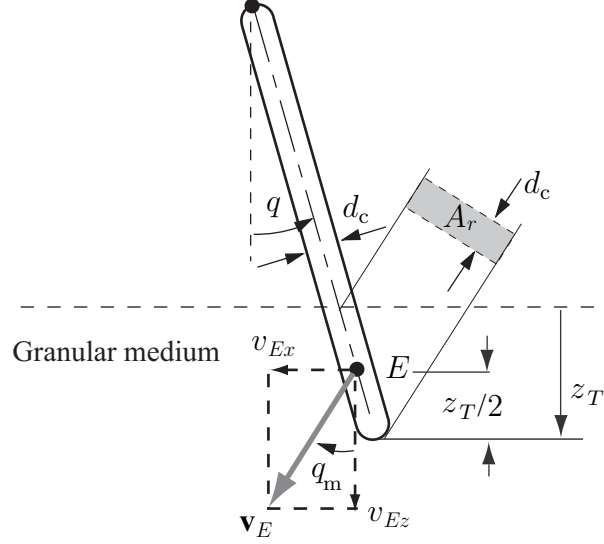


Figure 3.2: Moving angle, q_m , of a link in planar motion

resistance force of a small sphere type object is calculated as

$$\begin{aligned}
 \mathbf{F}_R &= \mathbf{F}_d + \mathbf{F}_{sh} + \mathbf{F}_{sv} \\
 &= \left[-v_{C_x} \eta_d \rho_g \frac{\pi d_s^2}{4} \sqrt{v_{C_x}^2 + v_{C_z}^2} - \text{sign}(v_{C_x}) \eta_h g \rho_g q_z^2 d_s \right] \mathbf{i}_0 \\
 &\quad \left[-v_{C_z} \eta_d \rho_g \frac{\pi d_s^2}{4} \sqrt{v_{C_x}^2 + v_{C_z}^2} - \text{sign}(v_{C_z}) \eta_v (q_z/d_s)^\lambda g \rho_g \frac{\pi d_s^3}{6} \right] \mathbf{k}_0, \quad (3.10)
 \end{aligned}$$

where q_z is the scalar value of the vertical position vector of the mass center C .

For a link in planar motion (see Fig. 3.2), the position and the velocity vector of the resistance force application point E should be defined in order to calculate the resistance force of link type objects. The reference area A_r is calculated as

$$A_r = d_c \frac{z_T}{\cos q} |\sin(q - q_m)|, \quad (3.11)$$

$$q_m = \tan^{-1} \left(\frac{v_{Ex}}{v_{Ez}} \right), \quad (3.12)$$

where q is the angle between vertical plane and the object and q_m represents the moving angle of the link penetrating the granular medium as shown in Fig. 3.2. The term, lateral

dimension l , for calculating the vertical static resistance force for this case is d_c and the immersed volume V is calculated with

$$V = \frac{\pi d_c^2}{4} \frac{z_T}{\cos q}. \quad (3.13)$$

Therefore the resistance force of a cylinder type link is calculated as

$$\begin{aligned} \mathbf{F}_R &= \mathbf{F}_d + \mathbf{F}_{sh} + \mathbf{F}_{sv} \\ &= \left[-v_{E_x} \eta_d \rho_g d_c \frac{z_T}{\cos q} \left| \sin \left(q - \tan^{-1} \left(\frac{v_{E_x}}{v_{E_z}} \right) \right) \right| \sqrt{v_{E_x}^2 + v_{E_z}^2} \right. \\ &\quad \left. - \text{sign}(v_{E_x}) \eta_h g \rho_g z_T^2 d_s \right] \mathbf{i}_0 \\ &\quad \left[-v_{E_z} \eta_d \rho_g d_c \frac{z_T}{\cos q} \left| \sin \left(q - \tan^{-1} \left(\frac{v_{E_x}}{v_{E_z}} \right) \right) \right| \sqrt{v_{E_x}^2 + v_{E_z}^2} \right. \\ &\quad \left. - \text{sign}(v_{E_z}) \eta_v (z_T/d_s)^\lambda g \rho_g \frac{\pi d_c^2}{4} \frac{z_T}{\cos q} \right] \mathbf{k}_0. \end{aligned} \quad (3.14)$$

CHAPTER 4

IMPACT OF RIGID OBJECTS

In this chapter, rigid bodies impacting a granular medium are studied. Their equations of motion (E.O.M.) are formulated and simulated. The resistance forces and the gravity forces are considered in the E.O.M.s of the system. The E.O.M.s are formulated using Newton-Euler equations. Other equations such as Lagrange's equation and Kane's dynamical equation also can be applied to find the E.O.M.s. The simulation results of the E.O.M.s are the same as Newton-Euler equations.

First, a one degree of freedom (D.O.F.) mathematical pendulum is studied. An oblique impact of a sphere also studied as the motion of a particle has two D.O.F. After modeling of the motion of a particle type sphere, the impacts of rigid bodies are studied. Single impact of a planar kinematic chain including a compound pendulum and a double pendulum are studied. Additionally the impact of a free rigid link is modeled as the special case of the single impact of a planar kinematic chain. In order to confirm the effect of resistance forces acting on multiple links simultaneously, multiple impacts of a planar kinematic chain are modeled.

As mentioned previously the planar motions of the models are described in a fixed cartesian coordinate system. The x -axis is horizontal, with the positive sense directed to the right, the z -axis is vertical, with the positive sense directed downward, and y -axis is perpendicular to the plane of motion. The unit vectors for the fixed frame are \mathbf{i}_0 , \mathbf{j}_0 , and \mathbf{k}_0 . The angle between the z -axis and the link i is denoted by q_i , ($i = 1, 2, 3, \dots, n$). The x and z -axis distances from the origin to a reference point are denoted by q_x and q_z respectively.

The simulation is performed using Mathematica and the equations of motion is solved by NDSolve function. When the fixed step is required to solve E.O.M.s, the applied step size is 10^{-6} s. Various initial impact angles are applied as initial conditions in simulations

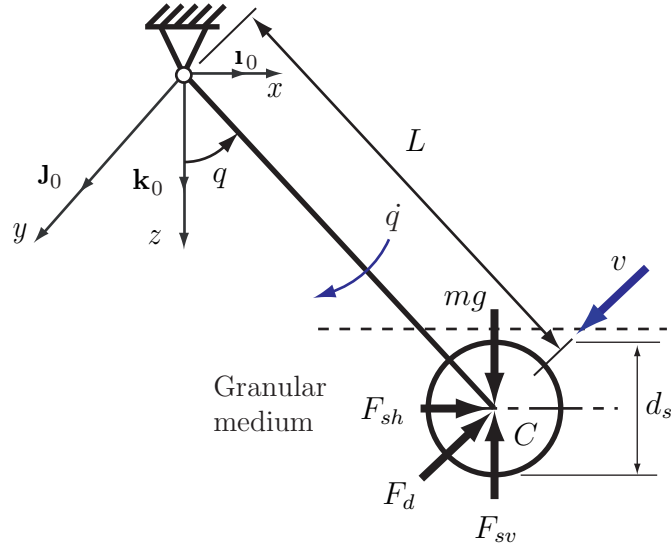


Figure 4.1: Free body diagram of a mathematical pendulum in impact

from low to high impact angle in order to confirm the effects of initial impact angles to the penetrating process from the impact moment until the kinematic chain stops. The simulation results are basically compared using different initial impact velocities from low to relatively high for the same initial impact angle.

In this study, the penetrating velocity and the penetrated distance are considered as the basic data for analyzing the impact with a granular medium. The penetrating velocity is analyzed by comparing the stopping times meaning the time intervals from the impact moment until the kinematic chains stop.

4.1 Impact of a rigid sphere

4.1.1 Impact of a mathematical pendulum

Modeling

First, the impact of a single mathematical pendulum into the granular material is modeled. For the mathematical pendulum the net forces acting on the sphere are the gravity \mathbf{G} , the static resistance force \mathbf{F}_s , and the dynamic frictional force \mathbf{F}_d as shown in Fig. 4.1.

All the forces act at the center of the mass of the sphere of the mathematical pendulum. In the vertical z -axis, the forces acting on the mathematical pendulum are composed of the gravity force \mathbf{G} , the vertical static resistance force \mathbf{F}_{sv} , and the vertical component of dynamic frictional force, \mathbf{F}_{dv} . The forces acting in x -axis are the horizontal static resistance force \mathbf{F}_{sh} and the horizontal component of dynamic frictional force, \mathbf{F}_{dh} . The Newton-Euler equation is given by

$$m_s L^2 \ddot{\mathbf{q}} \cdot \mathbf{J}_0 = \left[\mathbf{r}_C \times (\mathbf{G} + \mathbf{F}_s + \mathbf{F}_d) \right] \cdot \mathbf{J}_0, \quad (4.1)$$

where L is the length of the pendulum, q is the angle of pendulum with the vertical, and \ddot{q} is the angular acceleration. The vector \mathbf{r}_C is the position vector from the origin O to the mass center C and given as

$$\mathbf{r}_C = L \sin q \mathbf{i}_0 + L \cos q \mathbf{k}_0. \quad (4.2)$$

The vector of gravity force \mathbf{G} is also represented as

$$\mathbf{G} = m_s g \mathbf{k}_0. \quad (4.3)$$

All the forces acting on the sphere are assumed to have their application point at the mass center of the sphere, C . Therefore the velocity vector of the resistance force application point E and the dynamic frictional force \mathbf{F}_d calculated by Eq. (3.6) are represented as

$$\mathbf{v}_E = \mathbf{v}_C = L \dot{q} \cos q \mathbf{i}_0 - L \dot{q} \sin q \mathbf{k}_0 \quad (4.4)$$

$$\begin{aligned} \mathbf{F}_d &= -\mathbf{v}_E \eta_d \rho_g A_r |\mathbf{v}_E| = -\mathbf{v}_C \eta_d \rho_g A_r |\mathbf{v}_C| \\ &= \eta_d \rho_g A_r L^2 |\dot{q}| \left[-\dot{q} \cos q \mathbf{i}_0 + \dot{q} \sin q \mathbf{k}_0 \right], \end{aligned} \quad (4.5)$$

where the reference area is calculated as $A_r = \pi d_s^2/4$. The horizontal and vertical static resistance forces, \mathbf{F}_{sh} and \mathbf{F}_{vh} , are

$$\mathbf{F}_{sh} = -\text{sign}(\dot{q} \cos q) \eta_h g \rho_g z_T^2 d_s \mathbf{1}_0, \quad (4.6)$$

$$\mathbf{F}_{sv} = \text{sign}(\dot{q} \sin q) \eta_v (z_T/d_s)^\lambda g \rho_g V \mathbf{k}_0, \quad (4.7)$$

where the immersed volume is calculated as $V = \pi d_s^3/6$ and the immersed depth of the mathematical pendulum, z_T , is calculated as

$$z_T = L \cos q - L \cos q(0). \quad (4.8)$$

The initial condition $q(0)$ is the angle of the mathematical pendulum at the impact moment. The resistance force \mathbf{F}_R is represented by Eqs. (4.5), (4.6), (4.7), and (4.8) as

$$\begin{aligned} \mathbf{F}_R &= \mathbf{F}_d + \mathbf{F}_{sh} + \mathbf{F}_{sv} \\ &= - \left[\eta_d \rho_g \frac{\pi d_s^2}{4} L^2 |\dot{q}| \dot{q} \cos q + \text{sign}(\dot{q} \cos q) \eta_h g \rho_g \left(L \cos q - L \cos q(0) \right)^2 d_s \right] \mathbf{1}_0 \\ &\quad + \left[\eta_d \rho_g \frac{\pi d_s^2}{4} L^2 |\dot{q}| \dot{q} \sin q \right. \\ &\quad \left. + \text{sign}(\dot{q} \sin q) \eta_v \left(\frac{L \cos q - L \cos q(0)}{d_s} \right)^\lambda g \rho_g \frac{\pi d_s^3}{6} \right] \mathbf{k}_0. \end{aligned} \quad (4.9)$$

Simulation results

Figures 4.2, 4.3, and 4.4 represent the simulation results of the impact of the mathematical pendulum, depicted in Figs. 2.4 and 4.1. The length from the joint to the mass center of the sphere is $L = 0.5$ m, the diameter of the sphere is $d_s = 0.0254$ m, its density is $\rho_s = 7.7 \times 10^3$ kg/m³, and the density of the granular medium (sand) is $\rho_g = 2.5 \times 10^3$ kg/m³. The dynamic frictional force coefficient $\eta_d = 6.5$, the horizontal static resistance force coefficient $\eta_h = 8$, and the vertical static resistance force coefficients $\eta_v = 22$ and $\lambda = 1.1$ are used in the simulation. The gravitational acceleration g is utilized as 9.81 m/s²

Table 4.1: Stopping time of the mathematical pendulum into a granular medium

Impact angle ($^{\circ}$)	$\dot{q}(0)$ (rad/s)	t_s (s)
15	-1	0.0642752
	-3	0.0513544
	-5	0.0471527
45	-1	0.0381696
	-3	0.0295588
	-5	0.0267668
75	-1	0.0354039
	-3	0.0267909
	-5	0.0240349

in this study. The simulation is performed for the different impact angles ($q(0) = 15, 45,$ and 75°) and the different impact angular velocities ($\dot{q}(0) = -1, -3,$ and -5 rad/s) from the impact moment until the angular velocity \dot{q} becomes zero.

As shown in Figs. 4.2, 4.3, and 4.4, the penetrating angle increases when the initial impact angular velocity is increasing. However, the stopping time defined as the time interval from the impact moment until the angular velocity of the pendulum becomes zero, t_s , decreases as shown in table 4.1. The increasing of the initial velocity causes the stopping time into the granular medium to decrease. The faster the mass of the mathematical pendulum impacts the surface of the granular medium, the sooner it will come to a stop. This interesting phenomenon involving how rapidly a particle type rigid body vertically strikes the granular medium slowing down upon contact was reported in [51]. The results observed only in vertical impact are kept in the impact of the mathematical pendulum which has both horizontal and vertical components of penetrating motion as the initial impact velocity $v(0)$ at which a particle vertically impacts the medium increases the sooner it will come to a stop.

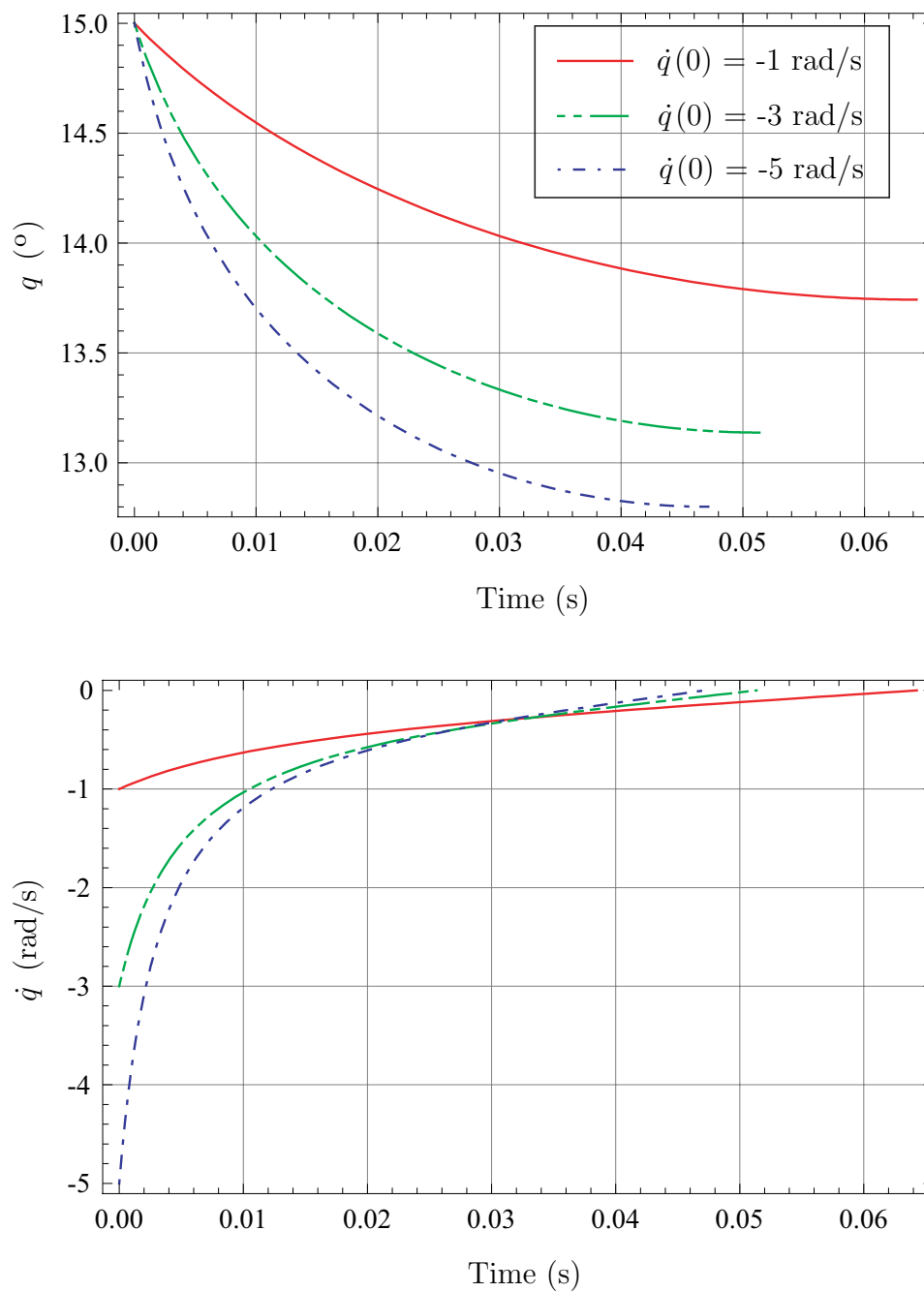


Figure 4.2: Impact results of the mathematical pendulum into a granular medium for $q(0) = 15^\circ$

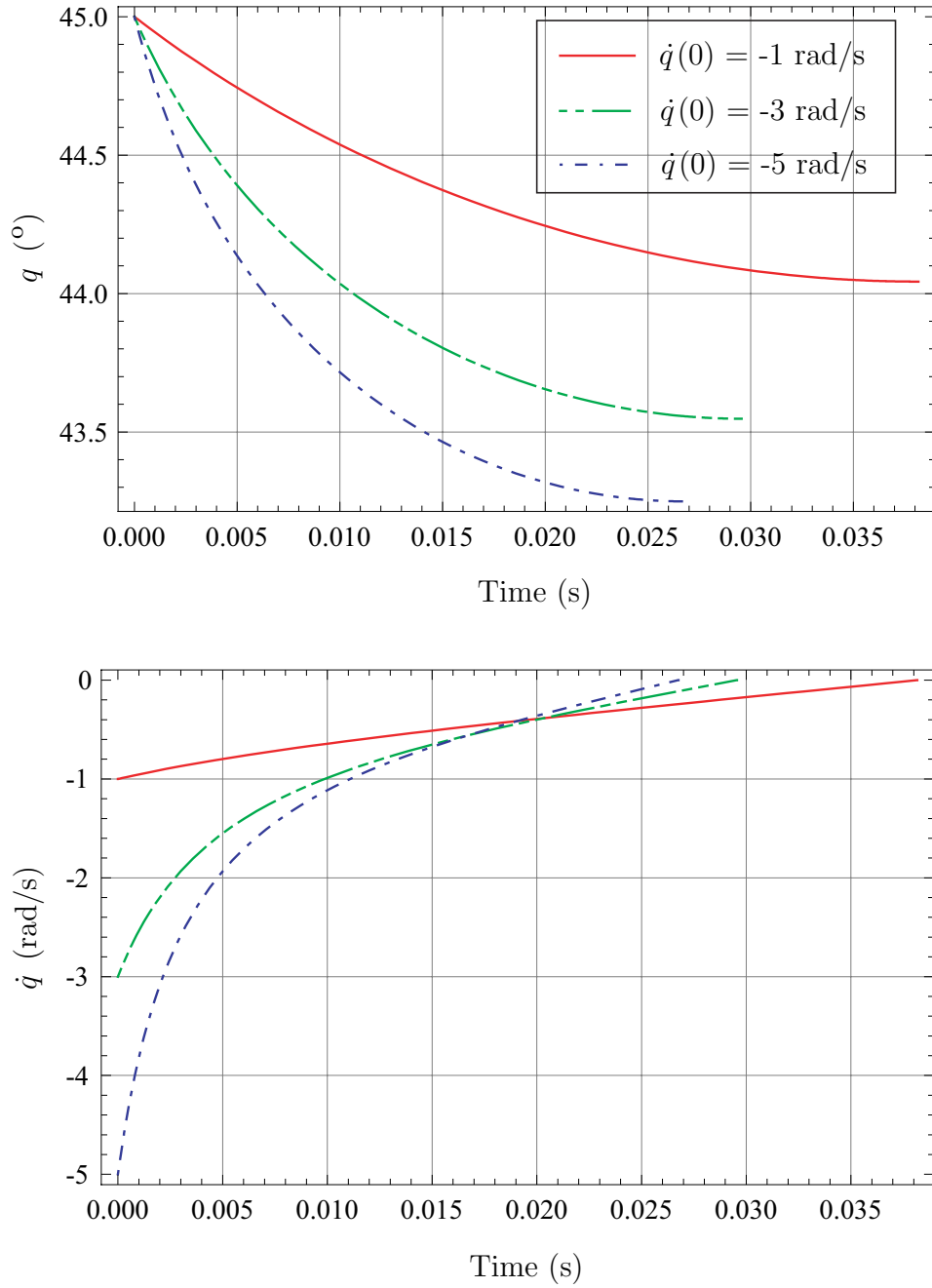


Figure 4.3: Impact results of the mathematical pendulum into a granular medium for $q(0) = 45^\circ$

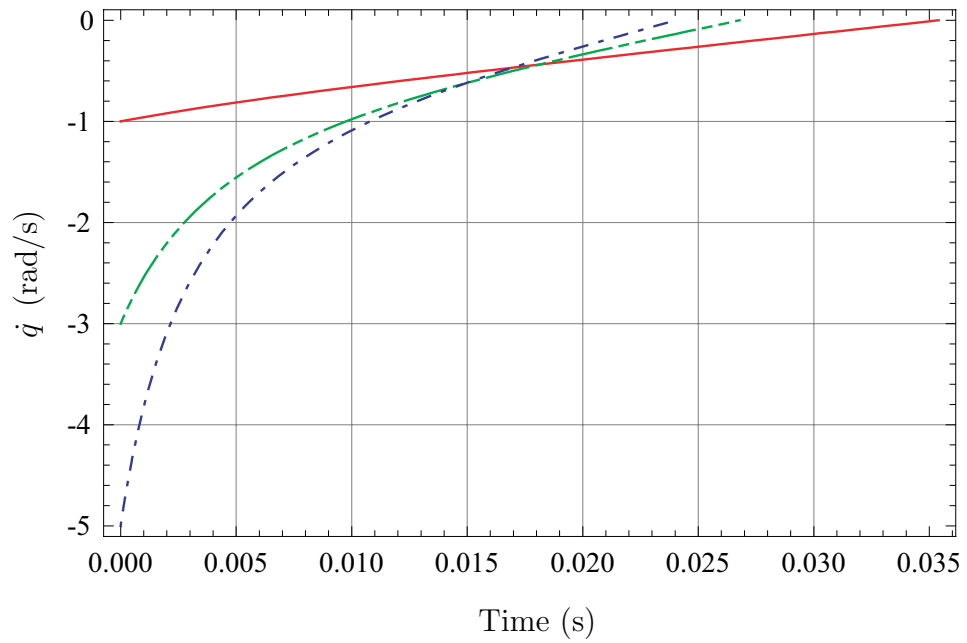
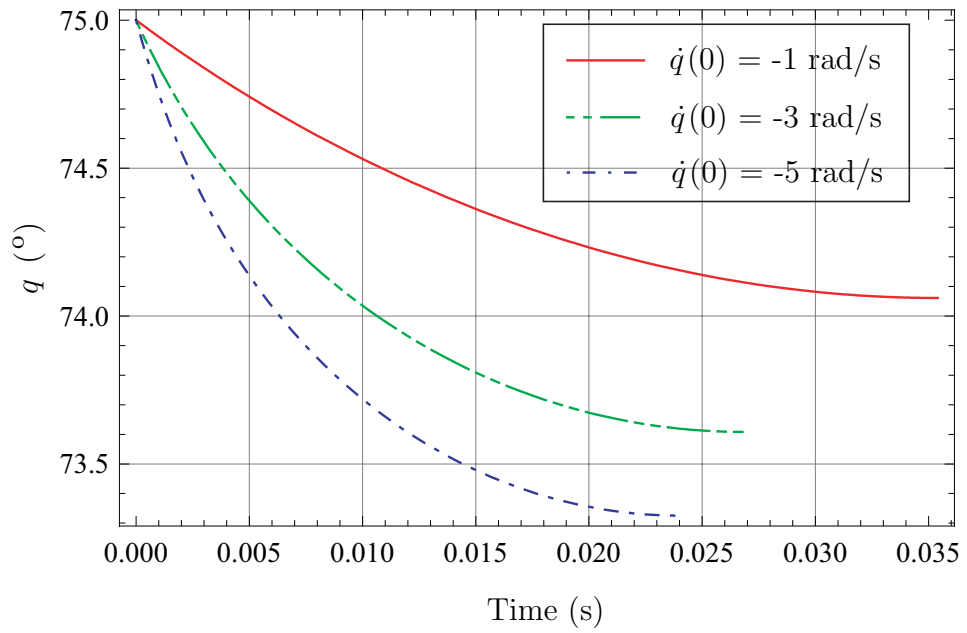


Figure 4.4: Impact results of the mathematical pendulum into a granular medium for $q(0) = 75^\circ$

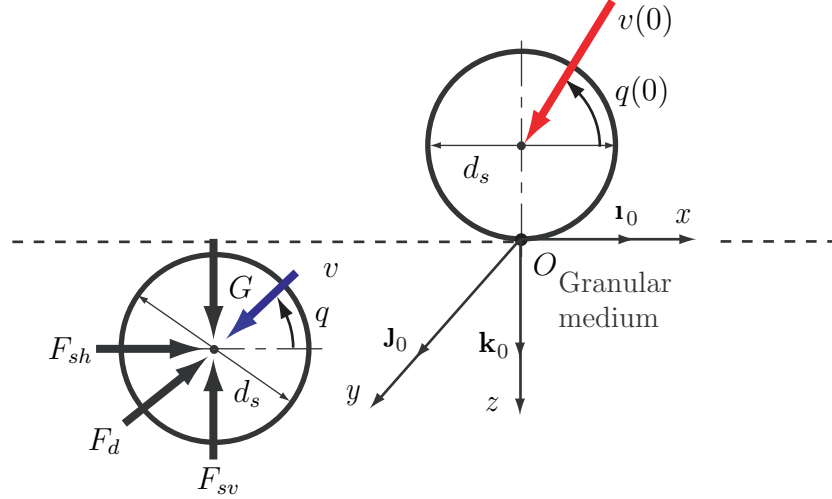


Figure 4.5: Free body diagram of a rigid sphere in oblique impact

4.1.2 Oblique impact of a rigid sphere

Modeling

The model of a planar oblique impact of a rigid sphere into a granular matter is presented. The net forces acting on the oblique planar impact penetrating a granular medium are the same as the previous case. The gravity force, the static resistance force \mathbf{F}_s , and the dynamic frictional force \mathbf{F}_d act as shown in Fig. 4.5. Neglecting the rotation of the body, Newton's second law for the sphere gives:

$$m_s \ddot{\mathbf{r}}_C = \mathbf{G} + \mathbf{F}_s + \mathbf{F}_d, \quad (4.10)$$

where $\ddot{\mathbf{r}}_C$ is the acceleration vector of the position vector of the mass center of the sphere, $\mathbf{r}_C = q_x \mathbf{i} + q_z \mathbf{k}$, and m_s is the mass of the sphere. There is no rebound at the impact moment regardless the initial velocity and the initial impact angle.

All the forces acting on the sphere are also assumed to have their resistance force application point at the center of the sphere. In the vertical z -axis, the forces acting on the sphere are: the gravity force \mathbf{G} , the vertical static resistance force, \mathbf{F}_{sv} , and the vertical component of dynamic frictional force \mathbf{F}_{dv} . The forces acting in x -axis are: the horizontal

static resistance force \mathbf{F}_{sh} and the horizontal component of dynamic frictional force, \mathbf{F}_{dh} . The vector of gravity force \mathbf{G} is represented as

$$\mathbf{G} = m_s g \mathbf{k}_0. \quad (4.11)$$

The resistance force \mathbf{F}_R is calculated by Eqs. (3.6), (3.7), and (3.9). Because the resistance force is assumed to act at the mass center C , the dynamic frictional force \mathbf{F}_d is calculated by Eq. (3.6) as

$$\begin{aligned} \mathbf{F}_d &= -\mathbf{v}_E \eta_d \rho_g A_r |\mathbf{v}_E| = -\mathbf{v}_C \eta_d \rho_g A_r |\mathbf{v}_C| \\ &= \eta_d \rho_g A_r \sqrt{\dot{q}_x^2 + \dot{q}_z^2} \left[-\dot{q}_x \mathbf{i}_0 - \dot{q}_z \mathbf{k}_0 \right]. \end{aligned} \quad (4.12)$$

The reference area A_r for the sphere is the same as that of the mathematical pendulum as

$$A_r = \frac{\pi d_s^2}{4}. \quad (4.13)$$

The horizontal and vertical static resistance forces, \mathbf{F}_{sh} and \mathbf{F}_{sv} , are

$$\mathbf{F}_{sh} = -\text{sign}(\dot{q}_x) \eta_h g \rho_g q_z^2 d_s \mathbf{i}_0, \quad (4.14)$$

$$\mathbf{F}_{sv} = -\text{sign}(\dot{q}_z) \eta_v (q_z/d_s)^\lambda g \rho_g V \mathbf{k}_0, \quad (4.15)$$

where the immersed volume V is calculated as the volume of the sphere.

$$V = \frac{\pi d_s^3}{6}. \quad (4.16)$$

Table 4.2: Stopping time of the rigid sphere into a granular medium

Impact angle (°)	$v_p(0)$ (m/s)	t_s (s)
15	1	0.0565723
	3	0.04457
	5	0.0376819
45	1	0.0364601
	3	0.0272604
	5	0.0243122
75	1	0.0324081
	3	0.0251294
	5	0.0227529

The resistance force \mathbf{F}_R , the sum of the dynamic frictional force vector \mathbf{F}_d and the static resistance force vector \mathbf{F}_s , is represented by the sum of Eqs. (4.12), (4.14), and (4.15) as

$$\begin{aligned}
 \mathbf{F}_R &= \mathbf{F}_d + \mathbf{F}_{sh} + \mathbf{F}_{sv} \\
 &= \begin{bmatrix} -\dot{q}_x \eta_d \rho_g \frac{\pi d_s^2}{4} \sqrt{\dot{q}_x^2 + \dot{q}_z^2} - \text{sign}(\dot{q}_x) \eta_h g \rho_g q_z^2 d_s \\ -\dot{q}_z \eta_d \rho_g \frac{\pi d_s^2}{4} \sqrt{\dot{q}_x^2 + \dot{q}_z^2} - \text{sign}(\dot{q}_z) \eta_v (q_z/d_s)^\lambda g \rho_g \frac{\pi d_s^3}{6} \end{bmatrix} \mathbf{1}_0 \\
 &\quad \begin{bmatrix} -\dot{q}_z \eta_d \rho_g \frac{\pi d_s^2}{4} \sqrt{\dot{q}_x^2 + \dot{q}_z^2} - \text{sign}(\dot{q}_z) \eta_v (q_z/d_s)^\lambda g \rho_g \frac{\pi d_s^3}{6} \end{bmatrix} \mathbf{k}_0. \quad (4.17)
 \end{aligned}$$

Simulation results

Figures 4.6, 4.7, and 4.8 represent the simulation results of the oblique impact of the sphere, depicted in Figs. 2.3 and 4.5. All data for the second simulation such as the density and the diameter of the sphere, the density of the granular medium, and the resistance force coefficients are applied as the same data applied to the simulation of the mathematical pendulum. The simulation is performed for the different impact angles ($q(0) = 15, 45,$ and 75°) and the different impact linear velocities ($v_p(0) = 1, 3,$ and 5 m/s) from the impact moment until the velocity of the sphere, v_p , becomes zero. The penetrating distance

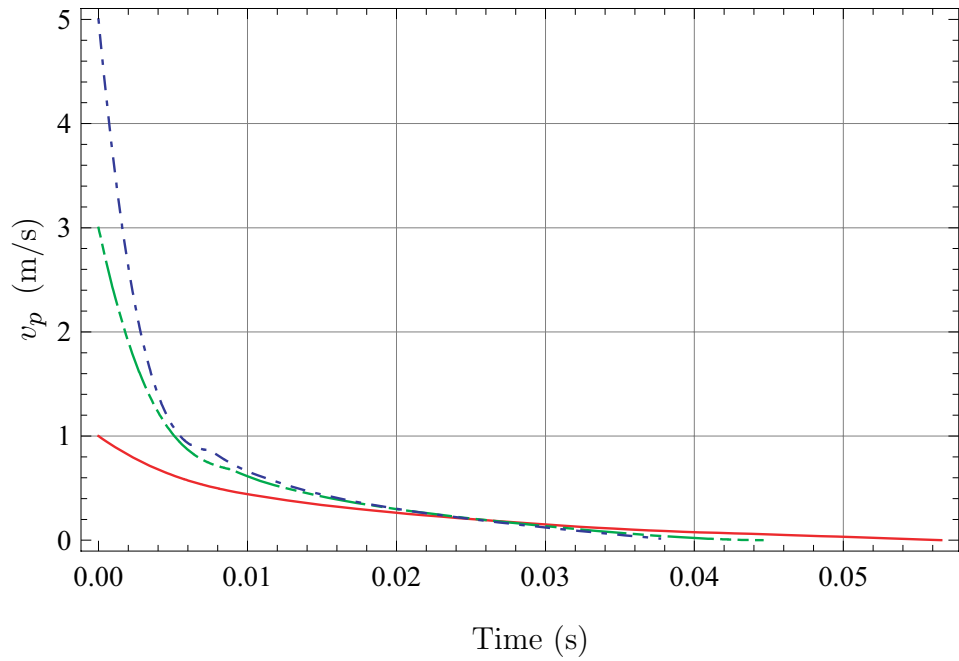
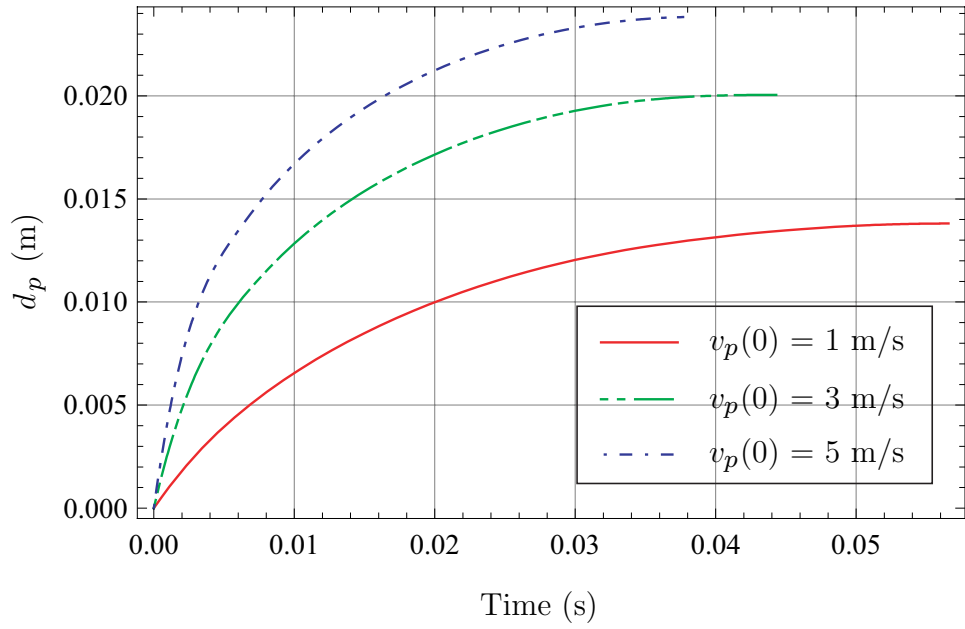


Figure 4.6: Impact results of the rigid sphere into a granular medium for $q(0) = 15^\circ$

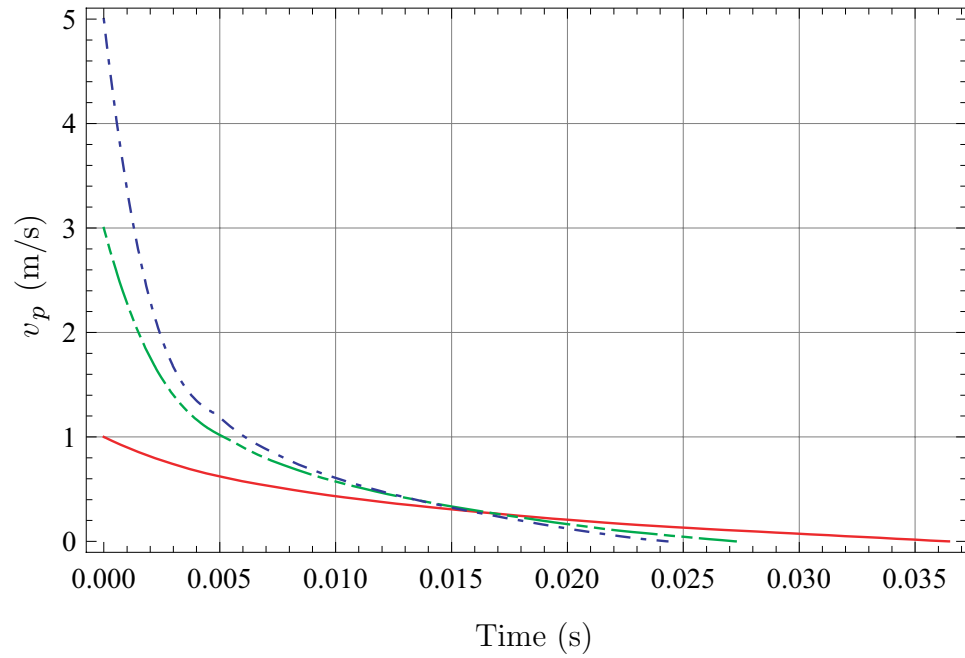
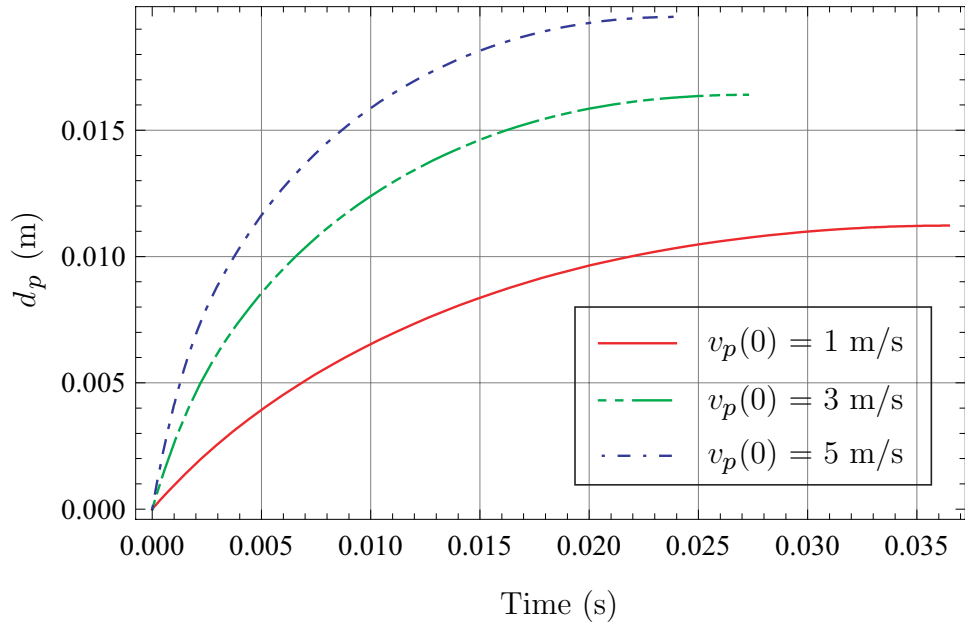


Figure 4.7: Impact results of the rigid sphere into a granular medium for $q(0) = 45^\circ$

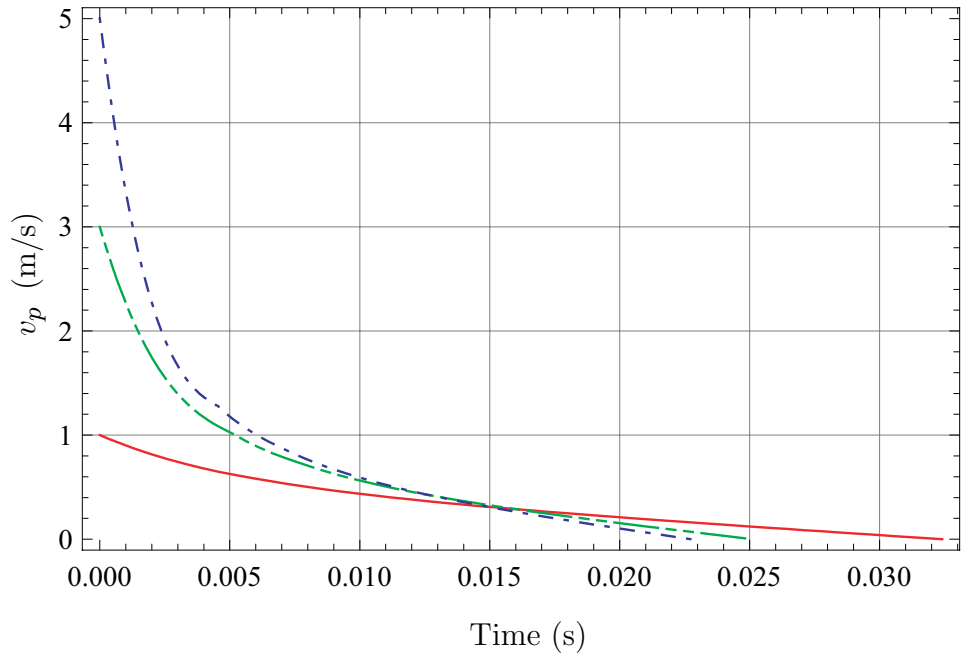
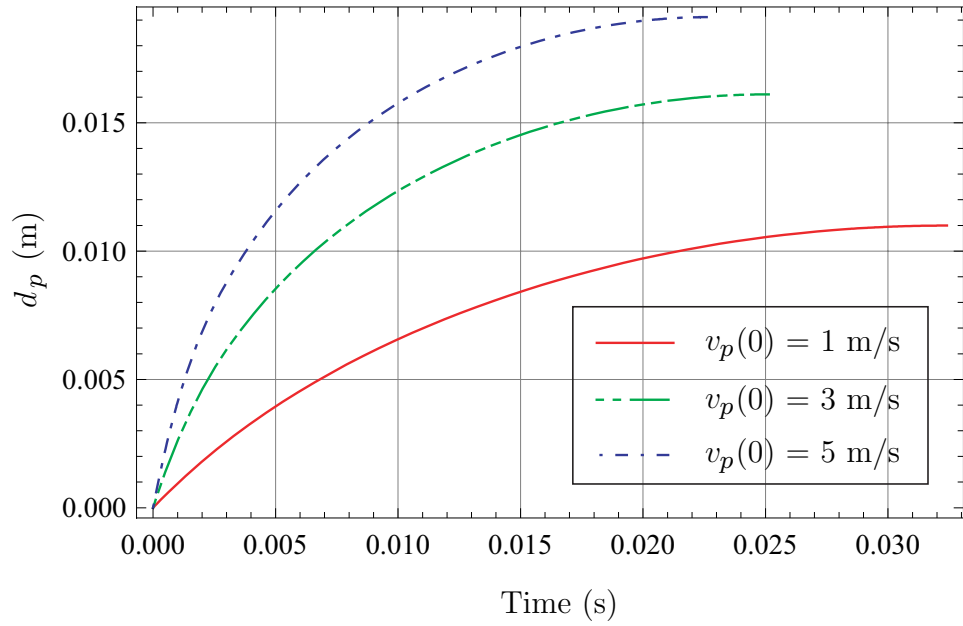


Figure 4.8: Impact results of the rigid sphere into a granular medium for $q(0) = 75^\circ$

($d_p = \int v_p dt$) increases but the penetrating motion of the rigid sphere comes to stops fast when the initial impact velocity $v(0)$ is increased as shown in Figs. 4.6, 4.7, and 4.8 and in table 4.2. These simulation results show that the results confirmed in the simulation for one D.O.F. motion of the particle type sphere as the mathematical pendulum and the vertical impact are kept in two D.O.F. motion of the particle type sphere.

4.2 Single impact with a granular medium

4.2.1 Impact of a free rigid link

Modeling

The model of the impact of a free rigid link into a granular matter is presented. Previous the impact of the sphere are modeled based on the motion of particle. However, from the impact of a rigid link the impact with a granular is modeled based on the motion of rigid body. In the vertical z -axis, the forces acting on the link are: the gravity force \mathbf{G} , the vertical static resistance force \mathbf{F}_{sv} , and the vertical component of the dynamic frictional force \mathbf{F}_d . The forces acting in x -axis are: the horizontal static resistance force \mathbf{F}_{sh} and the horizontal component of the dynamic frictional force \mathbf{F}_d . The gravity force \mathbf{G} acts at the center of mass, C , of the link and the resistance force, \mathbf{F}_R , including \mathbf{F}_s and \mathbf{F}_d acts at the point E , where point E is the centroid point of immersed part as shown in Fig. 4.9. The general equation of motion for the planar kinematic chain can be written in the following form

$$m_c \ddot{\mathbf{r}}_C \cdot \mathbf{i}_0 = (\mathbf{F}_s + \mathbf{F}_d) \cdot \mathbf{i}_0, \quad (4.18)$$

$$m_c \ddot{\mathbf{r}}_C \cdot \mathbf{k}_0 = (\mathbf{G} + \mathbf{F}_s + \mathbf{F}_d) \cdot \mathbf{k}_0, \quad (4.19)$$

$$I_C \ddot{\mathbf{q}} \cdot \mathbf{J}_0 = \left[\mathbf{r}_{CE} \times (\mathbf{F}_s + \mathbf{F}_d) \right] \cdot \mathbf{J}_0, \quad (4.20)$$

where $\ddot{\mathbf{r}}_C$ is the acceleration vector of the position vector of the mass center of the rigid bar, and $\ddot{\mathbf{q}}$ is the angular acceleration vector of the angular vector of pendulum with the

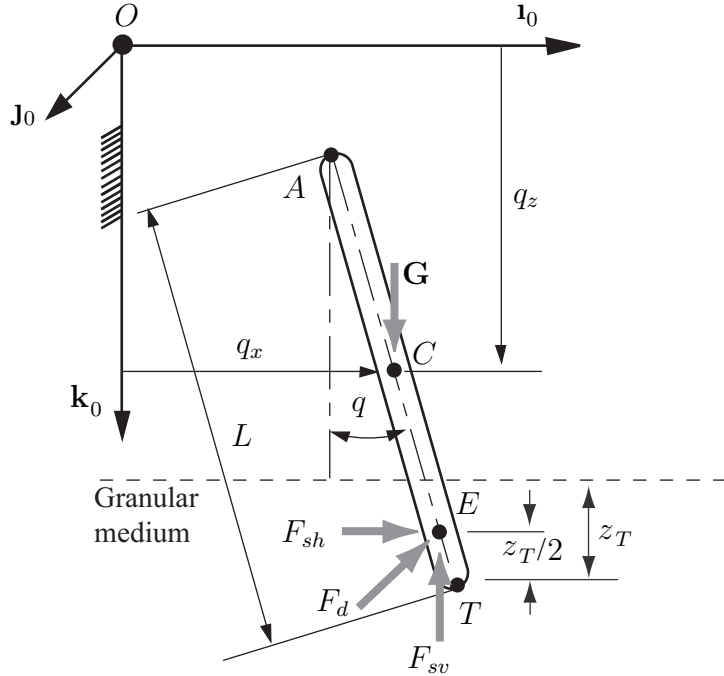


Figure 4.9: Free body diagram of a free rigid link in impact

vertical, $\mathbf{q} = q\mathbf{J}_0$. The position vector \mathbf{r}_{CE} represents vector from the mass center C to the resistance force application point E , m_c is the mass of the link, and $I_C = m_c L^2/12$ is the mass moment of inertia of the link with regard to its center.

$$\mathbf{r}_C = q_x \mathbf{i}_0 + q_z \mathbf{k}_0, \quad (4.21)$$

$$\ddot{\mathbf{q}} = \frac{d^2 q}{dt^2} \mathbf{J}_0. \quad (4.22)$$

The position vector from the mass center to the resistance force application point E , \mathbf{r}_{CE} , is represented as

$$\mathbf{r}_{CE} = L_{CE} \sin q \mathbf{i}_0 + L_{CE} \cos q \mathbf{k}_0, \quad (4.23)$$

where L_{CE} is the length between the mass center C and the resistance force application point E and calculated as

$$L_{CE} = \frac{L}{2} - \frac{z_T}{2 \cos q}. \quad (4.24)$$

The immersed depth of the end T , z_T , is expressed as

$$z_T = \mathbf{r}_C \cdot \mathbf{k} + \frac{L}{2} \cos q = q_z + \frac{L}{2} \cos q. \quad (4.25)$$

The velocity vector of the resistance force acting point E , \mathbf{v}_E , the reference area of the penetrating bar A_r , and the moving angle q_m for calculating the dynamic frictional force are represented as

$$\mathbf{v}_E = \frac{d\mathbf{r}_C}{dt} + \frac{d\mathbf{q}}{dt} \times \mathbf{r}_{CE} = (\dot{q}_x + L_{CE} \dot{q} \cos q) \mathbf{i} + (\dot{q}_z - L_{CE} \dot{q} \sin q) \mathbf{k}, \quad (4.26)$$

$$A_r = d_c \frac{z_T}{\cos q} |\sin(q - q_m)|, \quad (4.27)$$

$$q_m = \tan^{-1} \left(\frac{v_{Ex}}{v_{Ez}} \right) = \tan^{-1} \left(\frac{\dot{q}_x + L_{CE} \dot{q} \cos q}{\dot{q}_z - L_{CE} \dot{q} \sin q} \right). \quad (4.28)$$

The dynamic frictional force \mathbf{F}_d is calculated by Eq. (3.6) as

$$\begin{aligned} \mathbf{F}_d = & \eta_d \rho_g d_c \frac{z_T}{\cos q} \left| \sin \left(q - \tan^{-1} \left(\frac{\dot{q}_x + L_{CE} \dot{q} \cos q}{\dot{q}_z - L_{CE} \dot{q} \sin q} \right) \right) \right| \\ & \sqrt{\left(\dot{q}_x + L_{CE} \dot{q} \cos q \right)^2 + \left(\dot{q}_z - L_{CE} \dot{q} \sin q \right)^2} \\ & \left[- \left(\dot{q}_x + L_{CE} \dot{q} \cos q \right) \mathbf{i}_0 - \left(\dot{q}_z - L_{CE} \dot{q} \sin q \right) \mathbf{k}_0 \right]. \end{aligned} \quad (4.29)$$

The immersed volume V for calculating the static resistance force is calculated as

$$V = \frac{\pi d_c^2}{4} \frac{z_T}{\cos q}. \quad (4.30)$$

Hence, the horizontal and vertical static resistance forces, \mathbf{F}_{sh} and \mathbf{F}_{vh} , are

$$\mathbf{F}_{sh} = -\text{sign}(\dot{q}_x + L_{CE} \dot{q} \cos q) \eta_h g \rho_g z_T^2 d_c \mathbf{i}_0, \quad (4.31)$$

$$\mathbf{F}_{sv} = -\text{sign}(\dot{q}_z - L_{CE} \dot{q} \sin q) \eta_v \left(\frac{z_T}{d_c} \right)^\lambda g \rho_g \frac{\pi d_c^2}{4} \frac{z_T}{\cos q} \mathbf{k}_0. \quad (4.32)$$

The resistance force \mathbf{F}_R , the sum of the dynamic frictional force vector \mathbf{F}_d and the static resistance force vector \mathbf{F}_s , is represented by the sum of Eqs. (4.29), (4.31), and (4.32) as

$$\begin{aligned}
\mathbf{F}_R &= \mathbf{F}_d + \mathbf{F}_{sh} + \mathbf{F}_{sv} \\
&= \left[-\eta_d \rho_g d_c \frac{z_T}{\cos q} \left| \sin \left(q - \tan^{-1} \left(\frac{\dot{q}_x + L_{CE} \dot{q} \cos q}{\dot{q}_z - L_{CE} \dot{q} \sin q} \right) \right) \right| \right. \\
&\quad \sqrt{\left(\dot{q}_x + L_{CE} \dot{q} \cos q \right)^2 + \left(\dot{q}_z - L_{CE} \dot{q} \sin q \right)^2} \left(\dot{q}_x + L_{CE} \dot{q} \cos q \right) \\
&\quad \left. - \text{sign} \left(\dot{q}_x + L_{CE} \dot{q} \cos q \right) \eta_h g \rho_g z_T^2 d_c \right] \mathbf{i}_0 + \\
&\quad \left[-\eta_d \rho_g d_c \frac{z_T}{\cos q} \left| \sin \left(q - \tan^{-1} \left(\frac{\dot{q}_x + L_{CE} \dot{q} \cos q}{\dot{q}_z - L_{CE} \dot{q} \sin q} \right) \right) \right| \right. \\
&\quad \sqrt{\left(\dot{q}_x + L_{CE} \dot{q} \cos q \right)^2 + \left(\dot{q}_z - L_{CE} \dot{q} \sin q \right)^2} \left(\dot{q}_z - L_{CE} \dot{q} \sin q \right) \\
&\quad \left. - \text{sign} \left(\dot{q}_z - L_{CE} \dot{q} \sin q \right) \eta_v \left(\frac{z_T}{d_c} \right)^\lambda g \rho_g \frac{\pi d_c^2}{4} \frac{z_T}{\cos q} \right] \mathbf{k}_0. \tag{4.33}
\end{aligned}$$

Simulation results

Figure 4.10 represents the simulation results of the penetrating depth of the link end T , z_T , and the vertical velocity of link end T , v_{Tz} , of the impact of the vertically dropped cylinder type rigid link depicted in Figs. 2.5 and 4.9. The applied dimensions of the link are the length $L = 0.1524$ m and the diameter $d_c = 0.00635$ m. The density of the link, ρ_c , is also 7.7×10^3 kg/m³ and the density of a granular medium (sand), ρ_g , is 2.5×10^3 kg/m³.

The dynamic frictional force coefficient $\eta_d = 6.5$, the horizontal static resistance force coefficient $\eta_h = 8$, and the vertical static resistance force coefficients $\eta_v = 22$ and $\lambda = 1.1$ are used in the simulation. This simulation is performed for the different initial impact vertical

Table 4.3: Stopping time of the free link

$q(0)$ ($^{\circ}$)	$v_{Tz}(0)$ (m/s)	t_z (s)
0	1.53	0.0331795
	2.06	0.029688
	2.47	0.0277679
32	1.26	0.0275914
	1.87	0.0229915
	2.33	0.0206495
55	1.45	0.017818
	1.98	0.0150461
	2.43	0.0133007

velocities ($\dot{q}_z(0) = 1.53, 2.06,$ and 2.47 m/s) from the impact moment until the link stop. As shown in Fig. 4.10, the penetrating depth of the link increases but the time interval of the link decreases as initial impacting velocity increases. The resistance force acting at the rigid link is shown in Figs. 4.11 and 4.12. The dynamic frictional force depending on the velocity acts as governing resistance force at first. However, when the penetrating depth increases and the velocity of the link decreases, the static resistance force depending on the immersed depth acts as governing resistance force.

Figures 4.13 and 4.14 represent the simulation results performed for the different impact angle $q(0)$ and the different initial impact vertical velocities ($\dot{q}_z(0) = 1.26, 1.87,$ and 2.33 m/s for $q(0) = 32^{\circ}$, and $\dot{q}_z(0) = 1.45, 1.98,$ and 2.43 m/s for $q(0) = 55^{\circ}$). For these simulations, we observed a stopping time t_z representing the time interval from the moment of impact until the vertical velocity of the link end, v_{Tz} . Even though the link impacts obliquely, the penetrating depth of the link end T , z_T , increases but the vertical velocity of link end T , v_{Tz} , becomes zero fast when the initial vertical impact velocity increases as shown in Figs. 4.10, 4.13, and 4.14 and in table 4.3. This result shows that the relations among the

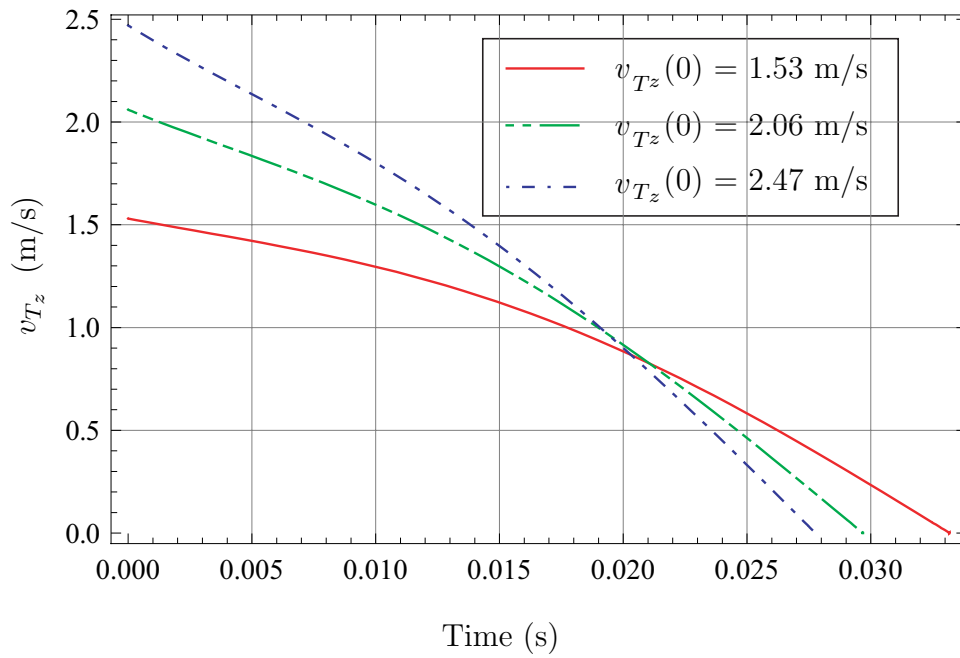
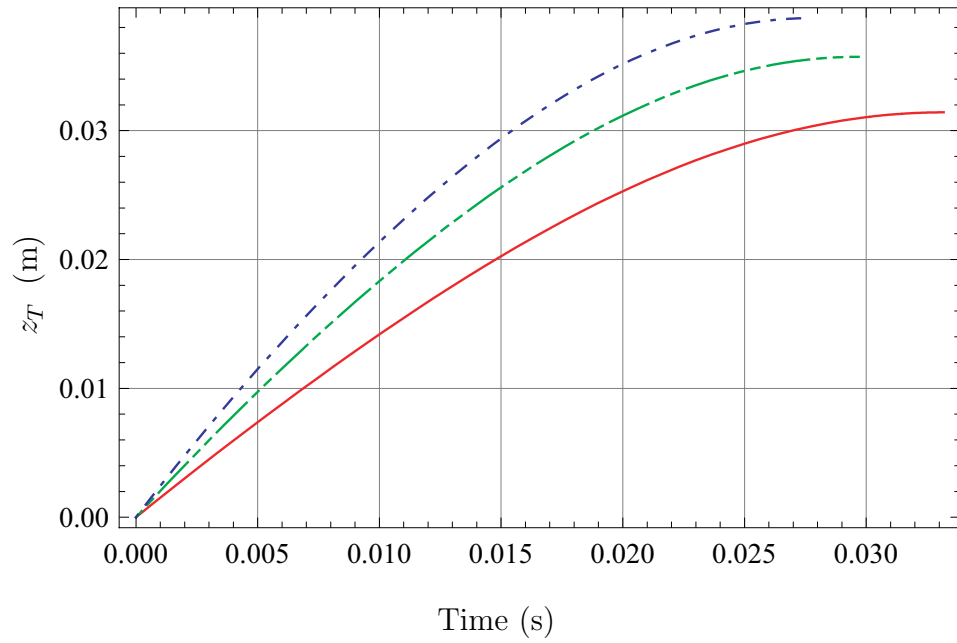


Figure 4.10: Impact results of the rigid cylinder type link for $q(0) = 0^\circ$

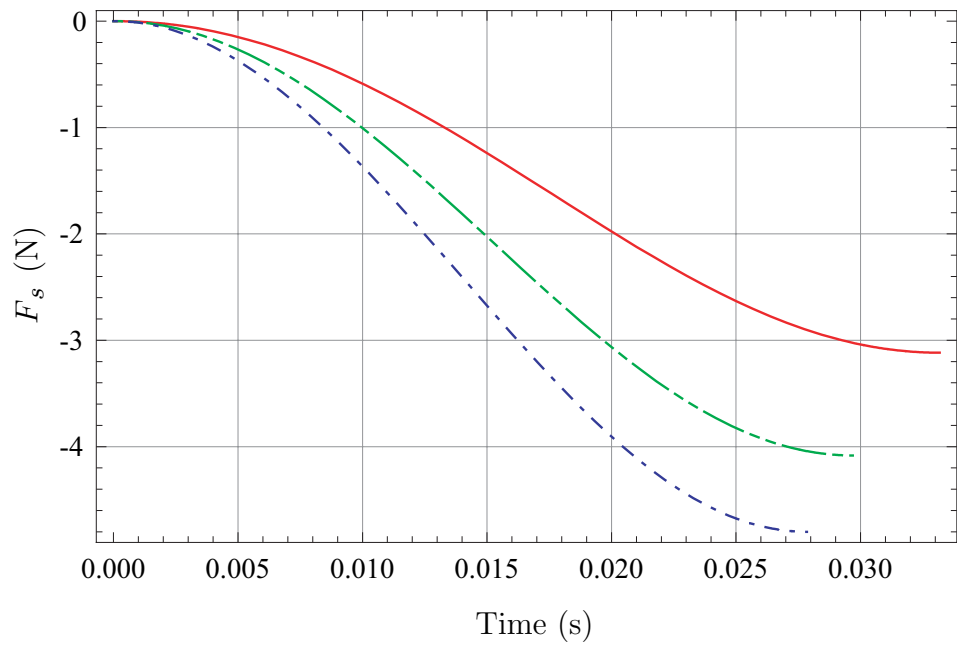
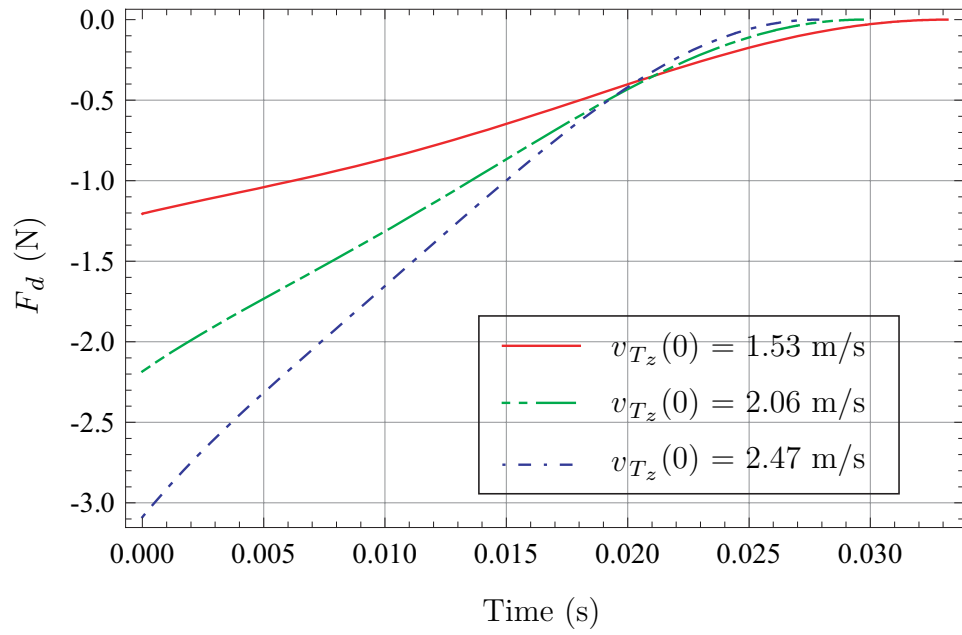


Figure 4.11: Resistance force F_d and F_s for $q(0) = 0^\circ$

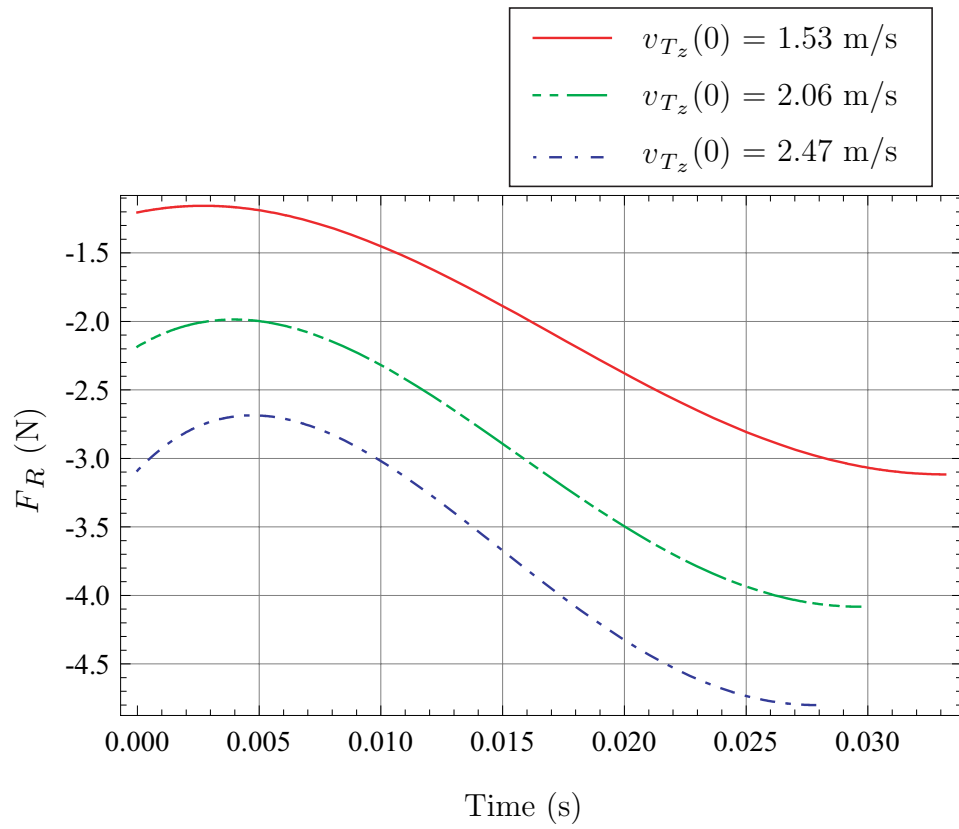


Figure 4.12: Total resistance force F_R for $q(0) = 0^\circ$

stopping time, the penetrating depth, and the initial impact velocity are kept in even multi D.O.F penetrating motion.

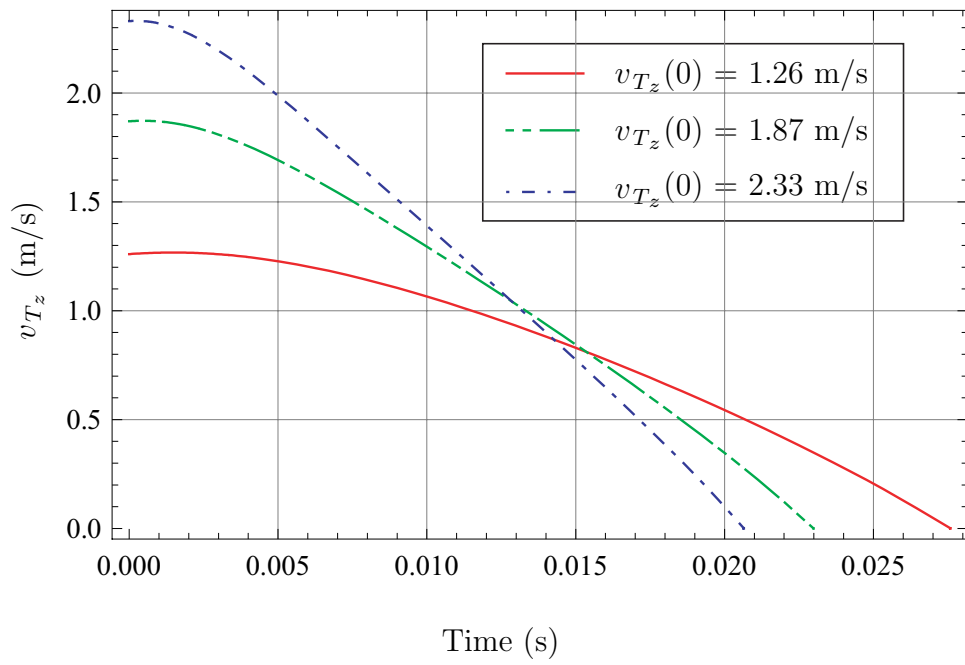
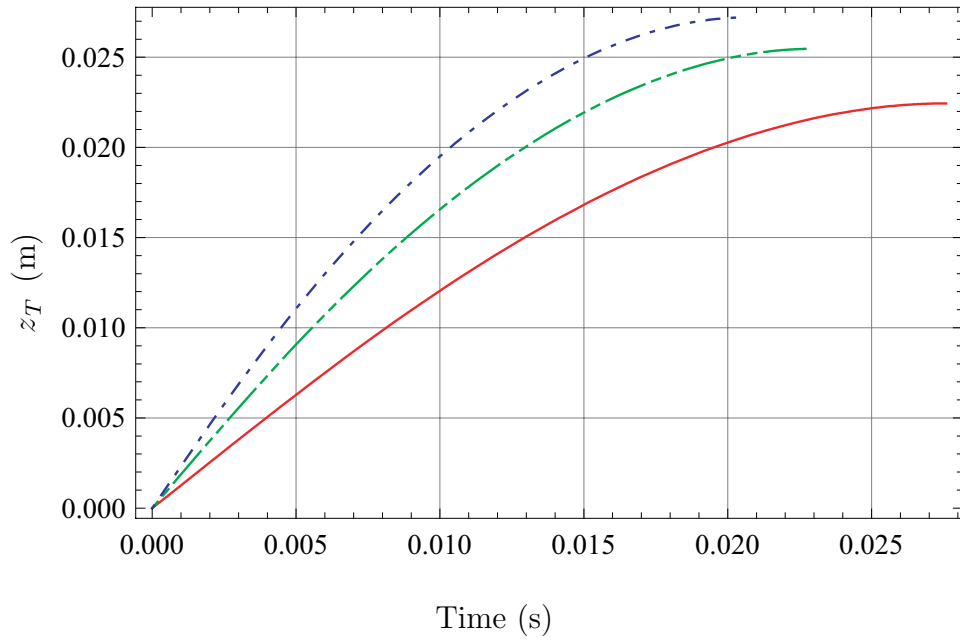


Figure 4.13: Impact results of the rigid cylinder type link for $q(0) = 32^\circ$

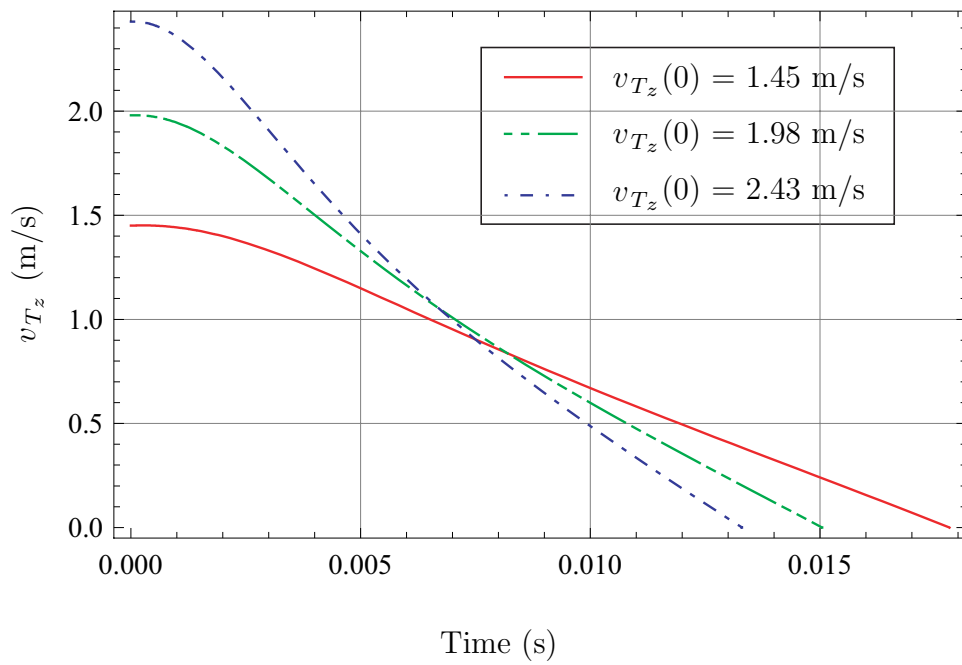
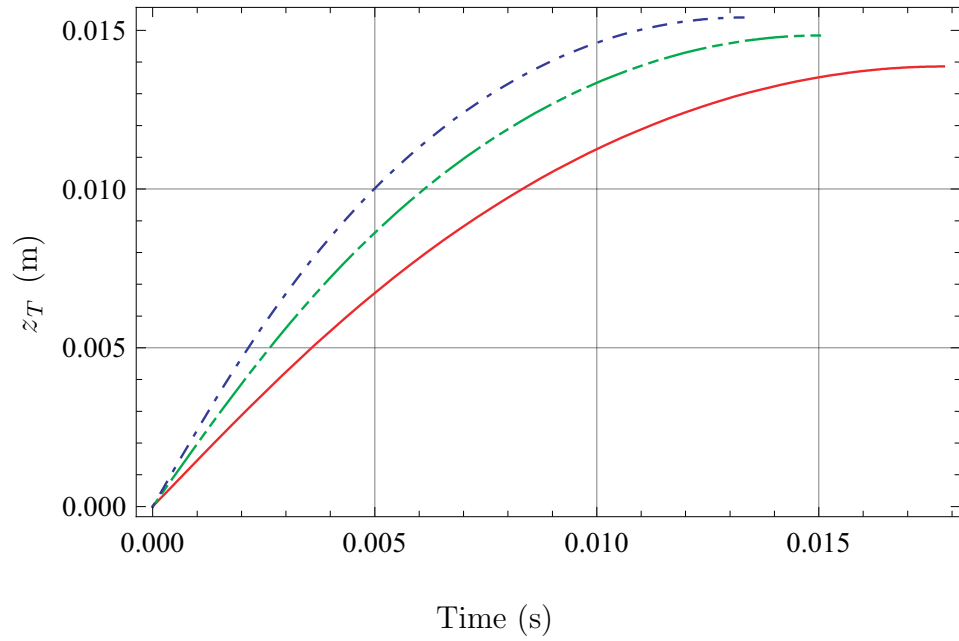


Figure 4.14: Impact results of the rigid cylinder type link for $q(0) = 55^\circ$

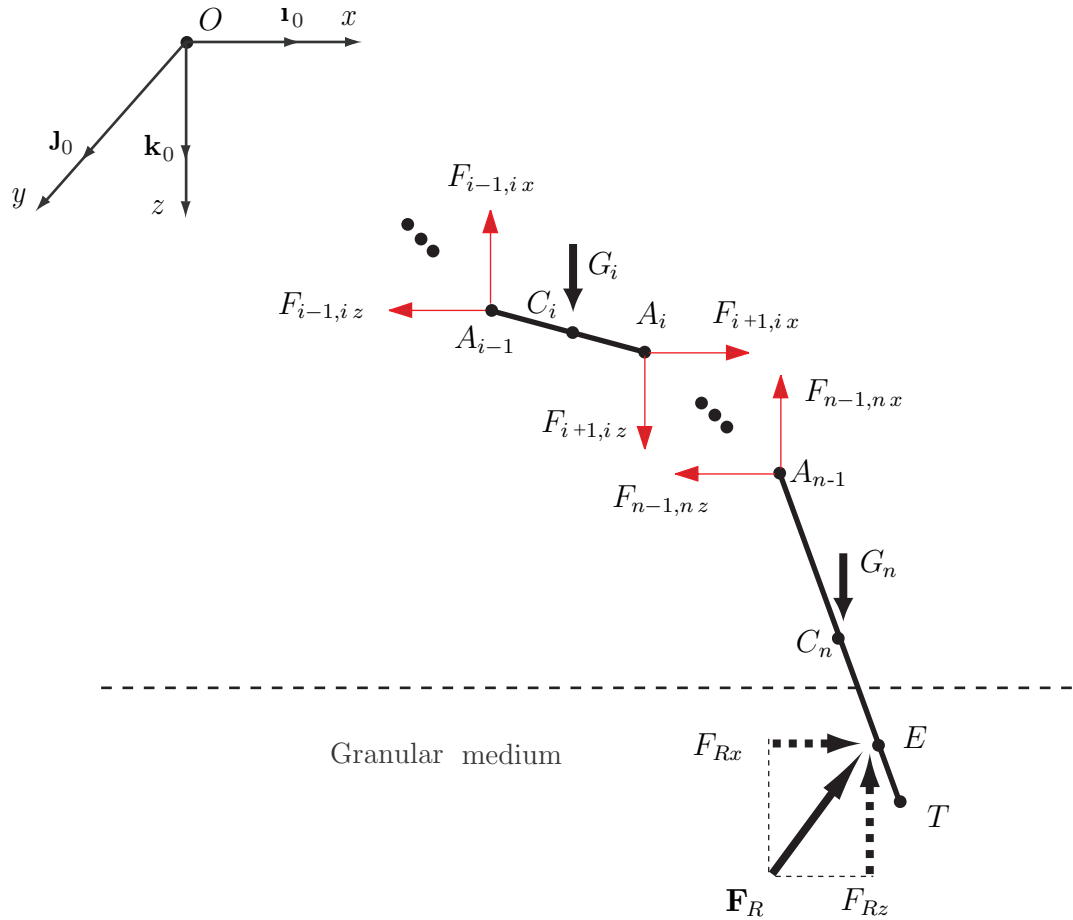


Figure 4.15: Free body diagram of a single impact of a planar kinematic chain

4.2.2 Impact of a planar kinematic chain

Modeling

As mentioned in chapter 2, the angles denoted by q_i s between the z -axis and the link i are the generalized coordinates. The external forces acting on the kinematic chain is the gravity force and the resistance forces as shown in Fig. 4.15. The gravity force \mathbf{G}_i acts at the center of mass, C_i , of the link i and the resistance force, \mathbf{F}_R including \mathbf{F}_s and \mathbf{F}_d , acts at the point E of the last link n , where the point E is the centroid of the immersed part as shown in Fig. 4.15. The general equation of motion for the planar kinematic chain can be

written in the following form

$$\mathbf{M}(\mathbf{q}) \ddot{\mathbf{q}} + \mathbf{C}(\dot{\mathbf{q}}, \mathbf{q}) + \mathbf{G}(\mathbf{q}) = \mathbf{T} + \mathbf{D}(\mathbf{q})\mathbf{F}, \quad (4.34)$$

where $\mathbf{q} = (q_1, \dots, q_n)^T$ is the $n \times 1$ generalized coordinates, $\mathbf{M}(\mathbf{q})$ is the $n \times n$ mass matrix, $\mathbf{C}(\dot{\mathbf{q}}, \mathbf{q})$ is an $n \times 1$ vector, $\mathbf{G}(\mathbf{q})$ is the $n \times 1$ gravity vector, \mathbf{T} is the $n \times 1$ joint moment vector, $\mathbf{D}(\mathbf{q})$ is an $n \times 2$ matrix, and $\mathbf{F} = (F_{R_x}, F_{R_z})^T$ is the resistance force vector.

Under the assumption that the joint moments do not exist, the Newton-Euler's equations is applied to formulate the differential equation of motion. For a compound pendulum ($n = 1$), the equation of motion can be written as

$$I \ddot{q} = \left(\mathbf{r}_C \times \mathbf{G} + \mathbf{r}_E \times \mathbf{F}_R \right) \cdot \mathbf{J}_0, \quad (4.35)$$

where I is the mass moment of inertia with regard to the joint. The vector \mathbf{r}_C representing the position vector from the joint to the mass center C is given as

$$\mathbf{r}_C = L_C \left(\sin q \mathbf{i}_0 + \cos q \mathbf{k}_0 \right), \quad (4.36)$$

where L_C is the length from the joint to the mass center of the pendulum. The position vector from the joint to the resistance force application point E , \mathbf{r}_E , and the resistance force \mathbf{F}_R will be formulated in the case of the n link multi kinematic chain and can be particularized for $n = 1$.

In the case of a multi link kinematic chain, a force and a moment equation for each link $i = 1, 2, \dots, n - 1$ can be written

$$m_i \mathbf{a}_{C_i} = \mathbf{F}_{i-1,i} + \mathbf{F}_{i+1,i} + \mathbf{G}_i, \quad (4.37)$$

$$I_i \ddot{q}_i = \left(\mathbf{r}_{C_i A_{i-1}} \times \mathbf{F}_{i-1,i} + \mathbf{r}_{C_i A_i} \times \mathbf{F}_{i+1,i} \right) \cdot \mathbf{J}_0, \quad (4.38)$$

and for the last link $i = n$

$$m_n \mathbf{a}_{C_n} = \mathbf{F}_{n-1,n} + \mathbf{G}_n + \mathbf{F}_R, \quad (4.39)$$

$$I_n \ddot{q}_n = \left(\mathbf{r}_{C_n A_{n-1}} \times \mathbf{F}_{n-1,n} + \mathbf{r}_{C_n E} \times \mathbf{F}_R \right) \cdot \mathbf{J}_0, \quad (4.40)$$

where m_i is the mass of the link i , I_i is the mass moment of inertia of the link i with regard to its center, and L_i is the length of the link i . The force $\mathbf{F}_{i-1,i}$ is the reaction force of the link $i-1$ on the link i at A_{i-1} , \mathbf{G}_i is the gravity force vector acting on the mass center C_i of the link i , and \mathbf{F}_R is the resistance force vector acting on the last link n . The vector \mathbf{a}_{C_i} is the acceleration vector of the position vector \mathbf{r}_{C_i} and $\mathbf{r}_{C_i A_{i-1}}$ is the position vector from the mass center of the link i to the point A_{i-1} of the link i . The gravity force vector \mathbf{G}_i , the acceleration vector \mathbf{a}_{C_i} , and the position vectors \mathbf{r}_{C_i} , $\mathbf{r}_{C_i A_{i-1}}$ are represented as

$$\mathbf{G}_i = m_i g \mathbf{k}_0, \quad (4.41)$$

$$\mathbf{r}_{C_i} = \left(\sum_{j=1}^{i-1} L_j \sin q_j + L_{C_i} \sin q_i \right) \mathbf{i}_0 + \left(\sum_{j=1}^{i-1} L_j \cos q_j + L_{C_i} \cos q_i \right) \mathbf{k}_0, \quad (4.42)$$

$$\begin{aligned} \mathbf{a}_{C_i} = \frac{d^2 \mathbf{r}_{C_i}}{dt^2} = & \left[\sum_{j=1}^{i-1} L_j (\ddot{q}_j \cos q_j - \dot{q}_j^2 \sin q_j) + L_{C_i} (\ddot{q}_i \cos q_i - \dot{q}_i^2 \sin q_i) \right] \mathbf{i}_0 \\ & - \left[\sum_{j=1}^{i-1} L_j (\ddot{q}_j \sin q_j + \dot{q}_j^2 \cos q_j) + L_{C_i} (\ddot{q}_i \sin q_i + \dot{q}_i^2 \cos q_i) \right] \mathbf{k}_0, \end{aligned} \quad (4.43)$$

$$\mathbf{r}_{C_i A_{i-1}} = -L_{C_i} \sin q_i \mathbf{i}_0 - L_{C_i} \cos q_i \mathbf{k}_0, \quad (4.44)$$

$$\mathbf{r}_{C_i A_i} = (L_i - L_{C_i}) \sin q_i \mathbf{i}_0 + (L_i - L_{C_i}) \cos q_i \mathbf{k}_0, \quad (4.45)$$

where L_{C_i} is the length from the joint A_{i-1} to the mass center C_i of the link i . The vector $\mathbf{r}_{C_n E}$ representing the position vector from the mass center of the last link n , C_n , to the resistance force acting point E is calculated from the vector \mathbf{r}_E representing the position

vector from the origin to the force acting point E as

$$\mathbf{r}_E = \left(\sum_{j=1}^{n-1} L_j \sin q_j + L_E \sin q_n \right) \mathbf{i}_0 + \left(\sum_{j=1}^{n-1} L_j \cos q_j + L_E \cos q_n \right) \mathbf{k}_0, \quad (4.46)$$

$$\mathbf{r}_{C_n E} = \mathbf{r}_E - \mathbf{r}_{C_n} = (L_E - L_{C_n}) (\sin q_n \mathbf{i}_0 + \cos q_n \mathbf{k}_0), \quad (4.47)$$

where L_E , the length from the last joint A_{n-1} to the resistance force acting point E , is represented as

$$L_E = L_n - \frac{1}{2} \frac{z_T}{\cos q_n}. \quad (4.48)$$

The immersed depth of the last link n , z_T , is calculated as

$$z_T = \sum_{i=1}^n L_i \cos q_i - \sum_{i=1}^n L_i \cos q_i(0), \quad (4.49)$$

where $q_i(0)$ is the initial impact angle of q_i .

The other variable of the resistance force vector $\mathbf{F}_R(\mathbf{v}_E, z_T)$, the velocity vector \mathbf{v}_E , is calculated as

$$\begin{aligned} \mathbf{v}_E &= \mathbf{v}_{C_n} + \mathbf{v}_{C_n E} = \frac{d\mathbf{r}_{C_n}}{dt} + q_n \mathbf{J}_0 \times \mathbf{r}_{C_n E} \\ &= \left(\sum_{j=1}^{n-1} L_j \dot{q}_j \cos q_j + L_E \dot{q}_n \cos q_n \right) \mathbf{i}_0 - \left(\sum_{j=1}^{n-1} L_j \dot{q}_j \sin q_j + L_E \dot{q}_n \sin q_n \right) \mathbf{k}_0. \end{aligned} \quad (4.50)$$

The reference area A_r and the moving angle q_m of the penetrating last link n for calculating the dynamic frictional force are represented as

$$A_r = d_c \frac{z_T}{\cos q_n} |\sin(q_n - q_m)|, \quad (4.51)$$

$$q_m = \tan^{-1} \left(-\frac{\sum_{j=1}^{n-1} L_j \dot{q}_j \cos q_j + L_E \dot{q}_n \cos q_n}{\sum_{j=1}^{n-1} L_j \dot{q}_j \sin q_j + L_E \dot{q}_n \sin q_n} \right). \quad (4.52)$$

Therefore the dynamic frictional force \mathbf{F}_d is given by Eq. (3.6) as

$$\begin{aligned} \mathbf{F}_d = & \eta_d \rho_g d_c \frac{z_T}{\cos q_n} \left| \sin \left(q_n - \tan^{-1} \left(-\frac{\sum_{j=1}^{n-1} L_j \dot{q}_j \cos q_j + L_E \dot{q}_n \cos q_n}{\sum_{j=1}^{n-1} L_j \dot{q}_j \sin q_j + L_E \dot{q}_n \sin q_n} \right) \right) \right| \\ & \sqrt{\left(\sum_{j=1}^{n-1} L_j \dot{q}_j \cos q_j + L_E \dot{q}_n \cos q_n \right)^2 + \left(\sum_{j=1}^{n-1} L_j \dot{q}_j \sin q_j + L_E \dot{q}_n \sin q_n \right)^2} \\ & \left[- \left(\sum_{j=1}^{n-1} L_j \dot{q}_j \cos q_j + L_E \dot{q}_n \cos q_n \right) \mathbf{i}_0 \right. \\ & \left. + \left(\sum_{j=1}^{n-1} L_j \dot{q}_j \sin q_j + L_E \dot{q}_n \sin q_n \right) \mathbf{k}_0 \right]. \end{aligned} \quad (4.53)$$

The immersed volume V for the static resistance force is calculated as

$$V = \frac{\pi d_c^2}{4} \frac{z_T}{\cos q}. \quad (4.54)$$

Hence, the horizontal and vertical static resistance forces, \mathbf{F}_{sh} and \mathbf{F}_{sv} are

$$\mathbf{F}_{sh} = -\text{sign} \left(\sum_{j=1}^{n-1} L_j \dot{q}_j \cos q_j + L_E \dot{q}_n \cos q_n \right) \eta_h g \rho_g z_T^2 d_c \mathbf{i}_0, \quad (4.55)$$

$$\mathbf{F}_{sv} = \text{sign} \left(\sum_{j=1}^{n-1} L_j \dot{q}_j \sin q_j + L_E \dot{q}_n \sin q_n \right) \eta_v \left(\frac{z_T}{d_c} \right)^\lambda g \rho_g \frac{\pi d_c^2}{4} \frac{z_T}{\cos q} \mathbf{k}_0, \quad (4.56)$$

The resistance force \mathbf{F}_R , the sum of the dynamic frictional force vector \mathbf{F}_d and the static resistance force vector \mathbf{F}_s , is represented by the sum of Eqs. (4.53), (4.55), and (4.56).

The joint reaction force $\mathbf{F}_{i-1,i}$ can be calculated using the relations $\mathbf{F}_{i+1,i} = -\mathbf{F}_{i,i+1}$ and Eqs. (4.37) and (4.39) as

$$\mathbf{F}_{i-1,i} = \sum_{j=i}^n m_j \mathbf{a}_{C_j} - \mathbf{G}_j - \mathbf{F}_R. \quad (4.57)$$

The equations of motion described by Eqs. (4.37), (4.38), (4.39), and (4.40) can be simplified and rewritten for each link $i = 1, 2, \dots, n - 1$

$$I_i \ddot{q}_i = - \left[L_{C_i} \left(\sin q_i \mathbf{1}_0 + \cos q_i \mathbf{k}_0 \right) \times \left(\sum_{j=i}^n m_j \mathbf{a}_{C_j} - \mathbf{G}_j - \mathbf{F}_R \right) + \left(L_i - L_{C_i} \right) \left(\sin q_i \mathbf{1}_0 + \cos q_i \mathbf{k}_0 \right) \times \left(\sum_{j=i+1}^n m_j \mathbf{a}_{C_j} - \mathbf{G}_j - \mathbf{F}_R \right) \right] \cdot \mathbf{J}_0 \quad (4.58)$$

and for the last link $i = n$

$$I_n \ddot{q}_n = \left[- L_{C_n} \left(\sin q_n \mathbf{1}_0 + \cos q_n \mathbf{k}_0 \right) \times \left(m_n \mathbf{a}_{C_n} - \mathbf{G}_n - \mathbf{F}_R \right) + \left(L_E - L_{C_n} \right) \left(\sin q_n \mathbf{1}_0 + \cos q_n \mathbf{k}_0 \right) \times \mathbf{F}_R \right] \cdot \mathbf{J}_0. \quad (4.59)$$

The final nonlinear equations of motion will have the form as

$$f_i \left(\ddot{q}_i, \dot{q}_i, m_i, L_i, g, F_R \right) = 0. \quad (4.60)$$

Simulation results of a compound pendulum

The dimensions of the rigid compound pendulum are shown in Fig. 4.16. The dimensions of the pendulum are the length $L_{p_1} = 0.78''$ ($= 0.019812$ m), $L_{p_2} = 0.6''$ ($= 0.01524$ m), $L_{p_3} = 9.4''$ ($= 0.23876$ m) and the diameter $d_{p_1} = 0.75''$ ($= 0.01905$ m), $d_{p_2} = 0.6''$ ($= 0.01524$ m), $d_{p_3} = d_c = 0.25''$ ($= 0.00635$ m). The density of the link, ρ_c , is also 7.7×10^3 kg/m³ and the density of a granular medium (sand), ρ_g , is applied as 2.5×10^3 kg/m³. The dynamic frictional force coefficient $\eta_d = 6.5$, the horizontal static resistance force coefficient $\eta_h = 8$, and the vertical static resistance force coefficients $\eta_v = 22$ and $\lambda = 1.1$ are used in the simulation. Figures 4.17, 4.18, 4.19, and 4.20 represent the simulation results of the impact of the rigid compound pendulum.

The simulations are performed for different impact angle $q(0)$ and different initial impact velocities ($\dot{q}(0) = -1.75, -3.38, \text{ and } -4.66$ rad/s for $q(0) = 22^\circ$, $\dot{q}(0) = -3.31, -6.24, \text{ and}$

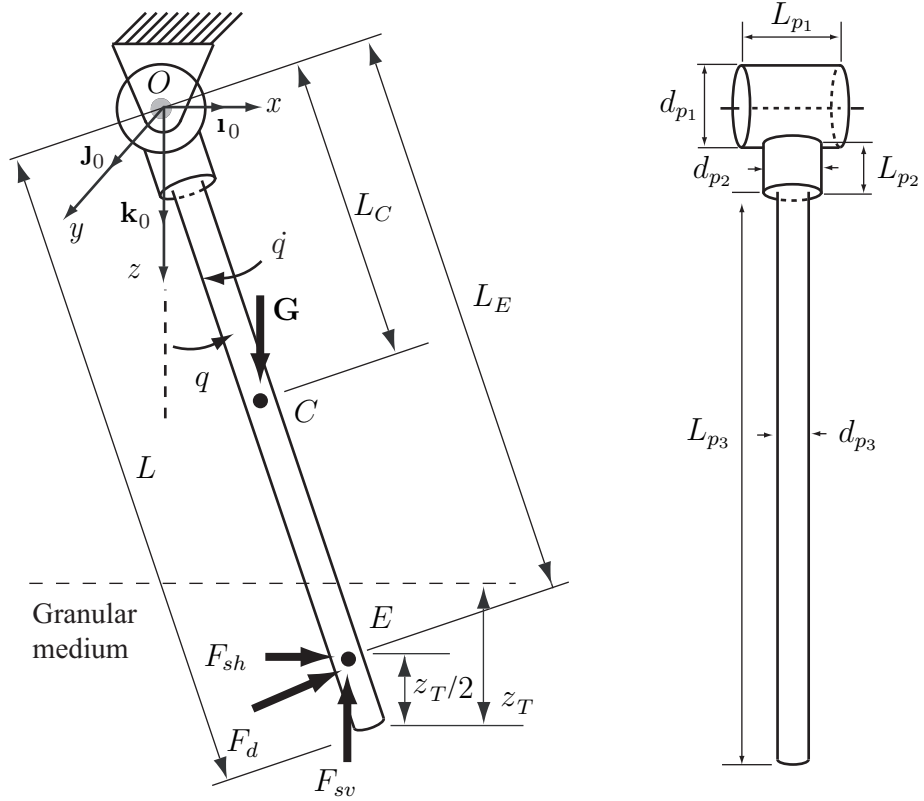


Figure 4.16: Compound pendulum

-8.41 rad/s for $q(0) = 31^\circ$, $\dot{q}(0) = -2.66, -6.47, \text{ and } -9.06$ rad/s for $q(0) = 45^\circ$, and $\dot{q}(0) = -2.70, -6.54, \text{ and } -9.17$ rad/s for $q(0)$ is 61.5°) from the impact moment until the angular velocity of the pendulum, \dot{q} , becomes zero. As shown in Figs. 4.17, 4.18, 4.19, and 4.20 and in table 4.4, the penetrating angle q of the pendulum increases but the time the angular velocity \dot{q} becomes zero decreases when the initial vertical impact velocity increases as the results of previous models.

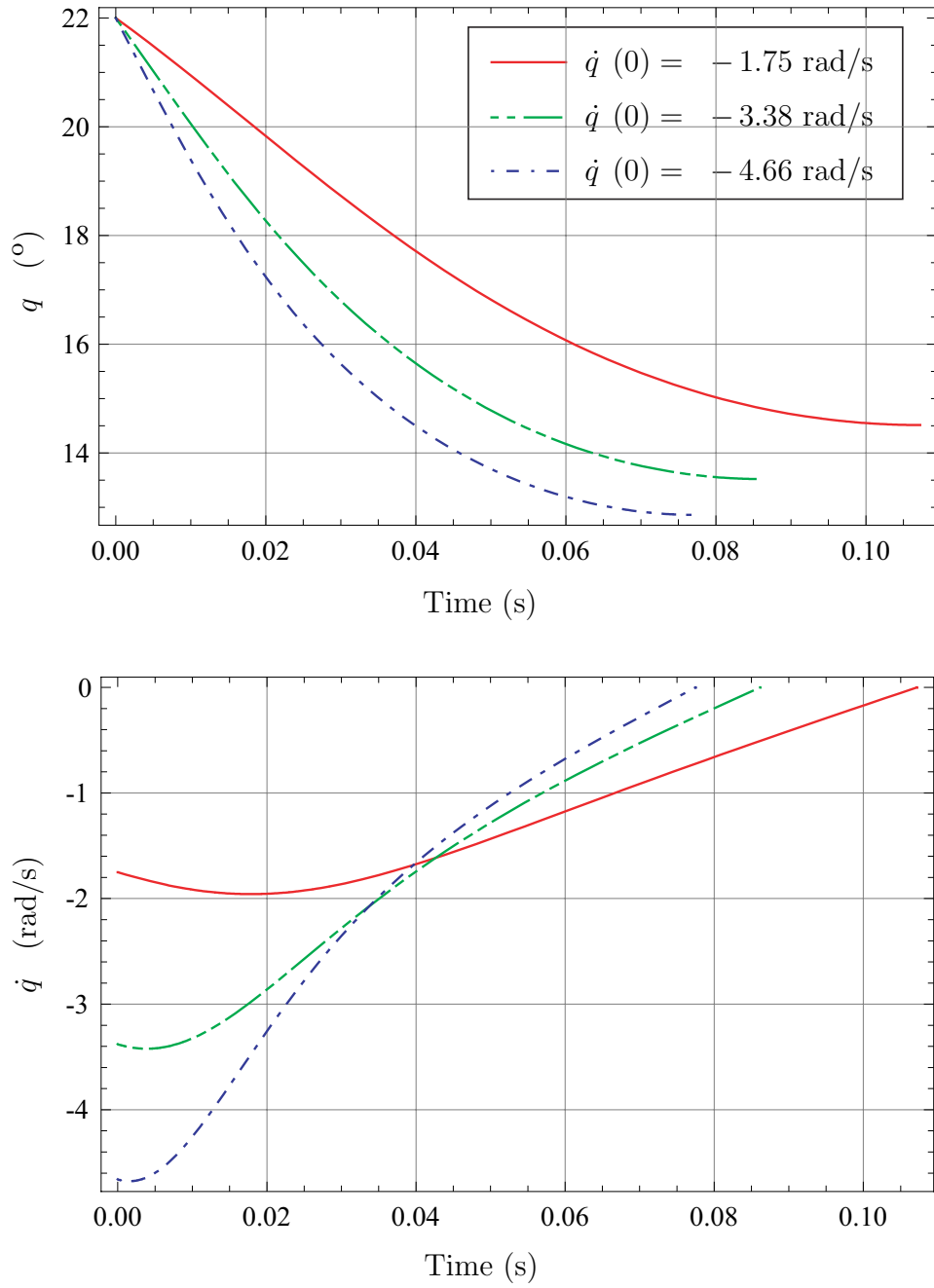


Figure 4.17: Impact results of the rigid compound pendulum for $q(0) = 22^\circ$

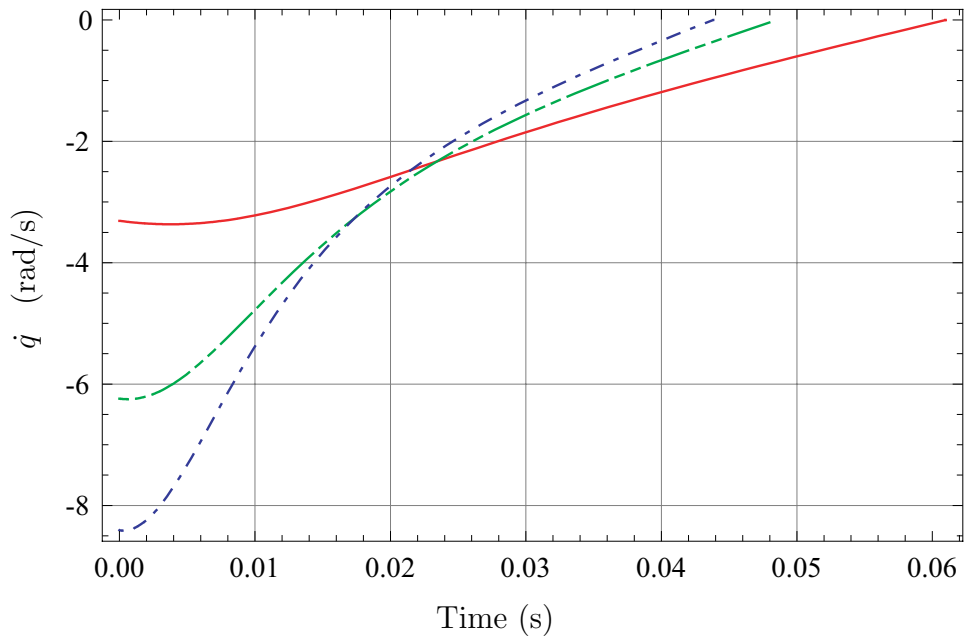
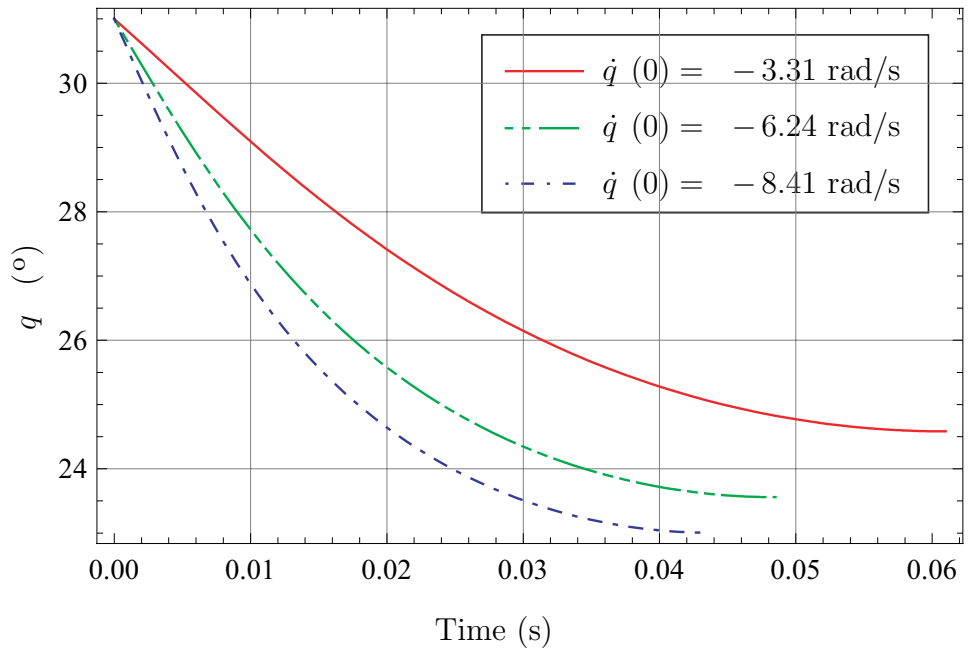


Figure 4.18: Impact results of the rigid compound pendulum for $q(0) = 31^\circ$

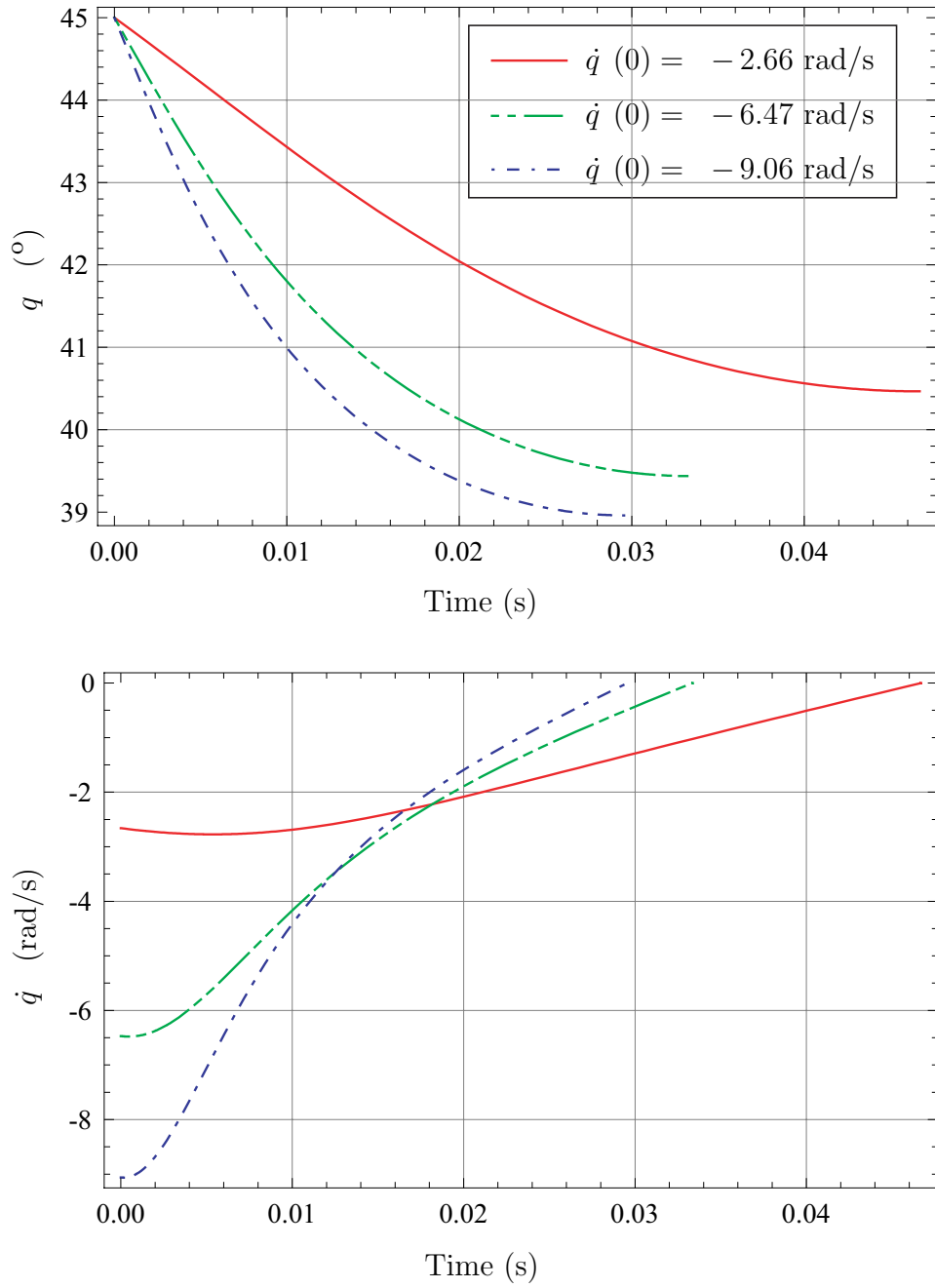


Figure 4.19: Impact results of the rigid compound pendulum for $q(0) = 45^\circ$

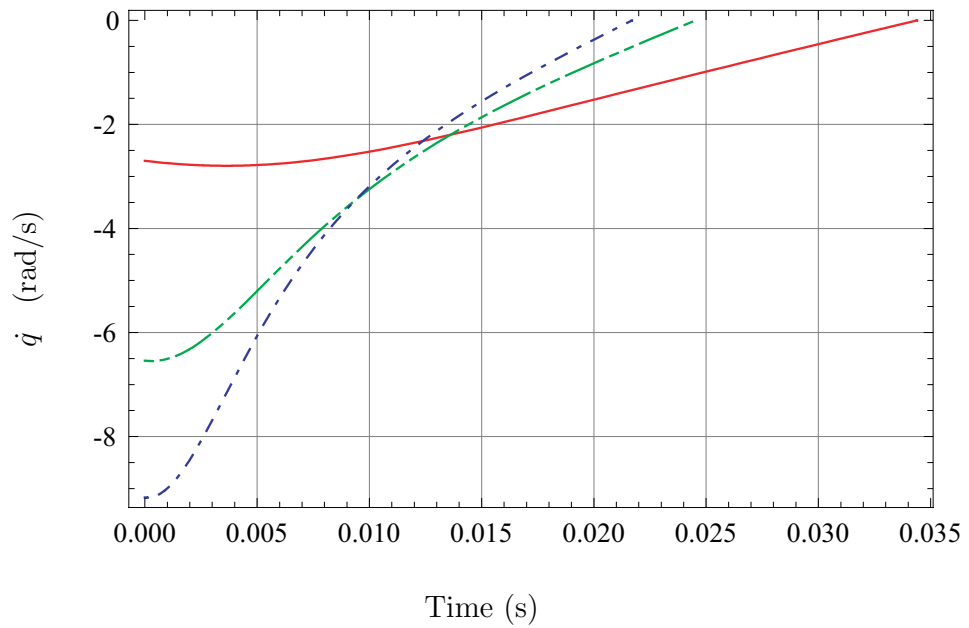
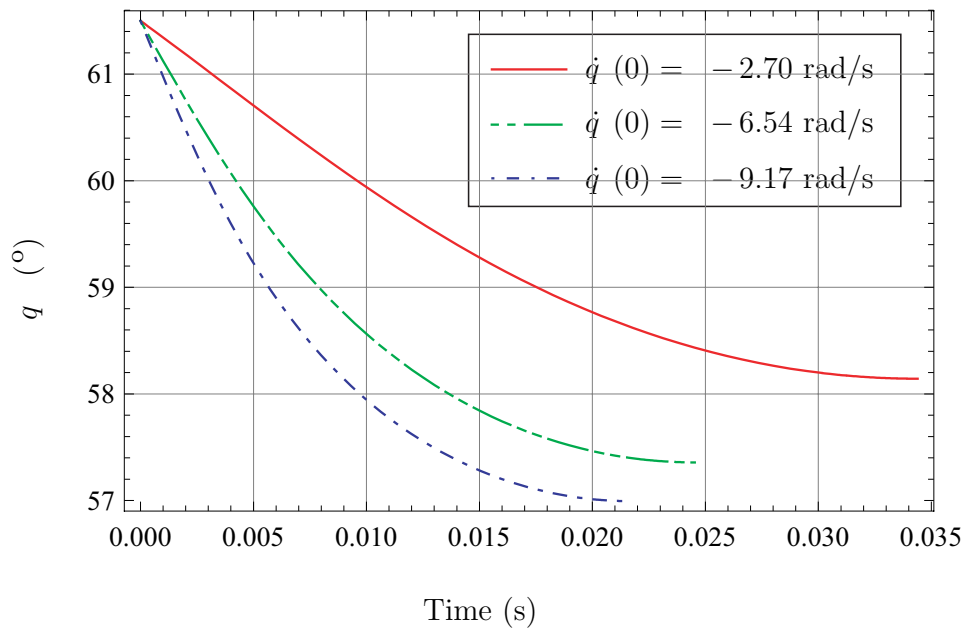


Figure 4.20: Impact results of the rigid compound pendulum for $q(0) = 61.5^\circ$

Table 4.4: Stopping time of the rigid compound pendulum

$q(0)$ ($^\circ$)	$\dot{q}(0)$ (rad/s)	t_s (s)
	-1.75	0.107212
22	-3.38	0.0861789
	-4.66	0.0775028
31	-3.31	0.0609829
	-6.24	0.0485081
	-8.41	0.043819
45	-2.66	0.046688
	-6.47	0.0333638
	-9.06	0.0295578
61.5	-2.70	0.0343956
	-6.54	0.0245294
	-9.17	0.0216994

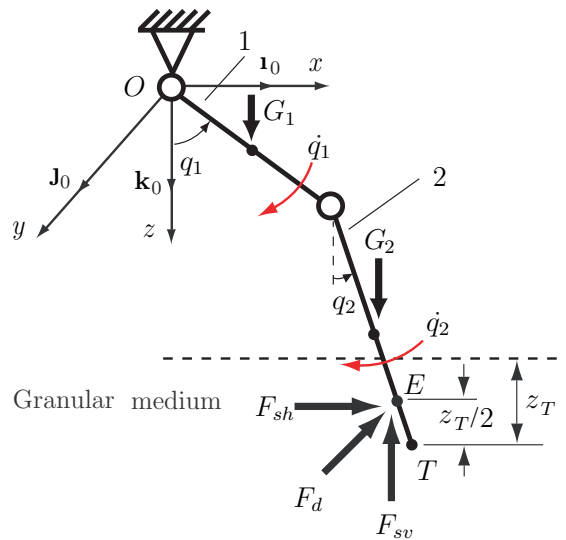


Figure 4.21: Double pendulum

Simulation results of a double pendulum

The double pendulum under consideration is shown in Fig. 4.21. As the numerical data applied to the simulation, the lengths of link 1 and 2, $L_1 = 0.2$ m and $L_2 = 0.6$ m, the diameter $d_c = 0.0254$ m, the density of the link $\rho_c = 7.7 \times 10^3$ kg/m³, and the density of a granular medium (sand) $\rho_g = 2.5 \times 10^3$ kg/m³, the dynamic frictional force coefficient $\eta_d = 6.5$, the horizontal static resistance force coefficient $\eta_h = 8$, and the vertical static resistance force coefficients $\eta_v = 22$ and $\lambda = 1.1$ are used in the simulation.

Figures 4.22 and 4.23 represent the simulation results for the double pendulum with the following initial conditions: $q_1(0) = 30^\circ$, $q_2(0) = 75^\circ$ ($q_1(0) < q_2(0)$) and $\dot{q}_1(0) = \dot{q}_2(0) = -1, -3, -5$ rad/s. The initial vertical tip velocity $v_{Tz}(0)$ of the impact point and horizontal one $v_{Tx}(0)$ are increasing. The total stopping time t_t is defined as the time starting from the impact moment until \dot{q}_1 and \dot{q}_2 become zero simultaneously ($\dot{q}_1(t_t) = \dot{q}_2(t_t) = 0$). For this case the total stopping time t_t is decreasing with the increasing of the initial velocity as shown in Fig. 4.22 and table 4.5. The vertical tip velocity v_{Tz} stops first and the total stopping time t_t is dictated by the horizontal tip velocities v_{Tx} as shown in Fig. 4.23. For this case the tip velocities v_{Tz} and v_{Tx} do not change the sign.

For this simulation, we also observed an additional stopping time t_z representing the time from the moment of impact until the vertical velocity of the pendulum tip, v_{Tz} , becomes

Table 4.5: Stopping time and penetrating depth results of the double pendulum for $q_1(0) = 30^\circ$ and $q_2(0) = 75^\circ$

$\dot{q}_1(0)$ (rad/s)	$\dot{q}_2(0)$ (rad/s)	t_t (s)	t_z (s)	z_T (m)
-1	-1	0.440289	0.0546257	0.0277009
-3	-3	0.309807	0.0355301	0.0347221
-5	-5	0.260902	0.0289713	0.0389723
	-1	0.319782	0.0450784	0.0288578
-5	-3	0.286156	0.0338793	0.0347693
	-5	0.260902	0.0289713	0.0389723

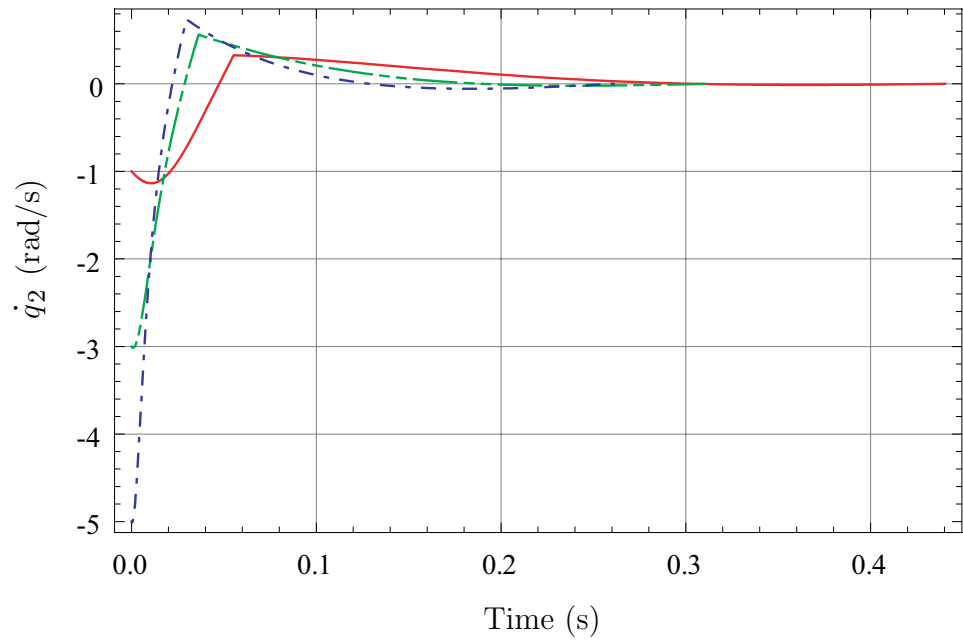
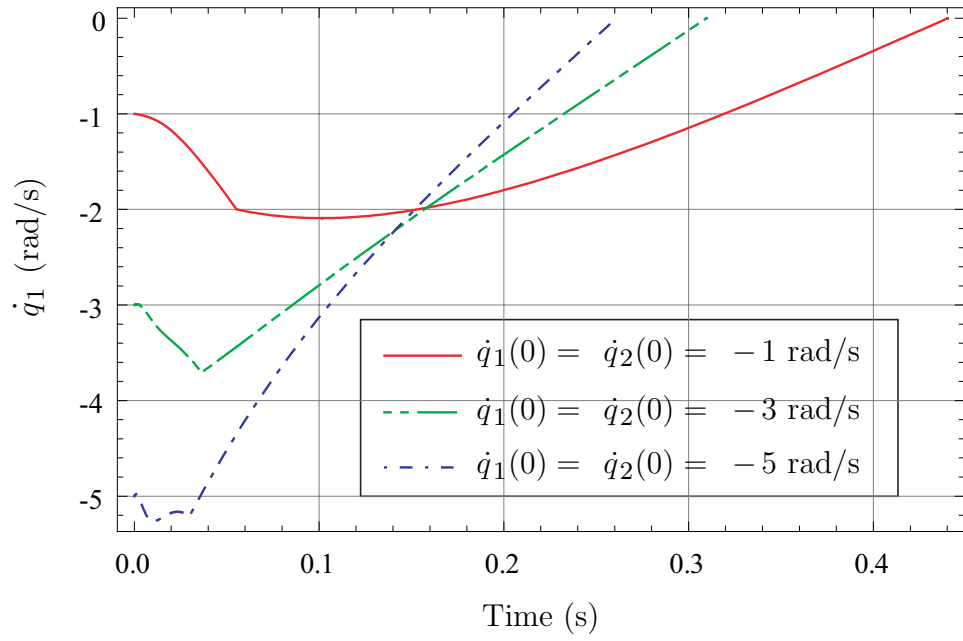


Figure 4.22: Angular velocities \dot{q}_1 and \dot{q}_2 results of the double pendulum impact for $q_1(0) = 30^\circ$, $q_2(0) = 75^\circ$, and $\dot{q}_1(0) = \dot{q}_2(0) = -1, -3, -5$ rad/s

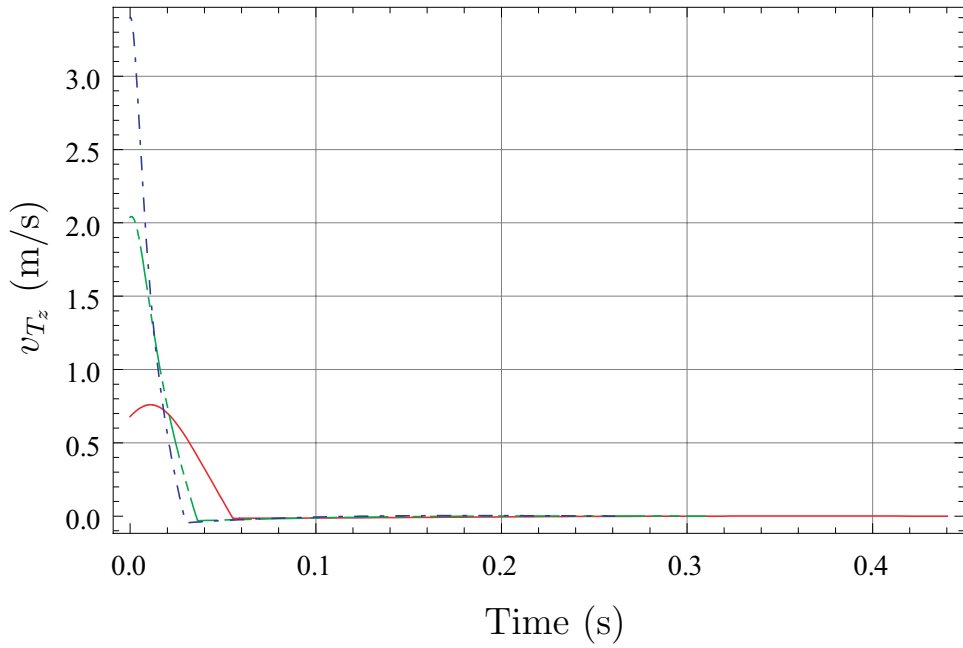
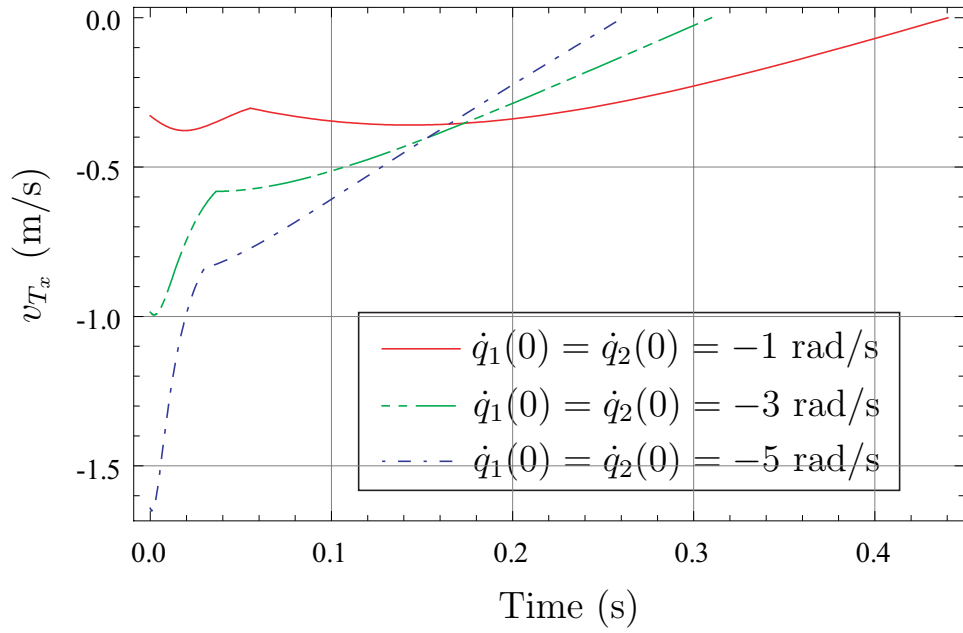


Figure 4.23: Velocities v_{Tx} and v_{Tz} results of the double pendulum impact for $q_1(0) = 30^\circ$, $q_2(0) = 75^\circ$, and $\dot{q}_1(0) = \dot{q}_2(0) = -1, -3, -5$ rad/s

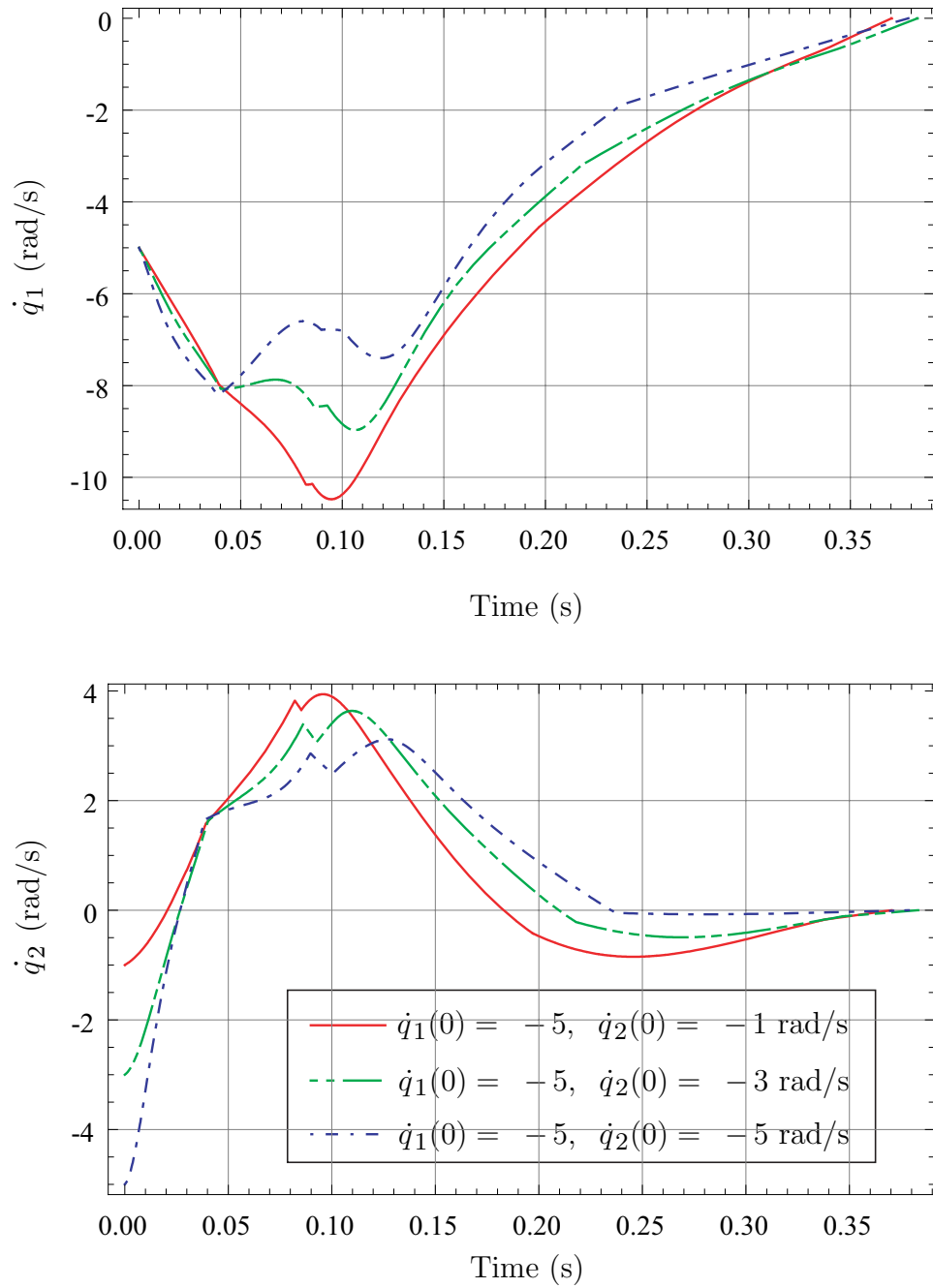


Figure 4.24: Angular velocities \dot{q}_1 and \dot{q}_2 results of the double pendulum impact for $q_1(0) = 75^\circ$, $q_2(0) = 30^\circ$, $\dot{q}_1(0) = -5$ rad/s, and $\dot{q}_2(0) = -1, -3, -5$ rad/s

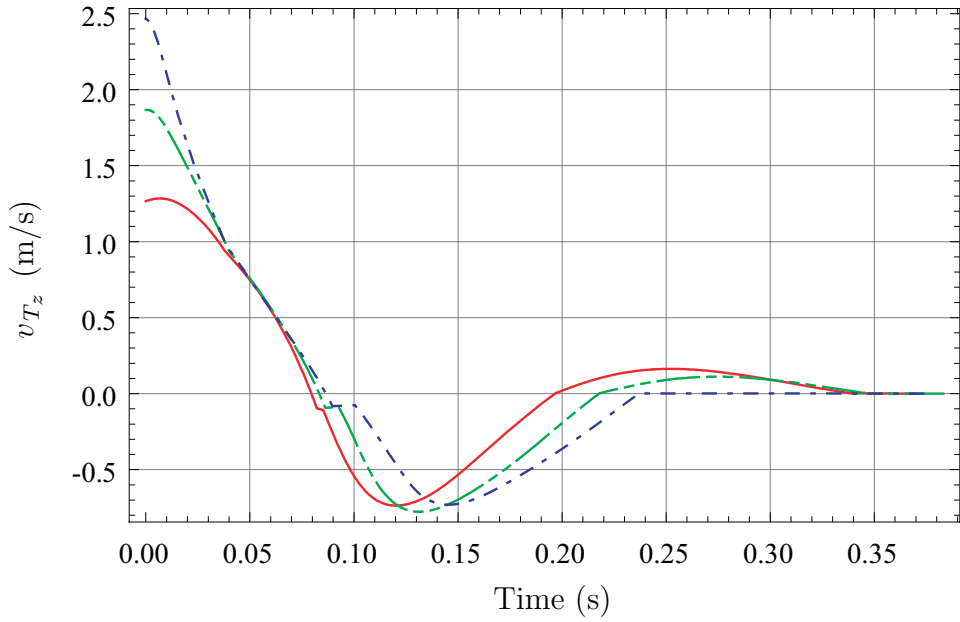
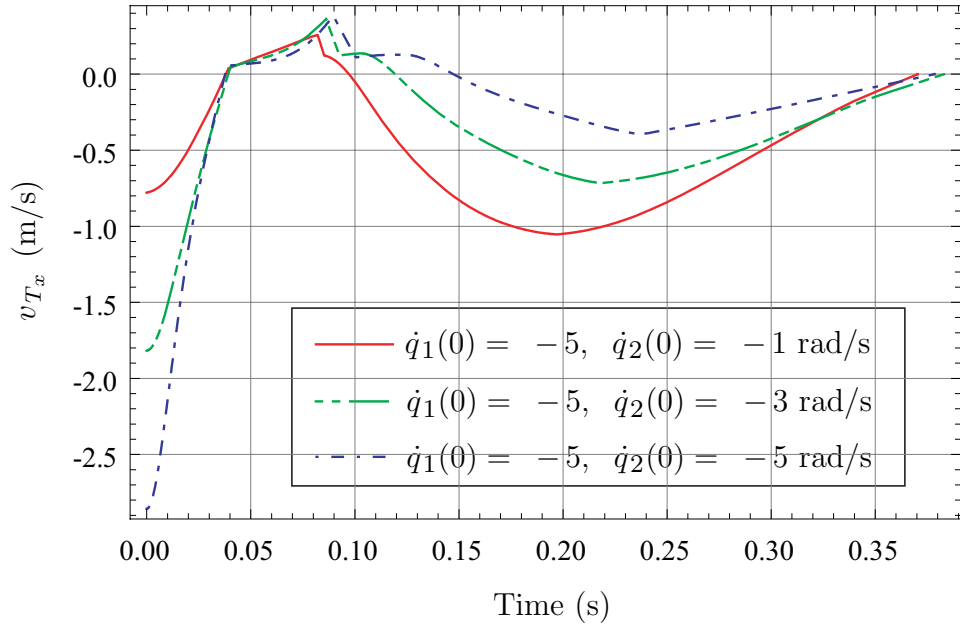


Figure 4.25: Velocities v_{T_x} and v_{T_z} results of the double pendulum impact for $q_1(0) = 75^\circ$, $q_2(0) = 30^\circ$, $\dot{q}_1(0) = -5$ rad/s, and $\dot{q}_2(0) = -1, -3, -5$ rad/s

zero. For this interval of time we represent the penetrating depth of the pendulum tip, z_T . As shown in table 4.5, the stopping time t_z is decreasing and the penetrating depth of the pendulum tip, z_T is increasing with the increasing of the initial velocity. Using different initial impact velocities, ($\dot{q}_1(0) = -5$ rad/s, $\dot{q}_2(0) = -1, -3, -5$ rad/s), the simulation results are presented in table 4.5. For these cases we can draw the same remarks about t_t , t_z , and z_T .

Using a different initial geometry for the links ($q_1(0) = 75^\circ$ and $q_2(0) = 30^\circ$ ($q_1(0) > q_2(0)$)) and initial impact velocity configurations ($\dot{q}_1(0) = -\dot{q}_2(0) = 1, 3, 5$ rad/s), the simulation results for t_t , t_z , and z_T are shown in table 4.6. For these simulations the total stopping time t_t and the stopping time for z direction are decreasing and the penetrating depth of the pendulum tip, z_T , is increasing with the initial impact velocities as previous initial geometric conditions.

A different phenomenon is observed for the same configurations ($q_1(0) = 75^\circ$ and $q_2(0) = 30^\circ$) but different initial velocities ($\dot{q}_1(0) = -5$ rad/s and $\dot{q}_2(0) = -1, -3, -5$ rad/s). The stopping times are almost the same at the end of the simulation time as shown in Figs. 4.24 and 4.25. The vertical tip velocity v_{Tz} stops first and the total stopping time t_t is dictated by the horizontal tip velocities v_{Tx} as shown in Fig. 4.25. For this case the vertical tip velocity v_{Tz} and the horizontal tip velocity v_{Tx} change the sign during the impact process. The stopping time behavior is also different from the previous case because for $\dot{q}_2(0) = -3$ rad/s the total stopping time t_t is increasing even though t_t is again decreasing for $\dot{q}_2(0) = -5$ rad/s as shown in table 4.6. Furthermore the stopping time t_z is increasing with the initial velocities for all the cases. The withdrawing motion ($v_{Tz} < 0$) of the link 2 happening during the impact process might affect the stopping time. From these simulation results for the initial impact conditions ($q_1(0)$ & $q_2(0)$ and $\dot{q}_1(0)$ & $\dot{q}_2(0)$), the stopping time of the double pendulum can be affected by the withdrawing motion of the link 2. The stopping times increase or decrease depending on the effects of the withdrawing motion. For this case the differences between stopping time are observed to be small. However, the

Table 4.6: Stopping time and penetrating depth results of the double pendulum for $q_1(0) = 75^\circ$ and $q_2(0) = 30^\circ$

$\dot{q}_1(0)$ (rad/s)	$\dot{q}_2(0)$ (rad/s)	t_t (s)	t_z (s)	z_T (m)
-1	-1	0.470185	0.133222	0.0674095
-3	-3	0.416271	0.112135	0.0826002
-5	-5	0.378573	0.0865091	0.0898785
	-1	0.370393	0.0795579	0.067502
-5	-3	0.383146	0.0833189	0.0810202
	-5	0.378573	0.0865091	0.0898785

penetrating depth of the pendulum tip z_T is increasing with the initial velocities the same as the previous simulation results.

4.3 Multiple impacts of a planar kinematic chain

Modeling

The angle between the z -axis and the link i is denoted by q_i , ($i = 1, 2, 3, \dots, n$). The x and z -axis distances from the origin to a point (joint A_1 in this model) are denoted by q_x and q_z respectively as shown in Fig. 2.7. The gravity force \mathbf{G}_i acts at the mass center C_i of the link i . The resistance force \mathbf{F}_{R_j} acts at the point E_j of the link j interacting with the granular medium, where the point E_j is the centroid point of the immersed part of the link j . The equations of motion for the planar kinematic chain with multiple contact points shown in Fig. 4.26 can be written in the following general form

$$\mathbf{M}(\mathbf{q})\ddot{\mathbf{q}} + \mathbf{C}(\mathbf{q}, \dot{\mathbf{q}}) + \mathbf{G}(\mathbf{q}) = \begin{bmatrix} \mathbf{T} \\ 0 \\ 0 \end{bmatrix} + \begin{bmatrix} \mathbf{D}_1(\mathbf{q}) \\ \mathbf{D}_2 \end{bmatrix} \mathbf{F}, \quad (4.61)$$

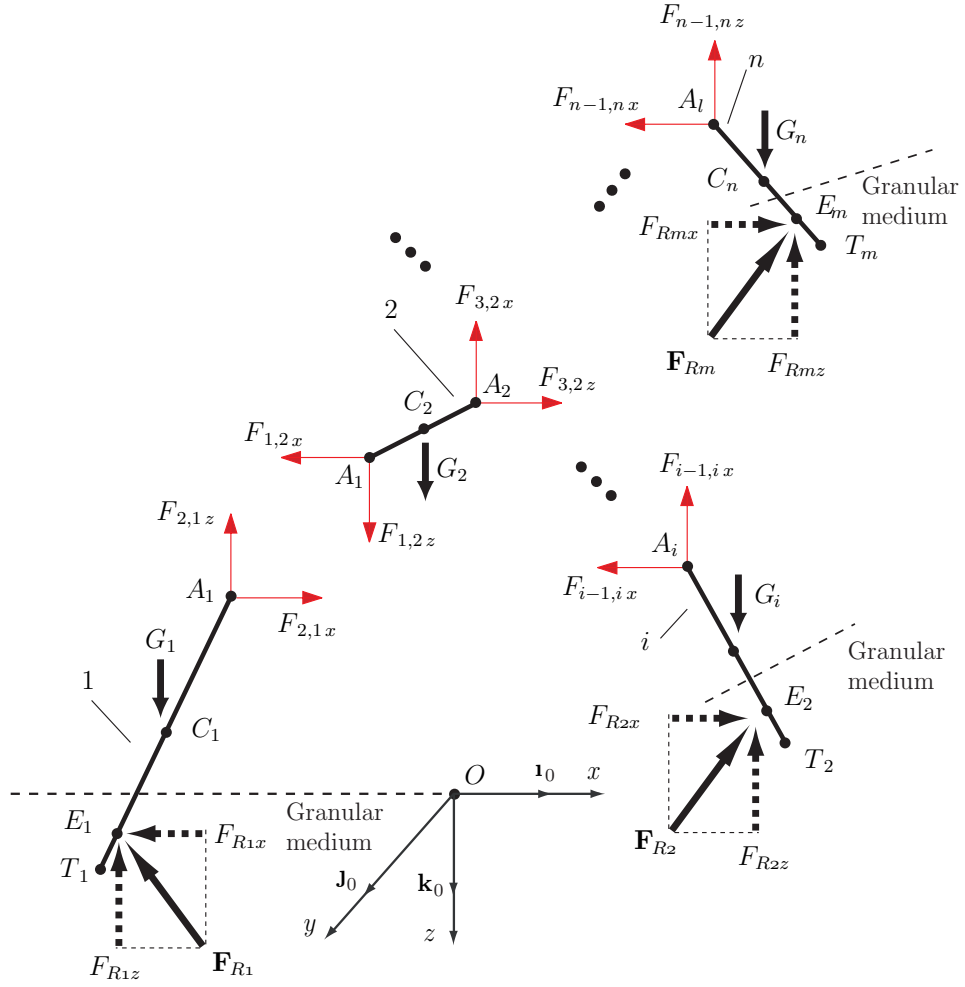


Figure 4.26: Free body diagram of multiple impacts of a planar kinematic chain

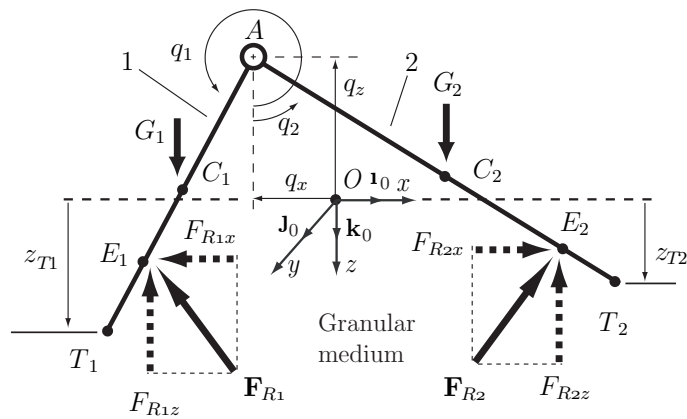


Figure 4.27: Two link kinematic chain with two impact points model

where $\mathbf{q} = (q_1, \dots, q_n, q_x, q_z)^T$ is the $(n + 2) \times 1$ -dimensional vector of generalized coordinates; $\dot{\mathbf{q}} = (\dot{q}_1, \dots, \dot{q}_n, \dot{q}_x, \dot{q}_z)^T$ is the $(n + 2) \times 1$ -dimensional vector of generalized velocities, $\ddot{\mathbf{q}} = (\ddot{q}_1, \dots, \ddot{q}_n, \ddot{q}_x, \ddot{q}_z)^T$ is the $(n + 2) \times 1$ -dimensional vector of generalized accelerations, $\mathbf{M}(\mathbf{q})$ is the $(n + 2) \times (n + 2)$ mass matrix, $\mathbf{C}(\mathbf{q}, \dot{\mathbf{q}})$ is a $(n + 2) \times 1$ vector, $\mathbf{G}(\mathbf{q})$ is the $(n + 2) \times 1$ vector of gravity terms, \mathbf{T} is the $n \times 1$ vector of joint moments, $\mathbf{D}_1(\mathbf{q})$ is an $n \times 2k$ matrix, $\mathbf{D}_2 = (1, 0, 1, 0, \dots; 0, 1, 0, 1, \dots)$ is the $2 \times 2k$ matrix, $\mathbf{F} = (F_{R_1x}, F_{R_1z}, F_{R_2x}, F_{R_2z}, \dots, F_{R_kx}, F_{R_kz})^T$ is the $2k \times 1$ vector of resistance forces, and the components F_{R_jx} and F_{R_jz} are the x -axis and the z -axis components of the resistance force \mathbf{F}_{R_j} respectively. Applying Newton-Euler's equations for the kinematic chain, the matrices \mathbf{M} , \mathbf{C} , \mathbf{G} , \mathbf{T} , \mathbf{D}_1 , \mathbf{D}_2 , and \mathbf{F} can be calculated for a specific example.

In this study, an ideal two link chain are considered as the simplified application of the kinematic chain model, as shown in Fig. 4.27. The number of D.O.F. is 4 and its generalized coordinates are $\mathbf{q} = (q_1, q_2, q_x, q_z)^T$. Under the same assumption that the joint moment does not exist, the Newton-Euler's equations give the governing differential equations for the two link chain:

$$m_1 \mathbf{a}_{C_1} = \mathbf{G}_1 + \mathbf{F}_{R_1} + \mathbf{F}_{2,1}, \quad (4.62)$$

$$m_2 \mathbf{a}_{C_2} = \mathbf{G}_2 + \mathbf{F}_{R_2} + \mathbf{F}_{1,2}, \quad (4.63)$$

$$\begin{aligned} I_1 \ddot{q}_1 \mathbf{J} &= \mathbf{r}_{C_1A} \times \mathbf{F}_{2,1} + \mathbf{r}_{C_1E_1} \times \mathbf{F}_{R_1} \\ &= \mathbf{r}_{C_1A} \times (m_1 \mathbf{a}_{C_1} - \mathbf{G}_1 - \mathbf{F}_{R_1}) + \mathbf{r}_{C_1E_1} \times \mathbf{F}_{R_1}, \end{aligned} \quad (4.64)$$

$$\begin{aligned} I_2 \ddot{q}_2 \mathbf{J} &= \mathbf{r}_{C_2A} \times \mathbf{F}_{1,2} + \mathbf{r}_{C_2E_2} \times \mathbf{F}_{R_2} \\ &= \mathbf{r}_{C_2A} \times (m_2 \mathbf{a}_{C_2} - \mathbf{G}_2 - \mathbf{F}_{R_2}) + \mathbf{r}_{C_2E_2} \times \mathbf{F}_{R_2}, \end{aligned} \quad (4.65)$$

where m_i is the mass of the link i , $I_i = m_i L_i^2/12$ is the mass moment of inertia of the link i with regard to its mass center C_i , and L_i is the length of the link i . The force $\mathbf{F}_{1,2}$ is the reaction force of the link 2 on the link 1 at the joint A and the force $\mathbf{F}_{2,1}$ is vice versa. \mathbf{G}_i is the gravity force vector acting on the mass center C_i of the link i , and \mathbf{F}_{R_i} is the resistance

force vector acting on the last link n . Equations (4.62) and (4.63) can be simplified when these equations are summed due to the characteristics of the reaction forces as

$$m_1 \mathbf{a}_{C_1} + m_2 \mathbf{a}_{C_2} = \mathbf{G}_1 + \mathbf{G}_2 + \mathbf{F}_{R_1} + \mathbf{F}_{R_2}. \quad (4.66)$$

Equation (4.66) can be divided into x and z components as

$$m_1 a_{C_1x} + m_2 a_{C_2x} = F_{R_1x} + F_{R_2x}, \quad (4.67)$$

$$m_1 a_{C_1z} + m_2 a_{C_2z} = G_1 + G_2 + F_{R_1z} + F_{R_2z}. \quad (4.68)$$

Finally the motion of the chain can be described by Eqs. (4.64), (4.65), (4.67), and (4.68).

The vector \mathbf{a}_{C_i} is the acceleration vector of the position vector \mathbf{r}_{C_i} . The position vector \mathbf{r}_{C_i} is represented as the sum of the vector \mathbf{r}_{OA} and the vector \mathbf{r}_{AC_i} . The vector \mathbf{r}_{OA} is the position vector from the origin O to the joint point A . The vector \mathbf{r}_{C_iA} is the position vector from the mass center of the link i , C_i , to the joint point A and $\mathbf{r}_{C_iE_i}$ is the position vector from the mass center of the link i , C_i , to the resistance force acting point of the link i , E_i . The position vector \mathbf{r}_{OA} , \mathbf{r}_{C_iA} , $\mathbf{r}_{C_iE_i}$, \mathbf{r}_{C_i} , and the acceleration vector \mathbf{a}_{C_i} , are represented as

$$\mathbf{r}_{OA} = q_x \mathbf{1}_0 + q_z \mathbf{k}_0, \quad (4.69)$$

$$\mathbf{r}_{C_iA} = -\frac{L_i}{2} \sin q_i \mathbf{1}_0 - \frac{L_i}{2} \cos q_i \mathbf{k}_0, \quad (4.70)$$

$$\mathbf{r}_{AC_i} = -\mathbf{r}_{C_iA} = \frac{L_i}{2} \sin q_i \mathbf{1}_0 + \frac{L_i}{2} \cos q_i \mathbf{k}_0, \quad (4.71)$$

$$\mathbf{r}_{C_iE_i} = \mathbf{r}_{AE_i} - \mathbf{r}_{AC_i} = \left(L_{E_i} - \frac{L_i}{2} \right) (\sin q_i \mathbf{1}_0 + \cos q_i \mathbf{k}_0), \quad (4.72)$$

$$\mathbf{r}_{C_i} = \mathbf{r}_{OA} + \mathbf{r}_{AC_i} = \left(q_x + \frac{L_i}{2} \sin q_i \right) \mathbf{1}_0 + \left(q_z + \frac{L_i}{2} \cos q_i \right) \mathbf{k}_0, \quad (4.73)$$

$$\mathbf{a}_{C_i} = \left[\ddot{q}_x + \frac{L_i}{2} (\ddot{q}_i \cos q_i - \dot{q}_i^2 \sin q_i) \right] \mathbf{1}_0 + \left[\ddot{q}_z - \frac{L_i}{2} (\ddot{q}_i \sin q_i + \dot{q}_i^2 \cos q_i) \right] \mathbf{k}_0, \quad (4.74)$$

where L_{E_i} , the length from the joint A to each resistance force acting point E_i , is calculated as

$$L_{E_i} = L_i - \frac{1}{2} \frac{z_{T_i}}{\cos q_i}. \quad (4.75)$$

The immersed depth of each link i , z_{T_i} , is calculated as

$$z_{T_i} = L_i \cos q_i + q_z. \quad (4.76)$$

Each static resistance force is depending on the immersed depth z_{T_i} . The velocity vector of the force acting point E_i , \mathbf{v}_{E_i} , for deciding the resistance forces is calculated from the position vector of each force acting point E_i , \mathbf{r}_{E_i} as

$$\mathbf{r}_{E_i} = \mathbf{r}_{OA} + \mathbf{r}_{AE_i} = (q_x + L_{E_i} \sin q_i) \mathbf{1} + (q_z + L_{E_i} \cos q_i) \mathbf{k}, \quad (4.77)$$

$$\mathbf{v}_{E_i} = \frac{d\mathbf{r}_{OA}}{dt} + q_i \mathbf{J} \times \mathbf{r}_{E_i} = (\dot{q}_x + L_{E_i} \dot{q}_i \cos q_i) \mathbf{1} + (\dot{q}_z - L_{E_i} \dot{q}_i \sin q_i) \mathbf{k}. \quad (4.78)$$

The resistance force \mathbf{F}_R is also calculated by Eqs. (3.6), (3.8), and (3.9). The reference area A_{r_i} and the moving angle q_{m_i} of the link i are calculated as

$$A_{r_i} = d_c \frac{z_{T_i}}{\cos q_i} |\sin(q_i - q_{m_i})|, \quad (4.79)$$

$$q_{m_i} = \tan^{-1} \left(\frac{\dot{q}_x + L_{E_i} \dot{q}_i \cos q_i}{\dot{q}_z - L_{E_i} \dot{q}_i \sin q_i} \right). \quad (4.80)$$

Therefore the dynamic frictional force acting at the link i , \mathbf{F}_{d_i} , is

$$\begin{aligned} \mathbf{F}_{d_i} &= \eta_d \rho_g d_c \frac{z_{T_i}}{\cos q_i} \left| \sin \left(q_i - \tan^{-1} \left(\frac{\dot{q}_x + L_{E_i} \dot{q}_i \cos q_i}{\dot{q}_z - L_{E_i} \dot{q}_i \sin q_i} \right) \right) \right| \\ &\quad \sqrt{\left(\dot{q}_x + L_{E_i} \dot{q}_i \cos q_i \right)^2 + \left(\dot{q}_z - L_{E_i} \dot{q}_i \sin q_i \right)^2} \\ &\quad \left[- \left(\dot{q}_x + L_{E_i} \dot{q}_i \cos q_i \right) \mathbf{1}_0 - \left(\dot{q}_z - L_{E_i} \dot{q}_i \sin q_i \right) \mathbf{k}_0 \right]. \end{aligned} \quad (4.81)$$

The immersed volume of the link i , V , is calculated as

$$V_i = \frac{\pi d_c^2}{4} \frac{z_{T_i}}{\cos q_i}. \quad (4.82)$$

The horizontal and vertical static resistance force of the link i , \mathbf{F}_{sh} and \mathbf{F}_{vh} , are

$$\mathbf{F}_{sh_i} = -\text{sign}\left(\dot{q}_x + L_{E_i} \dot{q}_i \cos q_i\right) \eta_h g \rho_g \left(L_i \cos q_i + q_z\right)^2 d_c \mathbf{1}_0, \quad (4.83)$$

$$\mathbf{F}_{sv_i} = -\text{sign}\left(\dot{q}_z - L_{E_i} \dot{q}_i \sin q_i\right) \eta_v \left(\frac{L_i \cos q_i + q_z}{d_c}\right)^\lambda g \rho_g \frac{\pi d_c^2}{4} \frac{z_{T_i}}{\cos q_i} \mathbf{k}_0. \quad (4.84)$$

The resistance force \mathbf{F}_R , the sum of the dynamic frictional force vector \mathbf{F}_d and the static resistance force vector \mathbf{F}_s , is represented as the sum of Eqs. (4.81), (4.83), and (4.84).

$$\begin{aligned} \mathbf{F}_{R_i} &= \mathbf{F}_{d_i} + \mathbf{F}_{sh_i} + \mathbf{F}_{sv_i} \\ &= \left[-\eta_d \rho_g d_c \frac{z_{T_i}}{\cos q_i} \left| \sin \left(q_i - \tan^{-1} \left(\frac{\dot{q}_x + L_{E_i} \dot{q}_i \cos q_i}{\dot{q}_z - L_{E_i} \dot{q}_i \sin q_i} \right) \right) \right| \right. \\ &\quad \sqrt{\left(\dot{q}_x + L_{E_i} \dot{q}_i \cos q_i \right)^2 + \left(\dot{q}_z - L_{E_i} \dot{q}_i \sin q_i \right)^2} \left(\dot{q}_x + L_{E_i} \dot{q}_i \cos q_i \right) \\ &\quad \left. -\text{sign}\left(\dot{q}_x + L_{E_i} \dot{q}_i \cos q_i\right) \eta_h g \rho_g \left(L_i \cos q_i + q_z\right)^2 d_c \right] \mathbf{1}_0 + \\ &\quad \left[-\eta_d \rho_g d_c \frac{z_{T_i}}{\cos q_i} \left| \sin \left(q_i - \tan^{-1} \left(\frac{\dot{q}_x + L_{E_i} \dot{q}_i \cos q_i}{\dot{q}_z - L_{E_i} \dot{q}_i \sin q_i} \right) \right) \right| \right. \\ &\quad \sqrt{\left(\dot{q}_x + L_{E_i} \dot{q}_i \cos q_i \right)^2 + \left(\dot{q}_z - L_{E_i} \dot{q}_i \sin q_i \right)^2} \left(\dot{q}_z - L_{E_i} \dot{q}_i \sin q_i \right) \\ &\quad \left. -\text{sign}\left(\dot{q}_z - L_{E_i} \dot{q}_i \sin q_i\right) \eta_v \left(\frac{L_i \cos q_i + q_z}{d_c}\right)^\lambda g \rho_g \frac{\pi d_c^2}{4} \frac{z_{T_i}}{\cos q_i} \right] \mathbf{k}_0. \quad (4.85) \end{aligned}$$

Simulation results

Figure 4.28 represents the simulation results of the vertical velocities of the ends T_1 and T_2 , v_{T_1z} and v_{T_2z} , of the two link chain shown in Fig. 4.27 with the following initial conditions: $q_1(0) = 330^\circ$, $q_2(0) = 45^\circ$, $\dot{q}_1(0) = \dot{q}_2(0) = 0$ rad/s, $v_{Ax}(0) = 0$ m/s, and $v_{Az}(0) = 1, 3, 5$ m/s. As the dimensions applied to this simulation, the length of link 1 $L_1 = 0.3$ m, the length of link 2 $L_2 = L_1 \cos q_1(0) / \cos q_2(0)$ m, and the diameter $d_c = 0.0254$ m are utilized. The density of the link $\rho_c = 7.7 \times 10^3$ kg/m³, the density of a granular medium (sand) $\rho_g = 2.5 \times 10^3$ kg/m³, the dynamic frictional force coefficient $\eta_d = 6.5$, the horizontal static resistance force coefficient $\eta_h = 8$, and the vertical static resistance force coefficients $\eta_v = 22$ and $\lambda = 1.1$ are applied in the simulation. For these initial conditions, the initial vertical velocities of the impact points T_1 and T_2 , $v_{T_1}(0)$ and $v_{T_2}(0)$, have the only vertical velocity components. The stopping times for the two ends, t_{zT_1} and t_{zT_2} , are defined as the time interval until the vertical velocities of the tips T_1 and T_2 , v_{T_1z} and v_{T_2z} , respectively become zero. For this case the stopping time t_{zT_1} is decreasing with the increasing of the initial velocity and the stopping time t_{zT_2} is also decreasing. It is observed that the vertical tip velocity of the long link, v_{T_2z} , stops much rapidly compared with the vertical tip velocity of the short link.

Using different combinations of the initial impact velocities for the links ($\dot{q}_1(0) = -\dot{q}_2(0) = 1, 3, 5$ rad/s and $v_{Ax}(0) = v_{Az}(0) = 0$ m/s) and the same initial geometry ($q_1(0) = 330^\circ$, $q_2(0) = 45^\circ$), the simulation results for the vertical direction velocities of the both ends of links are shown in Fig. 4.29. For these simulations the stopping times t_{zT_1} and t_{zT_2} are decreasing with the initial impact angular velocities. It is observed that the vertical tip velocity of the long link, v_{T_2z} , also stops fast compared with the vertical tip velocity of the short link. The same results have been noticed using different initial condition (symmetric cases: $-q_1(0) = q_2(0) = 15^\circ, 45^\circ$, and 75° , asymmetric cases: $q_1(0) = 330^\circ$, $q_2(0) = 60^\circ$ and 75°) for symmetric ($L_1 = L_2$) and asymmetric cases ($L_1 \neq L_2$).

Figures 4.30 and 4.31 show the simulation results in case when one end of a link is resting initially and the other link impacts the granular medium with some initial angular

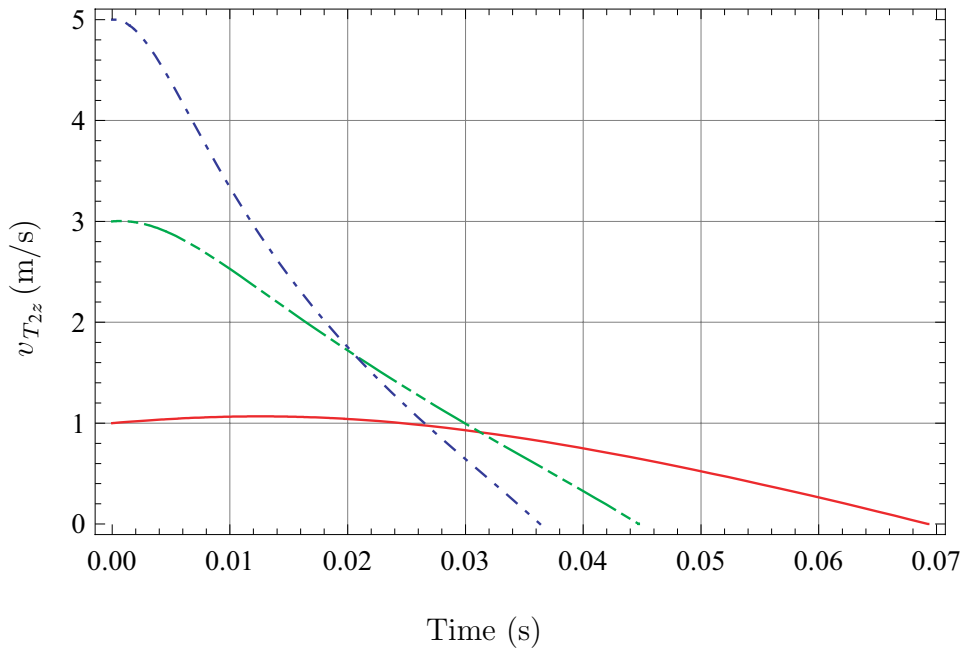
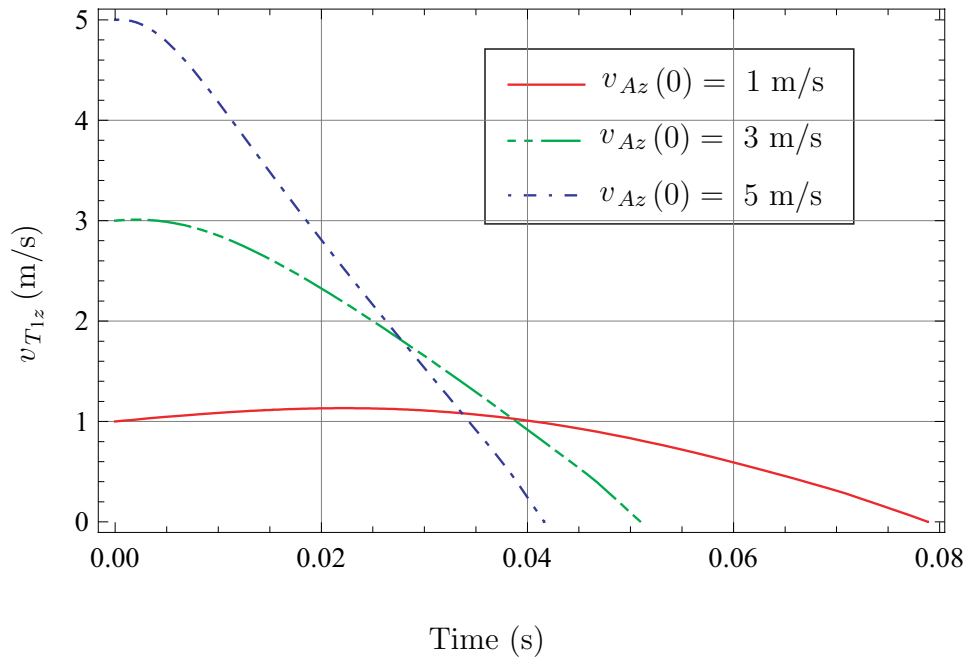


Figure 4.28: Velocities v_{T1z} and v_{T2z} results of the two link kinematic chain for $q_1(0) = 330^\circ$, $q_2(0) = 45^\circ$, and $v_{Az}(0) = 1, 3, 5$ m/s

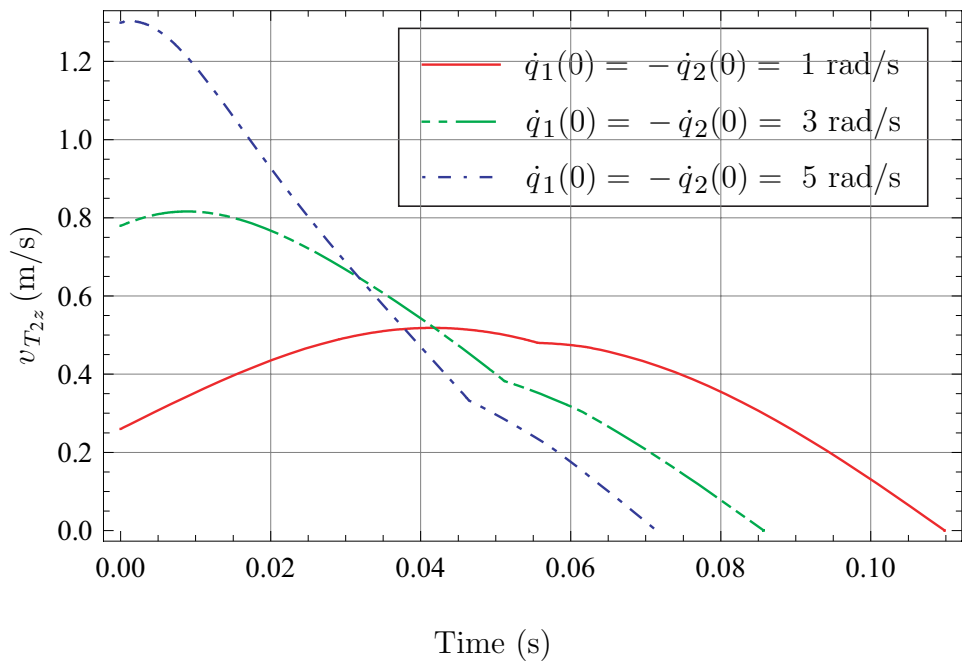
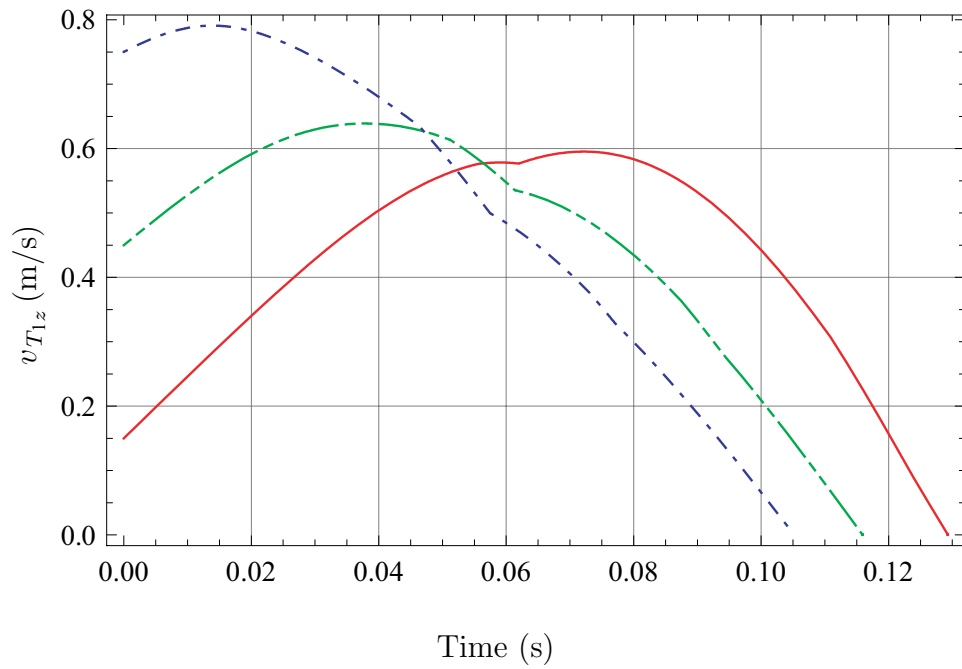


Figure 4.29: Velocities v_{T1z} and v_{T2z} results of the two link kinematic chain for $q_1(0) = 330^\circ$, $q_2(0) = 45^\circ$, and $\dot{q}_1(0) = -\dot{q}_2(0) = 1, 3, 5$ rad/s

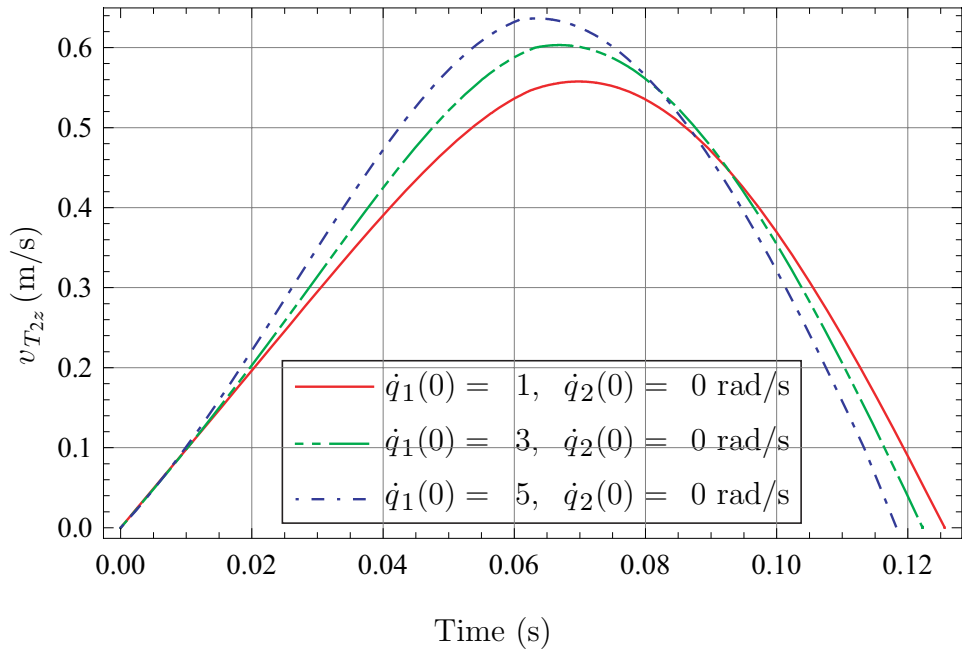
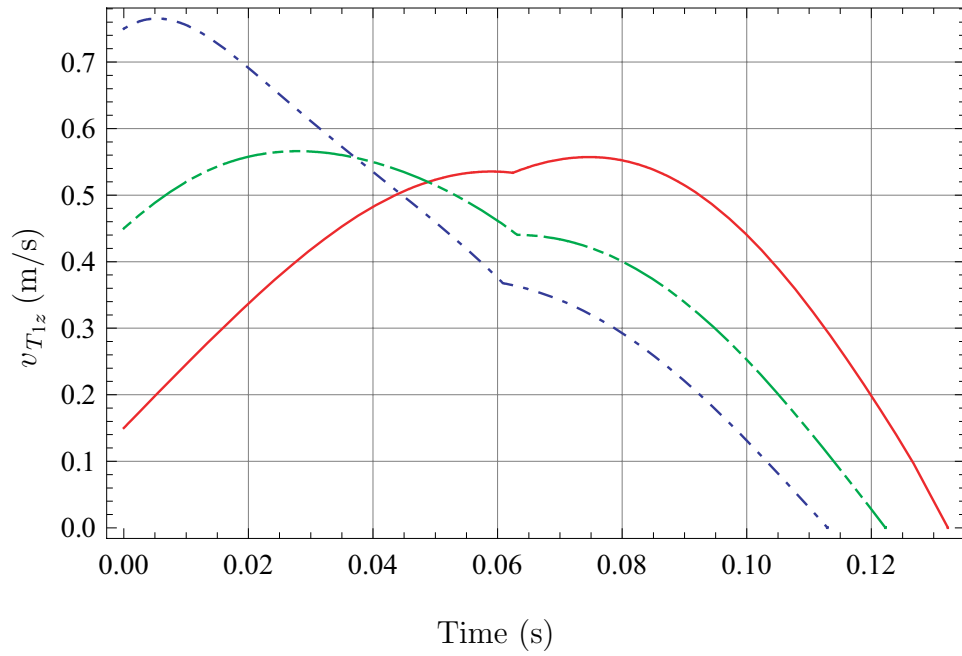


Figure 4.30: Velocities $v_{T_{1z}}$ and $v_{T_{2z}}$ results of the two link kinematic chain for $q_1(0) = 330^\circ$, $q_2(0) = 45^\circ$, and $\dot{q}_1(0) = 1, 3, 5$ rad/s

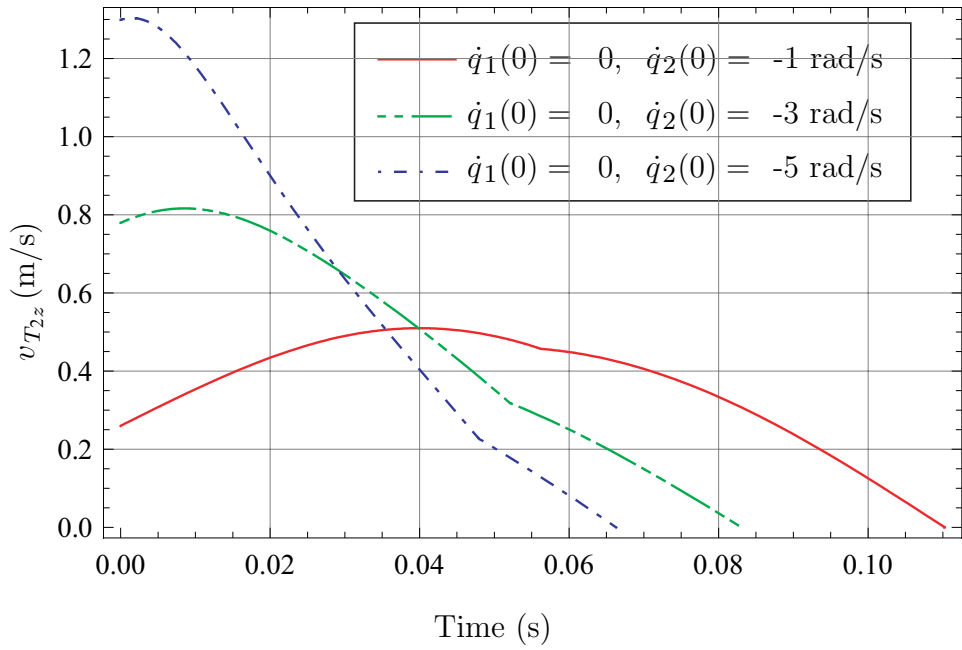
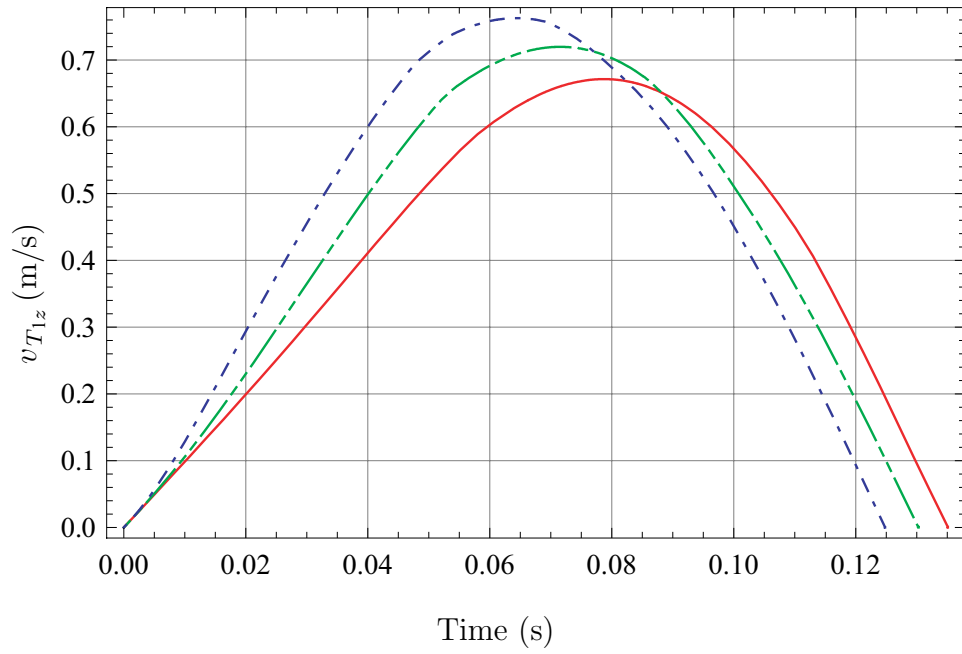


Figure 4.31: Velocities v_{T1z} and v_{T2z} results of the two link kinematic chain for $q_1(0) = 330^\circ$, $q_2(0) = 45^\circ$, and $\dot{q}_2(0) = -1, -3, -5$ rad/s

velocities. For the initial impact angles ($q_1(0) = 330^\circ$, $q_2(0) = 45^\circ$) and the initial impact velocities ($\dot{q}_1(0) = 1, 3, 5$ rad/s, $\dot{q}_2(0) = 0$ rad/s, and $v_{Ax}(0) = v_{Az}(0) = 0$ m/s), the stopping time of the impacting link, t_{zT1} , is decreasing with the increasing of the initial angular velocity and the stopping time of the resting link, t_{zT2} , is little affected by the initial impact angular velocity but decreasing when the initial impact angular velocity of link 1 is increasing as shown in Fig. 4.30. For the initial impact geometry ($q_1(0) = 330^\circ$, $q_2(0) = 60^\circ$), the tendency of the stopping times of the impacting link 1 and the resting link 2 is also kept as the same as the case of the initial impact angles ($q_1(0) = 330^\circ$, $q_2(0) = 45^\circ$). The simulation results in the case that the short link is resting initially and the long link impacts the granular medium are represented in Fig. 4.31. For the initial impact angles ($q_1(0) = 330^\circ$, $q_2(0) = 45^\circ$) and the initial impact velocities ($\dot{q}_1(0) = 0$ rad/s, $\dot{q}_2(0) = -1, -3, -5$ rad/s and $v_{Ax}(0) = v_{Az}(0) = 0$ m/s), the stopping time of the impacting link, t_{zT2} , is also decreasing with the increasing of the initial angular velocity and the stopping time of the resting link, t_{zT1} , is little affected by the initial impact angular velocity but decreasing when the initial impact angular velocity of link 2 is increasing as shown in Fig. 4.31. For the initial impact geometry ($q_1(0) = 330^\circ$, $q_2(0) = 60^\circ$), the similar results are observed as the case of the initial impact angles ($q_1(0) = 330^\circ$, $q_2(0) = 45^\circ$).

From these simulation results, the stopping time can be concluded as that for the cases when one link is resting and the other one is impacting the stopping time of the impact link is decreasing when the initial impact angular velocity increasing and the differences between the stopping time of the resting link is not conspicuous but the stopping time decreases with the initial impact angular velocity of the impact link.

Table 4.7: Stopping time results of two link chain for $q_1(0) = 330^\circ$ and $q_2(0) = 45^\circ$

$v_{Az}(0)(m/s)$	$\dot{q}_1(0)$ (rad/s)	$\dot{q}_2(0)$ (rad/s)	$t_{z_{T1}}$ (s)	$t_{z_{T2}}$ (s)
1	0	0	0.0788529	0.0693035
3	0	0	0.0509913	0.0447269
5	0	0	0.0416282	0.0363391
0	1	-1	0.129307	0.109857
0	3	-3	0.115935	0.0857099
0	5	-3	0.105224	0.0714128
0	1	0	0.132282	0.125619
0	3	0	0.122285	0.122267
0	5	0	0.112958	0.118263
0	0	-1	0.135093	0.110255
0	0	-3	0.130274	0.0830734
0	0	-5	0.124795	0.0662946

CHAPTER 5

IMPACT OF FLEXIBLE LINKS

In this chapter, the impact with a granular medium of a flexible link is studied in order to confirm the effects of the deformation of the link during the penetrating process. A cylinder type flexible link impacting a granular medium is utilized. The impacts of a free elastic link and of an elastic compound pendulum are modeled based on the rigid body models mentioned in chapter 4. The approach to the external forces such as the resistance and the gravity force is the same as that of the rigid body models. What is different from the rigid body impact modeling is the elastic deformation of a elastic link (the elastic mode shape).

Figure 5.1 shows a flexible link of length L , constant flexural rigidity EI , cross sectional area A_c , and density ρ_c . When there are no external forces acting on the link, small flexural vibrations of the link are governed by the following equation

$$EI \frac{\partial^4 x(z, t)}{\partial z^4} + \rho_c A_c \frac{\partial^2 x(z, t)}{\partial t^2} = 0. \quad (5.1)$$

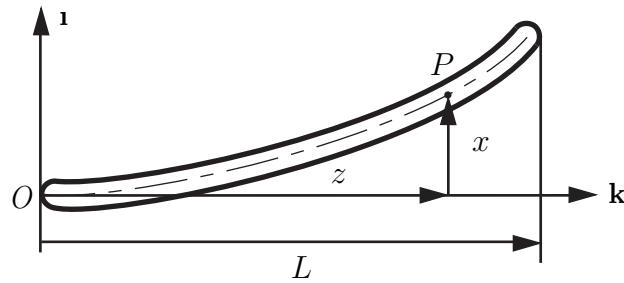


Figure 5.1: Transverse vibrations of a flexible link

The general solution of Eq. (5.1) can be expressed as

$$x(z, t) = \sum_{i=1}^{\infty} \Phi_i(z) q_i(t). \quad (5.2)$$

The functions of z and t , $\Phi_i(z)$ and $q_i(t)$, defined respectively as

$$\Phi_i = A \sin \frac{\lambda_i z}{L} + B \cos \frac{\lambda_i z}{L} + C \sinh \frac{\lambda_i z}{L} + D \cosh \frac{\lambda_i z}{L}, \quad (5.3)$$

and

$$q_i = \alpha_i \cos p_i t + \beta_i \sin p_i t, \quad (5.4)$$

where $\lambda_i, i = 1, \dots, \infty$ are the consecutive roots of the transcendental equation satisfying the boundary conditions of the flexible link.

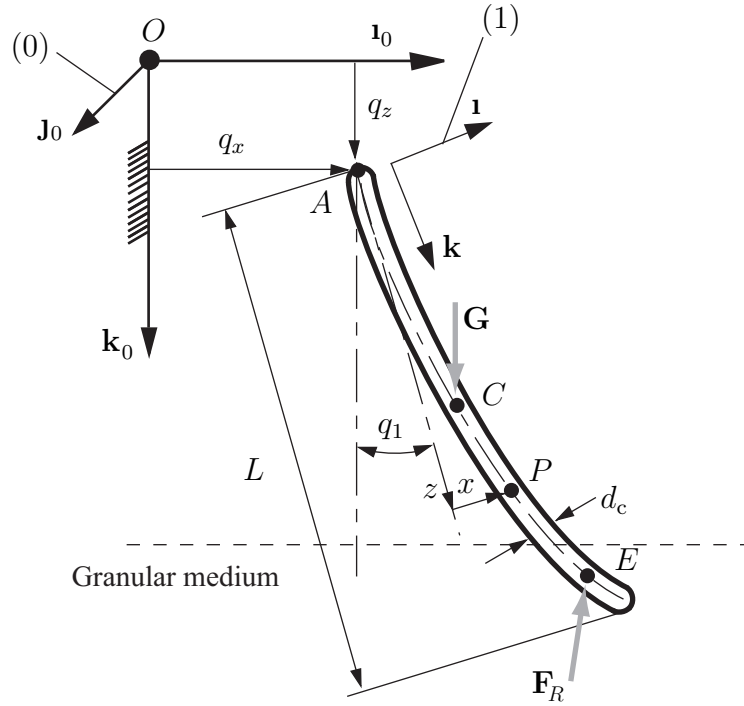


Figure 5.2: Free elastic link

5.1 Free elastic link

5.1.1 Transverse vibration of a free link

In Fig. 5.2, a schematic representation of a free elastic link is given. The shear force and the bending moment of the both ends of the link are always zero in the case of the free link. The boundary conditions (free ends) are

$$x''(0, t) = x''(L, t) = x'''(0, t) = x'''(L, t) = 0. \quad (5.5)$$

Using the boundary conditions given by Eq. (5.5), the relation between the constants A , B , C , and D can be written as

$$\begin{bmatrix} 0 & -\frac{\lambda_i^2}{L^2} & 0 & \frac{\lambda_i^2}{L^2} \\ -\frac{\lambda_i^2 \sin \lambda_i}{L^2} & -\frac{\lambda_i^2 \cos \lambda_i}{L^2} & \frac{\lambda_i^2 \sinh \lambda_i}{L^2} & \frac{\lambda_i^2 \cosh \lambda_i}{L^2} \\ -\frac{\lambda_i^3}{L^3} & 0 & \frac{\lambda_i^3}{L^3} & 0 \\ -\frac{\lambda_i^3 \cos \lambda_i}{L^3} & \frac{\lambda_i^3 \sin \lambda_i}{L^3} & \frac{\lambda_i^3 \cosh \lambda_i}{L^3} & \frac{\lambda_i^3 \sinh \lambda_i}{L^3} \end{bmatrix} \begin{bmatrix} A \\ B \\ C \\ D \end{bmatrix} = \begin{bmatrix} 0 \\ 0 \\ 0 \\ 0 \end{bmatrix}. \quad (5.6)$$

For non-zero solution, the determinant of the matrix of Eq. (5.6) should be zero as the following equation

$$\begin{vmatrix} 0 & -\frac{\lambda_i^2}{L^2} & 0 & \frac{\lambda_i^2}{L^2} \\ -\frac{\lambda_i^2 \sin \lambda_i}{L^2} & -\frac{\lambda_i^2 \cos \lambda_i}{L^2} & \frac{\lambda_i^2 \sinh \lambda_i}{L^2} & \frac{\lambda_i^2 \cosh \lambda_i}{L^2} \\ -\frac{\lambda_i^3}{L^3} & 0 & \frac{\lambda_i^3}{L^3} & 0 \\ -\frac{\lambda_i^3 \cos \lambda_i}{L^3} & \frac{\lambda_i^3 \sin \lambda_i}{L^3} & \frac{\lambda_i^3 \cosh \lambda_i}{L^3} & \frac{\lambda_i^3 \sinh \lambda_i}{L^3} \end{vmatrix} = 0. \quad (5.7)$$

The general solution satisfying these boundary conditions is calculated as

$$\Phi_i = \cos \frac{\lambda_i z}{L} + \cosh \frac{\lambda_i z}{L} - \frac{\cosh \lambda_i - \cos \lambda_i}{\sinh \lambda_i - \sin \lambda_i} \left(\sin \frac{\lambda_i z}{L} + \sinh \frac{\lambda_i z}{L} \right). \quad (5.8)$$

Equation (5.7) is simplified as

$$\cos \lambda_i \cosh \lambda_i = 1. \quad (5.9)$$

The roots of this characteristic equation are shown in table 5.1. The p_i variable from Eq. (5.4) is calculated as

$$p_i = \left(\frac{\lambda_i}{L} \right)^2 \left(\frac{EI}{\rho_c A_c} \right)^{1/2}. \quad (5.10)$$

The constants α_i and β_i of Eq. (5.4) depend upon the initial conditions. The functions $\Phi_i(z)$ satisfy the orthogonality relations

$$\int_0^L \Phi_i \Phi_j dz = L \delta_{ij} \quad (i, j = 1, \dots, \infty), \quad (5.11)$$

where δ_{ij} is the Kronecker delta, $\delta_{ij} = \begin{cases} 1, & \text{if } i = j, \\ 0, & \text{if } i \neq j. \end{cases}$

Table 5.1: Roots of characteristic equations for free elastic link
characteristic equation
root $(\cos \lambda_i \cosh \lambda_i = 1)$

λ_1	4.7300
λ_2	7.8532
λ_3	10.996
λ_4	14.137

5.1.2 Modeling

Kinematics

As shown in Fig. 5.2, the system is formed by an uniform flexible link of length L with the diameter d_c , the cross sectional area $A_c = \pi d_c^2/4$, the flexural rigidity EI , and the density ρ_c . Only planar motions of the link in a fixed reference frame (0) of unit vectors $[\mathbf{i}_0, \mathbf{j}_0, \mathbf{k}_0]$ will be considered.

To characterize the instantaneous configuration of the link, generalized coordinates q_x , q_z , and q_1 are employed. The generalized coordinate q_x denotes the distance from the end A to the vertical axis of the reference frame (0) and the generalized coordinate q_z denotes the distance from A to the horizontal axis of reference frame (0). The last generalized coordinate q_1 designates the radian measure of the rotation angle between the undeformed link and the vertical axis. These are the generalized coordinates of the rigid body.

A fixed reference frame (0) of unit vectors $[\mathbf{i}_0, \mathbf{j}_0, \mathbf{k}_0]$ and a mobile reference frame (1) of unit vectors $[\mathbf{i}, \mathbf{j}, \mathbf{k}]$ are considered. The unit vectors \mathbf{i}_0 , \mathbf{j}_0 , and \mathbf{k}_0 can be expressed as

$$\begin{aligned}\mathbf{i}_0 &= \cos q_1 \mathbf{i} + \sin q_1 \mathbf{k}, \\ \mathbf{j}_0 &= \mathbf{j}, \\ \mathbf{k}_0 &= -\sin q_1 \mathbf{i} + \cos q_1 \mathbf{k},\end{aligned}\tag{5.12}$$

and the unit vectors \mathbf{i} , \mathbf{j} , and \mathbf{k} can be also expressed as

$$\begin{aligned}\mathbf{i} &= \cos q_1 \mathbf{i}_0 - \sin q_1 \mathbf{k}_0, \\ \mathbf{j} &= \mathbf{j}_0, \\ \mathbf{k} &= \sin q_1 \mathbf{i}_0 + \cos q_1 \mathbf{k}_0.\end{aligned}\tag{5.13}$$

The deformations of the elastic link can be discussed in terms of the deformed displacement $x(z, t)$ of a generic point P on the link. The point P is situated at a distance z from

the end point A of the link. The displacement x can be expressed as

$$\begin{aligned} x(z, t) &= \sum_{i=1}^n \Phi_i(z) q_{1+i}(t), \\ &= \sum_{i=1}^n \left[\cos \frac{\lambda_i z}{L} + \cosh \frac{\lambda_i z}{L} - \frac{\cosh \lambda_i - \cos \lambda_i}{\sinh \lambda_i - \sin \lambda_i} \left(\sin \frac{\lambda_i z}{L} + \sinh \frac{\lambda_i z}{L} \right) \right] q_{1+i}(t), \end{aligned} \quad (5.14)$$

where $\Phi_i(z)$ is a shape function by z , the elastic generalized coordinate $q_{1+i}(t)$ is a function of time t , and i is any positive integer.

The position of the end A in (0) is

$$\mathbf{r}_A = q_x \mathbf{i}_0 + q_z \mathbf{k}_0. \quad (5.15)$$

The position vector from the end A to a generic point $P(x, z)$ of the elastic link in (0) is

$$\begin{aligned} \mathbf{r}_{AP} &= x \mathbf{i} + z \mathbf{k} = \left[\left(\sum_{i=1}^n \Phi_i(z) q_{1+i} \right) \mathbf{i} + z \mathbf{k} \right] \\ &= \left[\sum_{i=1}^n \Phi_i(z) q_{1+i} \cos q_1 + z \sin q_1 \right] \mathbf{i}_0 + \\ &\quad \left[- \sum_{i=1}^n \Phi_i(z) q_{1+i} \sin q_1 + z \cos q_1 \right] \mathbf{k}_0. \end{aligned} \quad (5.16)$$

The position vector of the point P of the elastic link in (0) is

$$\begin{aligned} \mathbf{r}_P &= \mathbf{r}_A + \mathbf{r}_{AP} \\ &= \left[q_x + \sum_{i=1}^n \Phi_i(z) q_{1+i} \cos q_1 + z \sin q_1 \right] \mathbf{i}_0 + \\ &\quad \left[q_z - \sum_{i=1}^n \Phi_i(z) q_{1+i} \sin q_1 + z \cos q_1 \right] \mathbf{k}_0. \end{aligned} \quad (5.17)$$

The velocity and acceleration vector of the arbitrary point P of the uniform elastic link in (0) is

$$\mathbf{v}_P = \frac{d}{dt} \mathbf{r}_P = \left[\dot{q}_x + \sum_{i=1}^n \left(\Phi_i(z) \dot{q}_{1+i} \cos q_1 - \Phi_i(z) q_{1+i} \dot{q}_1 \sin q_1 \right) + z \dot{q}_1 \cos q_1 \right] \mathbf{i}_0 + \left[\dot{q}_z - \sum_{i=1}^n \left(\Phi_i(z) \dot{q}_{1+i} \sin q_1 + \Phi_i(z) q_{1+i} \dot{q}_1 \cos q_1 \right) - z \dot{q}_1 \sin q_1 \right] \mathbf{k}_0, \quad (5.18)$$

$$\mathbf{a}_P = \frac{d}{dt} \mathbf{v}_P = \left[\ddot{q}_x + \sum_{i=1}^n \Phi_i(z) \left(\ddot{q}_{1+i} \cos q_1 - 2 \dot{q}_{1+i} \dot{q}_1 \sin q_1 - q_{1+i} \ddot{q}_1 \sin q_1 - q_{1+i} \dot{q}_1^2 \cos q_1 \right) + z \ddot{q}_1 \cos q_1 - z \dot{q}_1^2 \sin q_1 \right] \mathbf{i}_0 + \left[\ddot{q}_z - \sum_{i=1}^n \Phi_i(z) \left(\ddot{q}_{1+i} \sin q_1 + 2 \dot{q}_{1+i} \dot{q}_1 \cos q_1 + q_{1+i} \ddot{q}_1 \cos q_1 - q_{1+i} \dot{q}_1^2 \sin q_1 \right) - z \ddot{q}_1 \sin q_1 - z \dot{q}_1^2 \cos q_1 \right] \mathbf{k}_0. \quad (5.19)$$

The angular acceleration of the link in the reference frame (0) is

$$\boldsymbol{\alpha} = \dot{\boldsymbol{\omega}} = \ddot{q}_1 \mathbf{J}_0. \quad (5.20)$$

5.1.3 Equations of motion

The Newton-Euler's equations can be used to find the differential equations of motion. A force and a moment equation before impact can be written as

$$\int_0^L \rho_c A_c \mathbf{a}_P dz = \mathbf{G}, \quad (5.21)$$

$$\int_0^L \left(\mathbf{r}_{AP} \times \rho_c A_c \mathbf{a}_P \right) dz = \mathbf{r}_{AC} \times \mathbf{G}, \quad (5.22)$$

where \mathbf{G} is the gravity force acting on the mass center of the link and $\mathbf{r}_{AC} = \mathbf{r}_{AP}(z = 0.5L)$ is the position vector from A to the mass center C . Equation (5.21) is separated into x and z components.

The relationship in dz , a generic differential element of the link, between the external force \mathbf{F}_{ext} and the shear V can be expressed as

$$\mathbf{F}_{ext} \cdot \mathbf{1} dz + \frac{\partial V_P(z, t)}{\partial z} dz = \rho_c A_c \mathbf{a}_P(z, t) \cdot \mathbf{1} dz, \quad (5.23)$$

where $V_P(z, t)$ is the shear at a certain point P and all force terms are expressed in fixed reference frame (0) in terms of mobile frame (1) of $\mathbf{i}, \mathbf{j}, \mathbf{k}$. If the rotatory inertia is neglected, then $V(z, t)$ may be expressed in terms of the bending moment $M(z, t)$ as

$$\frac{\partial M(z, t)}{\partial z} = -V(z, t). \quad (5.24)$$

Since

$$M = EI \frac{\partial^2 x(z, t)}{\partial z^2}, \quad (5.25)$$

Eqs. (5.23) and (5.24) yield

$$EI \frac{\partial^4 x(z, t)}{\partial z^4} + \rho_c A_c \mathbf{a}(z, t) \cdot \mathbf{1} = \mathbf{F}_{ext} \cdot \mathbf{1}. \quad (5.26)$$

The variables of Eq. (5.26) are separated by Eq. (5.14) as

$$EI \sum_{i=1}^{\infty} \left(\frac{\lambda_i}{L} \right)^4 \Phi_i(z) q_{1+i}(t) + \rho_c A_c \mathbf{a}(z, t) \cdot \mathbf{1} = \mathbf{F}_{ext} \cdot \mathbf{1}. \quad (5.27)$$

Equation (5.27) is simplified by multiplying $\Phi_j(z)$ and integrating from 0 to L . By the orthogonality relations represented in Eq. (5.11), the first term of Eq. (5.27) becomes

$$\int_0^L EI \sum_{i=1}^{\infty} \left(\frac{\lambda_i}{L} \right)^4 \Phi_i(z) \Phi_j(z) q_{1+i}(t) dz = EI L \left(\frac{\lambda_j}{L} \right)^4 q_{1+j}(t), \quad (5.28)$$

and Eq. (5.27) becomes

$$EI L \left(\frac{\lambda_j}{L} \right)^4 q_{1+j}(t) + \int_0^L \rho_c A_c \mathbf{a}_P \cdot \mathbf{1} \Phi_j(z) dz = \int_0^L \mathbf{F}_{ext} \cdot \mathbf{1} \Phi_j(z) dz. \quad (5.29)$$

When the external force \mathbf{F}_{ext} is supposed to be a concentrated force on the link, \mathbf{F}_{ext} can be expressed as $\mathbf{F}_{ext}\delta(z - z_{act})$ and the right hand side of Eq. (5.29) can be rewritten as $\mathbf{F}_{ext} \cdot \mathbf{1}\Phi_i(z_{act})$. In the model, for the existing external force is \mathbf{G} , Eq. (5.29) becomes

$$EIL \left(\frac{\lambda_i}{L}\right)^4 q_{1+i}(t) + \int_0^L \rho_c A_c \mathbf{a}_P \cdot \mathbf{1}\Phi_i(z) dz = \mathbf{G} \cdot \mathbf{1}\Phi_i\left(\frac{L}{2}\right). \quad (5.30)$$

Equations (5.21), (5.22), and (5.30) are the equations of motion for the elastic free link before the impact.

When the multiple external forces \mathbf{F}_{ext_k} ($k = 1, \dots, n$) including the resistance force of the granular medium, the governing equations of motion, Eqs. (5.21), (5.22), and (5.30), can be written as

$$\int_0^L \rho_c A_c \mathbf{a}_P dz = \mathbf{G} + \sum_{k=1}^n \mathbf{F}_{ext_k}, \quad (5.31)$$

$$\int_0^L (\mathbf{r}_{AP} \times \rho_c A_c \mathbf{a}_P) dz = \mathbf{r}_{AC} \times \mathbf{G} + \sum_{k=1}^n \mathbf{r}_{AE_k} \times \mathbf{F}_{ext_k}, \quad (5.32)$$

$$EIL \left(\frac{\lambda_i}{L}\right)^4 q_{1+i}(t) + \int_0^L \rho_c A_c \mathbf{a}_P \cdot \mathbf{1}\Phi_i(z) dz = \mathbf{G} \cdot \mathbf{1}\Phi_i\left(\frac{L}{2}\right) + \sum_{k=1}^n \mathbf{F}_{ext_k} \cdot \mathbf{1}\Phi_i(L_{E_k}), \quad (5.33)$$

where \mathbf{r}_{AE_k} is the position vector from the end A to the external force \mathbf{F}_{ext_k} acting point E_k and L_{E_k} is the length from the end A to the external force application point E_k . In the case of the impact of the elastic free link, external forces are restricted to the resistance force \mathbf{F}_R . The equations of motion of the elastic free link during the impact with the granular medium are given as

$$\int_0^L \rho_c A_c \mathbf{a}_P dz = \mathbf{G} + \mathbf{F}_R, \quad (5.34)$$

$$\int_0^L (\mathbf{r}_{AP} \times \rho_c A_c \mathbf{a}_P) dz = \mathbf{r}_{AC} \times \mathbf{G} + \mathbf{r}_{AE} \times \mathbf{F}_R, \quad (5.35)$$

$$EIL \left(\frac{\lambda_i}{L}\right)^4 q_{1+i}(t) + \int_0^L \rho_c A_c \mathbf{a}_P \cdot \mathbf{1}\Phi_i(z) dz = \mathbf{G} \cdot \mathbf{1}\Phi_i\left(\frac{L}{2}\right) + \mathbf{F}_R \cdot \mathbf{1}\Phi_i(L_E), \quad (5.36)$$

where $\mathbf{r}_{AE} = \mathbf{r}_{AP}(z = L_E)$ is the position vector from A to the resistance force application point E and the length from the end A to E , L_E , is calculated as

$$L_E = L - \frac{z_T}{2 \cos q_1}. \quad (5.37)$$

The immersed depth z_T , the vertical component of the position vector of the end point T , is calculated by Eq. (5.17) as $z_T = \mathbf{r}_P(z = L) \cdot \mathbf{k}_0$.

The resistance force \mathbf{F}_R is calculated by Eqs. (3.6), (3.8), and (3.9). The dynamic frictional force \mathbf{F}_d is

$$\begin{aligned} \mathbf{F}_d &= -\mathbf{v}_E \eta_d \rho_g A_r |\mathbf{v}_E| \\ &= -\eta_d \rho_g A_r \left[\left(\dot{q}_x + \sum_{i=1}^n \left(\Phi_i(L_E) \dot{q}_{1+i} \cos q_1 - \Phi_i(L_E) q_{1+i} \dot{q}_1 \sin q_1 \right) + L_E \dot{q}_1 \cos q_1 \right)^2 + \right. \\ &\quad \left. \left(\dot{q}_z - \sum_{i=1}^n \left(\Phi_i(L_E) \dot{q}_{1+i} \sin q_1 + \Phi_i(L_E) q_{1+i} \dot{q}_1 \cos q_1 \right) - L_E \dot{q}_1 \sin q_1 \right)^2 \right]^{0.5} \\ &\quad \left[\left(\dot{q}_x + \sum_{i=1}^n \left(\Phi_i(L_E) \dot{q}_{1+i} \cos q_1 - \Phi_i(L_E) q_{1+i} \dot{q}_1 \sin q_1 \right) + L_E \dot{q}_1 \cos q_1 \right) \mathbf{i}_0 + \right. \\ &\quad \left. \left(\dot{q}_z - \sum_{i=1}^n \left(\Phi_i(L_E) \dot{q}_{1+i} \sin q_1 + \Phi_i(L_E) q_{1+i} \dot{q}_1 \cos q_1 \right) - L_E \dot{q}_1 \sin q_1 \right) \mathbf{k}_0 \right], \quad (5.38) \end{aligned}$$

where the velocity vector \mathbf{v}_E is the velocity of the resistance force acting point E and this vector calculated by Eq. (5.18) as $\mathbf{v}_E = \mathbf{v}_P(z = L_E)$. The reference area A_r is

$$A_r = \frac{d_c z_T}{\cos q_1} |\sin(q_1 - q_m)|. \quad (5.39)$$

The moving angle q_m is calculated as

$$\begin{aligned}
q_m &= \tan^{-1} \left(\frac{v_{Ex}}{v_{Ez}} \right) \\
&= \tan^{-1} \left[\frac{\dot{q}_x + \sum_{i=1}^n \left(\Phi_i(L_E) \dot{q}_{1+i} \cos q_1 - \Phi_i(L_E) q_{1+i} \dot{q}_1 \sin q_1 \right) + L_E \dot{q}_1 \cos q_1}{\dot{q}_z - \sum_{i=1}^n \left(\Phi_i(L_E) \dot{q}_{1+i} \sin q_1 + \Phi_i(L_E) q_{1+i} \dot{q}_1 \cos q_1 \right) - L_E \dot{q}_1 \sin q_1} \right].
\end{aligned} \tag{5.40}$$

The horizontal and vertical static resistance force \mathbf{F}_{sh} , \mathbf{F}_{vh} are

$$\begin{aligned}
\mathbf{F}_{sh} &= -\text{sign} \left[\dot{q}_x + \sum_{i=1}^n \left(\Phi_i(L_E) \dot{q}_{1+i} \cos q_1 - \Phi_i(L_E) q_{1+i} \dot{q}_1 \sin q_1 \right) + L_E \dot{q}_1 \cos q_1 \right] \\
&\quad \eta_h g \rho_g z_T^2 d_c \mathbf{1}_0,
\end{aligned} \tag{5.41}$$

$$\begin{aligned}
\mathbf{F}_{sv} &= -\text{sign} \left[\dot{q}_z - \sum_{i=1}^n \left(\Phi_i(L_E) \dot{q}_{1+i} \sin q_1 + \Phi_i(L_E) q_{1+i} \dot{q}_1 \cos q_1 \right) - L_E \dot{q}_1 \sin q_1 \right] \\
&\quad \eta_v \left(\frac{z_T}{d_c} \right)^\lambda g \rho_g V \mathbf{k}_0,
\end{aligned} \tag{5.42}$$

where the immersed volume V is calculated as

$$V = \frac{\pi d_c^2}{4} \frac{z_T}{\cos q_1}. \tag{5.43}$$

The resistance force \mathbf{F}_R , the sum of the dynamic frictional force vector \mathbf{F}_d and the static resistance force vector \mathbf{F}_s , is represented as the sum of Eqs. (5.38), (5.41), and (5.42).

5.1.4 Simulation results

Figures 5.3, 5.4, 5.5, and 5.6 show the simulation results for the impact of the elastic free link shown in Fig. 5.2. The simulations are performed for different impact angles and different initial impact velocities ($\dot{q}_z(0) = 1.26, 1.87, \text{ and } 2.33$ m/s for $q_1(0) = 32^\circ$, and $\dot{q}_z(0) = 1.45, 1.98, \text{ and } 2.43$ m/s for $q_1(0) = 55^\circ$). The initial deformation conditions are

Table 5.2: Stopping time of the elastic and the rigid free link

$q_1(0)$ ($^\circ$)	$\dot{q}_z(0)$ (m/s)	$t_{s,r}$ (s)	$t_{s,e}$ (s)
32	1.26	0.0275914	0.0275865
	1.87	0.0229915	0.0229956
	2.33	0.0206495	0.0206516
55	1.45	0.017818	0.0178181
	1.98	0.0150461	0.0150411
	2.43	0.0133007	0.0133043

applied as $q_2(0) = 0$ m and $\dot{q}_2(0) = 0$ m/s. The dimensions of the elastic free link applied to this simulation are completely the same as those applied for the simulation of the impact of the rigid free link as $L = 0.1524$ m, the diameter $d_c = 0.00635$ m, and the density $\rho_c = 7.7 \times 10^3$ kg/m³. The flexural rigidity EI is applied as 15.1642 N m². The density of a granular medium (sand), ρ_g , is applied as 2.5×10^3 kg/m³. The dynamic frictional force coefficient is $\eta_d = 6.5$, the horizontal static resistance force coefficient is $\eta_h = 8$, and the vertical static resistance force coefficients are $\eta_v = 22$ and $\lambda = 1.1$. The simulations are performed from the impact moment until the vertical penetrating velocity of the end T of the link, v_{Tz} , becomes zero and the first mode of the shape function of Eq. (5.8) is only considered ($\lambda_1=4.7300$). As shown in Figs. 5.3 and 5.5, the velocity of the end T of the link, v_{Tz} , becomes zero more quickly when the initial impact velocity increases. The simulation results of the elastic free link compared with the results of the rigid free link are shown in table 5.2. These simulation results show that the stopping time of the impact of a free link decreases whether a rigid link or an elastic one as the velocity of the impact moment increases. The deformation of the link, q_2 , increases when the initial impact velocity and angle increase as shown in Figs. 5.4 and 5.6. We do not observe much difference between the rigid model and the flexible model for our particular system. The elastic deformations will be important for longer and more elastic links and multiple impacts with the sand where the vibrations are more important.

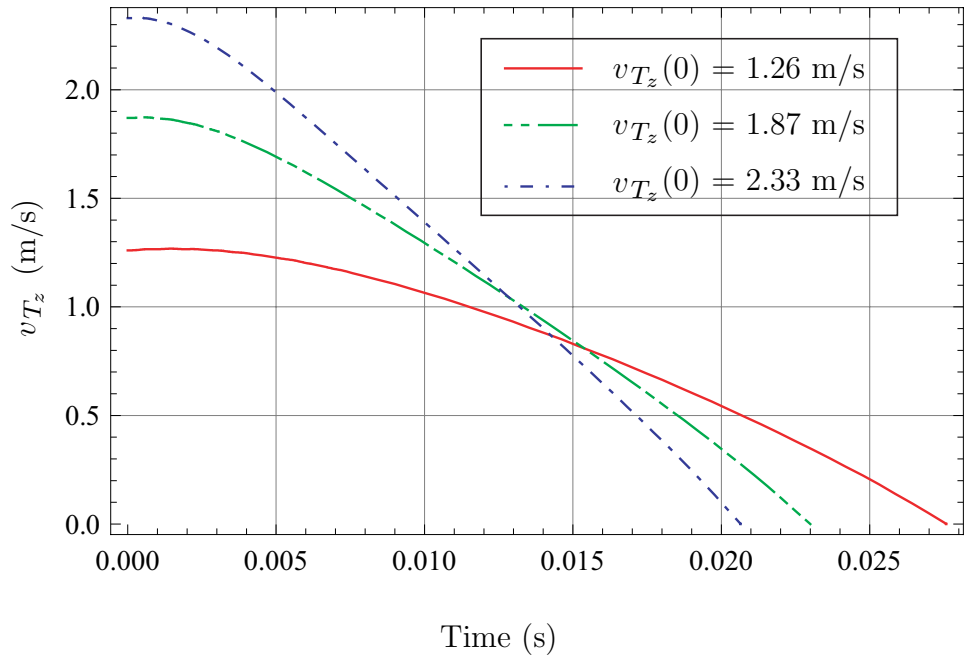
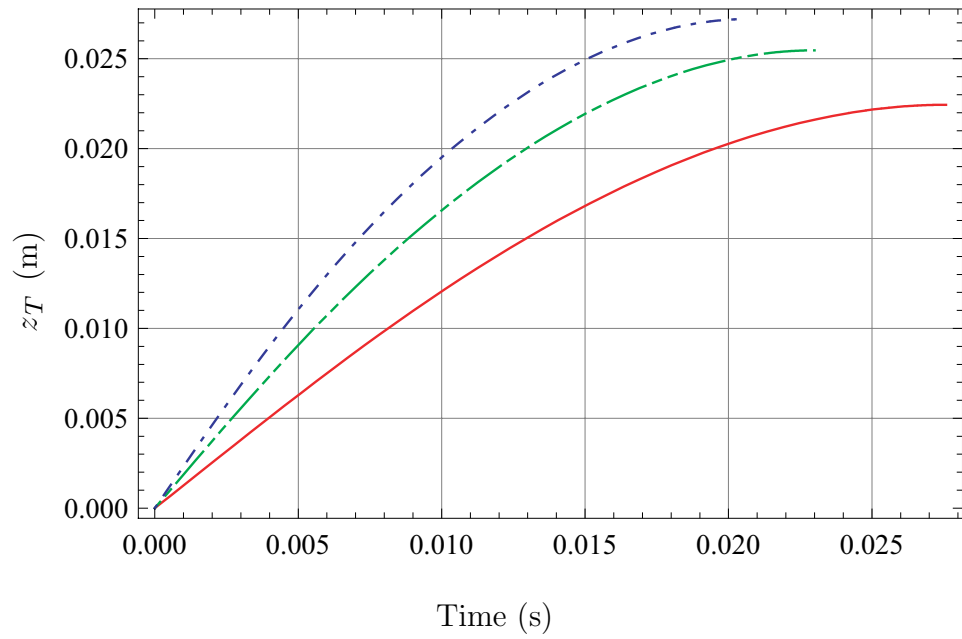


Figure 5.3: Displacement z_T and velocity v_{T_z} results of the flexible link for $q_1(0) = 32^\circ$ and $\dot{q}_z(0) = 1.26, 1.87, 2.33$ m/s

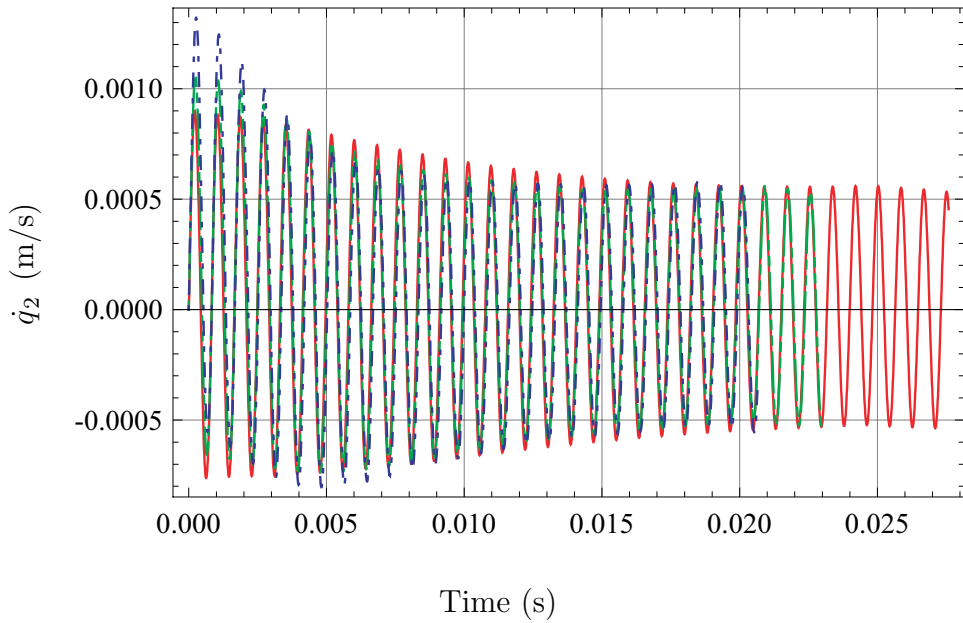
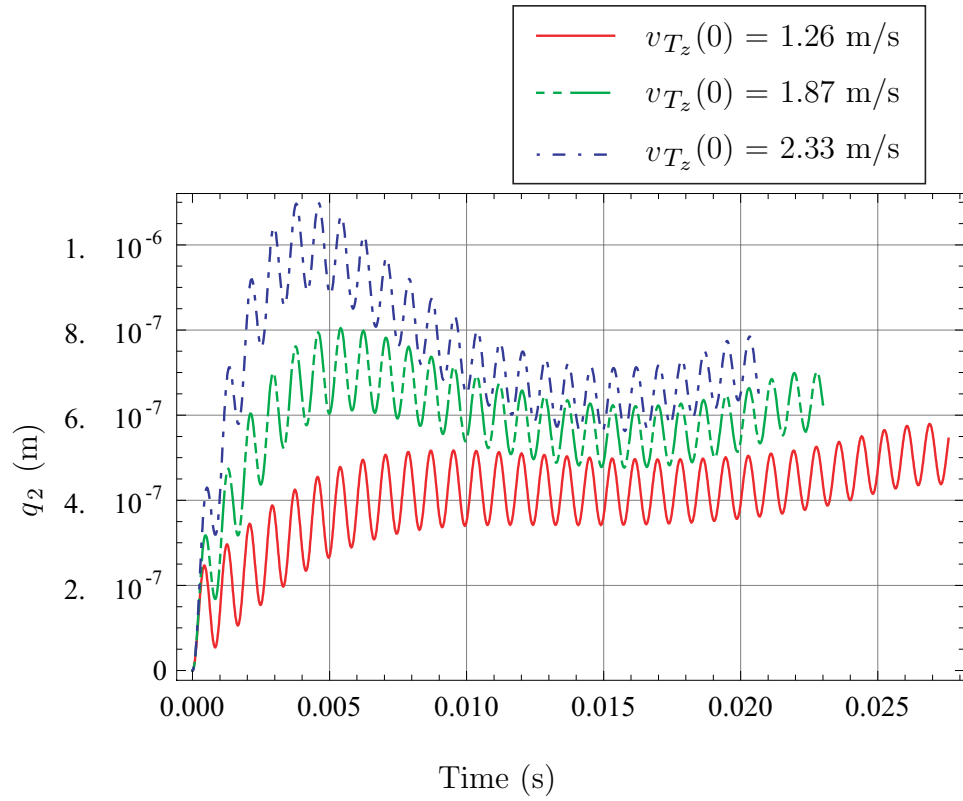


Figure 5.4: Displacement q_2 and velocity \dot{q}_2 results of the flexible link for $q_1(0) = 32^\circ$ and $\dot{q}_z(0) = 1.26, 1.87, 2.33$ m/s

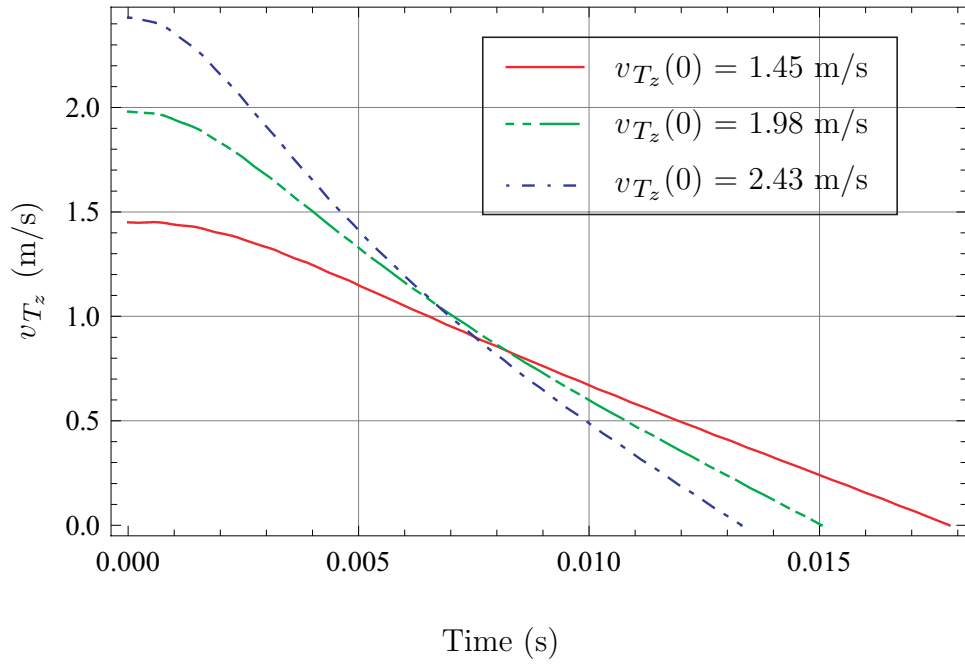
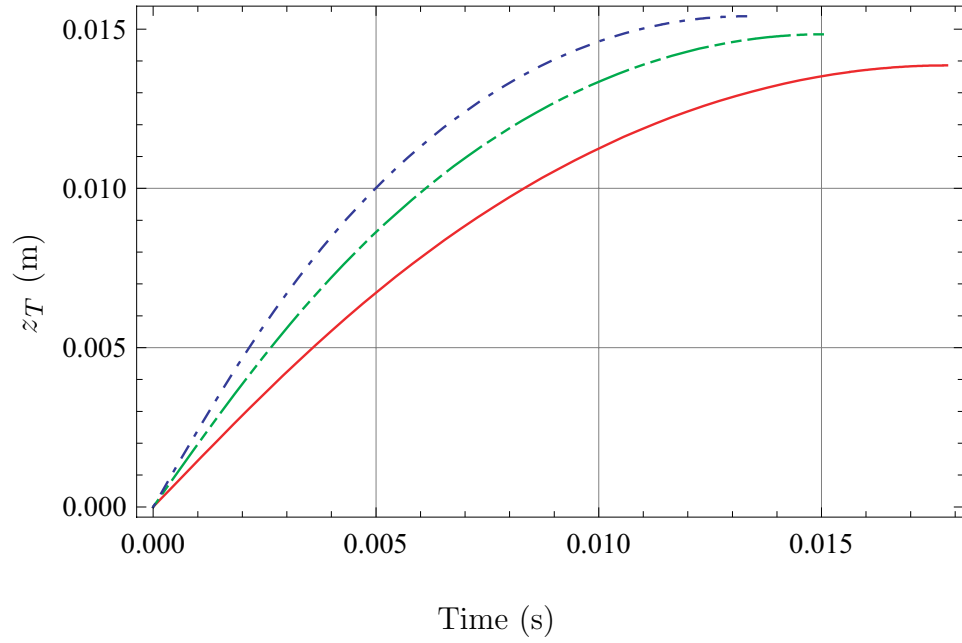


Figure 5.5: Displacement z_T and velocity v_{T_z} results of the flexible link for $q_1(0) = 55^\circ$ and $\dot{q}_z(0) = 1.45, 1.98, 2.43$ m/s

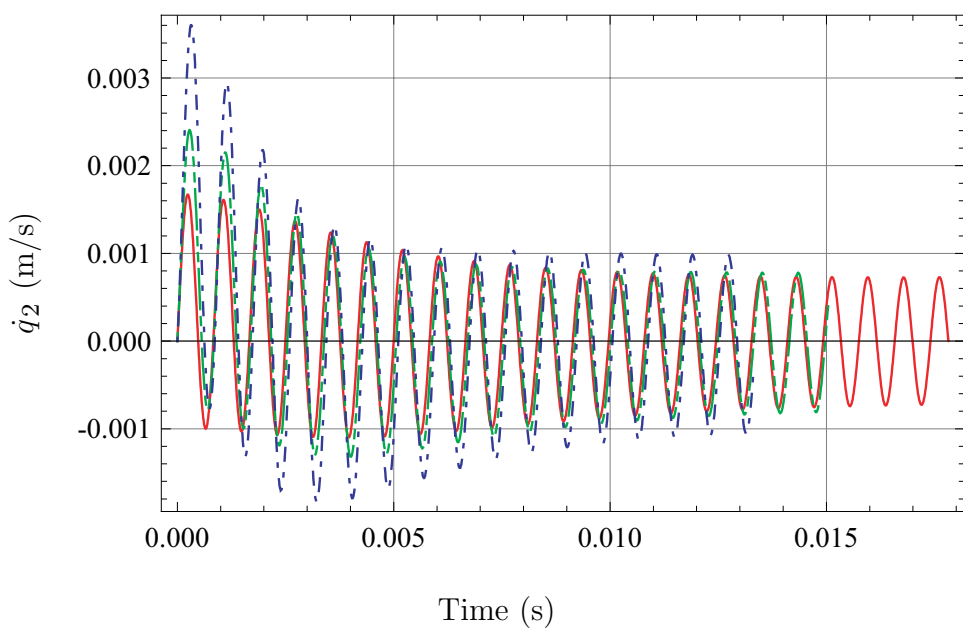
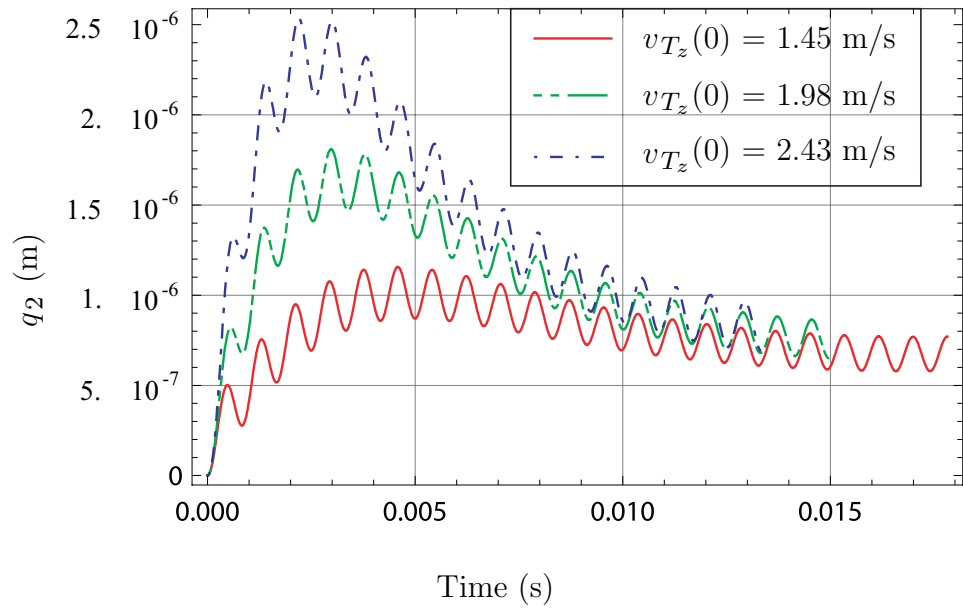


Figure 5.6: Displacement q_2 and velocity \dot{q}_2 results of the flexible link for $q_1(0) = 55^\circ$ and $\dot{q}_z(0) = 1.45, 1.98, 2.43$ m/s

5.2 Elastic compound pendulum

5.2.1 Transverse vibration of an elastic compound pendulum

In the case of an articulated elastic pendulum composed of one end supported by a joint as shown in Fig. 5.7, the boundary conditions for this pendulum (articulated at one end free at the other end) can be written as

$$x(0, t) = x''(0, t) = x''(L, t) = x'''(L, t) = 0. \quad (5.44)$$

Using the boundary conditions given by Eq. (5.44), the relation between constants A , B , C , and D can be attained as

$$\begin{bmatrix} 0 & 1 & 0 & 1 \\ 0 & -\frac{\lambda_i^2}{L^2} & 0 & \frac{\lambda_i^2}{L^2} \\ -\frac{\lambda_i^2 \sin \lambda_i}{L^2} & -\frac{\lambda_i^2 \cos \lambda_i}{L^2} & \frac{\lambda_i^2 \sinh \lambda_i}{L^2} & \frac{\lambda_i^2 \cosh \lambda_i}{L^2} \\ -\frac{\lambda_i^3 \cos \lambda_i}{L^3} & \frac{\lambda_i^3 \sin \lambda_i}{L^3} & \frac{\lambda_i^3 \cosh \lambda_i}{L^3} & \frac{\lambda_i^3 \sinh \lambda_i}{L^3} \end{bmatrix} \begin{bmatrix} A \\ B \\ C \\ D \end{bmatrix} = \begin{bmatrix} 0 \\ 0 \\ 0 \\ 0 \end{bmatrix}. \quad (5.45)$$

For non-zero solution, the determinant of the matrix of Eq. (5.45) should be zero and the general solution satisfying these boundary conditions is calculated as

$$\Phi_i = \frac{\sinh \lambda_i}{\sin \lambda_i} \sin \frac{\lambda_i x}{L} + \sinh \frac{\lambda_i x}{L}. \quad (5.46)$$

The characteristic equation of which roots satisfy Eq. (5.46) is calculated as

$$\cos \lambda_i \sinh \lambda_i - \sin \lambda_i \cosh \lambda_i = 0. \quad (5.47)$$

The roots of this characteristic equation are shown in table 5.3.

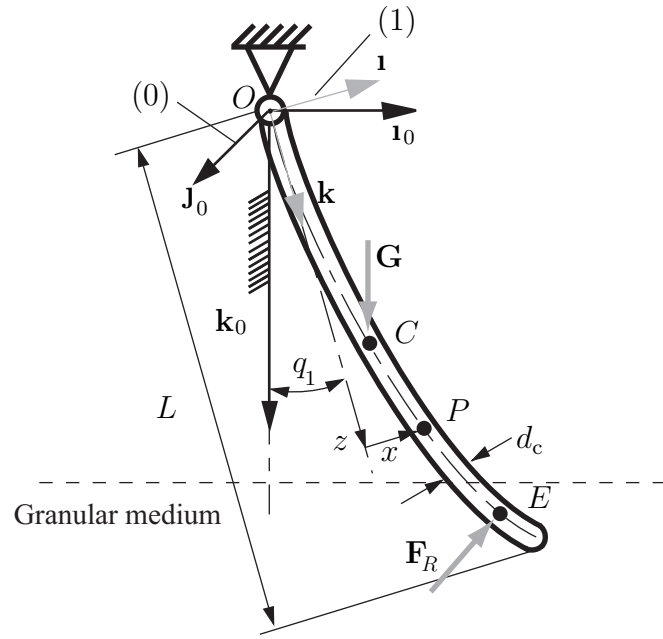


Figure 5.7: Articulated elastic compound pendulum

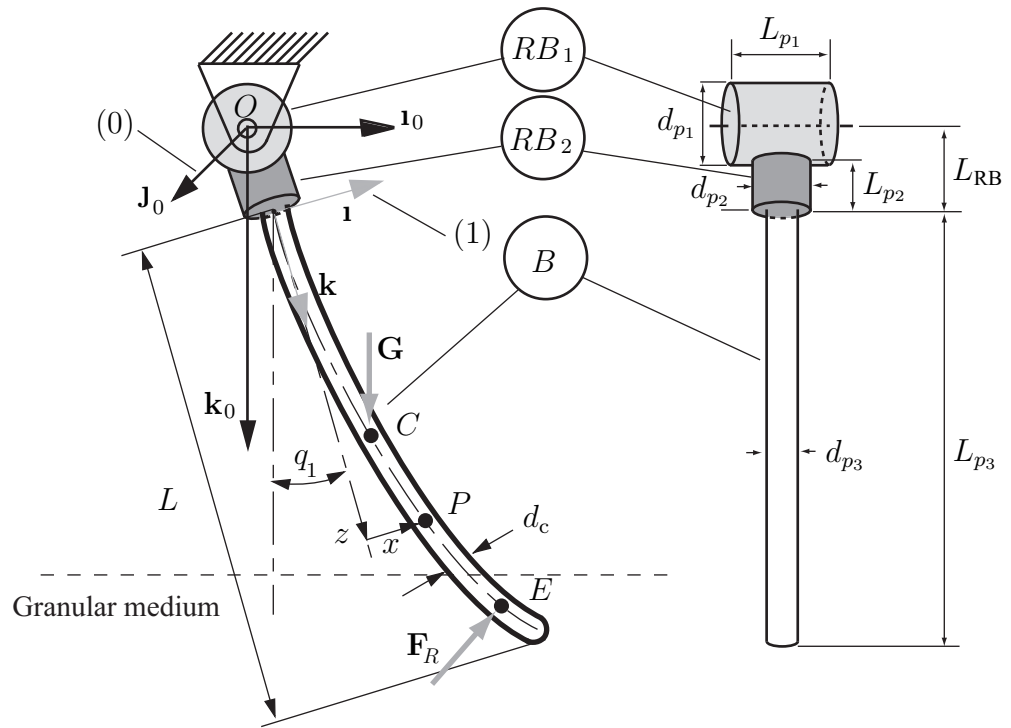


Figure 5.8: Cantilevered elastic compound pendulum

In the case of the cantilevered elastic compound pendulum composed of one end supported by a rigid body shown in Fig. 5.8, the boundary conditions (cantilevered at one end and free at the other end) can be written as

$$x(0, t) = x'(0, t) = x''(L, t) = x'''(L, t) = 0. \quad (5.48)$$

Using the boundary conditions given by Eq. (5.48), the relation between constants A , B , C , and D can be attained as

$$\begin{bmatrix} 0 & 1 & 0 & 1 \\ \frac{\lambda_i}{L} & 0 & \frac{\lambda_i}{L} & 0 \\ -\frac{\lambda_i^2 \sin \lambda_i}{L^2} & -\frac{\lambda_i^2 \cos \lambda_i}{L^2} & \frac{\lambda_i^2 \sinh \lambda_i}{L^2} & \frac{\lambda_i^2 \cosh \lambda_i}{L^2} \\ -\frac{\lambda_i^3 \cos \lambda_i}{L^3} & \frac{\lambda_i^3 \sin \lambda_i}{L^3} & \frac{\lambda_i^3 \cosh \lambda_i}{L^3} & \frac{\lambda_i^3 \sinh \lambda_i}{L^3} \end{bmatrix} \begin{bmatrix} A \\ B \\ C \\ D \end{bmatrix} = \begin{bmatrix} 0 \\ 0 \\ 0 \\ 0 \end{bmatrix}. \quad (5.49)$$

From Eq. (5.49), the constants A , B , C , and D can be calculated and the general solution satisfying these boundary condition is given as

$$\Phi_i = \cosh \frac{\lambda_i z}{L} - \cos \frac{\lambda_i z}{L} - \frac{\cosh \lambda_i + \cos \lambda_i}{\sinh \lambda_i + \sin \lambda_i} \left(\sinh \frac{\lambda_i z}{L} - \sin \frac{\lambda_i z}{L} \right). \quad (5.50)$$

The characteristic equation of which roots satisfy Eq. (5.50) is given as

$$\cos \lambda_i \cosh \lambda_i + 1 = 0. \quad (5.51)$$

The roots of this characteristic equation are shown in table 5.3.

Table 5.3: Roots of characteristic equations for elastic compound pendulum

root	characteristic equation of articulated elastic pendulum ($\cos \lambda_i \sinh \lambda_i - \sin \lambda_i \cosh \lambda_i = 0$)	characteristic equation of cantilevered elastic pendulum ($\cos \lambda_i \cosh \lambda_i + 1 = 0$)
λ_1	3.9266	1.8751
λ_2	7.0686	4.6941
λ_3	10.210	7.8548
λ_4	13.351	10.996

5.2.2 Modeling of an articulated elastic compound pendulum

As shown in Fig. 5.7, the system is formed by an uniform flexible link of length L with diameter d_c , the cross sectional area $A_c = \pi d_c^2/4$, the flexural rigidity EI , and the density ρ_c . To characterize the instantaneous configuration of the pendulum, generalized coordinates q_1 is employed. The generalized coordinate q_1 denotes the radian measure of the rotation angle between the undeformed pendulum and the vertical axis. A fixed reference frame (0) of unit vectors $[\mathbf{i}_0, \mathbf{j}_0, \mathbf{k}_0]$ and a mobile reference frame (1) of unit vectors $[\mathbf{i}, \mathbf{j}, \mathbf{k}]$ are considered. The unit vectors \mathbf{i}_0 , \mathbf{j}_0 , and \mathbf{k}_0 can be expressed as Eq. (5.12) and the unit vectors \mathbf{i} , \mathbf{j} , and \mathbf{k} can be also expressed as Eq. (5.13).

Kinematics

The deformations of the articulated elastic compound pendulum can be discussed in terms of the elastic displacement $x(z, t)$ of a generic point P on the pendulum. The point P is situated at a distance z from the origin point O . The displacement x can be expressed as

$$\begin{aligned}
 x(z, t) &= \sum_{i=1}^n \Phi_i(z) q_{1+i}(t), \\
 &= \sum_{i=1}^n \left[\frac{\sinh \lambda_i}{\sin \lambda_i} \sin \frac{\lambda_i x}{L} + \sinh \frac{\lambda_i x}{L} \right] q_{1+i}(t), \tag{5.52}
 \end{aligned}$$

where $\Phi_i(z)$ is a shape function by the distance z , the elastic generalized coordinate $q_{1+i}(t)$ is a function of time t , and i is any positive integer for the articulated elastic compound pendulum. The position vector from origin point O to the generic point P of the elastic link in (0) is

$$\begin{aligned}\mathbf{r}_P &= x\mathbf{1} + z\mathbf{k} = \left[\left(\sum_{i=1}^n \Phi_i(z) q_{1+i} \right) \mathbf{1} + z\mathbf{k} \right] \\ &= \left[\sum_{i=1}^n \Phi_i(z) q_{1+i} \cos q_1 + z \sin q_1 \right] \mathbf{1}_0 + \\ &\quad \left[- \sum_{i=1}^n \Phi_i(z) q_{1+i} \sin q_1 + z \cos q_1 \right] \mathbf{k}_0.\end{aligned}\quad (5.53)$$

The velocity vector of the arbitrary point P of the uniform elastic link in (0) is

$$\begin{aligned}\mathbf{v}_P = \frac{d}{dt}\mathbf{r}_P &= \left[\sum_{i=1}^n \left(\Phi_i(z) \dot{q}_{1+i} \cos q_1 - \Phi_i(z) q_{1+i} \dot{q}_1 \sin q_1 \right) + z \dot{q}_1 \cos q_1 \right] \mathbf{1}_0 \\ &+ \left[- \sum_{i=1}^n \left(\Phi_i(z) \dot{q}_{1+i} \sin q_1 + \Phi_i(z) q_{1+i} \dot{q}_1 \cos q_1 \right) - z \dot{q}_1 \sin q_1 \right] \mathbf{k}_0,\end{aligned}\quad (5.54)$$

and the acceleration vector of the arbitrary point P in (0) is

$$\begin{aligned}\mathbf{a}_P &= \frac{d}{dt}\mathbf{v}_P \\ &= \left[\sum_{i=1}^n \Phi_i(z) \left(\ddot{q}_{1+i} \cos q_1 - 2\dot{q}_{1+i} \dot{q}_1 \sin q_1 - q_{1+i} \ddot{q}_1 \sin q_1 - q_{1+i} \dot{q}_1^2 \cos q_1 \right) \right. \\ &\quad \left. + z \ddot{q}_1 \cos q_1 - z \dot{q}_1^2 \sin q_1 \right] \mathbf{1}_0 \\ &+ \left[- \sum_{i=1}^n \Phi_i(z) \left(\ddot{q}_{1+i} \sin q_1 + 2\dot{q}_{1+i} \dot{q}_1 \cos q_1 + q_{1+i} \ddot{q}_1 \cos q_1 - q_{1+i} \dot{q}_1^2 \sin q_1 \right) \right. \\ &\quad \left. - z \ddot{q}_1 \sin q_1 - z \dot{q}_1^2 \cos q_1 \right] \mathbf{k}_0.\end{aligned}\quad (5.55)$$

The angular acceleration of the link in the reference frame (0) is

$$\boldsymbol{\alpha} = \dot{\boldsymbol{\omega}} = \ddot{q}_1 \mathbf{J}_0.\quad (5.56)$$

Equations of motion

The Newton-Euler's equations can be used to find the differential equations of motion. A moment equation before impact can be written as

$$\int_0^L (\mathbf{r}_P \times \rho_c A_c \mathbf{a}_P) dz = \mathbf{r}_C \times \mathbf{G}, \quad (5.57)$$

where \mathbf{G} is the gravity force acting on the mass center of the pendulum and $\mathbf{r}_C = \mathbf{r}_P(z = 0.5L)$ is the position vector from the origin O to the mass center C . One more governing equation of motion regarding the deformation of the pendulum has the same form with Eq. (5.29) as

$$E I L \left(\frac{\lambda_i}{L} \right)^4 q_{1+i}(t) + \int_0^L \rho_c A_c \mathbf{a}_P \cdot \mathbf{1} \Phi_i(z) dz = \int_0^L \mathbf{F}_{ext} \cdot \mathbf{1} \Phi_i(z) dz. \quad (5.58)$$

Because the external forces acting on the pendulum are the gravitational force \mathbf{G} at the mass center C and the joint reaction force \mathbf{F}_O at the origin O , the external forces \mathbf{F}_{ext} can be expressed as $\mathbf{G} \delta(z - 0.5L) + \mathbf{F}_O \delta(z)$ when the external force \mathbf{F}_{ext} is supposed to be concentrated one on the pendulum. The right hand side of Eq. (5.58) becomes $\mathbf{G} \cdot \mathbf{1} \Phi_i(0.5L) + \mathbf{F}_O \cdot \mathbf{1} \Phi_i(0)$. However, the value of $\Phi_i(0)$ is always zero in the model. Equation (5.58) becomes

$$E I L \left(\frac{\lambda_i}{L} \right)^4 q_{1+i}(t) + \int_0^L \rho_c A_c \mathbf{a}_P \cdot \mathbf{1} \Phi_i(z) dz = \mathbf{G} \cdot \mathbf{1} \Phi_i \left(\frac{L}{2} \right). \quad (5.59)$$

Equations (5.57) and (5.59) represent the equations of motion for the articulated elastic compound pendulum before the impact.

During impacting a granular medium, additionally added external force is restricted to the resistance force \mathbf{F}_R . The equations of motion of the articulated elastic pendulum

during the impact are given as

$$\int_0^L (\mathbf{r}_P \times \rho_c A_c \mathbf{a}_P) dz = \mathbf{r}_C \times \mathbf{G} + \mathbf{r}_E \times \mathbf{F}_R, \quad (5.60)$$

$$EI L \left(\frac{\lambda_i}{L} \right)^4 q_{1+i}(t) + \int_0^L \rho_c A_c \mathbf{a}_P \cdot \mathbf{i} \Phi_i(z) dz = \mathbf{G} \cdot \mathbf{i} \Phi_i \left(\frac{L}{2} \right) + \mathbf{F}_R \cdot \mathbf{i} \Phi_i(L_E), \quad (5.61)$$

where $\mathbf{r}_E = \mathbf{r}_P(z = L_E)$ is the position vector from the origin O to the resistance force application point E and the length from the origin O to E , L_E , is calculated as

$$L_E = L - \frac{z_T}{2 \cos q_1}. \quad (5.62)$$

The immersed depth z_T , the vertical component of the position vector of the end point T , is calculated by Eq. (5.53) as $z_T = \mathbf{r}_P(z = L) \cdot \mathbf{k}_0$. The resistance force \mathbf{F}_R is also calculated by Eqs. (3.6), (3.8), and (3.9). The dynamic frictional force \mathbf{F}_d is

$$\begin{aligned} \mathbf{F}_d &= -\mathbf{v}_E \eta_d \rho_g A_r |\mathbf{v}_E| \\ &= -\eta_d \rho_g A_r \left[\left(\sum_{i=1}^n \left(\Phi_i(L_E) \dot{q}_{1+i} \cos q_1 - \Phi_i(L_E) q_{1+i} \dot{q}_1 \sin q_1 \right) + L_E \dot{q}_1 \cos q_1 \right)^2 + \right. \\ &\quad \left. \left(- \sum_{i=1}^n \left(\Phi_i(L_E) \dot{q}_{1+i} \sin q_1 + \Phi_i(L_E) q_{1+i} \dot{q}_1 \cos q_1 \right) - L_E \dot{q}_1 \sin q_1 \right)^2 \right]^{0.5} \\ &\quad \left[\left(+ \sum_{i=1}^n \left(\Phi_i(L_E) \dot{q}_{1+i} \cos q_1 - \Phi_i(L_E) q_{1+i} \dot{q}_1 \sin q_1 \right) + L_E \dot{q}_1 \cos q_1 \right) \mathbf{i}_0 + \right. \\ &\quad \left. \left(- \sum_{i=1}^n \left(\Phi_i(L_E) \dot{q}_{1+i} \sin q_1 + \Phi_i(L_E) q_{1+i} \dot{q}_1 \cos q_1 \right) - L_E \dot{q}_1 \sin q_1 \right) \mathbf{k}_0 \right], \quad (5.63) \end{aligned}$$

where the velocity vector \mathbf{v}_E is the velocity of the resistance force acting point E and this vector calculated by Eq. (5.54) as $\mathbf{v}_E = \mathbf{v}_P(z = L_E)$. The reference area A_r is calculated

as

$$A_r = \frac{d_c z_T}{\cos q_1}. \quad (5.64)$$

The horizontal and vertical static resistance forces, \mathbf{F}_{sh} and \mathbf{F}_{vh} , are

$$\mathbf{F}_{sh} = -\text{sign} \left[\sum_{i=1}^n \left(\Phi_i(L_E) \dot{q}_{1+i} \cos q_1 - \Phi_i(L_E) q_{1+i} \dot{q}_1 \sin q_1 \right) + L_E \dot{q}_1 \cos q_1 \right] \eta_h g \rho_g z_T^2 d_c \mathbf{1}_0, \quad (5.65)$$

$$\mathbf{F}_{sv} = -\text{sign} \left[- \sum_{i=1}^n \left(\Phi_i(L_E) \dot{q}_{1+i} \sin q_1 + \Phi_i(L_E) q_{1+i} \dot{q}_1 \cos q_1 \right) - L_E \dot{q}_1 \sin q_1 \right] \eta_v \left(\frac{z_T}{d_c} \right)^\lambda g \rho_g V \mathbf{k}_0, \quad (5.66)$$

where the immersed volume V is calculated as

$$V = \frac{\pi d_c^2}{4} \frac{z_T}{\cos q_1}. \quad (5.67)$$

The resistance force \mathbf{F}_R , the sum of the dynamic frictional force vector \mathbf{F}_d and the static resistance force vector \mathbf{F}_s , is represented as the sum of Eqs. (5.63), (5.65), and (5.66).

5.2.3 Simulation results of the articulated elastic compound pendulum

Figures 5.9, 5.10, 5.11, 5.12, 5.13, and 5.14 show the simulation results for the elastic compound pendulum as shown in Fig. 5.7 with the following initial conditions: $q_1(0) = 30^\circ$, 60° , 75° , $\dot{q}_1(0) = -1, -3, -5$ rad/s, $q_2(0) = 0$ m, and $\dot{q}_2(0) = 0$ m/s. As the numerical data applied to this simulation, the length of pendulum is $L = 0.15$ m, the diameter is $d_c = 0.00635$ m, the density of the pendulum is $\rho_c = 7.7 \times 10^3$ kg/m³, the flexural rigidity is $EI = 15.1642$ N m², and the density of a granular medium (sand) is $\rho_g = 2.5 \times 10^3$ kg/m³. The dynamic frictional force coefficient $\eta_d = 6.5$, the horizontal static resistance

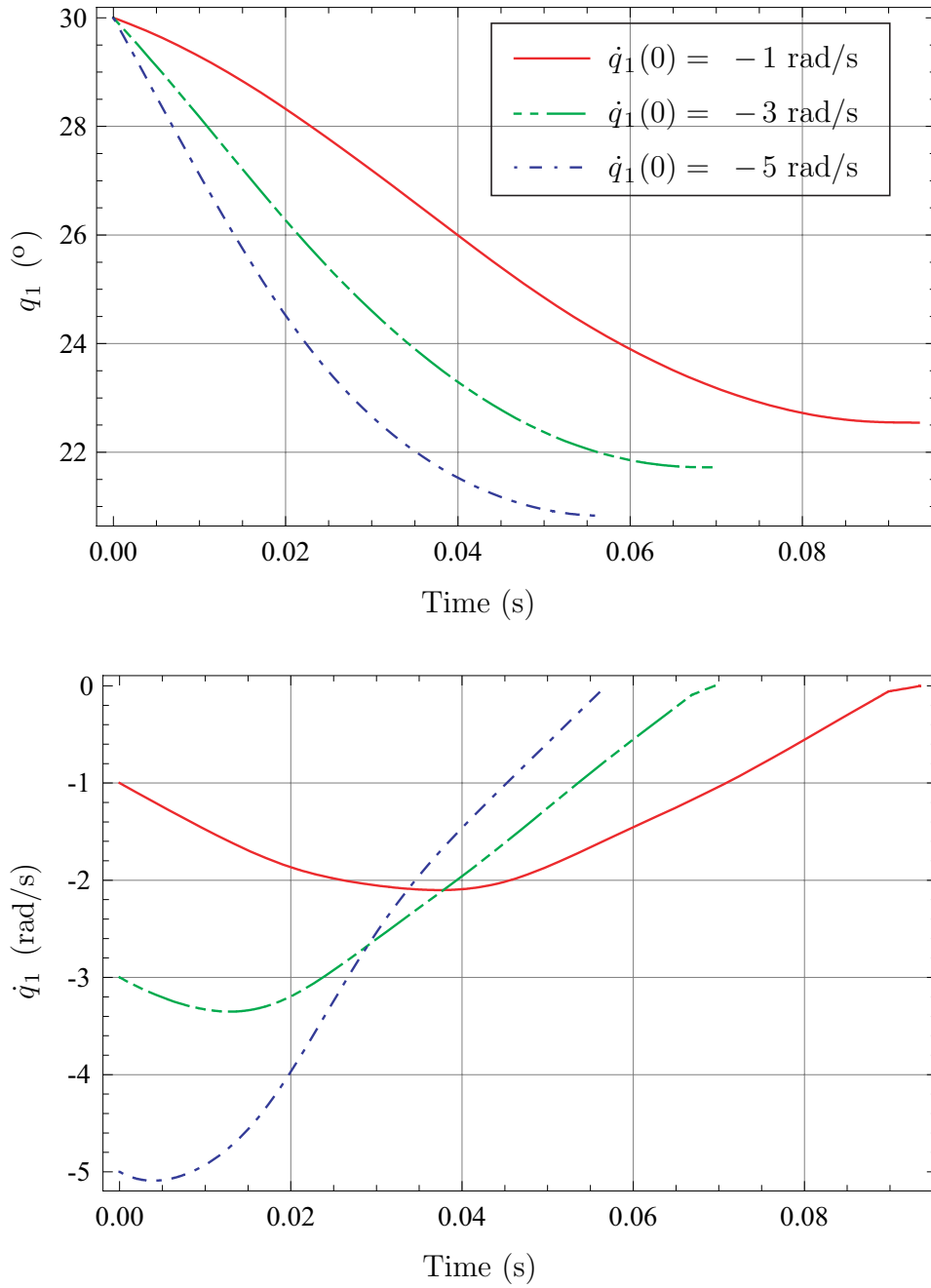


Figure 5.9: Angle q_1 and angular velocity \dot{q}_1 results of the articulated elastic compound pendulum for $q_1(0) = 30^\circ$ and $\dot{q}_1(0) = -1, -3, -5$ rad/s

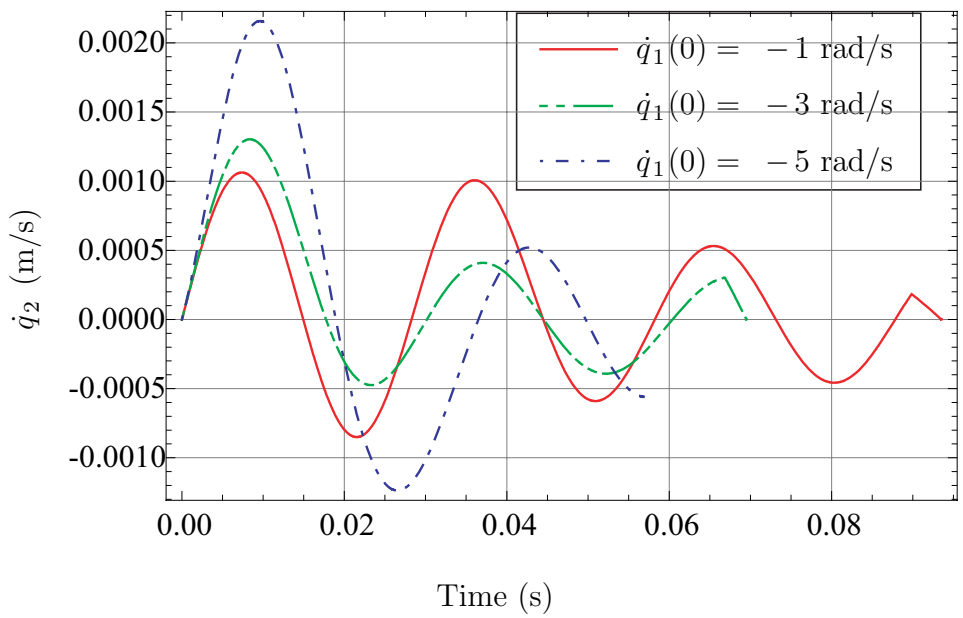
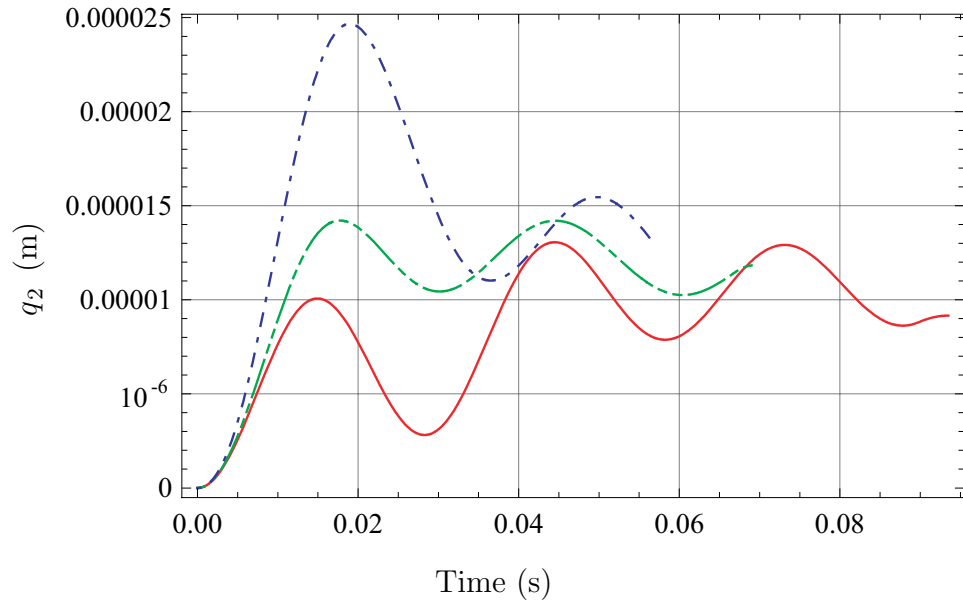


Figure 5.10: Displacement q_2 and velocity \dot{q}_2 results of the articulated elastic compound pendulum for $q_1(0) = 30^\circ$ and $\dot{q}_1(0) = -1, -3, -5$ rad/s

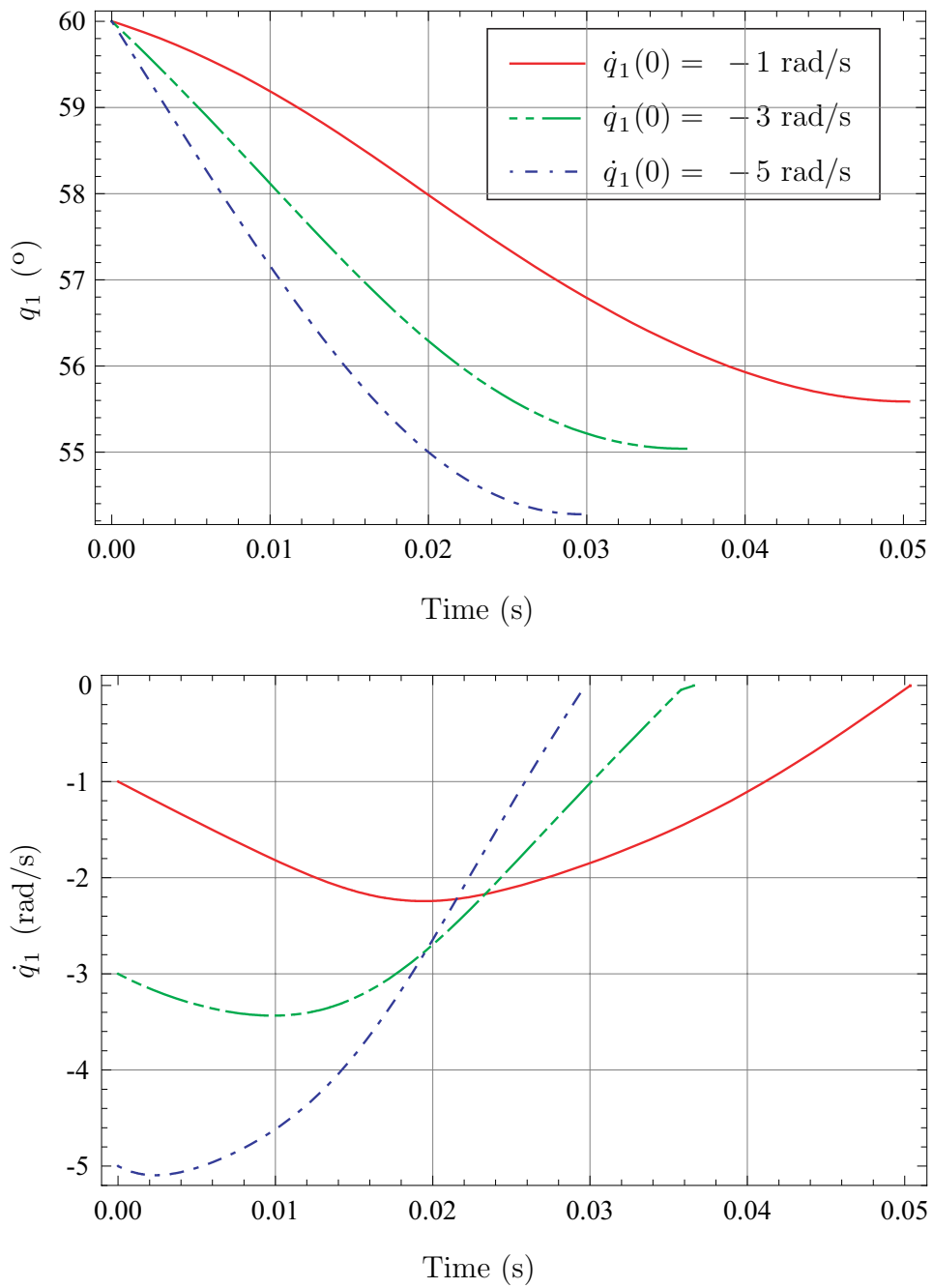


Figure 5.11: Angle q_1 and angular velocity \dot{q}_1 results of the articulated elastic compound pendulum for $q_1(0) = 60^\circ$ and $\dot{q}_1(0) = -1, -3, -5$ rad/s

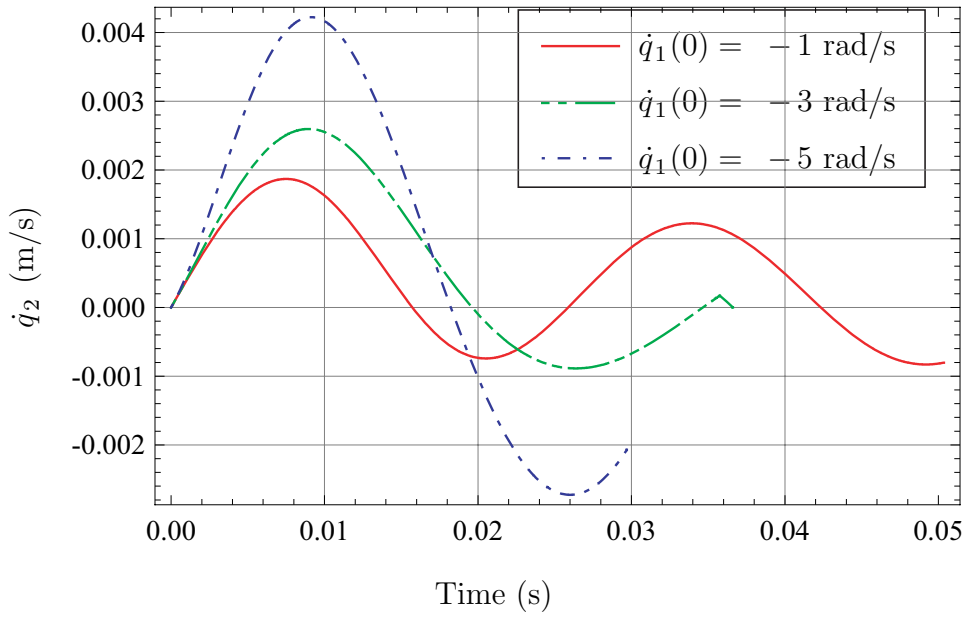
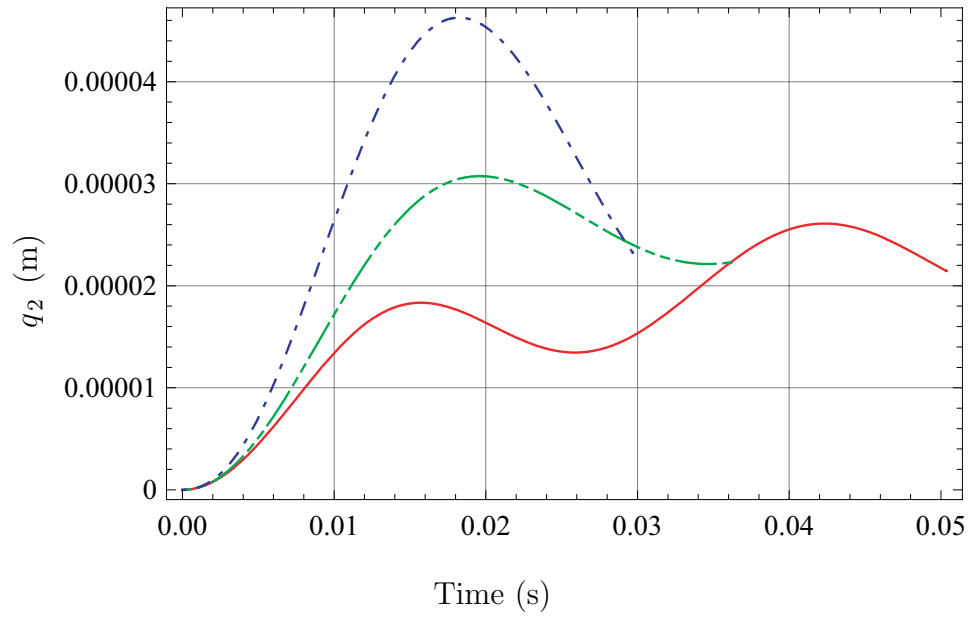


Figure 5.12: Displacement q_2 and velocity \dot{q}_2 results of the articulated elastic compound pendulum for $q_1(0) = 60^\circ$ and $\dot{q}_1(0) = -1, -3, -5$ rad/s

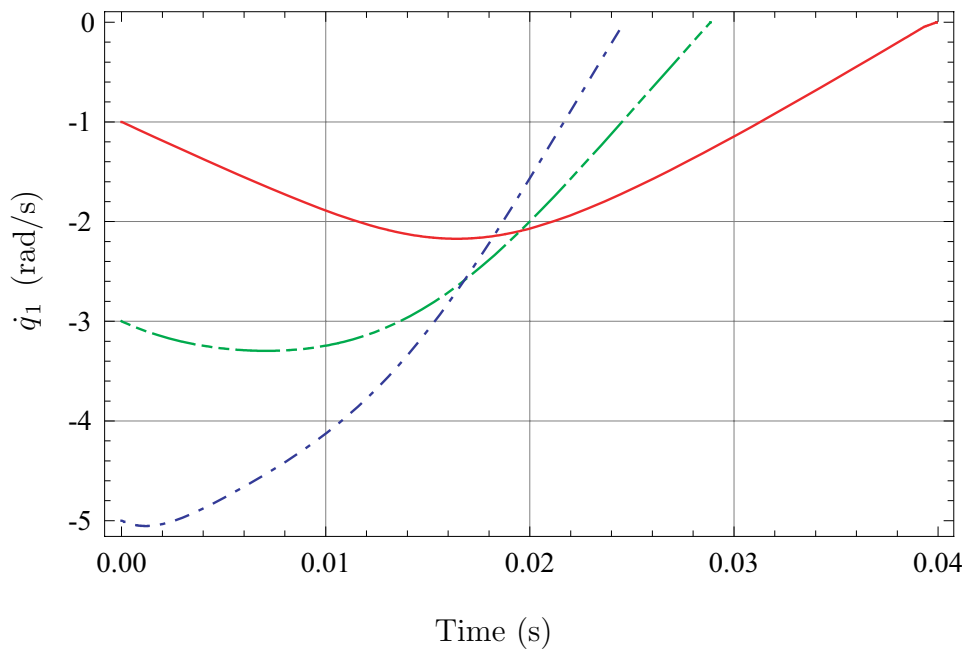
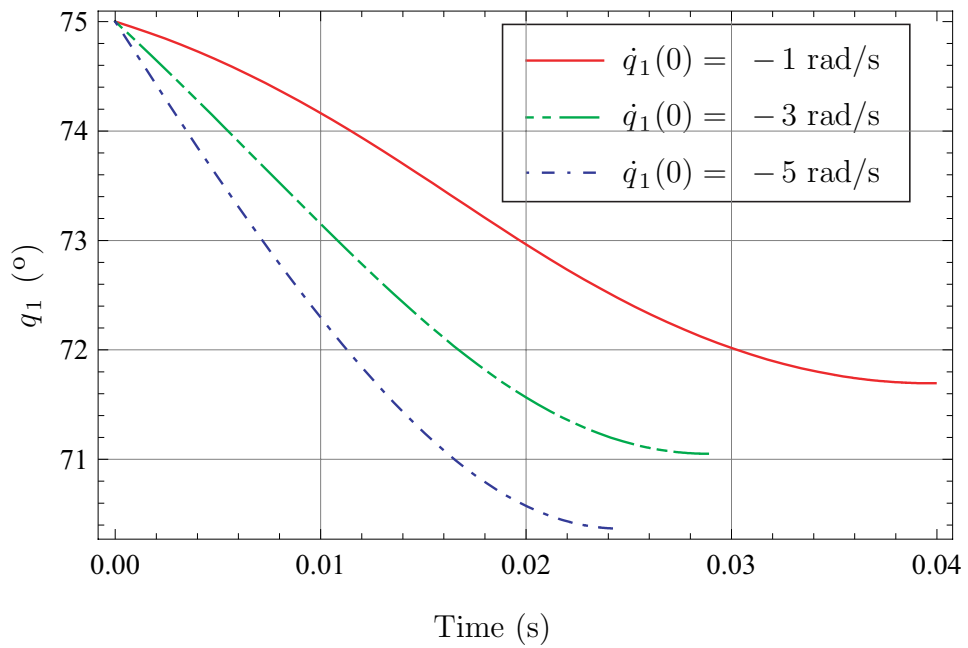


Figure 5.13: Angle q_1 and angular velocity \dot{q}_1 results of the articulated elastic compound pendulum for $q_1(0) = 75^\circ$ and $\dot{q}_1(0) = -1, -3, -5$ rad/s

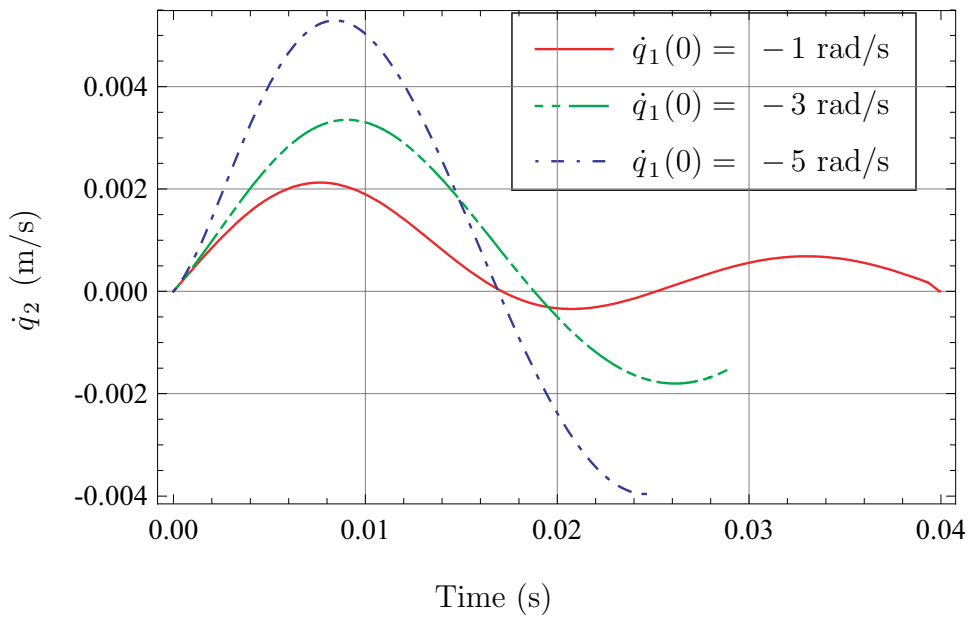
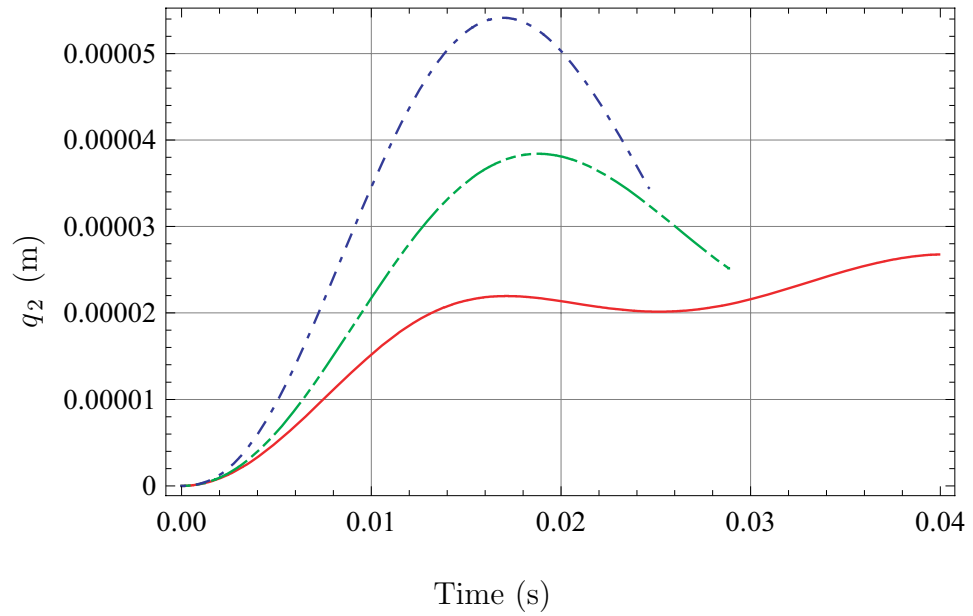


Figure 5.14: Displacement q_2 and velocity \dot{q}_2 results of the articulated elastic compound pendulum for $q_1(0) = 75^\circ$ and $\dot{q}_1(0) = -1, -3, -5$ rad/s

Table 5.4: Stopping time of the articulated elastic compound pendulum and the rigid one

$q_1(0)$ ($^\circ$)	$\dot{q}_1(0)$ (rad/s)	$t_{s,r}$ (s)	$t_{s,e}$ (s)
30	-1	0.0908846	0.0946034
	-3	0.068481	0.0700719
	-5	0.0574613	0.0573489
60	-1	0.047826	0.0509171
	-3	0.0353842	0.0372156
	-5	0.0292904	0.0299783
75	-1	0.0371793	0.0403826
	-3	0.0270217	0.0291454
	-5	0.0223565	0.024833

force coefficient $\eta_h = 8$, and the vertical static resistance force coefficients $\eta_v = 22$ and $\lambda = 1.1$ are used in the simulation. The simulations are performed from the impact moment until the angular velocity of the pendulum, \dot{q}_1 , becomes zero and the first mode of the shape function of Eq. (5.46) is only considered ($\lambda_1=3.9266$). As shown in Figs. 5.9, 5.11, and 5.13, the pendulum stops more quickly when the pendulum impact the granular medium with high velocity. This result means that the faster the impact velocity becomes the sooner the impact compound pendulum stops whether a rigid pendulum or an elastic one. The generalized coordinate q_2 showing the deformation of the pendulum becomes large when the initial impact velocity and angle increase as shown in Figs. 5.10, 5.12, and 5.14. Table 5.4 shows the compared results between the rigid and the elastic model. The differences between the rigid model and the flexible model are not also conspicuous for our particular system. The articulated elastic deformations of the compound pendulum will be important for longer and more elastic links.

5.2.4 Modeling of a cantilevered elastic compound pendulum

As shown in Fig. 5.8, the cantilevered elastic pendulum applied to modeling is supported by rigid bodies RB_1 and RB_2 . The rigid body RB_1 has the diameter d_{p_1} and the length L_{p_1} . The rigid body RB_2 has the diameter d_{p_2} and the length L_{p_2} . The flexible part of the pendulum, B , has an uniform flexible link of the length $L_{p_3} = L_B = L$, the diameter $d_{p_3} = d_c$, the cross sectional area $A_c = \pi d_c^2/4$, the flexural rigidity EI , and density ρ_c . The length from the origin to the rigid body end is $L_{RB} = d_{p_1}/2 + L_{p_2}$ and the density of the rigid bodies are the same as that of the elastic link. To characterize the instantaneous configuration of the pendulum, the generalized coordinates q_1 and q_{i+1} are employed. The generalized coordinate q_1 denotes the radian measure of the rotation angle between the undeformed pendulum and the horizontal axis. The generalized coordinate q_{i+1} denotes the deformation of the elastic link part of the pendulum. A fixed reference frame (0) of unit vectors $[\mathbf{i}_0, \mathbf{j}_0, \mathbf{k}_0]$ and a mobile reference frame (1) of unit vectors $[\mathbf{i}, \mathbf{j}, \mathbf{k}]$ are considered. The unit vectors $\mathbf{i}_0, \mathbf{j}_0$, and \mathbf{k}_0 can be expressed as Eq. (5.12) and the unit vectors \mathbf{i}, \mathbf{j} , and \mathbf{k} can be also expressed as Eq. (5.13).

Kinematics

The deformations of the cantilevered elastic compound pendulum can be also discussed in terms of the elastic displacement $x(z, t)$ of a generic point P on the elastic part B of the pendulum. The point P is situated at a distance z from the point at the first end of the elastic link B . The displacement x can be expressed as

$$\begin{aligned} x(z, t) &= \sum_{i=1}^n \Phi_i(z) q_{1+i}(t), \\ &= \sum_{i=1}^n \left[\cosh \frac{\lambda_i z}{L} - \cos \frac{\lambda_i z}{L} - \frac{\cosh \lambda_i + \cos \lambda_i}{\sinh \lambda_i + \sin \lambda_i} \left(\sinh \frac{\lambda_i z}{L} - \sin \frac{\lambda_i z}{L} \right) \right] q_{1+i}(t), \quad (5.68) \end{aligned}$$

where $\Phi_i(z)$ is a shape function of the elastic link by z , the elastic generalized coordinate $q_{1+i}(t)$ is a function of time t , and i is any positive integer.

The position of the mass center of the rigid body RB_1 is the origin point O and the position vector from the origin O to the mass center of the rigid body RB_2 , C_{RB2} , is represented as

$$\mathbf{r}_{C_{RB2}} = \frac{d_{p1} + L_{p2}}{2} (\sin q_1 \mathbf{1}_0 + \cos q_1 \mathbf{k}_0). \quad (5.69)$$

The position vector from the origin point O to a generic point P of the link B in (0) is

$$\begin{aligned} \mathbf{r}_P &= x \mathbf{1} + (L_{RB} + z) \mathbf{k} = \left[\left(\sum_{i=1}^n \Phi_i(z) q_{1+i} \right) \mathbf{1} + (L_{RB} + z) \mathbf{k} \right] \\ &= \left[\sum_{i=1}^n \Phi_i(z) q_{1+i} \cos q_1 + (L_{RB} + z) \sin q_1 \right] \mathbf{1}_0 + \\ &\quad \left[- \sum_{i=1}^n \Phi_i(z) q_{1+i} \sin q_1 + (L_{RB} + z) \cos q_1 \right] \mathbf{k}_0. \end{aligned} \quad (5.70)$$

The velocity vector of the generic point P of the elastic link B in (0) is

$$\begin{aligned} \mathbf{v}_P = \frac{d}{dt} \mathbf{r}_P &= \left[\sum_{i=1}^n \left(\Phi_i(z) \dot{q}_{1+i} \cos q_1 - \Phi_i(z) q_{1+i} \dot{q}_1 \sin q_1 \right) + (L_{RB} + z) \dot{q}_1 \cos q_1 \right] \mathbf{1}_0 \\ &+ \left[- \sum_{i=1}^n \left(\Phi_i(z) \dot{q}_{1+i} \sin q_1 + \Phi_i(z) q_{1+i} \dot{q}_1 \cos q_1 \right) - (L_{RB} + z) \dot{q}_1 \sin q_1 \right] \mathbf{k}_0, \end{aligned} \quad (5.71)$$

and the acceleration vector of the point P in (0) is

$$\begin{aligned} \mathbf{a}_P &= \frac{d}{dt} \mathbf{v}_P \\ &= \left[\sum_{i=1}^n \Phi_i(z) \left(\ddot{q}_{1+i} \cos q_1 - 2 \dot{q}_{1+i} \dot{q}_1 \sin q_1 - q_{1+i} \ddot{q}_1 \sin q_1 - q_{1+i} \dot{q}_1^2 \cos q_1 \right) \right. \\ &\quad \left. + (L_{RB} + z) \ddot{q}_1 \cos q_1 - (L_{RB} + z) \dot{q}_1^2 \sin q_1 \right] \mathbf{1}_0 \\ &+ \left[- \sum_{i=1}^n \Phi_i(z) \left(\ddot{q}_{1+i} \sin q_1 + 2 \dot{q}_{1+i} \dot{q}_1 \cos q_1 + q_{1+i} \ddot{q}_1 \cos q_1 - q_{1+i} \dot{q}_1^2 \sin q_1 \right) \right. \\ &\quad \left. - (L_{RB} + z) \ddot{q}_1 \sin q_1 - (L_{RB} + z) \dot{q}_1^2 \cos q_1 \right] \mathbf{k}_0. \end{aligned} \quad (5.72)$$

The angular acceleration of the link in the reference frame (0) is

$$\boldsymbol{\alpha} = \dot{\boldsymbol{\omega}} = \ddot{q}_1 \mathbf{J}_0. \quad (5.73)$$

Equations of motion

The Newton-Euler's equations can be used to find the differential equation of motion. A moment equation before impact can be written as

$$I_{RB} \ddot{\mathbf{q}}_1 + \int_0^L (\mathbf{r}_P \times \rho_c A_c \mathbf{a}_P) dz = \mathbf{r}_{C_{RB2}} \times \mathbf{G}_{RB2} + \mathbf{r}_C \times \mathbf{G}_B, \quad (5.74)$$

where I_{RB} is the mass moment of inertia of the rigid body and the gravity forces \mathbf{G}_{RB2} and \mathbf{G}_B are acting on the mass center of the rigid body RB_2 and on the flexible link B respectively. The vector \mathbf{r}_C is the position vector from origin point O to the mass center C of the flexible link ($\mathbf{r}_C = \mathbf{r}_P(z = 0.5L)$). One more governing equation of motion regarding deformation of the link has the same form as Eq. (5.29) and the equation becomes

$$EIL \left(\frac{\lambda_i}{L} \right)^4 q_{1+i}(t) + \int_0^L \rho_c A_c \mathbf{a}_P \cdot \mathbf{1} \Phi_i(z) dz = \int_0^L \mathbf{F}_{ext} \cdot \mathbf{1} \Phi_i(z) dz. \quad (5.75)$$

Because the external forces acting on the elastic link of the pendulum are the gravity force \mathbf{G}_B and the joint reaction force \mathbf{F}_{RB2} from the rigid body RB_2 , the external force \mathbf{F}_{ext} can be written as $\mathbf{G}_B \delta(z - 0.5L) + \mathbf{F}_{RB2} \delta(z)$ when the external force \mathbf{F}_{ext} is supposed to be concentrated one on the pendulum. Therefore the right hand side of Eq. (5.75) becomes $\mathbf{G}_B \cdot \mathbf{1} \Phi_i(0.5L) + \mathbf{F}_O \cdot \mathbf{1} \Phi_i(0)$. Because the value of $\Phi_i(0)$ is always zero in the model, Eq. (5.75) becomes

$$EIL \left(\frac{\lambda_i}{L} \right)^4 q_{1+i}(t) + \int_0^L \rho_c A_c \mathbf{a}_P \cdot \mathbf{1} \Phi_i(z) dz = \mathbf{G}_B \cdot \mathbf{1} \Phi_i \left(\frac{L}{2} \right). \quad (5.76)$$

Differential equations (5.74) and (5.76) represent the equations of motion for the cantilevered elastic pendulum before impact.

During impacting a granular medium, an additionally added external force is restricted to the resistance force \mathbf{F}_R . The equations of motion for the cantilevered elastic pendulum during impacting are given as

$$I_{RB} \ddot{\mathbf{q}}_1 + \int_0^L (\mathbf{r}_P \times \rho_c A_c \mathbf{a}_P) dz = \mathbf{r}_C \times \mathbf{G} + \mathbf{r}_E \times \mathbf{F}_R, \quad (5.77)$$

$$EIL \left(\frac{\lambda_i}{L}\right)^4 q_{1+i}(t) + \int_0^L \rho_c A_c \mathbf{a}_P \cdot \mathbf{1} \Phi_i(z) dz = \mathbf{G}_B \cdot \mathbf{1} \Phi_i\left(\frac{L}{2}\right) + \mathbf{F}_R \cdot \mathbf{1} \Phi_i(L_E), \quad (5.78)$$

where $\mathbf{r}_E = \mathbf{r}_P(z = L_E)$ is the position vector from the origin point O to the resistance force application point E . The length from the origin point O to the resistance force application point E , L_E , is calculated as

$$L_E = L - \frac{z_T}{2 \cos q_1}. \quad (5.79)$$

The immersed depth z_T , the vertical component of the position vector of the end point T , is calculated by Eq. (5.70) as $z_T = \mathbf{r}_P(z = L) \cdot \mathbf{k}_0$. The resistance force \mathbf{F}_R is also calculated by Eqs. (3.6), (3.8), and (3.9). The dynamic frictional force \mathbf{F}_d is

$$\begin{aligned} \mathbf{F}_d &= -\mathbf{v}_E \eta_d \rho_g A_r |\mathbf{v}_E| \\ &= -\eta_d \rho_g A_r \left[\left(\sum_{i=1}^n \left(\Phi_i(L_E) \dot{q}_{1+i} \cos q_1 - \Phi_i(L_E) q_{1+i} \dot{q}_1 \sin q_1 \right) + (L_{RB} + L_E) \dot{q}_1 \cos q_1 \right)^2 + \right. \\ &\quad \left. \left(- \sum_{i=1}^n \left(\Phi_i(L_E) \dot{q}_{1+i} \sin q_1 + \Phi_i(L_E) q_{1+i} \dot{q}_1 \cos q_1 \right) - (L_{RB} + L_E) \dot{q}_1 \sin q_1 \right)^2 \right]^{0.5} \\ &\quad \left[\left(+ \sum_{i=1}^n \left(\Phi_i(L_E) \dot{q}_{1+i} \cos q_1 - \Phi_i(L_E) q_{1+i} \dot{q}_1 \sin q_1 \right) + (L_{RB} + L_E) \dot{q}_1 \cos q_1 \right) \mathbf{1}_0 + \right. \\ &\quad \left. \left(- \sum_{i=1}^n \left(\Phi_i(L_E) \dot{q}_{1+i} \sin q_1 + \Phi_i(L_E) q_{1+i} \dot{q}_1 \cos q_1 \right) - (L_{RB} + L_E) \dot{q}_1 \sin q_1 \right) \mathbf{k}_0 \right], \quad (5.80) \end{aligned}$$

where the velocity vector \mathbf{v}_E is the velocity of the resistance force acting point E and this vector calculated by Eq. (5.42) as $\mathbf{v}_E = \mathbf{v}_P(z = L_E)$. The reference area A_r is represented as

$$A_r = \frac{d_c z_T}{\cos q_1}. \quad (5.81)$$

The horizontal and vertical static resistance forces, \mathbf{F}_{sh} and \mathbf{F}_{vh} , are

$$\mathbf{F}_{sh} = -\text{sign} \left[\sum_{i=1}^n \left(\Phi_i(L_E) \dot{q}_{1+i} \cos q_1 - \Phi_i(L_E) q_{1+i} \dot{q}_1 \sin q_1 \right) + (L_{RB} + L_E) \dot{q}_1 \cos q_1 \right] \eta_h g \rho_g z_T^2 d_c \mathbf{1}_0, \quad (5.82)$$

$$\mathbf{F}_{sv} = -\text{sign} \left[- \sum_{i=1}^n \left(\Phi_i(L_E) \dot{q}_{1+i} \sin q_1 + \Phi_i(L_E) q_{1+i} \dot{q}_1 \cos q_1 \right) - (L_{RB} + L_E) \dot{q}_1 \sin q_1 \right] \eta_v \left(\frac{z_T}{d_c} \right)^\lambda g \rho_g V \mathbf{k}_0, \quad (5.83)$$

where the immersed volume V is calculated as

$$V = \frac{\pi d_c^2}{4} \frac{z_T}{\cos q_1}. \quad (5.84)$$

The resistance force \mathbf{F}_R , the sum of the dynamic frictional force vector \mathbf{F}_d and the static resistance force vector \mathbf{F}_s , is represented as the sum of Eqs. (5.80), (5.82), and (5.83).

5.2.5 Simulation results of the cantilevered elastic compound pendulum

Figures 5.15, 5.16, 5.17, 5.18, 5.19, 5.20, 5.21, and 5.22 show the simulation results for the cantilevered elastic compound pendulum shown in Fig. 5.8. The dimensions applied to this simulation are the same as those applied for the simulation of the rigid compound pendulum. The flexural rigidity $EI = 15.1642 \text{ N m}^2$ are utilized and the other parameters are the same as those of the previous simulation. The simulations are performed for different

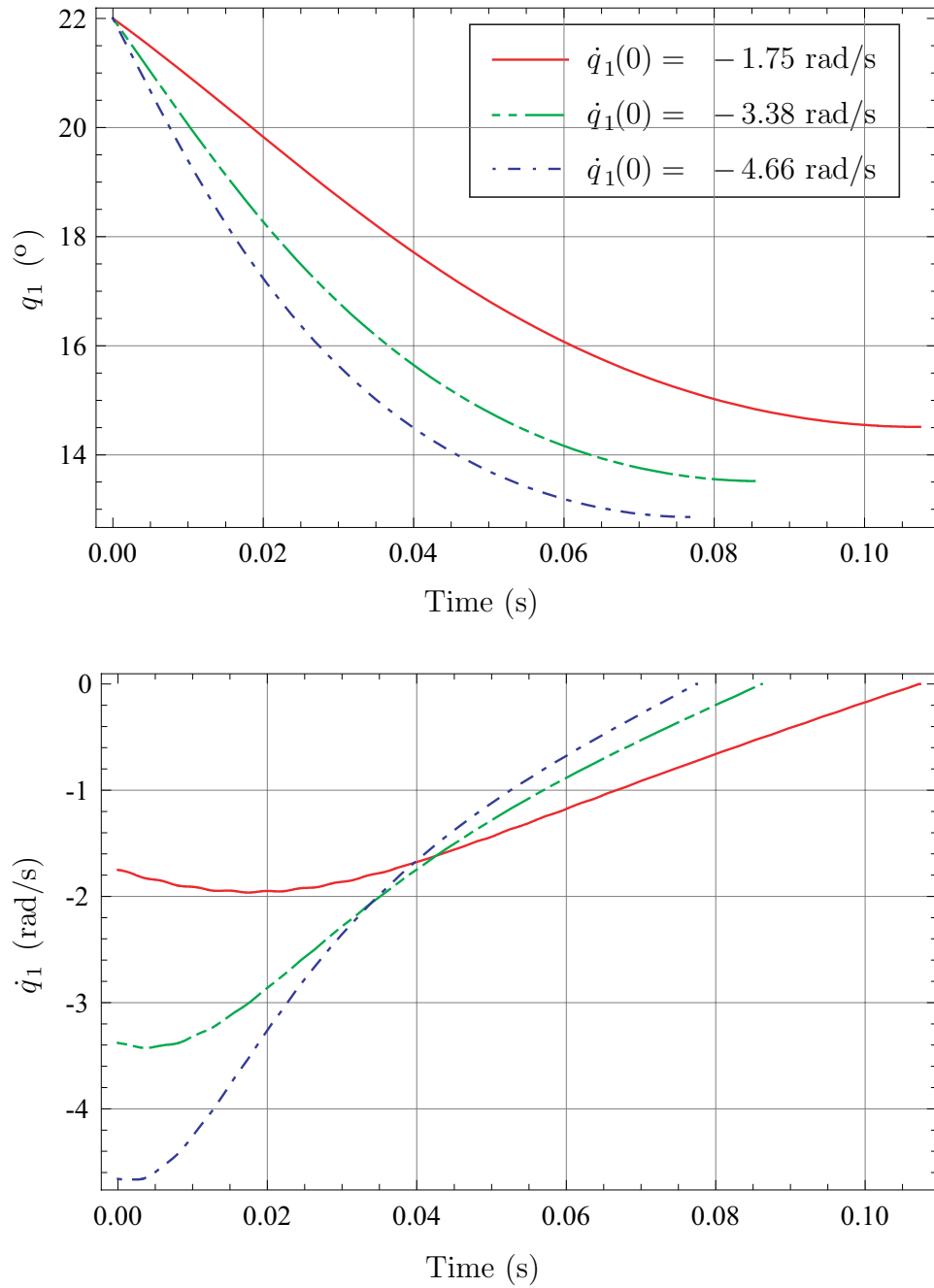


Figure 5.15: Angle q_1 and angular velocity \dot{q}_1 results of the cantilevered elastic compound pendulum for $q_1(0) = 22^\circ$ and $\dot{q}_1(0) = -1.75, -3.38, -4.66$ rad/s

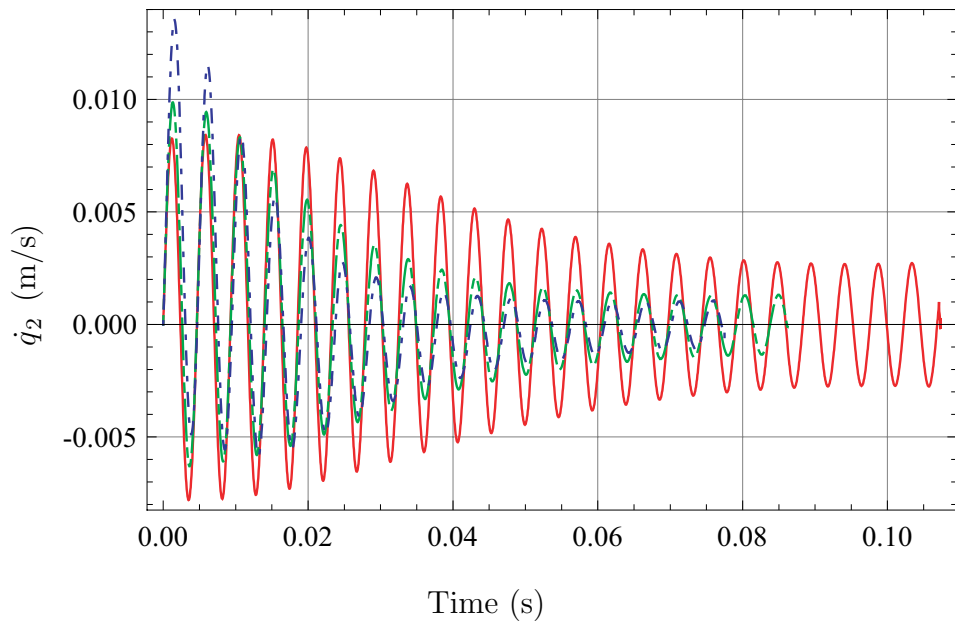
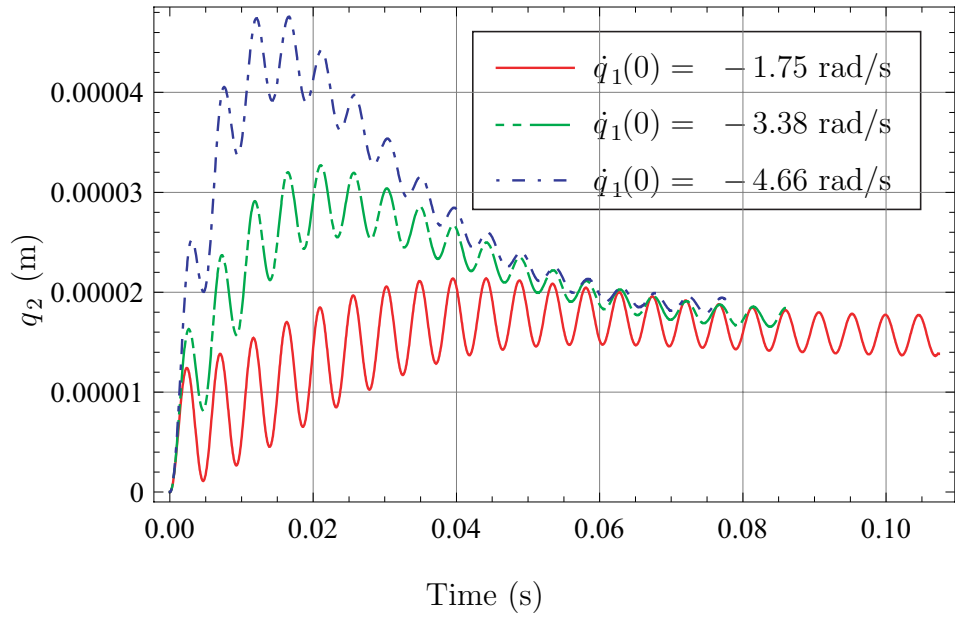


Figure 5.16: Displacement q_2 and velocity \dot{q}_2 results of the cantilevered elastic compound pendulum for $q_1(0) = 22^\circ$ and $\dot{q}_1(0) = -1.75, -3.38, -4.66$ rad/s

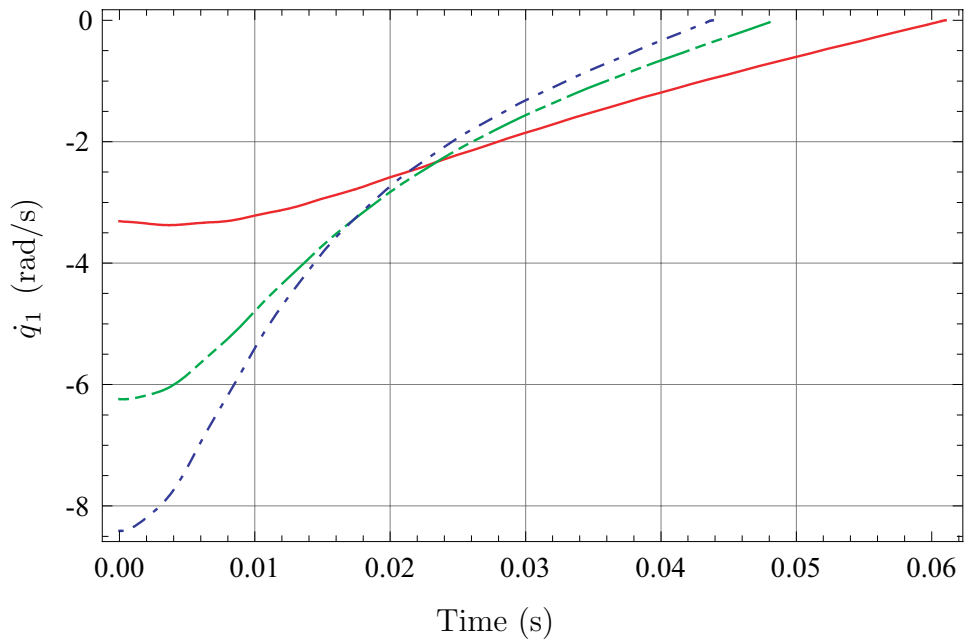
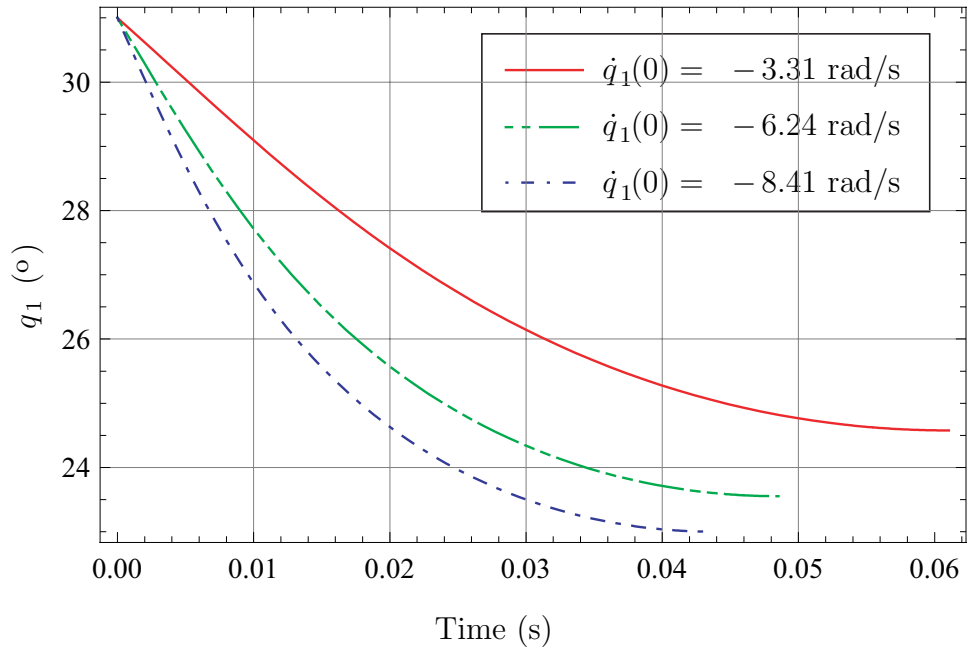


Figure 5.17: Angle q_1 and angular velocity \dot{q}_1 results of the cantilevered elastic compound pendulum for $q_1(0) = 31^\circ$ and $\dot{q}_1(0) = -3.31, -6.24, -8.41$ rad/s

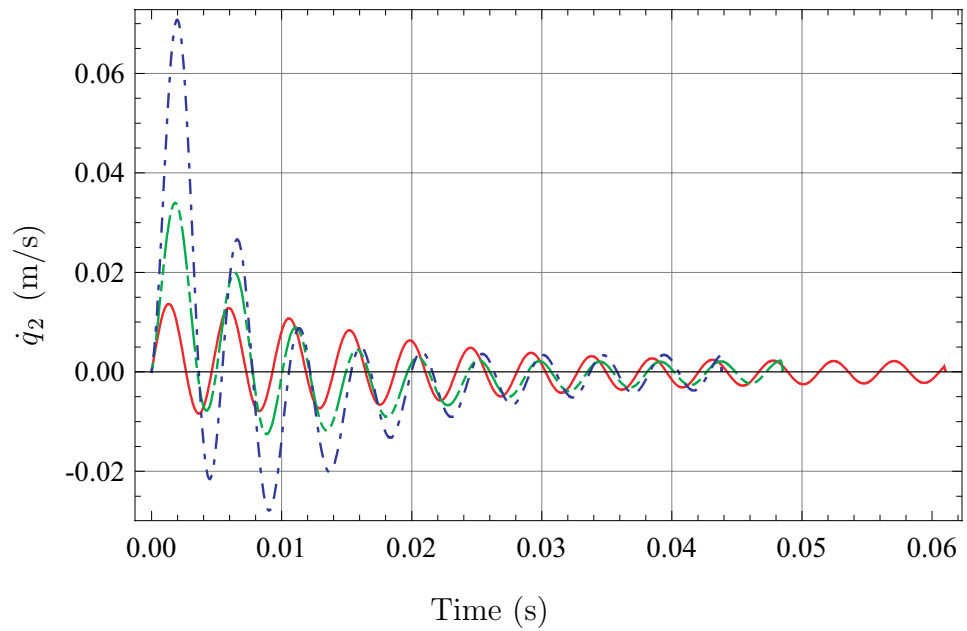
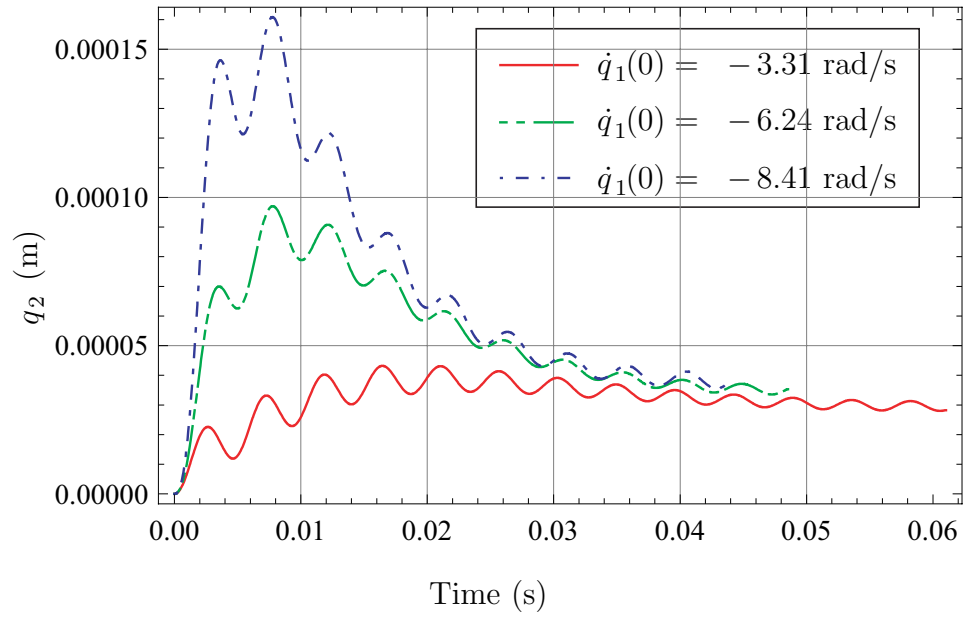


Figure 5.18: Displacement q_2 and velocity \dot{q}_2 results of the cantilevered elastic compound pendulum for $q_1(0) = 31^\circ$ and $\dot{q}_1(0) = -3.31, -6.24, -8.41$ rad/s

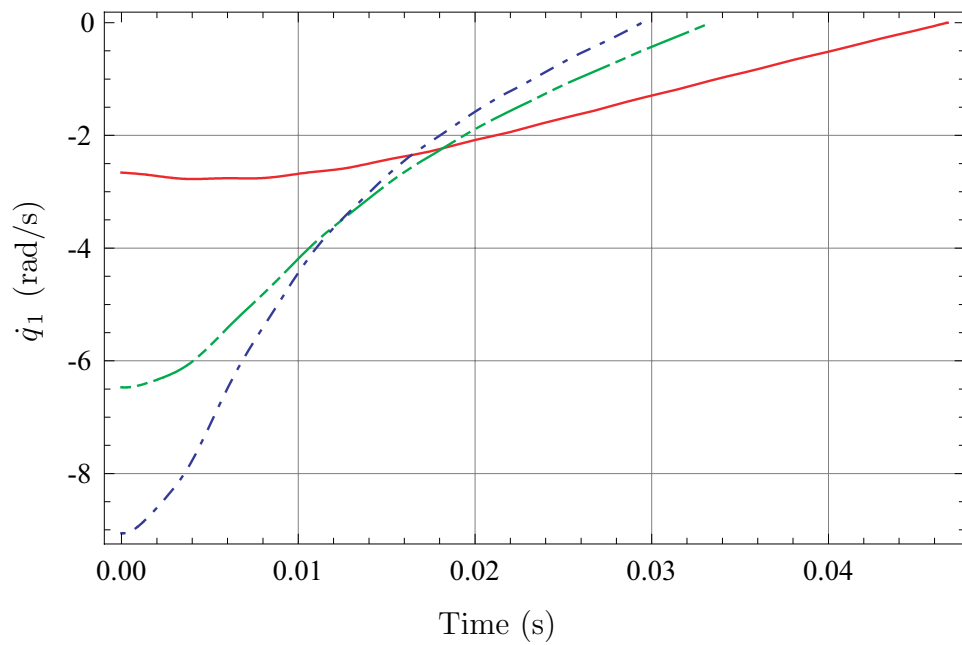
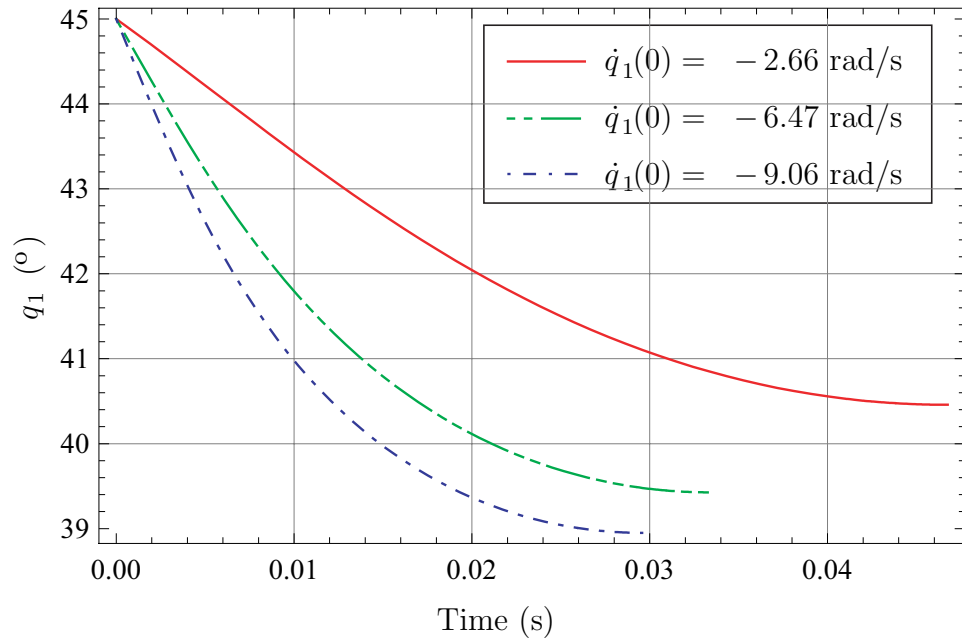


Figure 5.19: Angle q_1 and angular velocity \dot{q}_1 results of the cantilevered elastic compound pendulum for $q_1(0) = 45^\circ$ and $\dot{q}_1(0) = -2.66, -6.47, -9.06$ rad/s

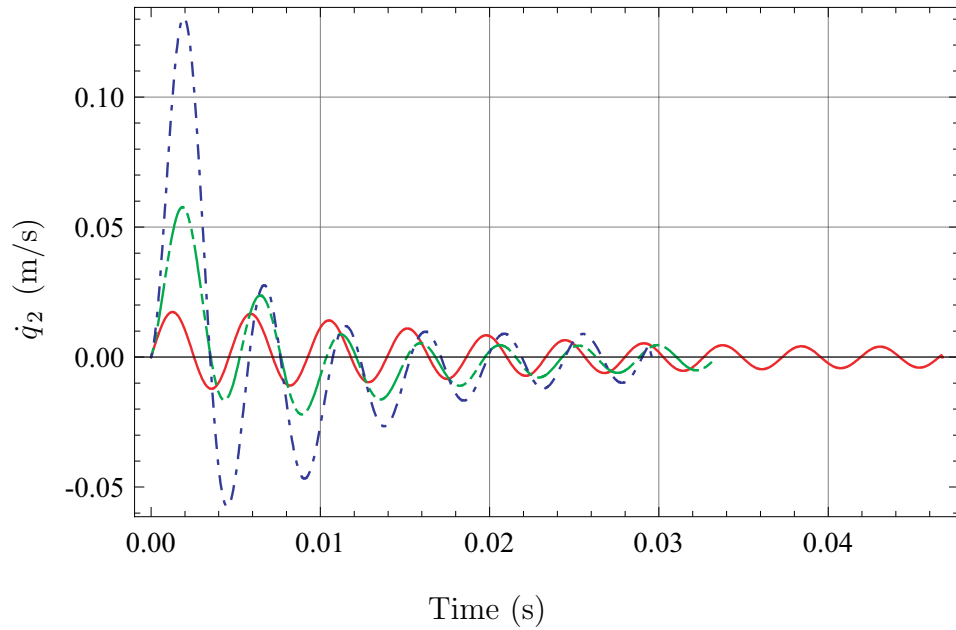
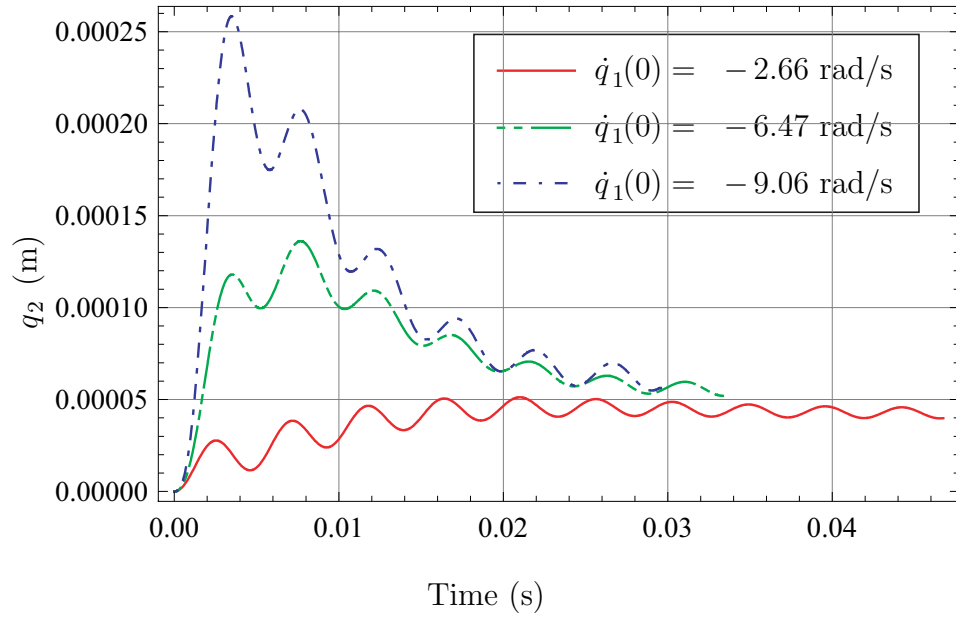


Figure 5.20: Displacement q_2 and velocity \dot{q}_2 results of the cantilevered elastic compound pendulum for $q_1(0) = 45^\circ$ and $\dot{q}_1(0) = -2.66, -6.47, -9.06$ rad/s

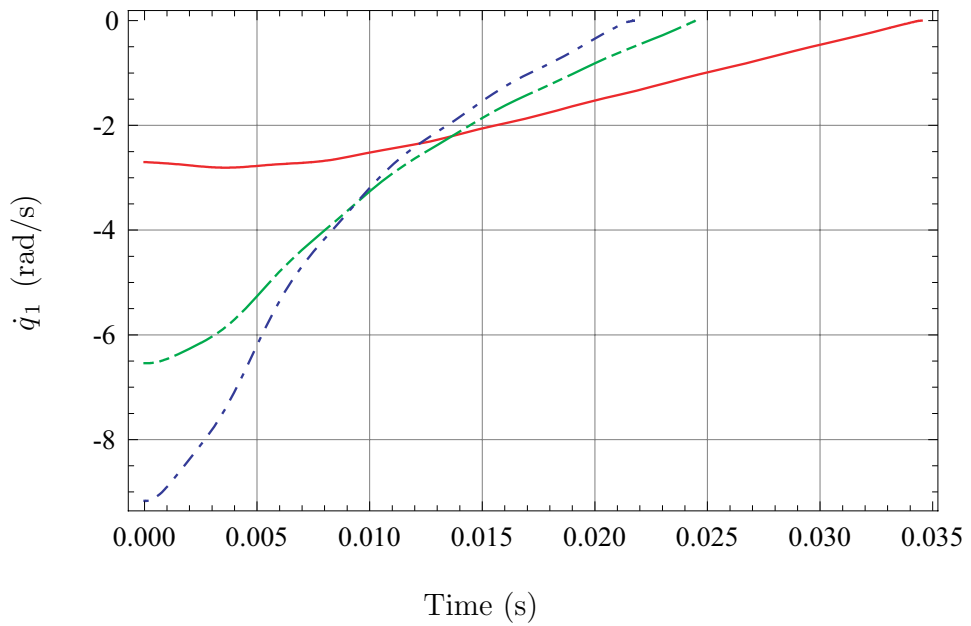
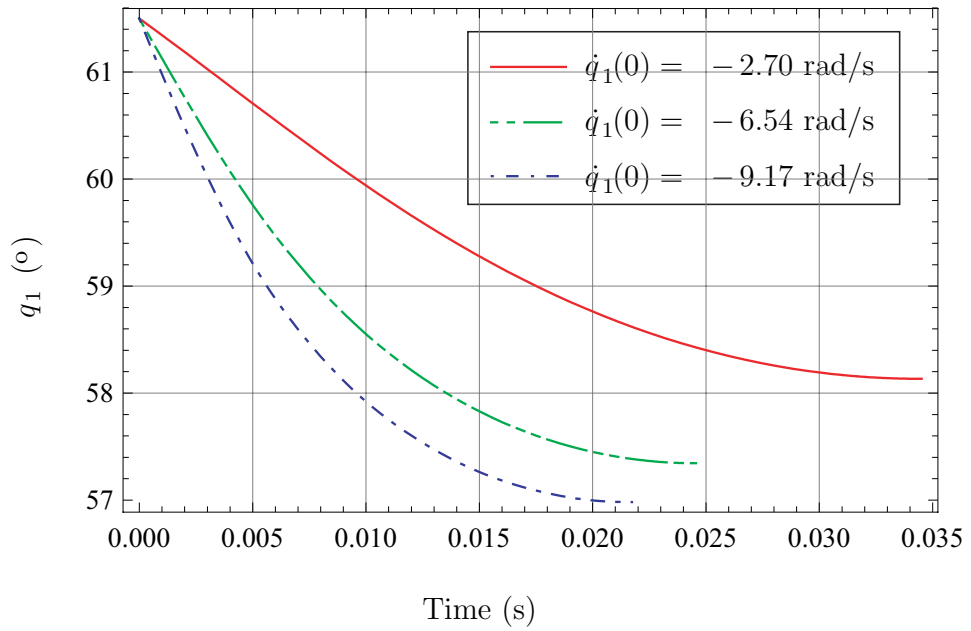


Figure 5.21: Angle q_1 and angular velocity \dot{q}_1 results of the cantilevered elastic compound pendulum for $q_1(0) = 61.5^\circ$ and $\dot{q}_1(0) = -2.70, -6.54, -9.17$ rad/s

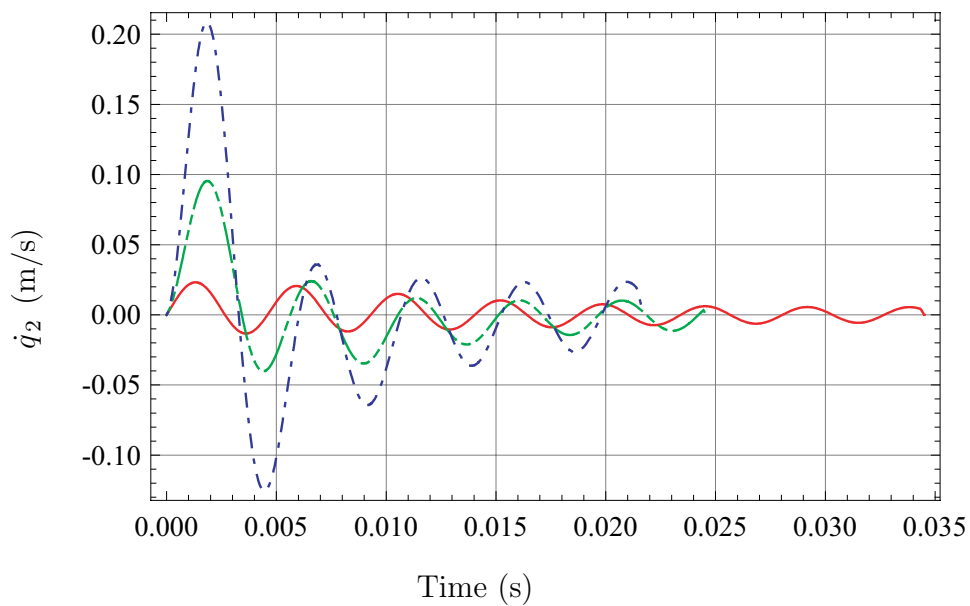
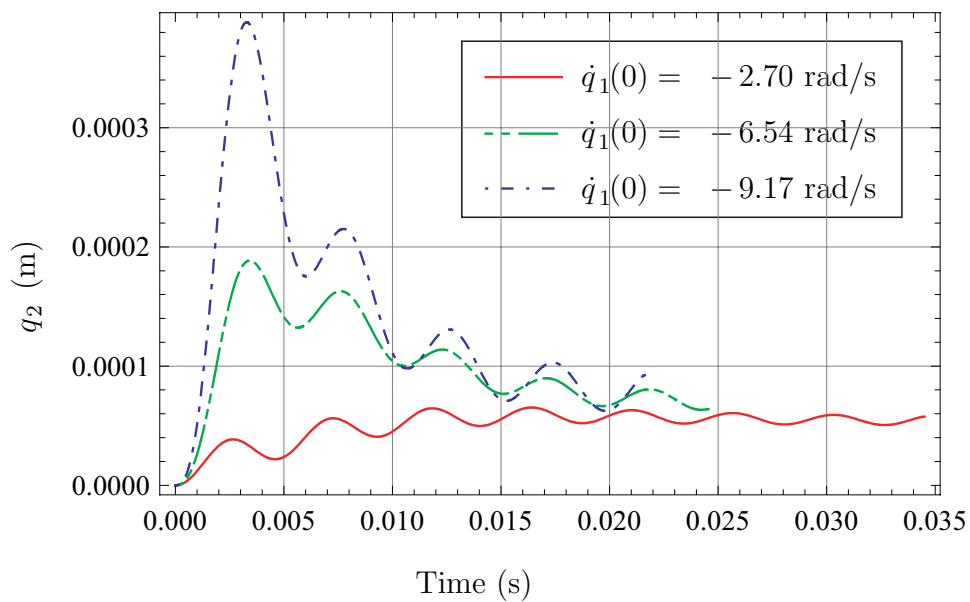


Figure 5.22: Displacement q_2 and velocity \dot{q}_2 results of the cantilevered elastic compound pendulum for $q_1(0) = 61.5^\circ$ and $\dot{q}_1(0) = -2.70, -6.54, -9.17$ rad/s

impact angles and different initial impact angular velocities ($\dot{q}(0) = -1.75, -3.38, \text{ and } -4.66$ rad/s for $q(0) = 22^\circ$, $\dot{q}(0) = -3.31, -6.24, \text{ and } -8.41$ rad/s for $q(0) = 31^\circ$, $\dot{q}(0) = -2.66, -6.47, \text{ and } -9.06$ rad/s for $q(0) = 45^\circ$, and $\dot{q}(0) = -2.70, -6.54, \text{ and } -9.17$ rad/s for $q(0)$ is 61.5°). from the impact moment until the angular velocity of the pendulum, \dot{q}_1 , becomes zero and the first mode of the shape function of Eq. (5.50) is only considered ($\lambda_1=1.8751$). As shown in Figs. 5.15, 5.17, 5.19, and 5.21, the pendulum stops more quickly when the pendulum impacts the granular medium with high velocity. The results that the faster the impact velocity becomes the sooner the compound pendulum stops are kept in the impact of the cantilevered elastic compound pendulum. The generalized coordinate q_2 showing the deformation of the pendulum becomes large when the initial impact velocity and angle increase as shown in Figs. 5.16, 5.18, 5.20, and 5.22. Table 5.5 shows the stopping time results for the rigid model, $t_{s,r}$, and the elastic model, $t_{s,e}$, and we do not observe much

Table 5.5: Stopping time of the cantilevered elastic compound pendulum and the rigid one

$q_1(0)$ ($^\circ$)	$\dot{q}_1(0)$ (rad/s)	$t_{s,r}$ (s)	$t_{s,e}$ (s)
22	-1.75	0.107212	0.107366
	-3.38	0.0861789	0.0861761
	-4.66	0.0775028	0.0774967
31	-3.31	0.0609829	0.0610354
	-6.24	0.0485081	0.0485343
	-8.41	0.043819	0.0438373
45	-2.66	0.046688	0.046748
	-6.47	0.0333638	0.0333414
	-9.06	0.0295578	0.029574
61.5	-2.70	0.0343956	0.0345101
	-6.54	0.0245294	0.0245555
	-9.17	0.0216994	0.021729

difference between the rigid model and the flexible model for our particular system. The elastic deformations of the cantilever elastic compound pendulum will be important for longer and more elastic links.

CHAPTER 6

EXPERIMENTS

In this chapter, the experimental system is introduced and the experimental results are represented. These results are compared with the results of the simulation. As experimental models, the vertical impact of a rigid cylinder type free link and the impact of a rigid compound pendulum are utilized. The data attained from the repeated experiments are averaged to minimize the effects of abnormalities such as fluctuation phenomenon which can occur during the experiments. The resistance force coefficients are calculated by the part of the experimental data.

6.1 Experimental system

Figures 6.1 and 6.2 show a free link and a compound pendulum. These two mechanical systems will be used for the experiments. For the free link shown in Fig. 6.1, the following dimensions are given: the length $L = 0.01524$ m and the diameter $d_c = 0.00635$ m. The density of the link is 7.7×10^3 kg/m³. The infra red (I.R.) markers are located at $0.1L$ and $0.5L$ as shown in Fig. 6.1. For the compound pendulum shown in Fig. 6.2, the following dimensions are given: the length $L_{p_1} = 0.019812$ m, $L_{p_2} = 0.01524$ m, $L_{p_3} = 0.23876$ m, the diameter $d_{p_1} = 0.01905$ m, $d_{p_2} = 0.01524$ m, and $d_{p_3} = 0.00635$ m. The density of the pendulum is 7.7×10^3 kg/m³. Two I.R. markers are located on the rotational joint point and the center of the L_{p_3} . In this study, as the motion capturing system to measure and digitize the position of the impact objects, Northern Digital Inc. (NDI) optotrak 3020 system is used. This system is composed of a position sensor, a control unit, a strober, I.R. markers, and a PC as shown in Fig. 6.3. The system can measure the position of the markers within the RMS accuracy of 0.1 mm and can track up to 256 markers simultaneously with

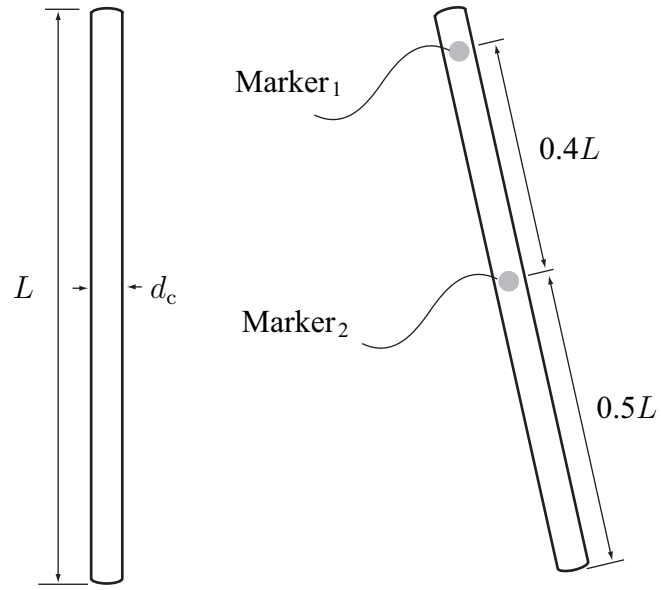


Figure 6.1: Free link applied for experiments

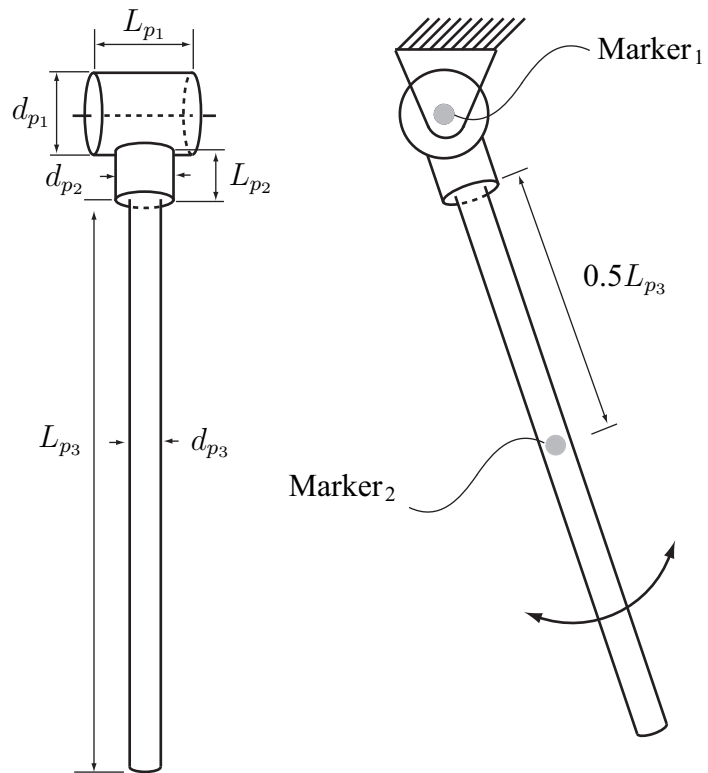


Figure 6.2: Compound pendulum applied for experiments

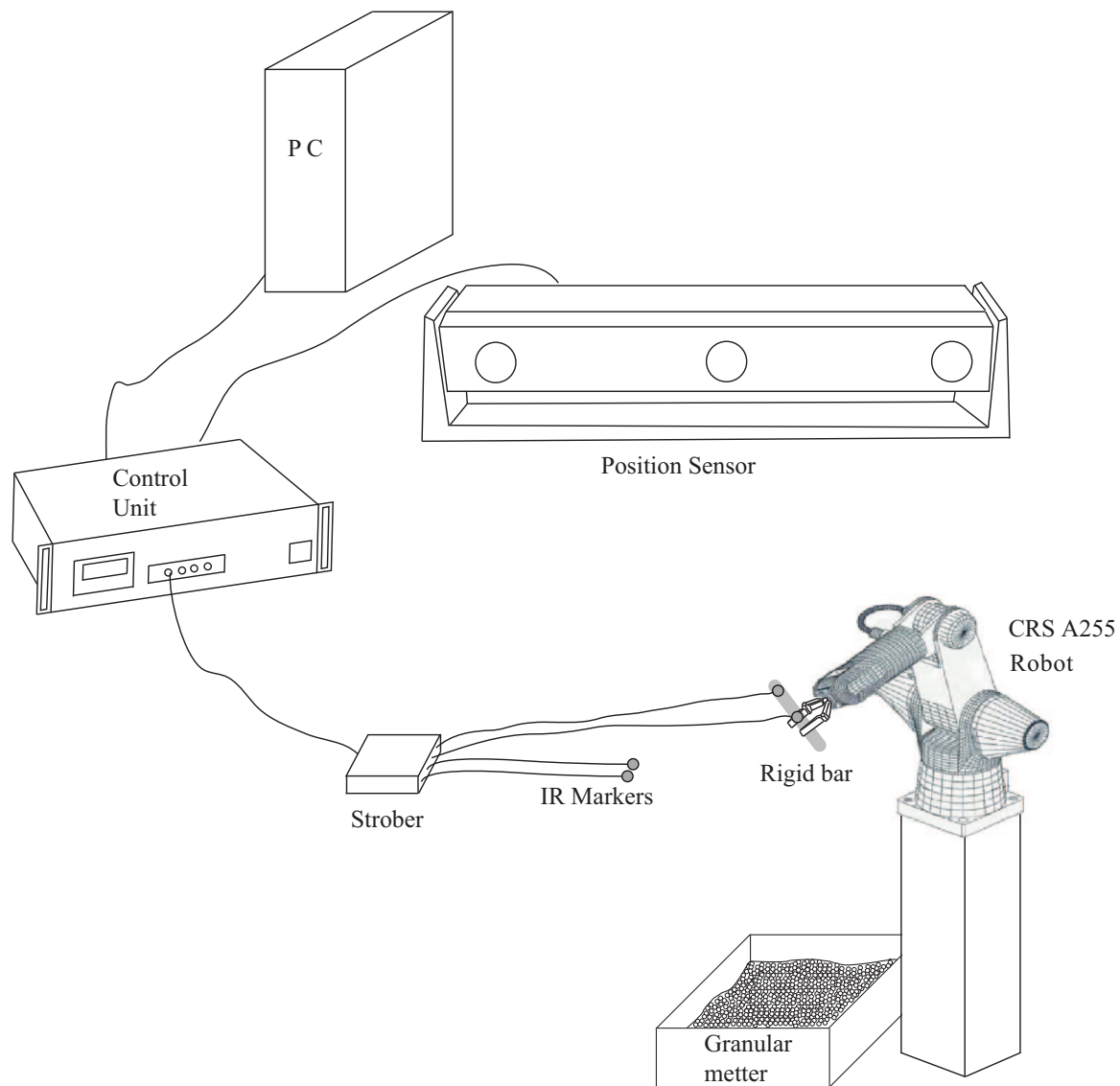


Figure 6.3: Motion measurement system Optotrak 3020

a sample up to 3500 markers/s [68]. The system does not require a calibration process. The motions of the free link and the compound pendulum are recorded using the two I.R. markers. The position sensor captures the position of the I.R. markers attached to the bodies at constant sample rates and measured 3D position data. The PC is used for operating software controlling the hardware system, saving and transform the measured data. In the experiments, the positions were measured with 3D data cartesian coordinate system at 500 frames/s.

There exist so many kinds of granular materials. Grains such as rice, soils including sand, and artificial granules such as fertilizer, glass beads, and ball bearings. The applied density of a granular medium for the simulations, ρ_g , is $2.5 \times 10^3 \text{ kg/m}^3$. The numerical value of the density is originated from the physical property of the granular medium, “Play sand” (Quikrete 1113-51) utilized in the impact experiments. The resistance force coefficients are: the dynamic frictional force coefficient $\eta_d = 6.5$, the horizontal static resistance force coefficient $\eta_h = 8$, and the vertical static resistance force coefficients $\eta_v = 22$ and $\lambda = 1.1$. These coefficients were determined from experimental data. The gravitational acceleration g is applied as 9.81 m/s^2 . The field of the low speed impact with a granular medium is related with developing multi-body kinematic chain system such as multi legged robots for surveillance or carrying and these systems cannot avoid slow impact with diversified outfield granular materials including soil and sand. From this view points, the sand is considered more appropriate and beneficial than glass beads or other artificial granular medium. The dimension of impact test box is $0.45 \text{ m} \times 0.32 \text{ m} \times 0.09 \text{ m}$ (W×L×H) and the height of the sand in the test bed is 0.075 m .

6.2 Experimental results

6.2.1 Impact of a free link

Figures 6.4, 6.5, and 6.6 represent the experimental and the simulation results for the impact of the free link shown in Figs. 6.1 and 4.9 for different impact angles and different

initial impact velocities ($\dot{q}_z(0) = 1.53, 2.06, \text{ and } 2.47 \text{ m/s}$ for $q(0) = 0^\circ$, $\dot{q}_z(0) = 1.26, 1.87, \text{ and } 2.33 \text{ m/s}$ for $q(0) = 32^\circ$, and $\dot{q}_z(0) = 1.45, 1.98, \text{ and } 2.43 \text{ m/s}$ for $q(0) = 55^\circ$) from the impact moment until the vertical velocity of the link end T , v_{T_z} , becomes zero. Thick lines show the results of experiments and black lines represent the simulation results. The simulation is performed based on the resistance force coefficients determined from the experimental results.

The penetrating depth of the link end T into the granular matter, z_T , is increasing with the initial velocity for all the cases as shown in Figs. 6.4, 6.5, and 6.6. However the stopping time into the granular matter is decreasing when the initial velocity is increasing as most simulation results represented in chapter 4 and 5. In these experiment and simulation, the stopping time is defined as the time period starting with the moment of impact and ending when the vertical velocity of the end T into the granular matter is zero.

Even though there are differences between the simulation and the experimental results, the tendency of the stopping time and the penetrating depth are not changed. In this study, a relative error [67] was calculated in order to compare the simulation and the experimental results. The relative error of between the simulation and the experimental results, γ , is defined as

$$\gamma = \left| \frac{q_E - q_S}{q_E} \right| \times 100, \quad (6.1)$$

where q_E and q_S mean a position result of experiments and simulations respectively. In the impact experiments of the link, q_E is considered as the position of the end T in the vertical direction, z_T . Table 6.1 shows the difference rate of the experiments and the simulation.

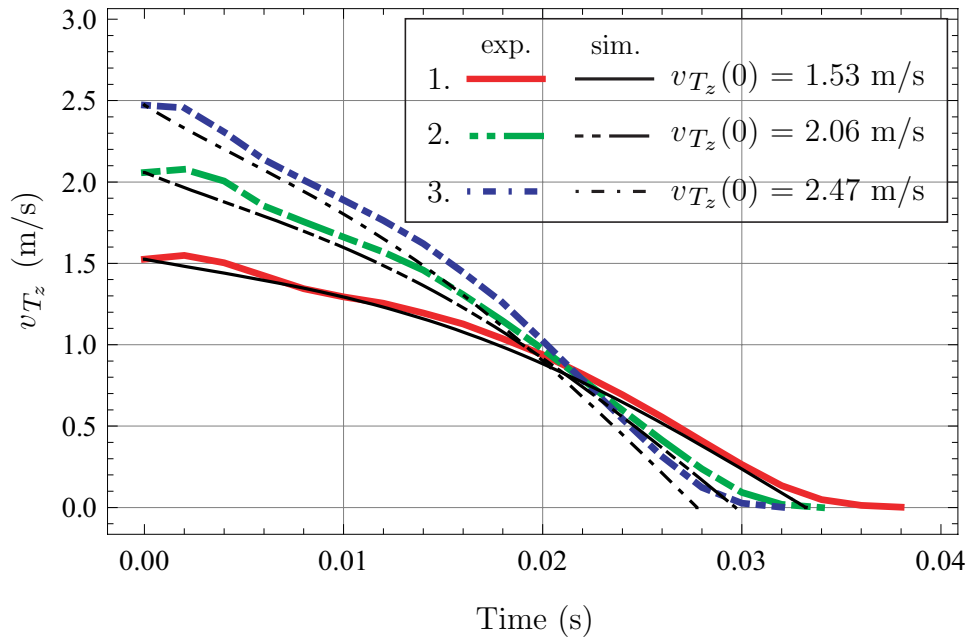
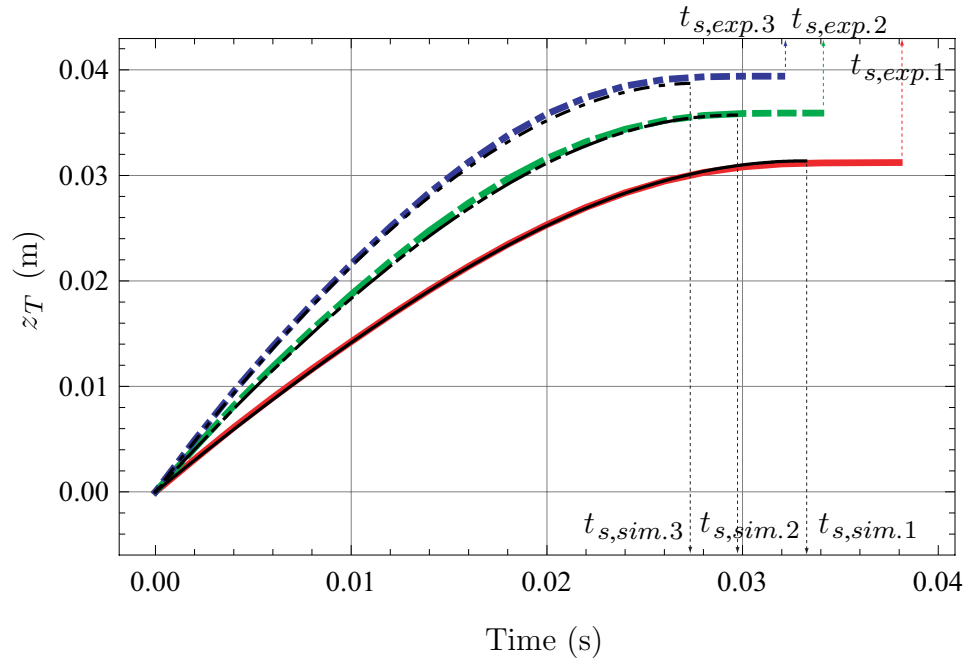


Figure 6.4: Experimental and simulation results of the cylinder type rigid link for $q(0) = 0^\circ$

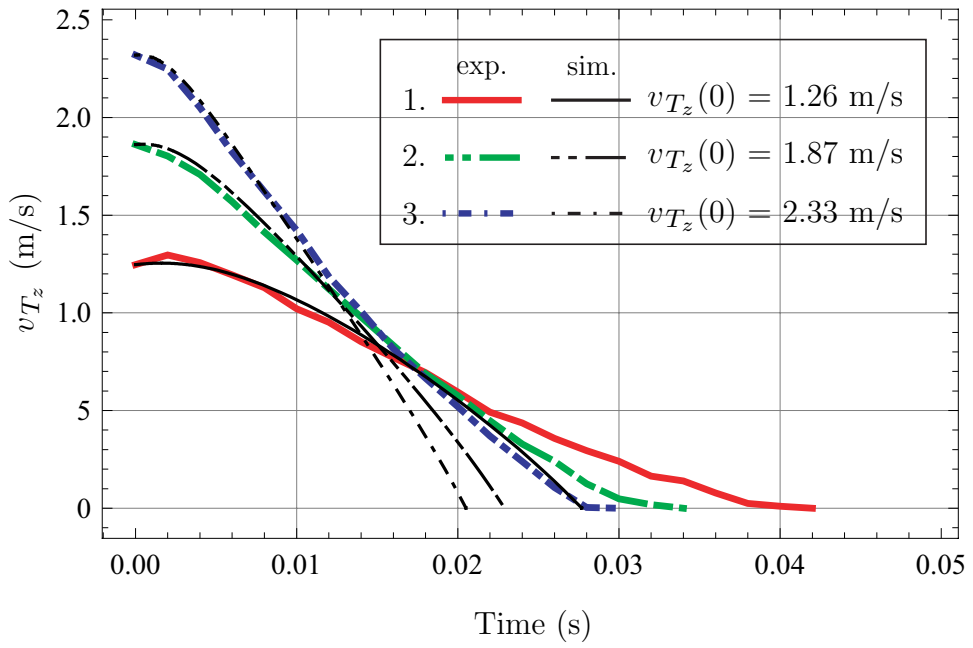
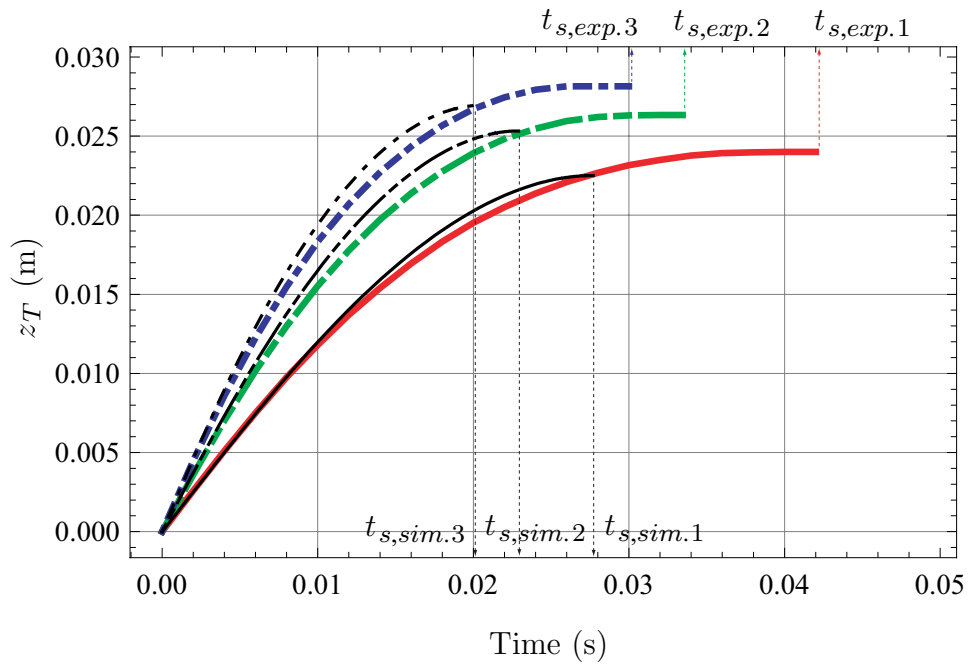


Figure 6.5: Experimental and simulation results of the cylinder type rigid link for $q(0) = 32^\circ$

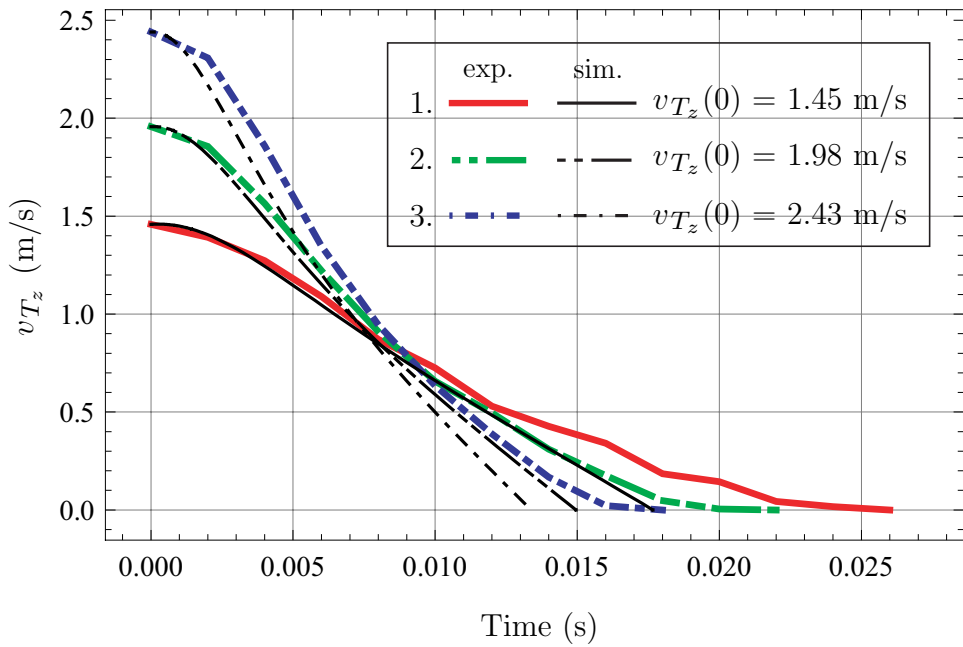
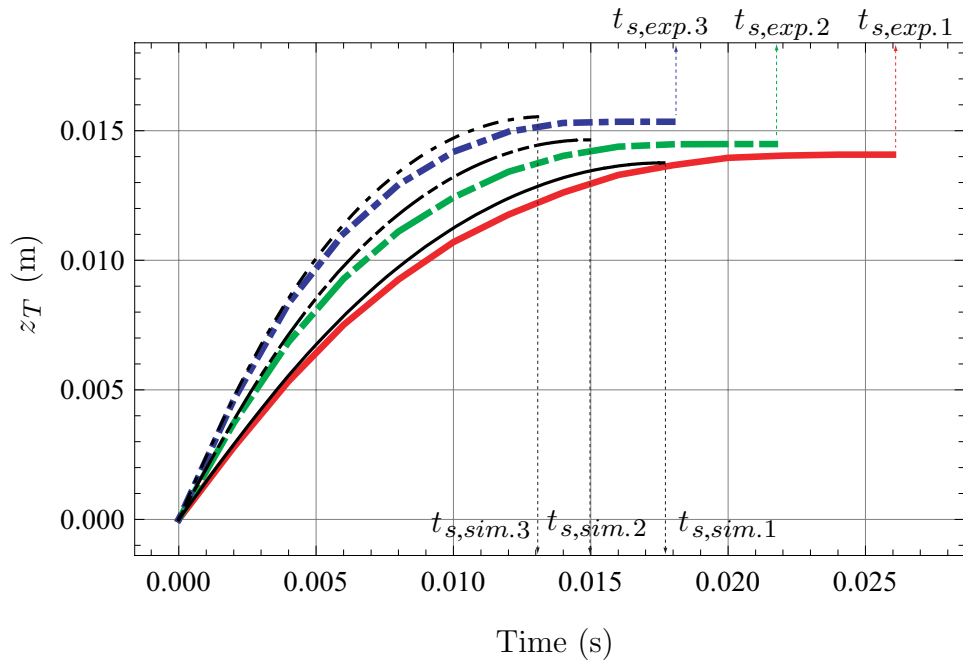


Figure 6.6: Experimental and simulation results of the cylinder type rigid link for $q(0) = 55^\circ$

Table 6.1: Relative error between the experimental and the simulation results of the free link

Impact angle ($^{\circ}$)	$v_{T_z}(0)$ (m/s)	γ (%)
0	1.53	0.52
	2.06	0.54
	2.47	1.68
32	1.26	6.19
	1.87	3.85
	2.33	4.28
55	1.45	2.25
	1.98	1.10
	2.43	1.32

6.2.2 Impact of a rigid compound pendulum

Figures 6.7, 6.8, 6.9, and 6.10 represent the penetrating angle q and the angular velocity \dot{q} of the experimental and the simulation results for the impact of the compound pendulum shown in Figs. 6.2–4.16. The experiments and the simulations are performed for different impact angles and different initial impact angular velocities ($\dot{q}(0) = -1.75, -3.38, \text{ and } -4.66$ rad/s for $q(0) = 22^{\circ}$, $\dot{q}(0) = -3.31, -6.24, \text{ and } -8.41$ rad/s for $q(0) = 31^{\circ}$, $\dot{q}(0) = -2.66, -6.47, \text{ and } -9.06$ rad/s for $q(0) \approx 45^{\circ}$, and $\dot{q}(0) = -2.70, -6.54, \text{ and } -9.17$ rad/s for $q(0)$ is 61.5°) from the impact moment until the angular velocity of the pendulum, \dot{q} , becomes zero. Thick lines show the results of experiments and black lines represent the simulation results. The resistance force coefficients are applied the same as those applied to the simulation of the impact of the free link.

The penetrating angle of the pendulum is increasing with the initial angular velocity for all the cases as shown in Figs. 6.7, 6.8, 6.9, and 6.10. These experimental results show also that the stopping time of the pendulum is decreasing as the results of the previous

experimental results when the initial velocity is increasing. In these experiment and simulation, the stopping time is defined as the time period starting with the moment of impact and ending when the velocity of the object into the granular matter is zero. The impact experiments and the simulation results by the compound pendulum show that the tendency of the stopping time is kept even in the case of the oblique impact with a granular medium. The phenomenon that the impact of a rigid body stops more rapidly as the initial impact velocity increases having been confirmed by the experiments and the simulation results by the impact of the free link which has initially only vertical impact velocity component is also observed in the impact process of the compound pendulum. Figure 6.11 shows the stopping time of the compound pendulum. The large markers are representing the simulation results and the small markers depict the simulation results. The stopping time decreases rapidly when the initial impact angular increases at the low angular velocity. However the decrease of the stopping time diminishes at the low angular velocity.

As shown in Figs 6.7, 6.8, 6.9, and 6.10, there are also differences between the simulation and the experimental results. Table 6.2 shows the relative errors of the experiments and the simulation. In this comparison, q_E and q_S mean a penetrating angular position results of the experiments and simulations respectively. As shown in the table 6.1 and 6.2, the penetrating end state of the simulation is almost the same as the that of the experiment even though there are some differences between the results of the stopping time.

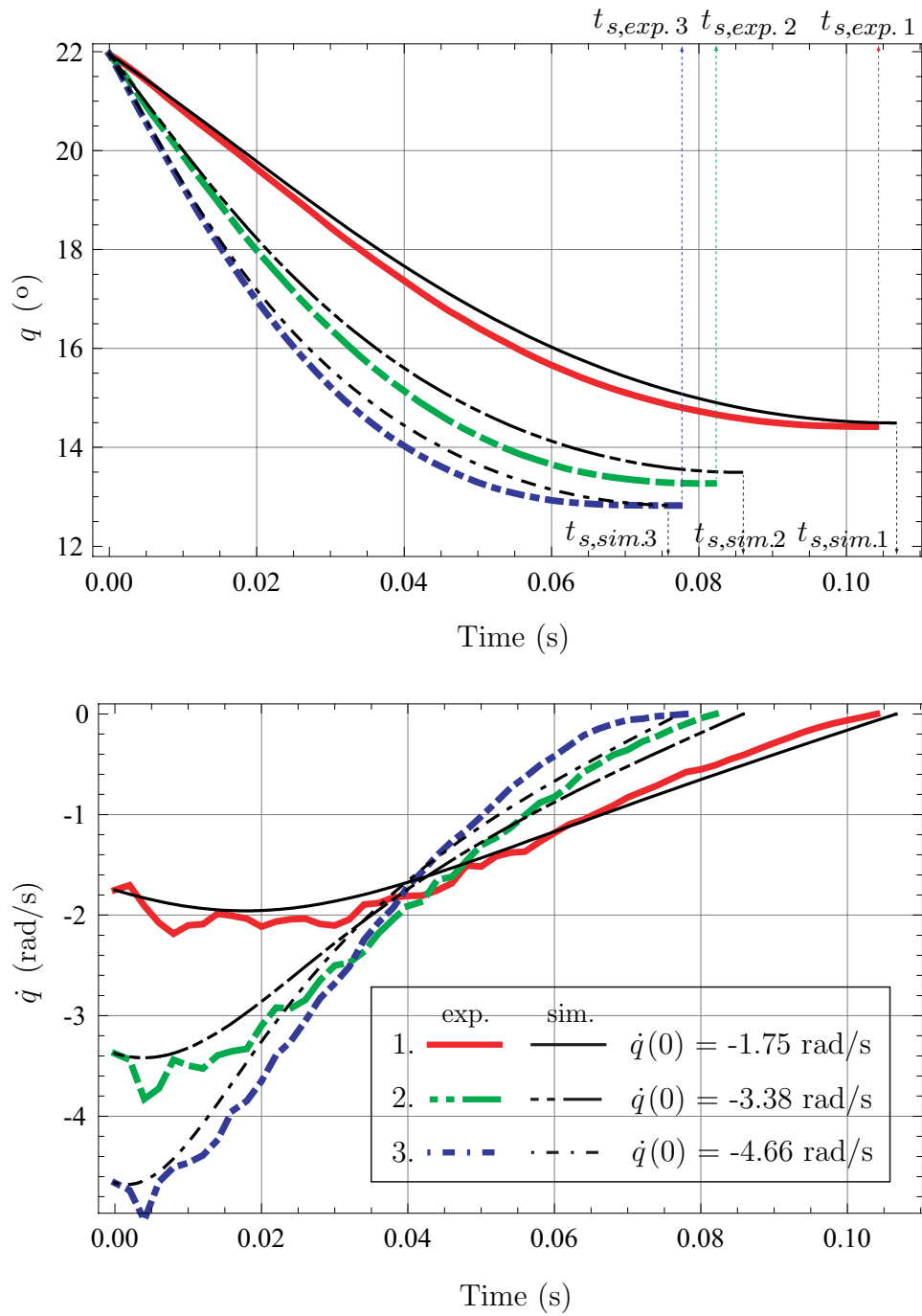


Figure 6.7: Experimental and simulation results of the compound pendulum for $q(0) = 22^\circ$

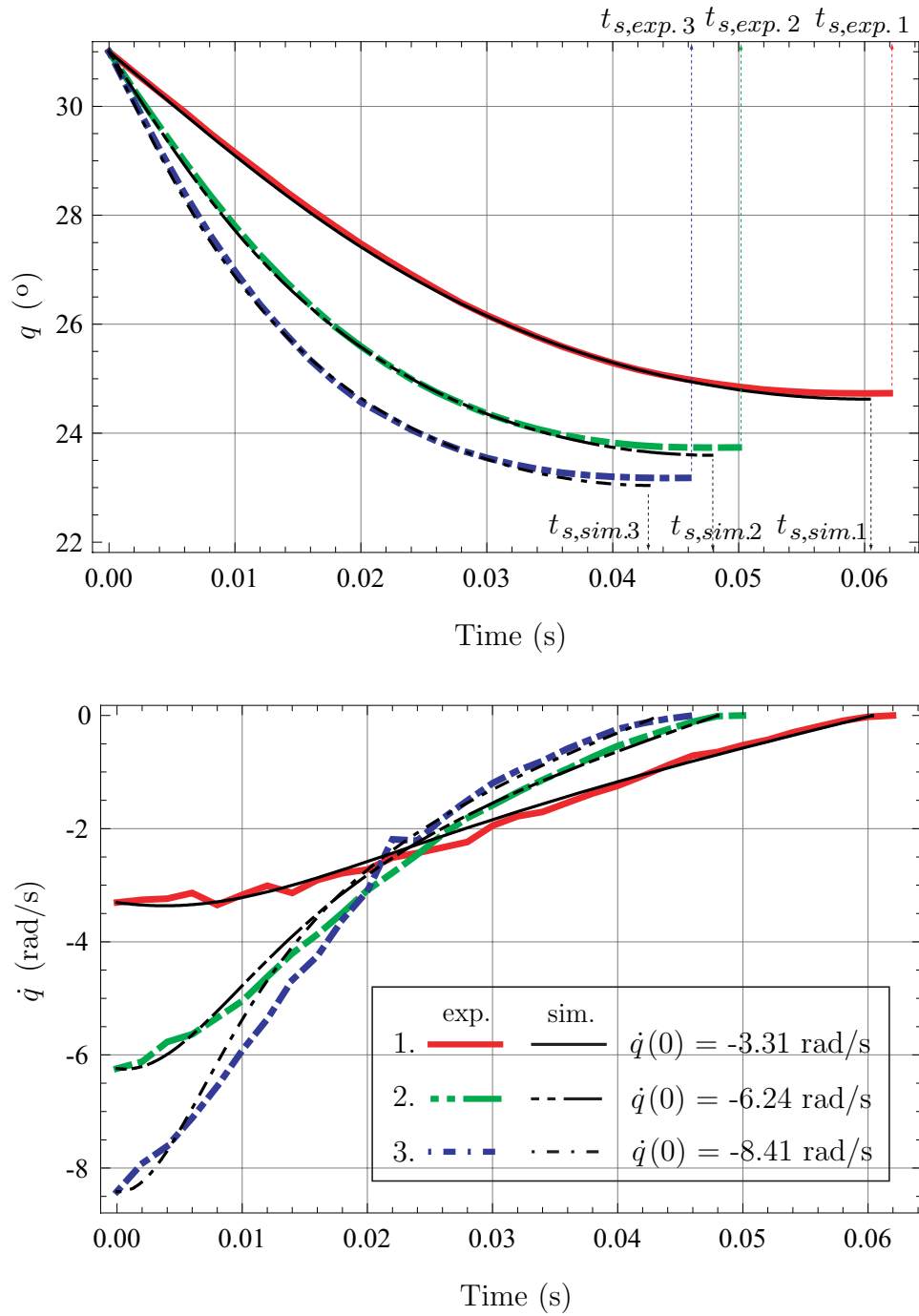


Figure 6.8: Experimental and simulation results of the compound pendulum for $q(0) = 31^\circ$

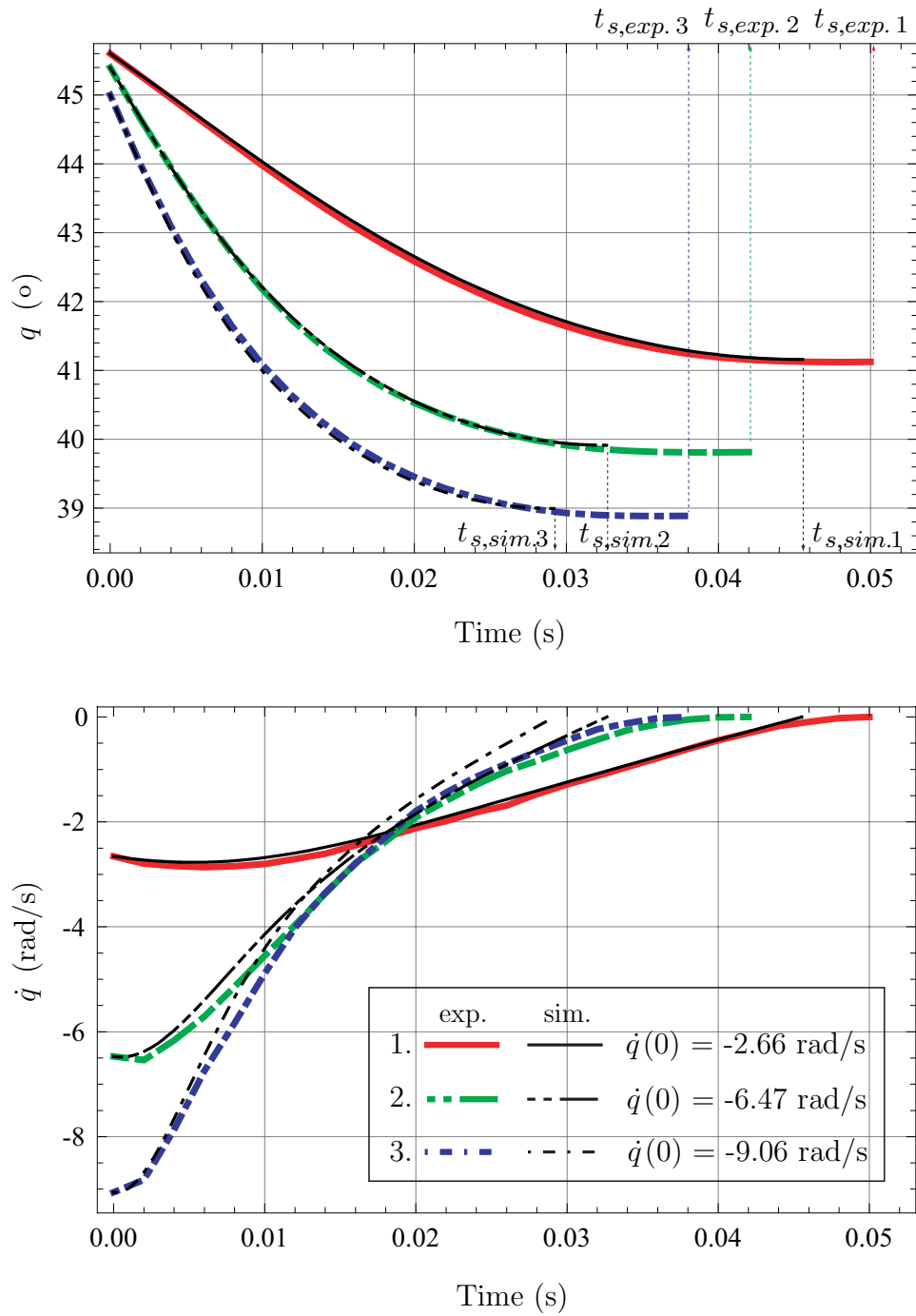


Figure 6.9: Experimental and simulation results of the compound pendulum for $q(0) \approx 45^\circ$

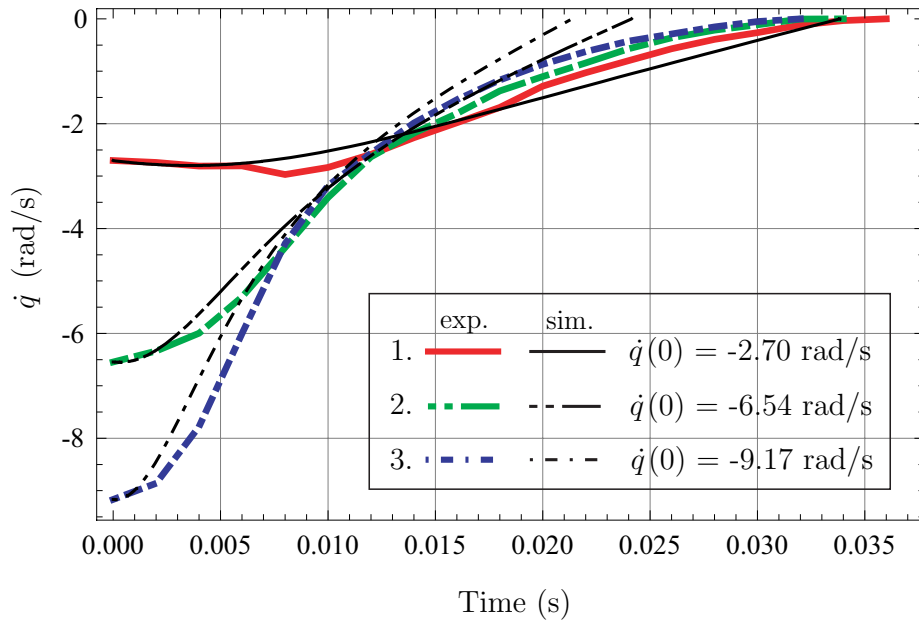
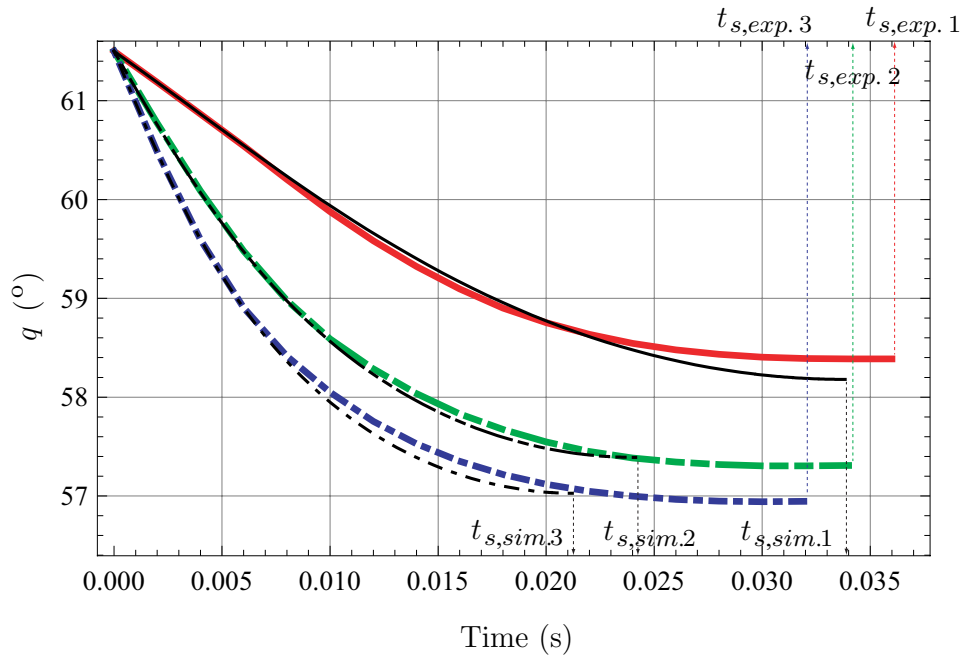


Figure 6.10: Experimental and simulation results of the compound pendulum for $q(0) = 61.5^\circ$

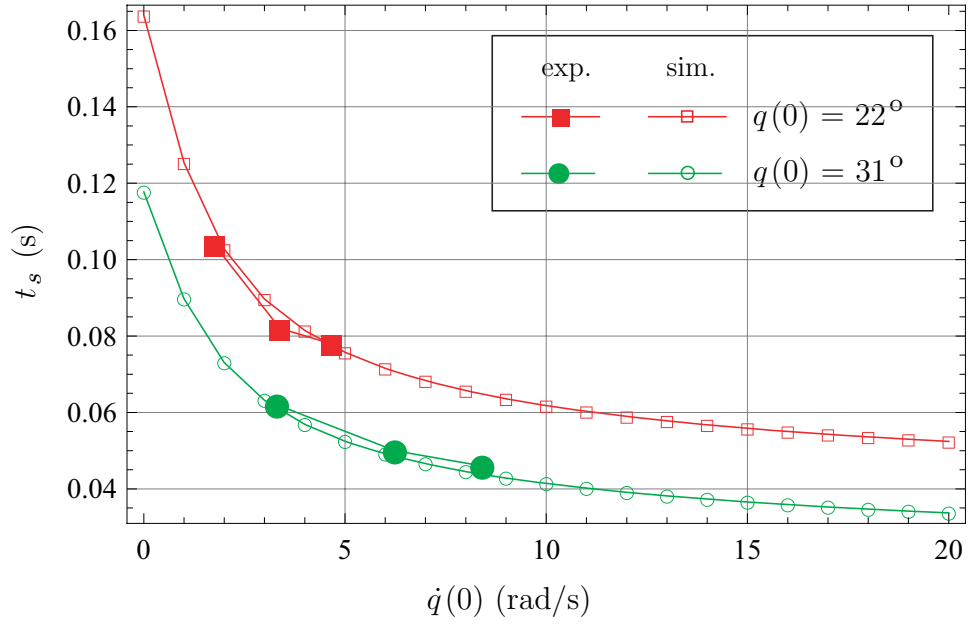


Figure 6.11: Stopping time results of the compound pendulum

Table 6.2: Relative error between the experimental and the simulation results of the compound pendulum

Impact angle ($^{\circ}$)	$q(0)$ (rad/s)	γ (%)
22	-1.75	1.00
	-3.38	2.58
	-4.66	0.02
31	-3.31	1.73
	-6.24	1.98
	-8.41	1.80
45	-2.66	0.81
	-6.47	1.82
	-9.06	1.74
61.5	-2.70	6.66
	-6.54	1.96
	-9.17	1.78

CHAPTER 7

CONCLUSION

In this study, the dynamics of the impact with a granular medium is studied. The most important force acting on the kinematic chain impacting with a granular medium is the resistance force generated by the granular medium from the impact moment until the process penetrating into the medium stops completely. Even though a granular medium is ubiquitous and the phenomenon of the impact with it takes place frequently whether artificially or naturally in industry and nature, the studies related with the low speed impact with the granular medium have not been sufficient for understanding the dynamics of the impact system compared with the field of high speed impact. Up to present, most studies are restricted to the impact of very low speed regime, to only vertical impact, or to the limited shape such as a sphere. However, it becomes possible to model the resistance force generated in a granular medium by separating the force as velocity-dependent (dynamic frictional force) and depth-dependent (static resistance force) in this study. With this approach, the problems concerning various shapes of kinematic chains, impact direction, and impact velocity can be solved as shown in chapter 4, 5, and 6.

From the one D.O.F. motion of a particle such as the mathematical pendulum of a sphere to the four D.O.F. motion of the multi impacts such as the two link kinematic chain with two impact points, the impacts of planar rigid kinematic chains are modeled, simulated, and some experimental results are presented. The simulations of the models of the mathematical pendulum and the oblique impact of a sphere are performed for the initial impact angle of 15, 45, 75° and for the various initial impact velocities. The simulation results show that the stopping time is decreasing when the initial velocity of the impact object is increasing which result had been reported in only vertical directional impact of a sphere. With these simulation results, it is confirmed that even in the oblique impact with

a granular medium the stopping time of an impacting sphere is decreasing when the initial impact velocity of the sphere is increasing. Even though the stopping time is decreasing, the penetrating distance of the sphere is increasing as the initial impact velocity is increasing for all the case of the oblique impact of the sphere including the mathematical pendulum.

As the rigid body model of a planar kinematic chain, the compound pendulum is modeled and simulated. Even though the compound pendulum has the one D.O.F, the motion of its rotating penetration is impeded by both horizontal and vertical resistance force components. The simulations performed for the initial impact angles (22, 31, 45, 61.5°) and for the initial impact angular velocities of (-1.75 ~ -9.17 rad/s) show the results that the fast the impact velocity of the pendulum is, the sooner it stops and the deeper it penetrates. This result means the impact model of a rigid body also is influenced by the initial impact velocity the same as those of the sphere.

The impact of a dropping link is simulated and observed in the vertical motion of the impact penetration for the initial impact angles (0, 32, 55°) and for the initial impact linear velocities (1.26 ~ 2.47 m/s). By the observation of the simulation from the impact moment until the velocity of the link end becomes zero, the stopping time and the penetrating depth also can be concluded as the same as those of previous impact models.

These simulation results are confirmed by the experimental results. Even though there exist differences in the stopping times between the results by the simulation and the experiments, the impact experiments of the rigid compound pendulum and the rigid free link show almost corresponding results with the simulation results. The observations of all impact model based on the their simulation results are considered as appropriate by comparing these results.

The simulation results of the impact of an elastic compound pendulum and an elastic free link exhibit the consistent results observed in rigid models. According to the observation of the simulation results, the phenomena that the decreased stopping time and the increased penetrating distance by the increased initial impact velocity happen also in elastic kinematic

chain models although small differences are observed between the elastic and the rigid models.

The consistent simulation results are observed to be kept even in the impact of multi link kinematic chain models such as the double pendulum and the two link kinematic chain with two impact points for most cases. However, in some cases the stopping time of the double pendulum models is not decreasing when the initial impact velocity is increasing. This result is considered to happen because the withdrawing motion of the rigid body of multi D.O.F. during the impact process might affect the stopping time. The stopping times are considered to increase or to decrease depending on the effects of the withdrawing motion.

Through this study, I extended the study of the low speed impacting a granular medium from the vertical direction impact to the oblique impact for the first time. For this study, the resistance forces are analyzed and the horizontal force component is integrated to the impact models. Based on this resistance force model, I could model different kinematic chains at low speed impact with the granular medium. I contributed an experimental set-up to validate the simulation results for kinematic links.

BIBLIOGRAPHY

- [1] S. Luding, "Shear flow modeling of cohesive and frictional fine powder," *Powder Technology* **158**, 45-50, 2005.
- [2] Peter Constantin, Elizabeth Grossman, and Muhittin Mungan, "Inelastic collisions of three particles on a line as a two-dimensional billiard," *Physica D* **83**, 409-420, 1995.
- [3] Elizabeth Grossman and Muhittin Mungan, "Motion of three inelastic particles on a ring," *Physical Review E* **53**(6), 6435-6449, 1996.
- [4] Tong Zhou and Leo P. Kadanoff, "Inelastic Collapse of Three Particles," *Physical Review E* **54**, 623-628, 1996.
- [5] Norbert Schörghofer and Tong Zhou, "Inelastic collapse of rotating spheres," *Physical Review E* **54**(5), 5511-5515, 1996.
- [6] Benjamin Painter, Meenakshi Dutt, and Robert P. Behringer, "Energy dissipation and clustering for a cooling granular material on a substrate," *Physica D* **175**, 43-68, 2003.
- [7] Meenakshi Dutt and Robert P. Behringer, "Effects of surface friction on a two-dimensional granular system: Cooling bound system," *Physical Review E* **70**, 061304(15), 2004.
- [8] Piroz. Zamankhan and Mohammad Hadi Bordbar, "Complex Flow Dynamics in Dense Granular Flows.Part I: Experimentation," *Journal of Applied Mechanics* **73**, 648-657, 2006.
- [9] Piroz Zamankhan and Jun Huang, "Complex Flow Dynamics in Dense Granular Flows.Part II: Simulations," *Journal of Applied Mechanics* **74**, 691-702, 2007.
- [10] Meenakshi Dutt and Robert P. Behringer, "Effects of surface friction on a two-dimensional granular system: Numerical model of a granular collider experiment," *Physical Review E* **75**, 021305(9), 2007.
- [11] Elizabeth Grossman, Tong Zhou, and E. Ben-Naim, "Towards Granular Hydrodynamics in Two-Dimensions," *Physical Review E* **55**(4), 4200-4206, 1997.
- [12] Gabriel I. Tardos, "A fluid mechanics approach to slow, frictional flow of powders," *Powder Technology* **92**, 61-74, 1997.
- [13] Gabriel I. Tardos, M. Irfan Khan, and David G. Schaeffer, "Forces on a slowly rotating, rough cylinder in a Couette device contacting a dry, frictional powder," *Physics of Fluids* **10**, 335-341, 1998.

- [14] Scott A. Hill and Gene F. Mazenko, “Nonlinear hydrodynamical approach to granular materials,” *Physical Review E* **63**, 031303(13), 2001.
- [15] Scott A. Hill and Gene F. Mazenko, “Granular clustering in a hydrodynamic simulation,” *Physical Review E* **67**, 061302(4), 2003.
- [16] Tong Zhou, “Effects of Attractors on the Dynamics of Granular Systems,” *Physical Review Letters* **80**(17), 3755-3758, 1998.
- [17] Brian Utter and Robert P. Behringer, “Self-diffusion in dense granular shear flows,” *Physical Review E* **69**, 031308(12), 2004.
- [18] Junfei Geng and Robert P. Behringer, “Diffusion and Mobility in a Stirred Dense Granular Material,” *Physical Review Letters* **93**, 238002(4), 2004.
- [19] G. Rousseaux, H. Caps, and J.-E. Wesfreid, “Granular size segregation in underwater sand ripples,” *European Physical Journal E* **13**, 213-219, 2004.
- [20] M. Davis, M. A. Koenders, “Oscillated densely packed granular media immersed in a fluid,” *Journal of Sound and Vibration* **308**, 526-540 2007.
- [21] John J. Drozd and Colin Denniston, “Velocity fluctuations in dense granular flows,” *Physical Review E* **78**, 041304(13), 2008.
- [22] Paul Melby, Alexis Prevost, David A. Egolf, and Jeffrey S. Urbach, “Depletion force in a bidisperse granular layer,” *Physical Review E* **76**, 051307(5), 2007.
- [23] James B. Knight, Christopher G. Fandrich, Chun Ning Lau, Heinrich M. Jaeger, and Sidney R. Nagel, “Density Relaxation in a Vibrated Granular Material,” *Physical Review E* **51**(5), 3957-3963, 1995
- [24] E. Ben-Naim, J. B. Knight, E. R. Nowak, H. M. Jaeger, and S. R. Nagel, “Slow relaxation in granular compaction,” *Physica D* **123**, 380-385, 1998.
- [25] Edmund R. Nowak, James B. Knight, Eli Ben-Naim, Heinrich M. Jaeger, and Sidney R. Nagel, “Density fluctuations in vibrated granular materials,” *Physical Review E* **57**(2), 1971-1982, 1998.
- [26] Christophe Josserand, Alexei Tkachenko, Daniel M. Mueth, and Heinrich M. Jaeger, “Memory Effects in Granular Material,” *Physical Review Letters* **85**, 3632-3635, 2000.
- [27] Fernando X. Villarruel, Benjamin E. Lauderdale, Daniel M. Mueth, and Heinrich M. Jaeger, “Compaction of rods: Relaxation and ordering in vibrated, anisotropic granular material,” *Physical Review E* **61**(6), 6914-6921, 2000.
- [28] Reuben Son, John A. Perez, and Greg A. Voth, “Experimental measurements of the collapse of a two-dimensional granular gas under gravity,” *Physical Review E* **78**, 041302(7), 2008.
- [29] Heinrich M. Jaeger, Sidney R. Nagel, and Robert P. Behringer, “Granular solids, liquids, and gases,” *Reviews of Modern Physics* **68**(4), 1259-1273, 1996.

- [30] S. N. Coppersmith, C.-h. Liu, S. Majumdar, O. Narayan, and T. A. Witten, “Model for force fluctuations in bead packs,” *Physical Review E* **53**, 4673-4685, 1996.
- [31] Daniel M. Mueth, Heinrich M. Jaeger, and Sidney R. Nagel, “Force distribution in a granular medium,” *Physical Review E* **57**, 3164-3169, 1998.
- [32] Alexei V. Tkachenko and Thomas A. Witten, “Stress propagation through frictionless granular material,” *Physical Review E* **60**, 687-698, 1999.
- [33] M. L. Nguyen and S. N. Coppersmith, “A scalar model of inhomogeneous elastic and granular media,” *Physical Review E* **62**, 5248-5262, 2000.
- [34] Daniel L. Blair, Nathan W. Mueggenburg, Adam H. Marshall, Heinrich M. Jaeger, and Sidney R. Nagel, “Force distributions in 3D granular assemblies: Effects of packing order and inter-particle friction,” *Physical Review E* **63**, 041304(9), 2001.
- [35] T. S. Majmudar and Robert P. Behringer, “Contact force measurements and stress-induced anisotropy in granular materials,” *Nature* **425**, 1079-1072, 2005.
- [36] Patrick Richard, Mario Nicodem, Renaud Ddlannay, Philippe Ribiere, and Daniel Bideau, “Slow relaxation and compaction of granular systems,” *Nature Materials* **4**, 121-128, 2005.
- [37] E. Knobloch, “Euler, the historical perspective,” *Physica D* **237**, 1887-1893, 2008.
- [38] X. W. Chen, X. L. Li, F. L. Huang, H. J. Wu, and Y. Z. Chen, “Damping function in the penetration/perforation struck by rigid projectiles,” *International Journal of Impact Engineering* **35**, 1314-1325, 2008.
- [39] R. Albert, M. A. Pfeifer, A.-L. Barabási, and P. Schiffer, “Slow Drag in a Granular Medium,” *Physical Review Letters* **82**, 205-208, 1999.
- [40] I. Albert, P. Tegzes, B. Kahng, R. Albert, J. G. Sample, M. Pfeifer, A.-L. Barabasi, T. Vicsek, and P. Schiffer, “Jamming and Fluctuations in Granular Drag,” *Physical Review Letters* **84**, 5122-5125, 2000.
- [41] I. Albert, P. Tegzes, R. Albert, J. G. Sample, A.-L. Barabási, T. Vicsek, B. Kahng, and P. Schiffer, “Stick-slip fluctuations in granular drag,” *Physical Review E* **64**, 031307(9), 2001.
- [42] I. Albert, J. G. Sample, A. J. Morss, S. Rajagopalan, A.-L. Barabási, and P. Schiffer, “Granular drag on a discrete object: Shape effects on jamming,” *Physical Review E* **64**, 061303(4), 2001.
- [43] M. B. Stone, R. Barry, D. P. Bernstein, M. D. Plec, Y. K. Tsui, and P. Schiffer, “Local jamming via penetration of a granular medium,” *Physical Review E* **70**, 041301(10), 2004.
- [44] G. Hill, S. Yeung, and S. A. Koehler, “Scaling vertical drag force in granular media,” *European Physics Letters* **72**, 137-142, 2005.

- [45] J. S. Uehara, M. A. Ambroso, R. P. Ojha, and D. J. Durian, “Low-speed impact craters in loose granular media,” *Physical Review Letters* **90**, 194301(4), 2003.
- [46] John R. de Bruyn and Amanda M. Walsh, “Penetration of spheres into loose granular media,” *Canadian Journal of Physics* **82**, 439-446, 2004.
- [47] Massimo Pica Ciamarra, Antonio H. Lara, Andrew T. Lee, Daniel I. Goldman, Inna Vishik, and Harry L. Swinney, “Dynamics of Drag and Force Distributions for Projectile Impact in a Granular Medium,” *Physical Review Letters* **92**, 194301(4), 2004.
- [48] L. S. Tsimring and D. Volfson, “Modeling of impact cratering in granular media,” in: R. Garcíá Rojo, H. J. Herrmann, S. McNamara(Eds.), *Powders and Grains 2005*, A.A.Balkema, Rotterdam, pp.1215-1223, 2005.
- [49] M. A. Ambroso, R. D. Kamien, and D. J. Durian, “Dynamics of shallow impact cratering,” *Physical Review E* **72**, 041305(4), 2005.
- [50] M. Hou, Z. Peng, R. Liu, K. Lu, and C. K. Chan, “Dynamics of a projectile penetrating in granular systems,” *Physical Review E* **72**, 062301(4), 2005.
- [51] H. Katsuragi and D. J. Durian, “Unified force law for granular impact cratering,” *Nature Physics* **3**, 420-423, 2007.
- [52] Simon J. de Vet and John R. de Bruyn, “Shape of impact craters in granular media,” *Physical Review E* **76**, 041306(6), 2007.
- [53] Detlef Lohse, Remco Rauhe, Raymond Bergmann, Devaraj van der Meer, “Creating a dry variety of quicksand,” *Nature* **432**, 689-690, 2004.
- [54] Seunghun Lee and Dan B. Marghitu, “Analysis of a rigid body obliquely impacting granular matter,” *Nonlinear Dynamics* (Accepted for publication).
- [55] William A. Allen, Earle B. Mayfield, and Harvey L. Morrison, “Dynamics of a Projectile Penetrating Sand,” *Journal of Applied Physics* **28**, 370-376, 1957.
- [56] William A. Allen, Earle B. Mayfield, and Harvey L. Morrison, “Dynamics of a Projectile Penetrating Sand. Part II,” *Journal of Applied Physics* **28**, 1331-1335, 1957.
- [57] Volkhard Buchholtz and Thorsten Pöschel, “Interaction of a granular stream with an obstacle,” *Granular Matter* **1**, 33-41, 1998.
- [58] Erin C. Rericha, Chris Bizon, Mark D. Shattuck, and Harry L. Swinney, “Shocks in Supersonic Sand,” *Physical Review Letters* **88**(1), 014302(4), 2002.
- [59] C. R. Wassgren, J. A. Cordova, R. Zenit, and A. Karion, “Dilute granular flow around an immersed cylinder,” *Physics of Fluids* **15**(11), 3318-3330, 2003.
- [60] Junfei Geng and Robert P. Behringer, “Slow drag in two-dimensional granular media,” *Physical Review E* **71**, 011302(19), 2005.

- [61] Rahul Bharadwaj, Carl Wassgren, and Roberto Zenit, “The unsteady drag force on a cylinder immersed in a dilute granular flow,” *Physics of Fluids* **18**, 043301(7), 2006.
- [62] E. L. Nelson, H. Katsuragi, and D. J. Durian, “Projectile interactions in granular impact cratering,” *Physical Review Letters* **101**(6), 068001(4), 2008.
- [63] B. Kahng, I. Albert, P. Schiffer, and A.-L. Barabási, “Modeling relaxation and jamming in granular media,” *Physical Review E* **64**, 051303(4), 2001.
- [64] T. S. Majmudar, M. Sperl, S. Luding, and Robert P. Behringer, “Jamming Transition in Granular Systems,” *Physical Review Letters* **98**, 058001(4), 2007.
- [65] Robert P. Behringer, Karen E. Daniels, Trushant S. Majmudar, and Matthias Sperl, “Fluctuations, correlations and transitions in granular materials: statistical mechanics for a non-conventional system,” *Philosophical transactions of the royal society A* **366**, 493-504, 2008.
- [66] Frank M. White, “Fluid Mechanics,” 4th ed., WCB McGraw-Hill, 1999.
- [67] Daniel L. Hopkins and Victoria L. McGuffin, “Three-Dimensional Molecular Simulation of Electrophoretic Separations,” *Analytical Chemistry* **70**, 1066-1075, 1998.
- [68] Optotrack brochure from <http://www.ndigital.com/>.

APPENDICES: MATHEMATICA PROGRAMS

APPENDIX A

MATHEMATICAL PENDULUM

```

ClearAll["Global`*"];
Off[General::spell];
Off[General::spell1];

(***) Dimensions and basic data (***)
(*length of pendulum [m]:          *)L = 0.5;
(*diameter [m]:                   *)ds = 0.0254;
(*density of spere [kg/m^3]:       *)rhos = 7.7 * 10^3;
(*volume of spere [m^3]:          *)Vs = Pi * ds^3 / 6;
(*mass of spere [kg]:              *)ms = Vs * rhos;
(*density of sand [kg/m^3]:        *)rhog = 2.5 * 10^3;
(*gravtaional acceleration [m/s^2]: *)g = 9.81;

(***) Kinematics (***)
(*position vector of C:            *)rC = {L * Sin[q[t]], 0, L * Cos[q[t]]};
(*Immersed depth of sphere:       *)zT = L * Cos[q[t]] - L * Cos[q0];
(*position vector of E:            *)rE = rC;
(*velocity vector of E:           *)vE = D[rE, t];

(***) Dynamics (***)
(*gravity force: *)G = {0, 0, ms * g};

(*dynamic frictional force: Fd*)
(*coefficient:   *)etad = 6.5;
(*reference area: *)Ar = Pi * ds^2 / 4;
(*H direction Fd: *)Fdh = -vE[[1]] * Ar * etad * rhog * (vE.vE)^0.5;
(*V direction Fd: *)Fdv = -vE[[3]] * Ar * etad * rhog * (vE.vE)^0.5;

(*static resistace force: Fs*)
(*coefficient:   *)etah = 8; etav = 21; lambda = 1.1;
(*horizontal Fs: *)Fsh = -Sign[vE[[1]]] * etah * rhog * g * ds^2 * zT;
(*vertical Fs:   *)Fsv = -Sign[vE[[3]]] * etav * (zT / ds)^lambda * g * rhog * Vs;

(*resistace force:*)FR = {Fdh + Fsh, 0, Fdv + Fsv};

(**** Equation of motion ****)
Eq = ms * L^2 * q''[t] == Cross[rC, (FR + G)][[2]];

(**** Initial condition ****)

```

```

(*initial angle:          *)q0 = 15 * Pi / 180;
(*initial angular velocity: *)dq0 = -1;

(***) Solving E.O.M (***)
sol = NDSolve[{Eq, q[0] == q0, q'[0] == dq0}, q, {t, 0, 1},
  MaxSteps -> Infinity, Method -> {"EventLocator", "Direction" -> 1,
  "Event" -> q'[t], "EventAction" -> Throw[tend = t;, "StopIntegration"],
  "EventLocationMethod" -> "LinearInterpolation",
  "Method" -> "ExplicitEuler"}];

Print["Stopping time of the pendulum is ", tend, " [s]"];
Plot[Evaluate[q[t] * 180 / Pi /. sol[[1]]], {t, 0, tend}, PlotRange -> All,
  GridLines -> Automatic, Frame -> True, FrameLabel -> {"Time (s)", "q (deg)"}]
Plot[Evaluate[q'[t] /. sol], {t, 0, tend}, PlotRange -> All,
  GridLines -> Automatic, Frame -> True, FrameLabel -> {"Time (s)", "dq (rad/s)"}]

```

APPENDIX B
OBLIQUE IMPACT OF A SPHERE

```

ClearAll["Global`*"];
Off[General::spell];
Off[General::spell1];

(***) Dimensions and basic data (***)
(*diameter [m]: *)ds = 0.0254;
(*density of spere [kg/m^3]: *)rhos = 7.7 * 10^3;
(*volume of spere [m^3]: *)Vs = Pi * ds^3 / 6;
(*mass of spere [kg]: *)ms = Vs * rhos;
(*density of sand [kg/m^3]: *)rhog = 2.5 * 10^3;
(*gravtaional acceleration [m/s^2]: *)g = 9.81;

(***) Kinematics (***)
(*position vector of C: *)rC = {qx[t], 0, qz[t]};
(*acceleration vector of C: *)aC = D[rC, {t, 2}];
(*position vector of E: *)rE = rC;
(*velocity vector of E: *)vE = D[rE, t];

(***) Dynamics (***)
(*gravity force: *)G = {0, 0, ms * g};

(*dynamic frictional force: Fd*)
(*coefficient: *)etad = 6.5;
(*reference area: *)Ar = Pi * ds^2 / 4;
(*H direction Fd: *)Fdh = -vE[[1]] * Ar * etad * rhog * (vE.vE)^0.5;
(*V direction Fd: *)Fdv = -vE[[3]] * Ar * etad * rhog * (vE.vE)^0.5;

(*static resistace force: Fs*)
(*coefficient: *)etah = 8; etav = 21; lambda = 1.1;
(*horizontal Fs: *)Fsh = -Sign[vE[[1]]] * etah * rhog * g * ds^2 * rC[[3]];
(*vertical Fs: *)
Fsv = -Sign[vE[[3]]] * etav * (rC[[3]] / ds)^lambda * g * rhog * Vs;

(*resistace force:*)FR = {Fdh + Fsh, 0, Fdv + Fsv};

(***) Equation of motion (***)
(*sum of all force: *)Fsum = ms * aC - FR - G;
(*sum of H direction force: *)Eq1 = Fsum[[1]] == 0;
(*sum of V direction force: *)Eq2 = Fsum[[3]] == 0;

```



```

(***) Initial condition (***)
(*initial angle:          *)q0 = 30 * Pi / 180;
(*initial velocity:      *)v0 = 1;
(*initial H direction velocity: *)dqx0 = -v0 * Cos[q0];
(*initial V direction velocity: *)dqz0 = v0 * Sin[q0];

(***) Solving E.O.M (***)
sol = NDSolve[{Eq1, Eq2, qx[0] == 0, qx'[0] == dqx0, qz[0] == 0, qz'[0] == dqz0},
  {qx, qz}, {t, 0, 1}, MaxSteps -> Infinity,
  Method -> {"EventLocator", "Direction" -> -1, "Event" -> vE[[3]], "EventAction" ->
    Throw[tend = t;, "StopIntegration"], "EventLocationMethod" ->
    "LinearInterpolation", "Method" -> "ExplicitEuler"}];

Print["Stopping time of the sphere is ", tend, " [s]"];
(*velocity: *)vel = FunctionInterpolation [
  Evaluate[Sqrt[qx'[t]^2 + qz'[t]^2] /. sol[[1]]], {t, 0, tend}];
(*distance: *)dis = Integrate[vel[t], t];
Plot[dis, {t, 0, tend}, PlotRange -> All, GridLines -> Automatic,
  Frame -> True, FrameLabel -> {"Time (s)", "d [m]"}]
Plot[vel[t], {t, 0, tend}, PlotRange -> All, GridLines -> Automatic,
  Frame -> True, FrameLabel -> {"Time (s)", "v [m/s]"}]

```

APPENDIX C
RIGID FREE LINK

```

ClearAll["Global`*"];
Off[General::spell];
Off[General::spell1];

(***) Dimensions and basic data (***)
(*length of link [m]:          *)L = 0.1524;
(*diameter [m]:              *)dc = 0.00635;
(*density of link [kg/m^3]:   *)rhoc = 7.7 * 10^3;
(*mass of link [kg]:         *)mc = rhoc * L * Pi * dc^2 / 4;
(*inertia [kg m^2]:         *)IC = mc * L^2 / 12;
(*density of sand [kg/m^3]:  *)rhog = 2.5 * 10^3;
(*gravtaional acceleration [m/s^2]: *)g = 9.81;

(***) Kinematics (***)
(*Position, velocity and acceleration vectors*)
(*pos. vector from O to C:   *)rC = {qx[t], 0, qz[t]};
(*acc. vector of rC:        *)aC = D[rC, {t, 2}];

(*pos. vector from C to P: *)rCP = {P * Sin[q[t]], 0, P * Cos[q[t]};
(*pos. vector from O to P: *)rP = rC + rCP;
(*vel. vector of rP:       *)vP = D[rP, t];
(*acc. vector of rP:       *)aP = D[vP, t];

(*pos. vector from O to T: *)rT = rP /. P -> 0.5 * L;
(*vel. vector from O to T: *)vT = vP /. P -> 0.5 * L;

(*immered depth of T:     *)zT = rT[[3]];
(*length from C to T:     *)LE = 0.5 * L - 0.5 * zT / Cos[q[t]];
(*pos. vector from O to E: *)rE = rP /. P -> LE;
(*vel. vector from O to E: *)vE = vP /. P -> LE;
(*pos. vector from C to E: *)rCE = rCP /. P -> LE;

(***) Dynamics (***)
(*G force on link: *)G = {0, 0, mc * g};

(** resistance force **)
(*dynamic frictional force: Fd*)
(*coefficient: *)etad = 6.5;
(*moving angle: *)qm = ArcTan[vE[[1]] / vE[[3]]];
(*reference area: *)Ar = dc * zT / Cos[q[t]] * Abs[Sin[q[t] - qm]];
(*H direction Fd: *)Fdh = -vE[[1]] * Ar * etad * rhog * Sqrt[vE.vE];

```

```

(*V direction Fd: *)Fdv = -vE[[3]] * Ar * etad * rhog * Sqrt[vE.vE];

(*static resistace force: Fs*)
(*coefficients: *)etah = 8; etav = 22; lambda = 1.1;
(*horizontal Fs: *)Fsh = -Sign[vE[[1]]] * etah * rhog * g * dc * zT^2;
(*imeresed vol.: *)V = Pi * dc^2 / 4 * (zT / Cos[q[t]]);
(*vertical Fs: *)Fsv = -Sign[vE[[3]]] * etav * (zT / dc) ^ lambda * g * rhog * V;

(*resistace force:*)FR = {Fdh + Fsh, 0, Fdv + Fsv};

(***) Equation of motion (***)
Fsum = mc * aC - G - FR;
Eq1 = Fsum[[1]] == 0;
Eq2 = Fsum[[3]] == 0;
Eq3 = IC * q'[t] == Cross[rCE, FR][[2]];

(***) Initial condition (***)
(*initial angle of link: *)q0 = 32 / 180 * Pi;
(*initial horizontal pos. of C: *)qx0 = 0;
(*initial vertical pos. of C: *)qz0 = -0.5 * L * Cos[q0];
(*initial horizontal vel of A: *)dqx0 = 0;
(*initial vertical vel of A: *)dqz0 = 1.26;
(*initial angular vel. of link: *)dq0 = 0;

(***) Solving E.O.M (***)
(*step size [s]: *)stepsize = 10^-6;
sol = NDSolve[{Eq1, Eq2, Eq3, qx[0] == qx0, qx'[0] == dqx0, qz[0] == qz0,
  qz'[0] == dqz0, q[0] == q0, q'[0] == dq0}, {qx, qz, q}, {t, 0, 1},
  MaxSteps -> Infinity, StartingStepSize -> stepsize, MaxStepFraction -> Infinity,
  Method -> {"EventLocator", "Direction" -> -1, "Event" -> vT[[3]],
  "EventAction" -> {Throw[tend = t - stepsize;, "StopIntegration"]},
  "EventLocationMethod" -> "LinearInterpolation",
  "Method" -> {"FixedStep", "Method" -> {"ExplicitRungeKutta"}}]];

Print["stopping time of link is ", tend, " [s]"]
Plot[Evaluate[rT[[3]] /. sol], {t, 0, tend}, PlotRange -> All,
  GridLines -> Automatic, Frame -> True, FrameLabel -> {"Time (s)", "zT (m)"}]
Plot[Evaluate[vT[[3]] /. sol], {t, 0, tend}, PlotRange -> All,
  GridLines -> Automatic, Frame -> True, FrameLabel -> {"Time (s)", "vTz (m/s)"}]

```

APPENDIX D
RIGID COMPOUND PENDULUM

```

ClearAll["Global`*"];
Off[General::spell];
Off[General::spell1];

(***) dimensions and basic data (***)
(*1 part diameter [m]:*) dp1 = 0.01905;
(*1 part length [m]: *) Lp1 = 0.01981;
(*2 part diameter [m]:*) dp2 = 0.01524;
(*2 part length [m]: *) Lp2 = 0.01524;
(*3 part diameter [m]:*) dp3 = 0.00635;
(*3 part length [m]: *) Lp3 = 0.23876;

(*1 part volume [m^3]:*) Vp1 = Pi * dp1^2 / 4 * Lp1;
(*2 part volume [m^3]:*) Vp2 = Pi * dp2^2 / 4 * Lp2;
(*3 part volume [m^3]:*) Vp3 = Pi * dp3^2 / 4 * Lp3;

(*density of link [kg/m^3]:*) rhoc = 7.7 * 10^3;
(*1 part mass [kg]: *) mp1 = Vp1 * rhoc;
(*2 part mass [kg]: *) mp2 = Vp2 * rhoc;
(*3 part mass [kg]: *) mp3 = Vp3 * rhoc;
(*actual mass [kg]: *) mc = mp2 + mp3;

(*1 part inertia [kg m^2]:*) Ip1 = mp1 * dp1^2 / 8;
(*2 part inertia [kg m^2]:*)
Ip2 = mp2 * (dp1 / 2 + Lp2 / 2)^2 + mp2 * (3 * dp2^2 / 4 + Lp2^2) / 12;
(*3 part inertia [kg m^2]:*)
Ip3 = mp3 * (dp1 / 2 + Lp2 + Lp3 / 2)^2 + mp3 * Lp3^2 / 12;
(*inertia of RB [kg m^2]: *) IO = Ip1 + Ip2 + Ip3;

(*length of flexible link [m]: *) L = dp1 / 2 + Lp2 + Lp3;
(*length to mass center of link [m]: *)
LC = ((dp1 / 2 + Lp2 / 2) * mp2 + (dp1 / 2 + Lp2 + Lp3 / 2) * mp3) / mc;
(*diameter of flexible link [m]: *) dc = dp3;
(*cross sectional area of link [m^2]:*) Ac = Pi * dc^2 / 4;
(*density of sand [kg/m^3]: *) rhog = 2.5 * 10^3;
(*gravtaional acceleration [m/s^2]: *) g = 9.81;

(***) Kinematics (***)
(*position vector from O to P: *) rP = {P * Sin[q[t]], 0, P * Cos[q[t]]};
(*velocity vector rP: *) vP = D[rP, t];

(*position vector from O to C: *) rC = rP /. P -> LC;

```

```

(*velocity vector rC:          *)vC = vP /. P -> LC;

(*position vector from O to T: *)rT = rP /. P -> L;
(*velocity vector rT:          *)vT = vP /. P -> L;

(*impact depth:                *) zT = L * Cos[q[t]] - L * Cos[q0];
(*length to E:                 *) LE = L - 0.5 * zT / Cos[q[t]];
(*position vector from O to E: *)rE = rP /. P -> LE;
(*velocity vector rE:          *)vE = vP /. P -> LE;

(***) Dynamics (***)
(*gravity force: *) G = {0, 0, mc * g};

(*dynamic frictional force: Fd*)
(*coefficient: *) etad = 6.5;
(*reference area: *) Ar = dc * zT / Cos[q[t]];
(*H direction Fd: *) Fdh = -vE[[1]] * Ar * etad * rhog * Sqrt[vE.vE];
(*V direction Fd: *) Fdv = -vE[[3]] * Ar * etad * rhog * Sqrt[vE.vE];

(*static resistace force: Fs*)
(*coefficients: *) etah = 8; etav = 21; lambda = 1.1;
(*horizontal Fs: *) Fsh = -Sign[vE[[1]]] * etah * rhog * g * dc * zT^2;
(*imeresed volume:*) V = Pi * dc^2 / 4 * (zT / Cos[q[t]]);
(*vertical Fs: *) Fsv = -Sign[vE[[3]]] * etav * (zT / dc) ^ lambda * g * rhog * V;

(*resistace force:*) FR = {Fdh + Fsh, 0, Fdv + Fsv};

(***) equation of motion (***)
Eq = IO * q''[t] == (Cross[rC, G] + Cross[rE, FR])[[2]];

(***) initial condition (***)
(*initial angle: *) q0 = 22 * Pi / 180;
(*initial velocity: *) dq01 = -1.75;

(***) solving E.O.M (***)
sol = NDSolve[{Eq, q[0] == q0, q'[0] == dq01}, q, {t, 0, 1},
  MaxSteps -> Infinity, Method -> {"EventLocator", "Event" -> q'[t],
  "EventAction" -> Throw[tend = t;, "StopIntegration"],
  "EventLocationMethod" -> "LinearInterpolation",
  "Method" -> "ExplicitEuler"}];

Print["stopping time of the compound pendulum is ", tend, " [s]"];
Plot[Evaluate[q[t] * 180 / Pi /. sol], {t, 0, tend}, PlotRange -> All,

```

```
GridLines -> Automatic, Frame -> True, FrameLabel -> {"Time (s)", "q (deg)"}]
Plot[Evaluate[q'[t] /. sol], {t, 0, tend}, PlotRange -> All,
GridLines -> Automatic, Frame -> True, FrameLabel -> {"Time (s)", "dq (rad/s)"}]
```

APPENDIX E
RIGID DOUBLE PENDULUM

```

ClearAll["Global`*"];
Off[General::spell];
Off[General::spell1];

(***) Dimensions and basic data (***)
(*density of links [kg/m^3]:          *)rhoc = 7.7 * 10^3;
(*diameter of links [m]:             *)dc = 0.0254;
(*length of link 1 [m]:              *)L1 = 0.2;
(*mass of link 1 [kg]:               *)m1 = rhoc * L1 * Pi * dc^2 / 4;
(*length of link 2 [m]:              *)L2 = L1 * 3;
(*mass of link 2 [kg]:               *)m2 = rhoc * L2 * Pi * dc^2 / 4;
(*mass inertia link 1 [kg m^2]:      *)IO = m1 / 3 * (L1^2);
(*mass inertia link 2 [kg m^2]:      *)IC2 = m2 / 12 * (L2^2);
(*gravtaional acceleration [m/s^2]: *)g = 9.81;
(*density of sand [kg/m^3]:          *)rhog = 2.5 * 10^3;

(***) Kinematics (***)
(*pos. vector from O to A of link 1: *)
rA = {L1 * Sin[q1[t]], 0, L1 * Cos[q1[t]]};
(*pos. vector from A to P of link 2: *)
rAP = {P * Sin[q2[t]], 0, P * Cos[q2[t]]};
(*pos. vector from O to P of link 2: *)rP = rA + rAP;
(*vel. vector of rP:                  *)vP = D[rP, t];
(*acc. vector of rP:                  *)aP = D[vP, t];

(*pos. vector from O to C1 of link 1: *)rC1 = rA / 2;
(*pos. vector from O to C2 of link 2: *)rC2 = rP /. P -> 0.5 * L2;
(*acc. vector of rC2:                  *)aC2 = aP /. P -> 0.5 * L2;

(*vel. vector of end of link 2, T:    *)vT = vP /. P -> L2;
(*immersed depth of end of link 2, T: *)
zT = (rP[[3]] /. {P -> L2}) - (L1 * Cos[q10] + L2 * Cos[q20]);
(*length from A to E of link 2:      *)LE = L2 - 0.5 * zT / Cos[q2[t]];

(*pos. vector from O to E of link 2: *)rE = rP /. P -> LE;
(*vel. vector of rE:                  *)vE = vP /. P -> LE;

(***) Dynamics (***)
(*G force on link1: *)G1 = {0, 0, m1 * g};
(*G force on link2: *)G2 = {0, 0, m2 * g};

```

```

(*dynamic frictional force: Fd*)
(*coefficient: *)etad = 6.5;
(*moving angle: *)qm = ArcTan[vE[[1]] / vE[[3]]];
(*reference area: *)Ar = dc * zT / Cos[q2[t]] * Abs[Sin[q2[t] - qm]];
(*H direction Fd: *)Fdh = -vE[[1]] * Ar * etad * rhog * Sqrt[vE.vE];
(*V direction Fd: *)Fdv = -vE[[3]] * Ar * etad * rhog * Sqrt[vE.vE];

(*static resistace force: Fs*)
(*coefficientss: *)
etah = 8; etav = Piecewise[{{22, vE[[3]] >= 0}, {0.5, vE[[3]] < 0}}];
lambda = 1.1;
(*horizontal Fs: *)Fsh = -Sign[vE[[1]]] * etah * rhog * g * dc * zT^2;
(*imeresed volume:*)V = zT / Cos[q2[t]] * dc^2 * Pi / 4;
(*vertical Fs: *)Fsv = -Sign[vE[[3]]] * etav * (zT / dc) ^ lambda * g * rhog * V;

(*resistace force:*)FR = {Fdh + Fsh, 0, Fdv + Fsv};

(***) Equation of motion (***)
Eq1 = IO * q1''[t] == (Cross[rC1, G1] + Cross[rA, (-m2 * aC2 + G2 + FR)] [[2]]);
Eq2 = IC2 * q2''[t] ==
  (Cross[(rA - rC2), (m2 * aC2 - G2 - FR)] + Cross[(rE - rC2), FR]) [[2]];

(***) Initial condition (***)
(*initial angle of link 1: *)q10 = 30 / 180 * Pi;
(*initial angle of link 2: *)q20 = 75 / 180 * Pi;
(*initial angular velocity of link 1:*)dq110 = -1;
(*initial angular velocity of link 2:*)dq210 = -1;

(**** Solving E.O.M ****)
(*step size [s]: *)stepsize = 10^-6;
sol = NDSolve[{Eq1, Eq2, q1[0] == q10, q1'[0] == dq110, q2[0] == q20,
  q2'[0] == dq210}, {q1, q2}, {t, 0, 1}, MaxSteps -> Infinity,
  StartingStepSize -> stepsize, MaxStepFraction -> Infinity,
  Method -> {"EventLocator", "Direction" -> 1, "Event" -> q1'[t],
  "EventAction" -> Throw[tend = t - stepsize, "StopIntegration"],
  "EventLocationMethod" -> "LinearInterpolation",
  "Method" -> {"FixedStep", "Method" -> "ExplicitRungeKutta"}}];

Print["Complete stopping time of double pendulum is ", tend, " [s]"];
Plot[Evaluate[q1[t] * 180 / Pi /. sol], {t, 0, tend}, PlotRange -> All,
  GridLines -> Automatic, Frame -> True, FrameLabel -> {"Time (s)", "q1 (deg)"}]
Plot[Evaluate[q2[t] * 180 / Pi /. sol], {t, 0, tend}, PlotRange -> All,
  GridLines -> Automatic, Frame -> True, FrameLabel -> {"Time (s)", "q2 (deg)"}]
Plot[Evaluate[q1'[t] /. sol], {t, 0, tend}, PlotRange -> All,

```



```
GridLines → Automatic, Frame → True, FrameLabel → {"Time (s)", "dq1 (rad/s)"}]
Plot[Evaluate[q2'[t] /. sol], {t, 0, tend}, PlotRange → All,
GridLines → Automatic, Frame → True, FrameLabel → {"Time (s)", "dq2 (rad/s)"}]
```

APPENDIX F
TWO LINK KINEMATIC CHAIN WITH TWO IMPACT POINTS

```

ClearAll["Global`*"];
Off[General::spell];
Off[General::spell1];

(***) Dimensions and basic data (***)
(*diameter of links [m]:          *)dc = 0.0254;
(*density of links [kg/m^3]:      *)rhoc = 7.7 * 10^3;
(*length of link 1 [m]:          *)L1 = 0.3;
(*mass of link 1 [kg]:           *)m1 = rhoc * L1 * Pi * dc^2 / 4;
(*length of link 2 [m]:          *)L2 = L1 * Cos[q10] / Cos[q20];
(*mass of link 2 [kg]:           *)m2 = rhoc * L2 * Pi * dc^2 / 4;
(*mass inertia link 1 [kg m^2]:   *)IC1 = m1 / 12 * (L1^2);
(*mass inertia link 2 [kg m^2]:   *)IC2 = m2 / 12 * (L2^2);
(*density of sand [kg/m^3]:      *)rhog = 2.5 * 10^3;
(*gravtaional acceleration [m/s^2]: *)g = 9.81;

(***) Kinematics (***)
(*Position, velocity and acceleration vectors*)
(*pos. vector from O to A: *)rOA = {qx[t], 0, qz[t]};
(*pos. vector from A to P1: *)rAP1 = {P1 * Sin[q1[t]], 0, P1 * Cos[q1[t]]};
(*pos. vector from O to P1: *)rP1 = rOA + rAP1;
(*vel. vector of rP1: *)vP1 = D[rP1, t];
(*acc. vector of rP1: *)aP1 = D[vP1, t];

(*pos. vector from O to T1: *)rT1 = rP1 /. P1 -> L1;
(*vel. vector from O to T1: *)vT1 = vP1 /. P1 -> L1;

(*pos. vector from A to C1: *)rAC1 = rAP1 /. P1 -> 0.5 * L1;
(*pos. vector from C1 to A: *)rC1A = -rAC1;
(*pos. vector from O to C1: *)rC1 = rP1 /. P1 -> 0.5 * L1;
(*acc. vector of rC1: *)aC1 = aP1 /. P1 -> 0.5 * L1;

(*pos. vector from A to P2: *)rAP2 = {P2 * Sin[q2[t]], 0, P2 * Cos[q2[t]]};
(*pos. vector from O to P2: *)rP2 = rOA + rAP2;
(*vel. vector of rP2: *)vP2 = D[rP2, t];
(*acc. vector of rP2: *)aP2 = D[vP2, t];

(*pos. vector from O to T2: *)rT2 = rP2 /. P2 -> L2;
(*vel. vector from O to T2: *)vT2 = vP2 /. P2 -> L2;

(*pos. vector from A to C2: *)rAC2 = rAP2 /. P2 -> 0.5 * L2;
(*pos. vector from C2 to A: *)rC2A = -rAC2;

```

```

(*pos. vector from O to C2: *)rC2 = rP2 /. P2 → 0.5 * L2;
(*acc. vector of rC2:      *)aC2 = aP2 /. P2 → 0.5 * L2;

(*immersed depth of T1:    *)zT1 = rT1[[3]];
(*length from A to E1:    *)LE1 = L1 - 0.5 * zT1 / Cos[q1[t]];
(*pos. vector from A to E1: *)rAE1 = rAP1 /. P1 → LE1;
(*pos. vector from O to E1: *)rE1 = rP1 /. P1 → LE1;
(*pos. vector from C1 to E1:*)rCE1 = rAE1 - rAC1;
(*vel. vector of rE1:     *)vE1 = vP1 /. P1 → LE1;

(*immersed depth of T2:    *)zT2 = rT2[[3]];
(*length from A to E2:    *)LE2 = L2 - 0.5 * zT2 / Cos[q2[t]];
(*pos. vector from A to E2: *)rAE2 = rAP2 /. P2 → LE2;
(*pos. vector from O to E2: *)rE2 = rP2 /. P2 → LE2;
(*pos. vector from C2 to E2:*)rCE2 = rAE2 - rAC2;
(*vel. vector of rE2:     *)vE2 = vP2 /. P2 → LE2;

(** Dynamics **)
(*G force on link1: *)G1 = {0, 0, m1 * g};
(*G force on link2: *)G2 = {0, 0, m2 * g};

(** resistance force 1*)
(*dynamic frictional force 1: Fd1*)
(*coefficient:      *)etad = 6.5;
(*moving angle 1:  *)qm1 = ArcTan[vE1[[1]] / vE1[[3]]];
(*reference area 1:*)Ar1 = dc * zT1 / Cos[q1[t]] * Abs[Sin[q1[t] - qm1]];
(*H direction Fd1: *)Fdh1 = -vE1[[1]] * Ar1 * etad * rhog * Sqrt[vE1.vE1];
(*V direction Fd1: *)Fdv1 = -vE1[[3]] * Ar1 * etad * rhog * Sqrt[vE1.vE1];

(*static resistace force 1: Fsv1*)
(*coefficients:     *)
etah = 8; etav1 = Piecewise[{{22, vE1[[3]] >= 0}, {0.5, vE1[[3]] < 0}}];
lambda1 = Piecewise[{{1.1, vE1[[3]] >= 0}, {1.1, vE1[[3]] < 0}}];
(*horizontal Fsv1: *)Fsh1 = -Sign[vE1[[1]]] * etah * rhog * g * dc * zT1^2;
(*immeresed vol.1: *)V1 = Pi * dc^2 / 4 * (zT1 / Cos[q1[t]]);
(*vertical Fsv1:   *)
Fsv1 = -Sign[vE1[[3]]] * etav1 * (zT1 / dc) ^ lambda1 * g * rhog * V1;

(*resistace force 1:*)FR1 = {Fdh1 + Fsh1, 0, Fdv1 + Fsv1};

(** resistance force 2*)
(*dynamic frictional force 2: Fd2*)
(*moving angle 2:  *)qm2 = ArcTan[vE2[[1]] / vE2[[3]]];
(*reference area 2:*)Ar2 = dc * zT2 / Cos[q2[t]] * Abs[Sin[q2[t] - qm2]];
(*H direction Fd2: *)Fdh2 = -vE2[[1]] * Ar2 * etad * rhog * Sqrt[vE2.vE2];
(*V direction Fd2: *)Fdv2 = -vE2[[3]] * Ar2 * etad * rhog * Sqrt[vE2.vE2];

```

```

(*static resistace force 2: Fs2*)
(*coefficients: *)
etav2 = Piecewise[{{22, vE2[[3]] >= 0}, {0.5, vE2[[3]] < 0}}];
lambda2 = Piecewise[{{1.1, vE2[[3]] >= 0}, {1.1, vE2[[3]] < 0}}];
(*horizontal Fs2: *)Fsh2 = -Sign[vE2[[1]]] * etah * rhog * g * dc * zT2^2 ;
(*immeresed vol.2: *)V2 = Pi * dc^2 / 4 * (zT2 / Cos[q2[t]]);
(*vertical Fs2: *)
Fsv2 = -Sign[vE2[[3]]] * etav2 * (zT2 / dc) ^ lambda2 * g * rhog * V2;

(*resistace force 2:*)FR2 = {Fdh2 + Fsh2, 0, Fdv2 + Fsv2};

(***) Equation of motion (***)
Fsum = m1 * aC1 + m2 * aC2 - G1 - G2 - FR1 - FR2;
Eqx = Fsum[[1]] == 0;
Eqz = Fsum[[3]] == 0;
Eq1 =
  IC1 * q1''[t] = (Cross[rC1A, (m1 * aC1 - G1 - FR1)] + Cross[rC1E1, FR1])[[2]];
Eq2 = IC2 * q2''[t] = (Cross[rC2A, (m2 * aC2 - G2 - FR2)] + Cross[rC2E2, FR2])[[2]];

(***) Initial condition (***)
(*initial angle of link 1: *)q10 = (2 * Pi - 30 / 180 * Pi) // N;
(*initial angle of link 2: *)q20 = (45 / 180 * Pi) // N;
(*initial horizontal pos. of A: *)qx0 = 0;
(*initial vertical pos. of A: *)qz0 = -L2 * Cos[q20];

(*initial horizontal vel of A: *)dqx0 = 0;
(*initial vertical vel of A: *)dqz0 = 1;
(*initial angular vel. of link 1:*)dq10 = 0;
(*initial angular vel. of link 2:*)dq20 = 0;

(***) Solving E.O.M (***)
(*step size [s]: *)stepsize = 10^-6;
sol = NDSolve[{{Eq1, Eq2, Eqx, Eqz, q1[0] == q10, q1'[0] == dq10, q2[0] == q20,
  q2'[0] == dq20, qx[0] == qx0, qx'[0] == dqx0, qz[0] == qz0, qz'[0] == dqz0},
  {q1, q2, qx, qz}, {t, 0, 1}, MaxSteps -> Infinity,
  StartingStepSize -> stepsize, MaxStepFraction -> Infinity,
  Method -> {"EventLocator", "Direction" -> -1,
    "Event" -> vT1[[3]], "EventAction" -> Throw[tend = t; "StopIntegration"],
    "EventLocationMethod" -> "LinearInterpolation",
    "Method" -> {"FixedStep", "Method" -> {"ExplicitRungeKutta"}}}];

Print["stopping time of link 1 is ", tend, " [s]"]
Plot[Evaluate[rT1[[3]] /. sol], {t, 0, tend}, PlotRange -> All,
  GridLines -> Automatic, Frame -> True, FrameLabel -> {"Time (s)", "zT1 (m)"}]
Plot[Evaluate[vT1[[3]] /. sol], {t, 0, tend}, PlotRange -> All,
  GridLines -> Automatic, Frame -> True, FrameLabel -> {"Time (s)", "vT1z (m/s)"}]

```

APPENDIX G
ELASTIC FREE LINK

```

ClearAll["Global`*"];
Off[General::spell];
Off[General::spell1];

(***) Dimensions and basic data (***)
(*length of link [m]:                *)L = 0.1524;
(*diameter [m]:                      *)dc = 0.00635;
(*cross sectional area of link [m^2]:*)Ac = Pi * dc^2 / 4;
(*density of link [kg/m^3]:          *)rhoc = 7.7 * 10^3;
(*density per unit length [kg/m]:    *)rhoa = rhoc * Ac;
(*mass of link [kg]:                 *)mc = rhoa * L;
(*young's modulus [Pa]:              *)Ec = 190 * 10^9;
(*2nd inertia [m^4]:                 *)Ic = Pi * dc^4 / 64;
(*product of E I:                    *)EI = Ec * Ic;
(*density of sand [kg/m^3]:          *)rhog = 2.5 * 10^3;
(*gravaitional acceleration [m/s^2]: *)g = 9.81;
(*lambda finding:                    *)
lam = lam /. FindRoot[{Cos[lam] * Cosh[lam] == 1}, {lam, 4}];

(***) Kinematics (***)
(* (0) - Fix reference frame attached to
   the ground with the unit vectors {i0, j0, k0} *)
(* (1) - Mobile reference frame attached to the
   base with the unit vectors {i, j, k} *)

(* Transformation matrix from (1) to (0) *)
R10 = {{Cos[q1[t]], 0, -Sin[q1[t]]},
        {0, 1, 0}, {Sin[q1[t]], 0, Cos[q1[t]]}};

(* Transformation matrix from (0) to (1) *)
R01 = {{Cos[q1[t]], 0, Sin[q1[t]]},
        {0, 1, 0}, {-Sin[q1[t]], 0, Cos[q1[t]]}};

(* Elastic deflection of the flexible free link *)
(*shape function: *)
phi = Cos[lam * z / L] + Cosh[lam * z / L] - (Cosh[lam] - Cos[lam]) /
      (Sinh[lam] - Sin[lam]) * (Sin[lam * z / L] + Sinh[lam * z / L]);
(*deflection:      *)x = phi * q2[t];

(** Pos. and Vel. vector of left tip of the
   beam in (0) expressed in terms of (0) {i0,j0,k0} *)
(*pos. vector from 0 to A: *)rA = {qx[t], 0, qz[t]};
(*vel. vector of rA:      *)vA = D[rA, t];

```

```

(** Pos. and Acc. vector of a current point P on the
    beam in (0) expressed in terms of (0) {i0,j0,k0} *)
(*pos. vector from A to P: *)rAP = {x, 0, z}.R10;
(*pos. vector from O to P: *)rP = rA + rAP;
(*vel. vector of rP:      *)vP = D[rP, t];
(*acc. vector of rP:      *)aP = D[vP, t];

(*pos. vector A to P w/o def.:*)rAP0 = {0, 0, z}.R10;
(*pos. vector O to P w/o def.:*)rP0 = rA + rAP0;
(*vel. vector rP w/o def.:   *)vP0 = D[rP0, t];

(** Pos. and Vel. vector of the end T2 on the
    beam in (0) expressed in terms of (0) {i0,j0,k0} *)
(*pos. vector from O to T: *)rT = rP /. z -> L;
(*vel. vector of rT:      *)vT = vP /. z -> L;

(** Pos. vector from A to the mass center C of the
    beam in (0) expressed in terms of (0) {i0,j0,k0} *)
(*pos. vector from A to C: *)rAC = rAP /. z -> 0.5 * L;

(** vector from the origin O to the resistance application point E*)
(*immersed depth of T:    *)zT = rT[[3]];
(*length from A to E:    *)LE = L - 0.5 * zT / Cos[q1[t]];
(*pos. vector from O to E: *)rE = rP /. z -> LE;
(*vel. vector of rE:     *)vE = vP /. z -> LE;

(** Pos. vector from the end A to the resistance application
    point E in (0) expressed in terms of (0) {i0,j0,k0} *)
(*pos. vector from A to E: *)rAE = rAP /. z -> LE;

(***) Dynamics (***)
(*gravity force: *) G = {0, 0, mc * g};

(*dynamic frictional force: Fd*)
(*coefficient:   *) etad = 6.5;
(*moving angle:  *) qm = ArcTan[vE[[1]] / vE[[3]]];
(*reference area: *) Ar = dc * zT / Cos[q1[t]] * Abs[Sin[q1[t] - qm]];
(*H direction Fd: *) Fdh = -vE[[1]] * etad * rhog * Ar * Sqrt[vE.vE];
(*V direction Fd: *) Fdv = -vE[[3]] * etad * rhog * Ar * Sqrt[vE.vE];

(*static resistace force: Fs*)
(*coefficients:  *) etah = 8; etav = 22; lambda = 1.1;
(*horizontal Fs: *) Fsh = -Sign[vE[[1]]] * etah * rhog * g * dc * zT^2;
(*immerded volume: *) V = zT / Cos[q1[t]] * dc^2 * Pi / 4;
(*vertical Fs:   *) Fsv = -Sign[vE[[3]]] * etav * (zT / dc) ^ lambda * g * rhog * V;

(* total FR:      *) FR = {Fdh + Fsh, 0, Fdv + Fsv};

```

```

(***) Equations of motion (***)
dFB = rhoa * aP;
FBx = Integrate[dFB[[1]], {z, 0, L}];
FBz = Integrate[dFB[[3]], {z, 0, L}];
FB = {FBx, 0, FBz};

Fsum = FB - G - FR;
Eq1 = Fsum[[1]] == 0;
Eq2 = Fsum[[3]] == 0;
Eq3 = Chop[Integrate[Cross[rAP, dFB][[2]], {z, 0, L}]] ==
  Cross[rAC, G][[2]] + Cross[rAE, FR][[2]];
Eq4 = EI * (lam / L) ^ 4 * L * q2[t] +
  Chop[Integrate[(dFB.R01)[[1]] * phi, {z, 0, L}]] ==
  (G.R01)[[1]] * (phi /. z -> 0.5 * L) + (FR.R01)[[1]] * (phi /. z -> LE);

(***) Initial condition (***)
(*initial horizontal pos. of A: *)qx0 = 0;
(*initial vertical pos. of A: *)qz0 = -L * Cos[q10];
(*initial angle: *)q10 = 55 * Pi / 180;
(*initial deflection: *)q20 = 0;
(*initial horizontal vel of A: *)dqx0 = 0;
(*initial vertical vel of A: *)dqz0 = 2.43;
(*initial angular velocity: *)dq10 = 0;
(*initial deflection derivative:*)dq20 = 0;

(***) Solving E.O.M (***)
(*step size [s]: *)stepsize = 10^-6;
sol = NDSolve[{Eq1, Eq2, Eq3, Eq4, qx[0] == qx0, qx'[0] == dqx0, qz[0] == qz0,
  qz'[0] == dqz0, q1[0] == q10, q1'[0] == dq10, q2[0] == q20, q2'[0] == dq20},
  {qx, qz, q1, q2}, {t, 0, 1}, MaxSteps -> Infinity,
  StartingStepSize -> stepsize, MaxStepFraction -> Infinity,
  Method -> {"EventLocator", "Direction" -> -1, "Event" -> vT[[3]],
  "EventAction" -> {Throw[tend = t - stepsize;, "StopIntegration"]},
  "EventLocationMethod" -> "LinearInterpolation",
  "Method" -> {"FixedStep", "Method" -> {"ExplicitRungeKutta"}}}];

Print["stopping time of the elastic link in vertical direction, t_s, is ",
  tend, "[s]"];
Plot[Evaluate[zT /. sol], {t, 0, tend}, PlotRange -> All,
  GridLines -> Automatic, Frame -> True, FrameLabel -> {"Time (s)", "zT (m)"}]
Plot[Evaluate[vT[[3]] /. sol], {t, 0, tend}, PlotRange -> All,
  GridLines -> Automatic, Frame -> True, FrameLabel -> {"Time (s)", "vTz (m/s)"}]
Plot[Evaluate[q2[t] /. sol], {t, 0, tend}, PlotRange -> All,
  GridLines -> Automatic, Frame -> True, FrameLabel -> {"Time (s)", "q2 (m)"}]
Plot[Evaluate[q2'[t] /. sol], {t, 0, tend}, PlotRange -> All,
  GridLines -> Automatic, Frame -> True, FrameLabel -> {"Time (s)", "dq2 (m/s)"}]

```

APPENDIX H
ELASTIC COMPOUND PENDULUM

```

ClearAll["Global`*"];
Off[General::spell];
Off[General::spell1];

(*** Dimensions and basic data ***)
(*length of link [m]:                *)L = 0.15;
(*diameter [m]:                      *)dc = 0.00635;
(*cross sectional area of link [m^2]:*)Ac = Pi * dc^2 / 4;
(*density of link [kg/m^3]:          *)rhoc = 7.7 * 10^3;
(*density per unit length [kg/m]:    *)rhoa = rhoc * Ac;
(*mass of link [kg]:                 *)mc = rhoa * L;
(*young's modulus [Pa]:              *)Ec = 190 * 10^9;
(*2nd inertia [m^4]:                 *)Ic = Pi * dc^4 / 64;
(*product of E I:                    *)EI = Ec * Ic;
(*density of sand [kg/m^3]:          *)rhog = 2.5 * 10^3;
(*gravaitional acceleration [m/s^2]: *)g = 9.81;
(*lambda finding:                    *)
lam = lam /. FindRoot[{Cos[lam] * Sinh[lam] - Sin[lam] * Cosh[lam] == 0}, {lam, 4}];

(*** Kinematics ***)
(* (0) - Fix reference frame attached to
   the ground with the unit vectors {i0, j0, k0} *)
(* (1) - Mobile reference frame attached to the
   base with the unit vectors {i, j, k} *)

(* transformation matrix from (1) to (0) *)
R10 = {{Cos[q1[t]], 0, -Sin[q1[t]]},
        {0, 1, 0}, {Sin[q1[t]], 0, Cos[q1[t]]}};

(* transformation matrix from (0) to (1) *)
R01 = {{Cos[q1[t]], 0, Sin[q1[t]]},
        {0, 1, 0}, {-Sin[q1[t]], 0, Cos[q1[t]]}};

(** elastic deflection of the flexible free link **)
(*shape function: *)
phi = Sinh[lam] / Sin[lam] * Sin[lam * z / L] + Sinh[lam * z / L];
(*deflection:     *)x = phi * q2[t];

(** position, velcocity,
and acceleration vector of a current point P on the
link in (0) expressed in terms of (0) {i0,j0,k0} *)
(*pos. vector from O to P: *)rP = {x, 0, z}.R10;

```



```

(*vel. vector of rP:      *)vP = D[rP, t];
(*acc. vector of rP:      *)aP = D[vP, t];

(** position and acceleration vector of the mass center C
on the beam in (0) expressed in terms of (0) {i0,j0,k0} *)
(*pos. vector from O to C: *)rC = rP /. z -> 0.5*L;
(*acc. vector of rC:      *)aC = aP /. z -> 0.5*L;

(** position and velocity vector of the end T on the
beam in (0) expressed in terms of (0) {i0,j0,k0} *)
(*pos. vector from O to T: *)rT = rP /. z -> L;

(** vector from the O to the resistance application point
E on the beam in (0) expressed in terms of (0) {i0,j0,k0} *)
(*immersed depth of T:    *)zT = rT[[3]] - L*Cos[q10];
(*length from O to E:    *)LE = L - 0.5*zT/Cos[q1[t]];
(*pos. vector from O to E: *)rE = rP /. z -> LE;
(*vel. vector of rE:     *)vE = vP /. z -> LE;

(** Dynamics **)
(*gravity force: *)G = {0, 0, mc*g};

(*dynamic frictional force: Fd*)
(*coefficient:   *)etad = 6.5;
(*reference area: *)Ar = dc*zT/Cos[q1[t]];
(*H direction Fd: *)Fdh = -vE[[1]]*Ar*etad*rhog*sqrt[vE.vE];
(*V direction Fd: *)Fdv = -vE[[3]]*Ar*etad*rhog*sqrt[vE.vE];

(*static resistance force: Fs*)
(*coefficient:   *)etah = 8; etav = 21; lambda = 1.1;
(*horizontal Fs: *)Fsh = -Sign[vE[[1]]]*etah*rhog*g*dc*zT^2;
(*immeresed volume:*)V = zT/Cos[q1[t]]*Ac;
(*vertical Fs:   *)Fsv = -Sign[vE[[3]]]*etav*(zT/dc)^lambda*g*rhog*V;

(*resistance force:*)FR = {Fdh + Fsh, 0, Fdv + Fsv};

(** Equation of motion **)
Eq1 = Chop[Integrate[Cross[rP, rhoa*aP][[2]], {z, 0, L}] ==
Cross[rC, G][[2]] + Cross[rE, FR][[2]];
Eq2 = EI*(lam/L)^4*L*q2[t] +
Chop[Integrate[(rhoa*aP.R01)[[1]]*phi, {z, 0, L}] ==
(G.R01)[[1]]*(phi /. z -> 0.5*L) + (FR.R01)[[1]]*(phi /. z -> LE)];

(** Initial condition **)
(*initial angle:      *)q10 = 60*Pi/180;

```

```

(*initial deflection:          *)q20 = 0;
(*initial angular velocity:   *)dq10 = -1;
(*initial deflection derivative:*)dq20 = 0;

(***) Solving E.O.M (***)
sol = NDSolve[{Eq1, Eq2, q1[0] == q10, q1'[0] == dq10, q2[0] == q20, q2'[0] == dq20},
  {q1, q2}, {t, 0, 1}, MaxSteps -> Infinity,
  Method -> {"EventLocator", "Event" -> q1'[t], "EventAction" ->
    Throw[tend = t;, "StopIntegration"], "EventLocationMethod" ->
    "LinearInterpolation", "Method" -> "ExplicitEuler"}];

Print["stopping time of the elastic compound pendulum is ", tend, "[s]"];
Plot[Evaluate[q1[t] * 180 / Pi /. sol], {t, 0, tend}, PlotRange -> All,
  GridLines -> Automatic, Frame -> True, FrameLabel -> {"Time (s)", "q1 (deg)"}]
Plot[Evaluate[q1'[t] /. sol], {t, 0, tend}, PlotRange -> All,
  GridLines -> Automatic, Frame -> True, FrameLabel -> {"Time (s)", "dq1 (rad/s)"}]
Plot[Evaluate[q2[t] /. sol], {t, 0, tend}, PlotRange -> All,
  GridLines -> Automatic, Frame -> True, FrameLabel -> {"Time (s)", "q2 (m)"}]
Plot[Evaluate[q2'[t] /. sol], {t, 0, tend}, PlotRange -> All,
  GridLines -> Automatic, Frame -> True, FrameLabel -> {"Time (s)", "dq2 (m/s)"}]

```